

Research on the Applicability of  
Metal Foam Based Sandwich Materials  
for Friction Stir Welded Ship Structures  
with Sufficient Fatigue Life Time

HADEWICH DE MEESTER





# Research on the Applicability of Metal Foam Based Sandwich Materials for Friction Stir Welded Ship Structures with Sufficient Fatigue Life Time

HADEWICH DE MEESTER

to obtain the degree of,  
Master of Science in Marine Technology,  
at the Delft University of Technology,  
to be defended publicly on Thursday February 28, 2019 at 13:00.

Examination committee: Dr. ir. D.L. Schott,  
*Associate professor Transport Engineering and Logistics, TU-Delft*  
Dr. ir. R.C. Alderliesten,  
*Associate professor Fatigue, Damage Tolerance and Durability, TU-Delft*  
Dr. ir. M.J.M. Hermans,  
*Associate professor, Materials Science and Engineering, TU Delft*  
Dr. ir. J.H. den Besten,  
*Assistant professor Ship and Offshore Structures, TU-Delft*  
Ir. E. Huiskamp,  
*Research engineer, DAMEN Shipyards Group*

*This thesis is confidential and cannot be made public until February 28, 2022.*





“Vlinder worden is alleen weggelegd voor dappere rupsen zonder vliegangst.”

— Frans Hofmeester



# Acknowledgements

I am indebted to many people who contributed to the realisation of this thesis, but most of all, to those active at the maritime structural department of the Technical University of Delft, in particular Mr. Henk den Besten and Mr. Mirek Kaminski, at the material science department of the Technical University of Delft, in particular Mrs. Vera Popovich, and at the structural research department of DAMEN Shipyard Gorinchem, in particular Mr. Ewoud Huiskamp and Mr. Don Hoogendoorn. They all have stimulated me to prepare and finalise this thesis.

The Welding Institute Technology Centre in Yorkshire derives my gratitude for hosting me during the friction stir welding process. Along all the co-workers, I would like to express my special appreciation for Mr. Stephen Cater and Mr. Christopher Stanhope. Furthermore, I am grateful to thank Mr. Ben van de Geer and Mr. Stefan Schmuck of Havel Metal Foam to visit DAMEN Shipyard Gorinchem to enlarge my experience with the metal foam based sandwich material.

I will never forget the relentless energy and enthusiasm of the my co-students which was boosting at difficult moments, in particular Mr. Rik Hendrickx and Mr. Hugo Verhelst. Furthermore, Mr. Hugo Verhelst and Mr. Maarten van der Leij were splendid sparring partners for scientific input and research.

Not only as a token of politeness, but also as a sign of my deepest appreciation and love, I name my parents and my sister.



# Contents

<b>Abstract</b>	<b>v</b>
<b>Nomenclature</b>	<b>vii</b>
<b>Introduction</b>	<b>1</b>
<b>1 Comparative analysis of sandwich materials and conventional solids at the material level</b>	<b>5</b>
1 Introduction . . . . .	5
2 Methodology . . . . .	5
3 Results . . . . .	6
4 Discussion . . . . .	23
<b>2 Structural and economical modelling of metal foam based sandwich materials at the stiffened panel level</b>	<b>25</b>
1 Introduction . . . . .	25
2 Methodology . . . . .	25
3 Results . . . . .	37
4 Discussion . . . . .	48
<b>3 Metallographic and fatigue analysis of corner adstir fillet stationary shoulder friction stir welded double sided T-joints</b>	<b>51</b>
1 Introduction . . . . .	51
2 Methodology . . . . .	53
3 Results . . . . .	61
4 Discussion . . . . .	71
<b>Closing comments</b>	<b>75</b>
<b>A</b>	<b>79</b>
1 Introduction to sandwich materials . . . . .	79
2 Material properties of sandwich materials . . . . .	80
3 Equivalent material properties of sandwich materials . . . . .	82
4 Optimal ratio of core and face sheet thickness of sandwich materials . . . . .	84
5 Comparison of material properties of sandwich materials to conventional solid materials . . . . .	88
<b>B</b>	<b>93</b>
1 Design constraints for conventional solid material . . . . .	93
2 Design constraints for sandwich material . . . . .	102
3 Input for cost calculation model . . . . .	107

<b>C</b>		<b>111</b>
1	Test machine specification . . . . .	111
2	Estimation of required force . . . . .	113
3	Statistical analysis of fatigue data . . . . .	117
4	Log-likelihood principle . . . . .	118
5	Effective notch stress distribution . . . . .	121
<b>Bibliography</b>		<b>125</b>

# Abstract

Research to analyse and/or develop novel materials and techniques is necessary to address competition and safeguard craftsmanship in shipbuilding. In this master thesis, two new approaches to reduce the production and maintenance costs are studied: {metal foam core, metal face sheet} sandwich materials and corner adstir fillet stationary shoulder friction stir welding (FSW). The current project is a preparatory analysis for the research in which the two components will be combined. It is anticipated that their combination may generate more added value due to mutual reinforcement.

The study of metal foam based sandwich materials showed that looking at the material level, the {aluminium foam core, steel face sheet} sandwich material is theoretically promising with respect to the conventional steel solid plate in specific situations and applications. When the sandwich material is implemented as part of the stiffened panel, the expected benefit could not be realised. This confirms the search for a more selective use, such in naval vessels when one needs a high resistance to impacts and blasting, and when one wants to conserve the limited internal space.

Compared with the currently existing arc welding technique of double sided T-joints, the corner adstir fillet stationary shoulder FSW scores better on hardness and fatigue resistance of the weld. Since the properties of the weld material correspond to those of the parent material, the weld can no longer be seen as the weakest link of the structure. The fatigue experiment occasionally revealed a new failure type at the undercut, being a sharp corner created by the modified FSW shoulder. This second failure type did not impact on the overall expected failure resistance; however, the limited occurrence does not allow a final statistical interpretation.

Based upon our analyses, there is not yet a place for widespread use of {aluminium foam core, steel face sheet} sandwich materials, but there is an added value for the corner adstir fillet stationary shoulder FSW.



# Nomenclature

## Latin symbols

$A$	area / elongation
$A_c$	actual surface area of impression
$A_{eff}$	effective area
$A_{f,g}$	area girder flange
$A_{f,s}$	area stiffener flange
$A_g$	area girder
$AG$	shear stiffness
$AG_p$	shear stiffness conventional solid plate
$AG_{sm}$	shear stiffness sandwich material
$AG$	shear stiffness
$A_{HP}$	area Holland profile
$Al_{HP}$	circumference area Holland profile
$A_p$	area conventional solid plate
$A_{paint}$	paint area
$A_s$	area stiffener
$A_{weld}$	weld seam area
$A_{w,g}$	area girder web
$A_{w,s}$	area stiffener web
$B$	beam moulded ship
$C$	fatigue resistance constant / scaling factor
$C_{bw}$	weld load carrying stress coefficient
$CE_{mat,E}$	bending stiffness material cost efficiency
$CE_{mat,\sigma}$	bending strength material cost efficiency
$CE_{tot,E}$	bending stiffness total cost efficiency
$CE_{tot,\sigma}$	bending strength total cost efficiency
$C_{fuel}$	specific fuel cost
$C_{mat}$	specific material cost
$C_{mat,p}$	specific material cost conventional solid plate
$C_{mat,sm}$	specific material cost sandwich material
$C_{paint}$	specific painting cost
$C_{prod}$	specific production cost
$C_{oper}$	specific operational cost
$C_{tot}$	specific total cost

$C_w$	buckling coefficient
$C_{weld}$	specific welding cost
$C_{\epsilon,mat}$	material cost
$C_{\epsilon,prod}$	production cost
$C_{\epsilon,oper}$	operational cost
$C_{\epsilon,tot}$	total cost
$D$	flexural stiffness / depth ship
$D_p$	flexural stiffness conventional solid plate
$D_{sm}$	flexural stiffness sandwich material
$D_x$	flexural stiffness x-direction
$D_y$	flexural stiffness y-direction
$E$	Young's modulus
$E_c$	Young's modulus core
$E_{eq}$	equivalent Young's modulus
$E_{eq,sm}$	equivalent Young's modulus sandwich material
$E_f$	Young's modulus face sheet
$E_p$	Young's modulus conventional solid plate
$F$	in-plane load / force / corresponding distribution function
$F_{gl}$	global in-plane load
$F_{max}$	maximum force applied in test machine
$F_{min}$	minimum force applied in test machine
$G$	shear modulus
$G_c$	shear modulus core
$G_f$	shear modulus face sheet
$H$	effective torsional stiffness
$I$	moment of inertia
$I_g$	moment of inertia girder
$I_{HP}$	moment of inertia Holland profile
$I_p$	moment of inertia conventional solid plate
$I_s$	moment of inertia stiffener
$I_{sm}$	moment of inertia sandwich material
$K_p$	in-plane stiffness conventional solid plate
$K_{sm}$	in-plane stiffness sandwich material
$K_t$	stress concentration factor
$L$	length moulded ship / indenter load / likelihood
$\mathcal{L}$	log-likelihood
$M$	bending moment
$M_{gl}$	global hull bending moment
$M_{gl,hog}$	global hull bending moment hogging
$M_{gl,sag}$	global hull bending moment sagging
$M_{max}$	maximum bending moment
$M_s$	still water bending moment / bending moment stiffener
$M_w$	wave bending moment

$N$	(total) number of cycles until failure
$P_E$	Euler buckling load
$P_{E,s}$	Euler buckling load stiffener
$P_{E,g}$	Euler buckling load girder
$Q$	shear force
$Q_p$	shear force conventional solid plate
$R_m$	tensile strength
$R_{p,0.2}$	proof stress
$S$	statical moment of area / stress range
$S_e$	effective notch stress range
$S_f$	fatigue limit
$S_n$	nominal stress range
$S_{n,eff}$	effective nominal stress range
$V_{weld}$	weld seam volume
$W$	weight
$W_p$	weight conventional solid plate
$W_{sm}$	weight sandwich material
$W_{tot}$	total weight
$Z$	section modulus
$Z_g$	section modulus girder
$Z_{HP}$	section modulus Holland profile
$Z_s$	section modulus stiffener
$Z_{sm}$	section modulus sandwich material
$a$	width stiffened panel
$a_{eff}$	effective girder length
$b$	width
$c_l$	confidence level
$d$	mean diagonal length
$d_{sm}$	distance between centre-lines of opposite face sheets
$d_u$	distance between centre of two upper rollers
$d_1$	lever bottom roller
$d_2$	lever upper roller
$e_{diff}$	difference in neutral axis height
$e_{outer}$	outer fibre distance
$e_{outer,g}$	outer fibre distance girder
$e_{outer,p}$	outer fibre distance conventional solid plate
$e_{outer,s}$	outer fibre distance stiffener
$e_{outer,sm}$	outer fibre distance sandwich material
$e_x$	height of neutral axis in x-direction
$e_y$	height of neutral axis in y-direction
$h$	height
$h_{mb}$	height of modification block

$f$	natural frequency / probability density function
$f_E$	specific Euler buckling load
$f_{gl}$	specific global in-plane load
$g$	acceleration of gravity
$h$	height cross plate
$h_{eff}$	effective height
$h_{eq}$	equivalent height
$h_{f,g}$	girder flange height
$h_{f,s}$	stiffener flange height
$h_{HP}$	height Holland profile
$h_{min}$	minimal thickness
$h_p$	conventional solid plate thickness
$h_{p,max}$	upper limit conventional solid plate thickness
$h_{p,min}$	lower limit conventional solid plate thickness
$h_{sm}$	sandwich plate thickness
$h_{w,g}$	girder web height
$h_{w,g,max}$	upper limit girder web height
$h_{w,g,min}$	lower limit girder web height
$h_{w,s}$	stiffener web height
$k$	Euler buckling coefficient
$l$	length length stiffened panel
$l_{mb}$	length modification block
$l_{1,c}$	first length central roller notch
$l_{1,u}$	first length upper roller notch
$l_{2,c}$	second length central roller notch
$l_{2,u}$	second length upper roller notch
$m$	amount of longitudinal bulkheads / fatigue resistance slope
$n$	amount of longitudinal stiffeners
$p$	water pressure
$q$	number of girders
$q_{max}$	upper limit number of girders
$q_{min}$	lower limit number of girders
$r$	fillet radius
$r_b$	radius bottom roller
$r_c$	radius central roller
$r_l$	load ratio
$r_u$	radius upper roller
$s$	radius of circle inscribed in hexagonal cell
$s_g$	girder spacing
$s_{g,eff}$	effective girder spacing
$s_s$	stiffener spacing
$s_{s,eff}$	effective stiffener spacing
$t_c$	core thickness / depth central roller notch

$t_{c,max}$	upper limit core thickness
$t_{c,min}$	lower limit core thickness
$\hat{t}_{c,1}$	first core thickness criterion
$\hat{t}_{c,2}$	second core thickness criterion
$t_f$	face sheet thickness
$t_{f1}$	top face sheet thickness
$t_{f2}$	bottom face sheet thickness
$t_{f,g}$	girder flange thickness
$t_{f,min}$	lower limit face sheet thickness
$t_u$	depth upper roller notch
$t_{w,g}$	girder web thickness
$t_{w,s}$	stiffener web thickness
$t_1$	thickness bottom plate
$t_2$	thickness cross plate
$u$	amount of transversal bulkheads
$w$	width
$w_c$	specific weight core
$w_f$	specific weight face sheet
$w_p$	specific weight conventional solid plate
$w_{sm}$	specific weight sandwich material
$x$	longer side of plate
$y$	shorter side of plate
$z$	level at which shear stress is determined

## Greek symbols

$\alpha$	(half) notch angle
$\beta$	factor to calculate plate stress at center, simply supported / stress angle
$\beta_1$	factor to calculate plate stress at center of long edge, clamped
$\beta_2$	factor to calculate plate stress at center, clamped
$\gamma$	time period
$\delta$	data type (failure = 1, run-out = 0)
$\delta_g$	deflection girder
$\hat{\delta}_g$	allowable deflection girder
$\delta_s$	deflection stiffener
$\hat{\delta}_s$	allowable deflection stiffener
$\zeta_a, \zeta_s$	first blunt body eigenvalue of antisymmetry part
$\lambda_a, \lambda_s$	first eigenvalue of antisymmetry part
$\mu$	discount factor / mean
$\mu_a, \mu_s$	stress amplitude of antisymmetry part
$\mu_{S_f}$	mean according to fatigue limit
$\nu$	Poisson ratio
$\nu_c$	Poisson ratio core
$\nu_f$	Poisson ratio face sheet
$\nu_p$	Poisson ratio conventional solid plate
$\xi$	discount ratio
$\rho$	density
$\rho_c$	density core
$\rho_{eq}$	equivalent density
$\rho_{eq,sm}$	equivalent density sandwich material
$\rho_f$	density face sheet / fictitious notch radius
$\rho_g$	density girder
$\rho_p$	density conventional solid plate
$\rho_s$	density stiffener
$\rho_{sm}$	density sandwich material
$\rho_w$	density sea water
$\rho^*$	micro-structural length
$\sigma$	stress / standard deviation
$\sigma_b$	bending stress
$\sigma_{b,max}$	maximum bending stress
$\sigma_{b,p}$	bending stress conventional solid plate
$\sigma_{b,sm}$	bending stress sandwich material
$\sigma_{cl}$	standard deviation according to confidence level
$\hat{\sigma}_{dimp,f}$	critical dimpling stress face sheet
$\hat{\sigma}_E$	critical Euler buckling stress
$\sigma_{eq}$	equivalent stress
$\sigma_f$	stress face sheet / structural field stress

$\hat{\sigma}_f$	fatigue strength
$\sigma_g$	stress girder
$\sigma_{gl}$	global hull force stress
$\sigma_m$	membrane stress
$\sigma_{m,p}$	membrane stress conventional solid plate
$\sigma_{m,sm}$	membrane stress sandwich material
$\sigma_{max}$	peak stress
$\sigma_n$	notch stress
$\sigma_p$	stress conventional solid plate
$\sigma_s$	stress stiffener / structural stress
$\sigma_{S_f}$	standard deviation according to fatigue limit
$\hat{\sigma}_u$	allowable ultimate stress
$\hat{\sigma}_{wr}$	allowable wrinkling stress
$\hat{\sigma}_{wr,f}$	allowable wrinkling stress face sheet
$\hat{\sigma}_y$	allowable yielding stress
$\hat{\sigma}_{y,c}$	allowable yielding stress core
$\hat{\sigma}_{y,f}$	allowable yielding stress face sheet
$\hat{\sigma}_{y,g}$	allowable yielding stress girder
$\hat{\sigma}_{y,p}$	allowable yielding stress conventional solid plate
$\hat{\sigma}_{y,s}$	allowable yielding stress stiffener
$\tau$	shear stress
$\tau_c$	shear stress core
$\tau_{c,max}$	maximum shear stress core
$\tau_f$	shear stress face sheet
$\tau_{f,max}$	maximum shear stress face sheet
$\tau_p$	shear stress conventional solid plate
$\tau_{sm}$	shear stress sandwich material
$\hat{\tau}_y$	allowable shear yielding stress
$\hat{\tau}_{y,c}$	allowable shear yielding stress core
$\hat{\tau}_{y,f}$	allowable shear yielding stress face sheet
$\hat{\tau}_{y,g}$	allowable shear yielding stress girder
$\hat{\tau}_{y,p}$	allowable shear yielding stress conventional solid plate
$\hat{\tau}_{y,s}$	allowable shear yielding stress stiffener
$\omega$	circular frequency
$\{\chi_s, \chi_a\}$	first eigenvalue coefficient of antisymmetry part
$\{\omega_s, \omega_a\}$	first blunt body eigenvalue coefficient of antisymmetry part
$\phi$	loading factor

## Abbreviations

AS	advancing side of the FSW weld
ASo	aluminium solid
AfCAFSa	{aluminium foam core, aluminium face sheet} sandwich
AfCSFSa	{aluminium foam core, steel face sheet} sandwich
AhCAFSa	{aluminium honeycomb core, aluminium face sheet} sandwich
AR	aspect ratio
CDF	corresponding distribution function
Cr	chromium
Cu	copper
DS	double sided
Fe	iron
FEM	finite element model
FSW	friction stir welding
HaZ	heat affected zone
HB	Brinell hardness
HCF	high cycle fatigue
HCl	hydrochloric acid
HF	hydrofluoric acid
HNO <sub>3</sub>	nitric acid
H <sub>2</sub> O	distilled water
HP	Holland profile
HV	Vickers hardness
IIW	International Institute of Welding
LCF	low cycle fatigue
LD	longitudinal direction
MCF	medium cycle fatigue
MfMS	metal foam metal sandwich
Mg	magnesium
MhMS	metal honeycomb metal sandwich
MIG	metal inert gas
MLE	maximum likelihood estimate
Mn	manganese
Ni	nickel
NPV	net present value
OS	one sided
PDF	probability density function
PeCAFSa	{polymer elastomer core, aluminium face sheet} sandwich
PfCPFSa	{polymer foam core, polymer face sheet} sandwich
PM	parent material
PVC	polyvinyl chloride
PUR	polyurethane

QI	quasi-isotropic
RS	retreating side of the FSW weld
SCF	stress concentration factor
SSo	steel solid
Si	silicon
SPo	Stan Pontoon
TD	transversal direction
Ti	titanium
TIG	tungsten inert gas
TMaZ	thermomechanically affected zone
TWI	The Welding Institute
UD	uni-directional
Zn	Zinc



# Introduction

Two major principles are necessary to address competition and safeguard craftsmanship: continuous development of the internal knowledge and adoption of the latest technologies. As this is the rule for all businesses, it regards also the ship industry. Shipyards face an increasing construction complexity, a demand for higher technical capacity and a call for shorter lead times and reduction of costs, such as initial purchase, maintenance and operational costs during the life cycle of the vessel. [38]

The standard shipbuilding process includes a concept and preliminary design, a detailed design, a production design and the actual production, identified by Eyres and Bruce [30]. The design phase is prescribed in rules and regulations of a classification society and authorities, and is characterised by an iterative process in which a cluster of possible concept designs is narrowed to one final design that will go in production. The production process consists of the fabrication of the required small parts (primary, secondary and tertiary stiffening components), part assembly, block assembly, grand block assembly and hull assembly. Block outfitting (installation of pipes and equipment) is exerted simultaneously in different phases. A well considered planning of the whole complex production process is therefore essential. When the vessel has been completed, sea trials take place to check if all the predetermined properties are sufficient.

During the operational life, a vessel is being subjected to the environment itself and the service load. Besides those two influence factors, the fatigue life time of the vessel is determined by the chosen material (surface integrity, welding technique) and the geometry (structural design). [23] To make sure that maintenance and repair work is done in the least possible time with the highest efficiency and the optimum cost, a maintenance plan must be drawn up.

To accomplish the demand of the customer to reduce the building cost and the maintenance cost, production efficiency is the key concept [30]. The latter can be achieved by three different approaches: (1) effective production planning, (2) smart designing using novel materials, and (3) better working methods using efficient welding techniques [27, 33, 64].

In this thesis, the focus will lie on two aspects: smart designing using novel materials, in particular metal foam based sandwich materials, and better working methods using efficient welding techniques, such as corner adstir fillet stationary shoulder friction stir welding (FSW) .

This master thesis research is a preparatory analysis for a larger project where a combination of both subjects is intended. As mentioned before, the production and maintenance costs are mainly influenced by the amount and the joining type between the different structures to construct the hull of the ship. Since the use of sandwich materials is linked to a lower amount of welds, and the friction stir welding technique will influence the weld type, the two niches could reinforce each other.

The concept of using two co-operating face sheets that are separated by a distance (core), dates back to the 1820's and has been first discussed and analysed separately by two researchers Duleau and Fairbairn. In the 1930's, England and the United States allowed the first commercial application of bonded sandwich composites, leading its widespread acceptance with a lot of inventions followed. The first prototypes of sandwich materials were small planes used in World War Two,

the Mosquito aircraft for example. Since then, more research has been done giving rise to a lot of publications, to more modification and to more frequent application of the sandwich material concept. [76]

The first widely used core material was balsa wood, but the transformation to polyvinyl chloride (PVC) and polyurethane (PUR) core was made in the late 1950's due to the demand for an application in constructions, having weight as a critical factor. Today, further development of the core and face sheets is carried out in an effort to further reduce the weight of the material in general, leading to metal based sandwich materials success. Sandwich materials are promising in mechanical, failure and functional properties: they are stiffer than a dense sheet of equal mass, they have better tensile properties, they could avoid possible problems with surface damage, they have good insulation features et cetera.[80]

Sandwich materials show a potential to incorporate smart functionality. Smart designing, including smart functionality has as objective to simplify the structural design and subsequently be effective to reduce the overall weight of the vessel [42]. For the operational cost earning, an overall weight reduction of the ship is namely essential for lowering the fuel consumption. This may also be achieved by a simplification of the ship structural geometry, following the implementation of novel materials. One important consideration with novel materials is that they must still be economical feasible for the shipyard to implement. To add this economical aspect to this thesis, the Technical University of Delft entered into a partnership with DAMEN Shipyards by implementing the concepts on real ship and financial data.

Effective maintenance planning and increase of the fatigue life time of the vessel are considered to reduce the maintenance costs, since fatigue is one of the main deterioration mechanisms that affect the longevity of ship structures [39]. According to Josefson et al. [42], low heat input welding processes have potential to reduce the residual stresses remaining after the joining process. Over the recent years, several low heat input processes have stand out as an alternative to the conventional higher heat input welding technique, in particular submerged arc welding, tandem welding, double sided processes, plasma arc welding, keyhole TIG welding, laser beam welding, laser hybrid welding and friction stir welding. In this thesis the fatigue life time is investigated for the novel corner welding technique, namely corner adstir fillet stationary shoulder friction stir welding.

This master thesis consists of three different competences of research: mathematical modelling, economical modelling and practical testing, which are structured into three separate research chapters:

1. *Comparative analysis of sandwich materials and conventional solids at the material level*

The first chapter is confined to a comparison study of four different sandwich materials, in particular {metal foam core, metal face sheet}, {metal honeycomb core, metal face sheet}, {polymer elastomer core, metal face sheet} and {polymer foam core, polymer face sheet} sandwich materials, and will give an answer to the research question: How do material properties of {metal foam core, metal face sheet} sandwich materials compare to other types of sandwich materials and to the conventional solid material?

2. *Structural and economical modelling of metal foam based sandwich materials at the stiffened panel level*

The study is restricted to {metal foam core, metal face sheet} sandwich materials for the economical analysis of the second chapter and gives a solution to the research question: What is the mechanical added value if {aluminium foam core, steel face sheet} sandwich materials are implemented as part of the stiffened panel with respect to the conventional steel solid material and is it economically feasible in DAMEN vessels?

3. *Metallographic and fatigue analysis of corner adstir fillet stationary shoulder friction stir welded double sided T-joints*

The third chapter is involved to response to the research question: What is the fatigue resistance of a double sided T-joint using corner adstir fillet stationary shoulder friction stir welding compared to arc welding?

Since in the current stage of the research every chapter is a small research on its own, the introduction, the methodology, the results and the discussion will be formulated for each research chapter separately. At the end, closing comments are formulated to reflect on the initial goal stated in the introduction and to combine the findings of each research chapter.



# Chapter 1 | Comparative analysis of sandwich materials and conventional solids at the material level

## 1 Introduction

A product comprising a highly porous core and two face sheets is called a sandwich material. The different layers are firmly attached to each other by a bonding. The bonding type will vary depending on the type of sandwich materials and the material choice of the separate layers. [6]

The first research chapter has as objective to map a selection of characteristics of four chosen sandwich materials and a conventional aluminium solid (ASo) material. The four chosen sandwich material types are the closed cell {aluminium foam core, aluminium face sheet} sandwich (AfCAFSa), the {aluminium honeycomb core, aluminium face sheet} sandwich (AhCAFSa), the {polymer elastomer core, aluminium face sheet} sandwich (PeCAFSa) and the {polymer foam core, polymer face sheet} sandwich (PfCPFSa) materials. The characteristics are divided in five subcategories: general properties, mechanical properties, failure properties, functional properties and practical properties. The comparative analysis of the selected general, functional and practical properties is based on existing literature. For the selected mechanical and failure properties, mathematical modelling is used implementing renewed and adapted formulas. With respect to Chapter 2, the mechanical and failure properties are also determined for the conventional steel solid (SSo) and the {aluminium foam core, steel face sheet} sandwich (AfCSFSa) material. For the comparison based on literature, solely the aluminium configuration is assumed, due to the available amount of knowledge in literature.

## 2 Methodology

To compare the four chosen sandwich material types, as shown in Figure 1.1, mutually and to the conventional solid material, first the general properties as the manufacturing of the sandwich material itself and the joining techniques at structural level and at detail level are reflected. The mechanical properties related to bending with yield failure are compared using equivalent material properties. Differences in failure modes are examined thereafter. Because sandwich materials have their main application in multi-functional problems, the functional properties as thermal, electric, impact, vibrations and corrosion are compared. Finally, the practical aspects are looked at from the viewpoint of a shipyard: Are the plate dimensions of the produced material sufficient? What is the price, and how is this related to the obtained benefits? What is the environmental impact of the material these days?

Table 1.1 gives an overview of the chosen face sheet and core material types of the sandwich materials and the conventional solids.

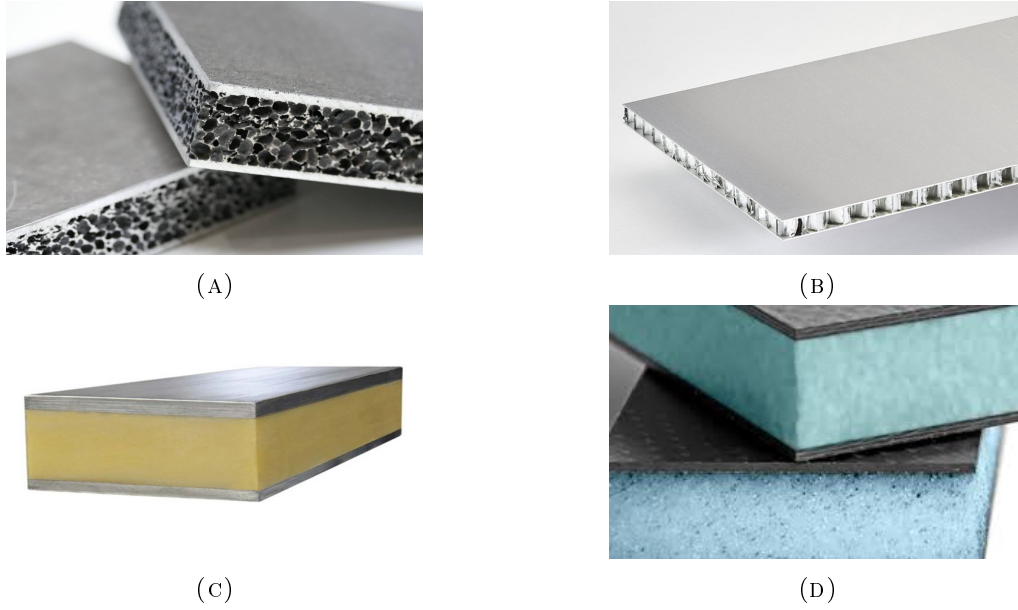


FIGURE 1.1: Overview of the four types of sandwich materials (two face sheets + core) (size not comparable). (A) {aluminium foam core, aluminium face sheet} sandwich (AfCAFSa), (B) {aluminium honeycomb core, aluminium face sheet} sandwich (AhCAFSa), (C) {polymer elastomer core, aluminium face sheet} sandwich (PeCAFSa) and (D) {polymer foam core, polymer face sheet} sandwich (PfCPFSa)

TABLE 1.1: Overview of the chosen material choice of the conventional solid materials and sandwich materials. FRP = fibre-reinforced polymer, PUR = polyurethane, PVC = polyvinyl chloride

Material	ASo	SSo	AfCAFSa	AfCSFSa	AhCAFSa	PeCAFSa	PfCPFSa
Face sheet	aluminium	steel	aluminium	steel	aluminium	aluminium	glass FRP
Core	/	/	aluminium	aluminium	aluminium	PUR	PVC

### 3 Results

#### 3.1 General properties

##### 3.1.1 Manufacture of sandwich material

For the manufacturing of a **AfCAFSa** material, two production methods exist, in particular ex-situ bonding and in-situ bonding.

In ex-situ bonding, a solid metal foam panel is bonded to two dense face sheets either by adhesive bonding, diffusion bonding or brazing. The procedure is visualised in Figure 1.2a. The main disadvantage of ex-situ bonding is that no metallic bonding is obtained.

For in-situ bonding, a semi-solid or even liquid state of the metal foam is used. There are three different ways to realise an in-situ bonding. One way is to start with a three-layer metal composite, consisting of a foamable aluminium alloy sheet between two metal face sheets created by extrusion or powder rolling. Expansion of the core is followed after heating to the foaming temperature of the core, while the face sheets remain solid and firmly attached to the core layer (Figure 1.2b). The main advantage is that a full metallic bonding is obtained.

In order to avoid the additional process step of making a three-layer composite, one aimed to try to form directly a metal foam sandwich structure, by expanding a core sheet of foamable precursor, while the two face sheets are kept at the originally intended distance. This method is

shown in Figure 1.2c. However, difficulties arise to obtain a full metallic bond due to the oxide layers on the face sheets.

The last possible method is based on a manipulation of the foaming process, to create automatically a dense skin at both sides during foaming without using face sheets (Figure 1.2d). [5]

In the comparison, the in-situ bonding with a full metallic bonding (type 2) is used.

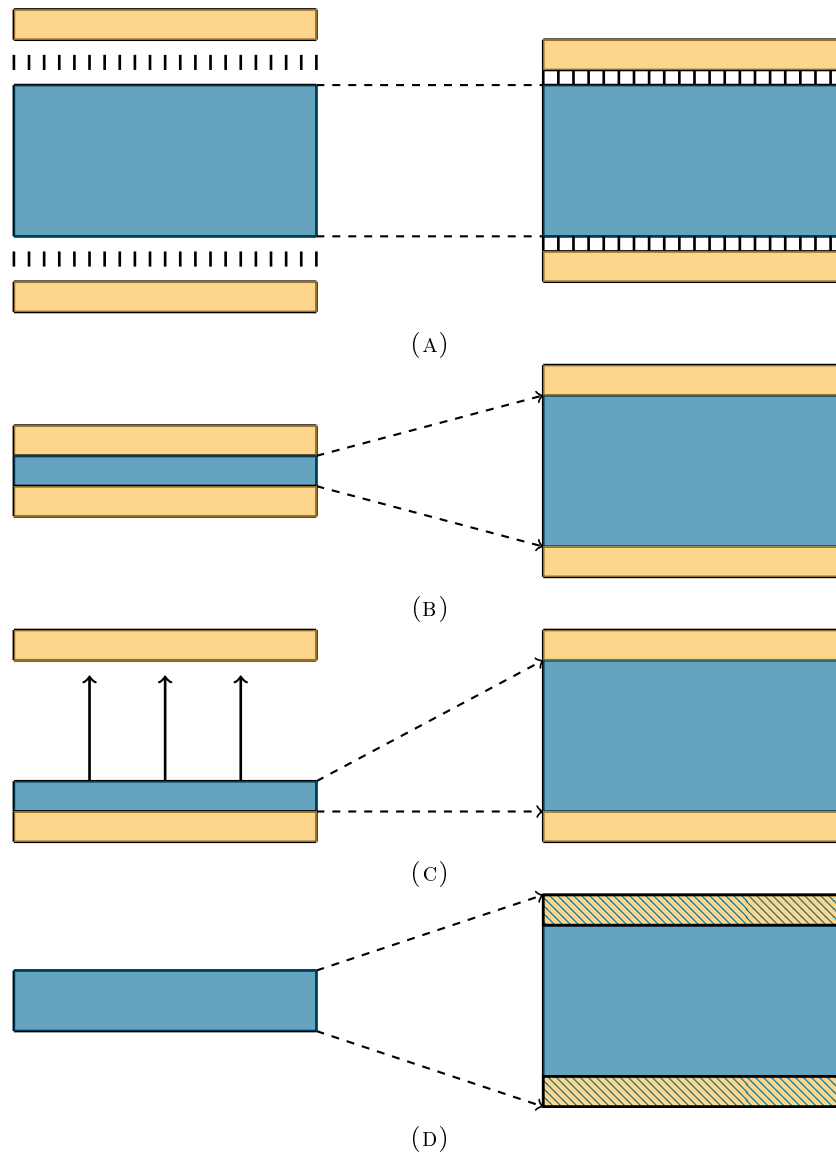


FIGURE 1.2: *Manufacturing techniques of {aluminium foam core, aluminium face sheet} sandwich (AfCAFSa) material [5]. (A) ex-situ bonding, (B) in-situ bonding: foaming of three-layer composite, (C) in-situ bonding: expanding foam between two face sheets and (D) in-situ bonding: structural / integral foams*

The manufacture process for **AhCAFSa** materials is the ex-situ bonding as described above, since the honeycomb core is made separately and is already seen as a structure on its own when the bonding is performed. As such, no metallic bonding is present.

The production of the **PeCAFSa** material is done by a press joining rolling technique as visualised in Figure 1.3. The two-steps procedure has to be repeated twice, once for the lower metal face sheet and once for the upper metal face sheet. In the first step, one of the two metal face sheets is cleaned and coated with a layer of epoxy resin as the bonding glue. The metal is heated

to activate the resin. In the second step, the press joining rolling process is applied to merge the polymer core with the activated metal face sheet. Now one half of the sandwich material is created. Thereafter, the whole process should be repeated for the second metal face sheet. [13]

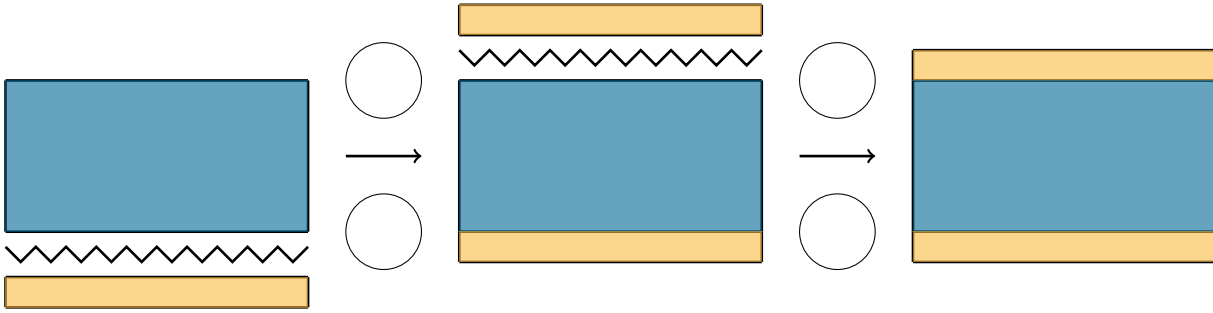


FIGURE 1.3: *Manufacturing technique of {polymer elastomer core, aluminium face sheet} sandwich (PeCAFSa) material [13]*

In the majority of cases, the production process of **PfCPFSa** materials requires a mould. The three layers of the sandwich material are consecutively placed in the mould as dry-material. The configuration is vacuumed and the resin is injected to bond the three layers at the same time. Compared to the fabrication of a less dense core (honeycomb), the procedure is more complicated since the vacuum process must be repeated three times, in particular creating face sheet 1 and 2 separately and the third step is to bond the face sheets with the honeycomb core. [80].

### 3.1.2 *Joining at structural level: butt-joint*

The joining of two **AfCAFSa** or two **AhCAFSa** structures is similar to that of two conventional solid plates: laser welding, tungsten inert gas (TIG), metal inert/active gas (MIG/MAG) welding and soldering/brazing. [3, 5, 51]

**Laser welding** The two materials are joined through the use of a laser, which results in a narrow, deep weld and high welding rates.

**TIG, MIG/MAG welding** TIG and MIG/MAG welding are both examples of the arc welding techniques. For TIG welding a long wolfram (tungsten) welding rod is used which will not be consumed during the welding process, due to its high fusion point. When the arc is burning between the weld piece and the welding rod, the fusion energy is produced. MIG/MAG welding makes use of a continuously feeding wire. MIG welding is performed in atmosphere of inert gas, which implies that the shielding gas will not react with other substances, while an atmosphere of reacting gases is present for MAG welding, and reflects that the shielding gas will react with the other substances.

**Soldering/brazing** The two materials are joined together by, first, melting the material itself and thereafter adding a filler metal into the joint. One should take care that the filler metal always has a lower melting point than the adjoining metal.

For **PeCAFSa** materials, welding is the main joining possibility. When a soft core is chosen, the core could be negatively affected by the melting of the foam. [35, 56],

**PfCPFSa** materials on the contrary must be glued and laminated to join two structures. The lamination process is very time consuming: first, both elements need to be cut off with a specific ratio. Then, the empty space must be padded by glueing multiple layers consecutively until the same strength and stability as the parent material is obtained. The property of the chosen glue must be in accordance with those of the core material itself. [80]

### 3.1.3 Joining at detail level: corner-joint

When two plates are placed perpendicular, a corner connection is present. This connection is mainly known from a plate-stiffener combination. Some possible corner-joints, in particular double sided (DS) T-joint options of two plates (combination of solid and sandwich material, or full sandwich material) are shown in Figure 1.4 to give an impression and arouse interest. These corner joints can also be applicable on one sided (OS) T-joints. In order to transfer the tensile stress through the face sheets and the shear stress through the core in the most optimal way, one should decide whether the stiffener should be welded on the base plate or through the base plate. Since all these options are not yet investigated for the **AfCAFSa** material, an analysis of the joining options for structural details will follow in a later stage of the larger research project.

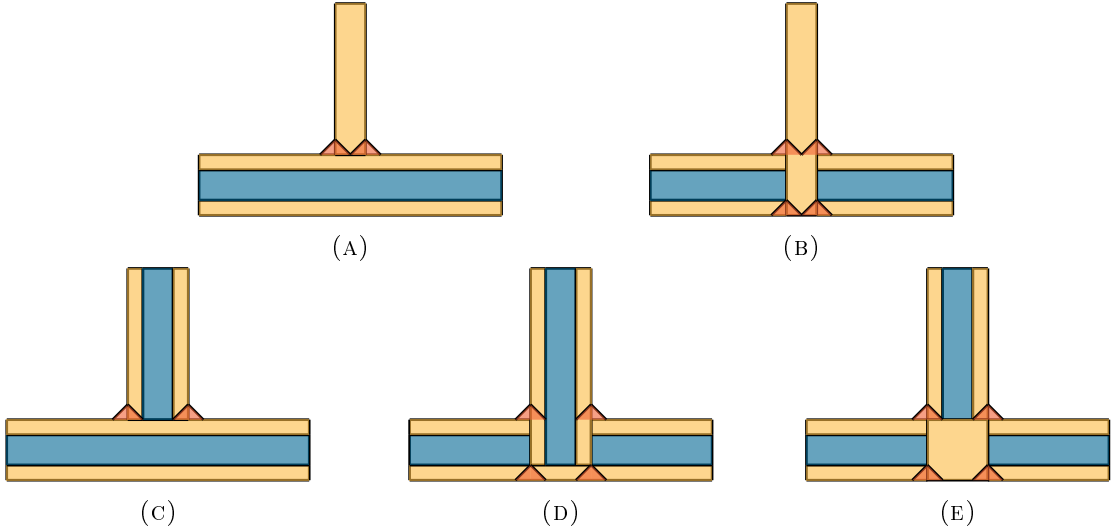


FIGURE 1.4: *Examples of corner joints (DS T-joints) using sandwich materials as base plate. In (A) and (B) the sandwich material and conventional solid material are joined together, while (C), (D) and (E) structures using two sandwich materials are visualised.*

### 3.1.4 Conclusion

When summarising the findings based on the existing literature, Table 1.2 illustrates the relation of the four chosen sandwich materials with respect to the conventional aluminium solid material. Concerning the manufacturing and joining possibilities, all sandwich materials need extra care. Within the group of sandwich material types, the **AfCAFSa** material can be seen as most promising followed by the **AhCAFSa** material, since these required production techniques are less complicated.

TABLE 1.2: *Qualitative comparison of selected general properties of the four chosen sandwich materials relative to the conventional solid material, based on personal judgement. (-) property is worse, (- -) property is much worse, (=) property is equal, (+) property is better, (++) property is much better*

Property		ASo	AfCAFSa	AhCAFSa	PeCAFSa	PfCPFSa
Manufacture	§3.1.1	1	-	--	--	--
Joining at structural level	§3.1.2	1	=	=	-	-
Joining at detail level	§3.1.3	1	-	-	-	-

### 3.2 Equivalent material properties

A specific ratio, one face sheet thickness divided by the overall material height ( $t_f/h_{sm}$ ), is created as a comparator to be able to calculate the equivalent sandwich material properties. A uniform material property is created for the sandwich material to equal the geometry of a conventional solid plate. The formulas for sandwich materials are based on the concepts of Pflug and Verpoest [61]. The specific geometry (Figure 1.5) is just a simple illustration, since the comparison of the equivalent material properties will be carried out per unit density. Because a sandwich material is composed of layers of different materials with different densities, an equivalent density  $\rho_{eq}$  has to be defined in the first place. The derivations of the used formulas are provided in Section 3, Supplement A.

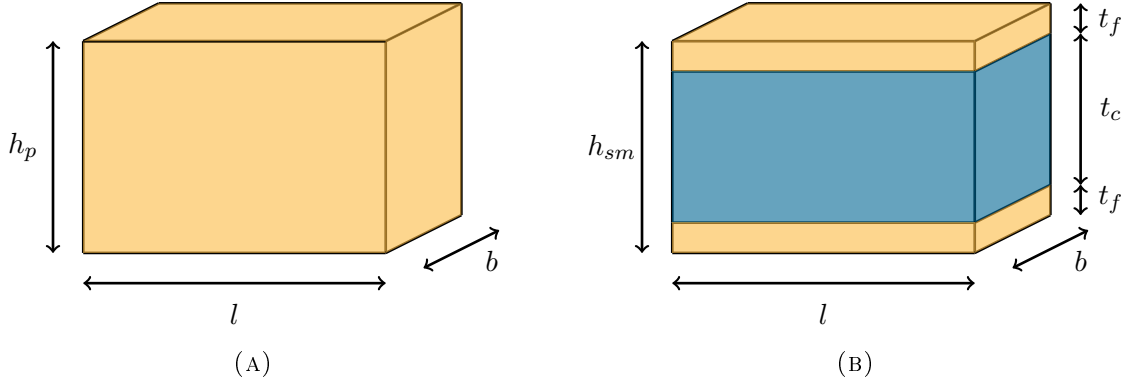


FIGURE 1.5: *Schematic illustration of the parameters to calculate the equivalent material properties of the sandwich material (B) with respect to the conventional solid material (A).*

Based on Allen [1, Chapter 11], the optimal relation between the thickness of the face sheets and the total thickness, having the lowest weight, can be derived for each design criterion with respect to yield; specific bending stiffness (Equation (1.1)) or specific bending strength (Equation (1.2)).

$$\frac{t_f}{h_{sm} E} = \frac{\rho_c}{4\rho_f + 2\rho_c} \quad (1.1)$$

$$\frac{t_f}{h_{sm} \sigma} = \frac{\rho_c}{2\rho_f + 2\rho_c} \quad (1.2)$$

The selection of the design criteria bending is based on the fact that bending is the largest advantage of sandwich materials with respect to conventional solids. In addition, stiffness and strength are most commonly used parameters in design processes. The relations are dependent on the density of the core and of the face sheet material. Equation (1.1) and Equation (1.2) are only valid for sandwich materials and cannot be applied for the conventional solid material, because the simplified flexural stiffness  $D_{sm}$  of a sandwich material is used to derive the optimal core height  $t_c$  and the face sheet thickness  $t_f$ . For the conventional solid plate it is assumed that  $t_f/h_p = 1/2$ .

As mentioned in the introduction, the conventional steel solid (SSo) and the {aluminium foam core, steel face sheet} sandwich (AfCSFSa) material are added in the comparison for the equivalent mechanical properties due to the fact a steel configuration is later on used for the structural and economical modelling (Chapter 2).

For a honeycomb core the characteristics are different looking at the longitudinal direction (LD) or the transversal direction (TD). In the comparison the value of the TD is used. For the FRP, the fibres can be laminated uni-directional (UD) or quasi-isotropic (QI). In the comparison the value of the quasi-isotropic laminated fibres are used. The latter is applied in the analysis, since an overall structure must incorporate loading and stresses in all directions. All the needed characteristics for the different material types are given in Table 1.3.

TABLE 1.3: *Approximate characteristics of different face sheet and core materials, where  $\rho$  is expressed in  $[kg/m^3]$ ,  $E$  is expressed in  $[MPa]$ ,  $\hat{\sigma}_y$  is expressed in  $[MPa]$ ,  $LD = longitudinal\ direction$ ,  $TD = transversal\ direction$ ,  $UD = uni-directional$ ,  $QI = quasi-isotropic$ . ( $\otimes$ ) range  $\rho = \{500 - 900\} [kg/m^3]$ . [37, 28, 80]*

Material	Density $\rho$	Young's Modulus $E$	Yield stress $\hat{\sigma}_y$
Aluminium	2755	70 000	120
Steel	7850	210 000	235
Aluminium foam	800 $\otimes$	760	10
Aluminium honeycomb LD	127	2 340	9.7
Aluminium honeycomb TD	127	2 340	9.7
Elastomer foam	1050	750	16
Glass FRP UD	2550	30 000	1 000
Glass FRP QI	2550	15 000	250
PVC foam	130	135	2.4

Based on Table 1.3, and following Equation (1.1) and Equation (1.2), the optimal ratios to obtain the largest specific bending stiffness and the largest specific bending strength can be determined for all material types (Table 1.4).

TABLE 1.4: *Optimal ratio of the face sheet thickness to the total thickness sandwich material for the chosen sandwich materials and the conventional solid materials.*

	<b>ASo</b>	<b>SSo</b>	<b>AfCAFSa</b>	<b>AfCSFSa</b>	<b>AhCAFSa</b>	<b>PeCAFSa</b>	<b>PfCAFSa</b>
$\frac{t_f}{h_{sm} E}$	1/2	1/2	6/100	2/100	1/100	8/100	1/100
$\frac{t_f}{h_{sm} \sigma}$	1/2	1/2	11/100	4/100	2/100	4/100	2/100

### 3.2.1 Density

In the derivation of the equivalent density (Equation (1.3)), it was assumed that the thickness of the sandwich material is equal to the thickness of the conventional solid plate,  $h_{sm} = h_p$  (see Section 3, Supplement A). [61] Depending on the design criterion (bending stiffness or bending strength) a different equivalent density is obtained, since the optimal ratio  $t_f/h_{sm}$  differs.

$$\rho_{eq} = \frac{2t_f}{h_{sm}}\rho_f + \frac{t_c}{h_{sm}}\rho_c = \rho_f - (\rho_f - \rho_c) \left(1 - 2\frac{t_f}{h_{sm}}\right) \quad (1.3)$$

Table 1.5 shows the values after substituting the corresponding density values based on Table 1.3 and the calculated ratio (Table 1.4). The core density has the largest share in the value of the equivalent density, yielding the lowest density for the **AhCAFSa** and the **PfCPFSa** core followed by the **AfCAFSa** and **AfCSFSa** core.

TABLE 1.5: Optimal equivalent density, expressed in  $[\text{kg}/\text{m}^3]$ , for the bending stiffness and bending strength criteria of the chosen sandwich materials and the conventional solid materials.  $\rho$  = density,  $E$  = Young's modulus,  $\sigma$  = bending stress

	ASo	SSo	AfCAFSa	AfCSFSa	AhCAFSa	PeCAFSa	PfCPFSa
$\rho_{eq,E}$	2760	7850	1050	1140	190	1320	190
$\rho_{eq,\sigma}$	2760	7850	1240	1450	240	1520	250

### 3.2.2 Specific bending stiffness efficiency

Because the values for the Young's modulus  $E$  largely differ between the face sheet and core types (Table 1.3), an equivalent bending stiffness  $E_{eq}$  is calculated for the sandwich materials using Equation (1.4) (see Section 3, Supplement A). The performance ratio for the bending stiffness efficiency is created by the equivalent bending stiffness  $E_{eq}$  and the equivalent density  $\rho_{eq,E}$ , following the relation derived by Ashby [2], in particular  $E_{eq}^{1/3}/\rho_{eq,E}$ , valid for the minimum weight design of stiff plates. In this way, the performance can be analysed qualitatively because it is made independently of a chosen thickness (specific equivalent bending stiffness). Using the optimal ratio for the stiffness design criterion, the largest value is calculated. [61] In the classical analysis of conventional structures, the shear deformation is regarded as less important for long beams because bending dominates, the shear part is only a fraction of the bending part. Therefore, it is not necessary to include the shear stiffness for the conventional plate. [80] Because sandwich materials have a larger thickness, the beam cannot be seen as slender, and therefore the shear contribution is more prominent.

$$E_{eq} = \frac{EI_{sm}}{I_p} = E_f + (E_f - E_c) \left(1 - 2\frac{t_f}{h_{sm}}\right)^3 \quad (1.4)$$

Figure 1.6 presents the location of the separate sandwich materials, on the map made by Ashby [2].

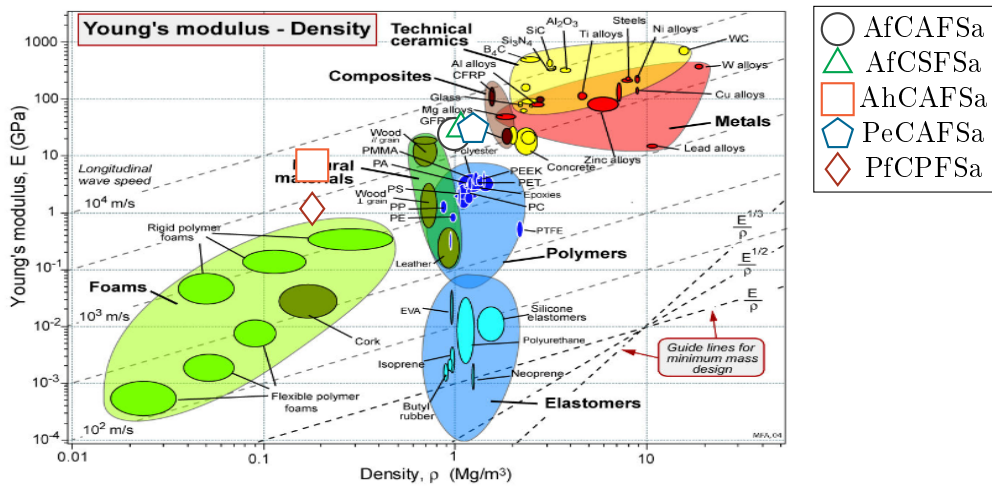


FIGURE 1.6: Material selection chart, by Young's modulus  $E_{eq}$  and density  $\rho_{eq}$ , derived and mapped by Ashby [2] for the sandwich materials.

Based on Figure 1.6 and Table 1.6, the specific stiffness performance of the **AhCAFSa** material is by far the highest, followed by the **PfCPFSa** material. The equivalent stiffness for the AfCAFSa and AfCSFSa is higher than for the AhCAFSa and PfCPFSa material for the optimal ratio, but

TABLE 1.6: *Optimal equivalent bending stiffness, expressed in  $[kN/m^2]$ , and specific efficiency, expressed in  $[kN^{1/3}m^{7/3}/kg]$ , of the chosen sandwich materials and the conventional solid materials.  $\rho$  = density,  $E$  = Young's modulus*

	ASo	SSo	AfCAFSa	AfCSFSa	AhCAFSa	PeCAFSa	PfCAFSa
$E_{eq}$	70000	210000	23900	29700	6800	29000	1200
$E_{eq}^{1/3}/\rho_{eq,E}$	0.0150	0.0076	0.0275	0.0271	0.1018	0.0232	0.0561

because the equivalent density of the AhCAFSa and PfCPFSa is one fifth of the value of the AfCAFSa and AfCSFSa, the obtained stiffness per equivalent density is much higher for the AhCAFSa and PfCPFSa configuration. [80]

### 3.2.3 Specific bending strength efficiency

For a qualitative comparison, the formulation  $\sigma_{eq}^{1/2}/\rho_{eq,\sigma}$  by Ashby [2] valid for the minimum weight design of strong plates, is suitable as a strength performance factor, so called specific equivalent bending strength. The factor includes that only the face sheets are able to carry the bending stress. The equivalent failure stress  $\sigma_{eq}$ , determined using Equation (1.5), and the equivalent density  $\rho_{eq,\sigma}$  are incorporated (see Section 3, Supplement A). Based on Ashby [2] the allowable yield stress  $\hat{\sigma}_y$  is applicable for metals and polymers as failure stress. Using the optimal ratio for the strength design criterion, the largest strength is calculated. [61]

$$\sigma_{eq} = \frac{\sigma_{b,p}}{\sigma_{b,sm}} = \hat{\sigma}_{y,f} 6 \frac{t_f}{h_{sm}} \left[ 1 - 2 \frac{t_f}{h_{sm}} + \frac{4}{3} \left( \frac{t_f}{h_{sm}} \right)^2 \right] \quad (1.5)$$

Figure 1.7 presents the location of the separate sandwich materials in the map created by Ashby [2].

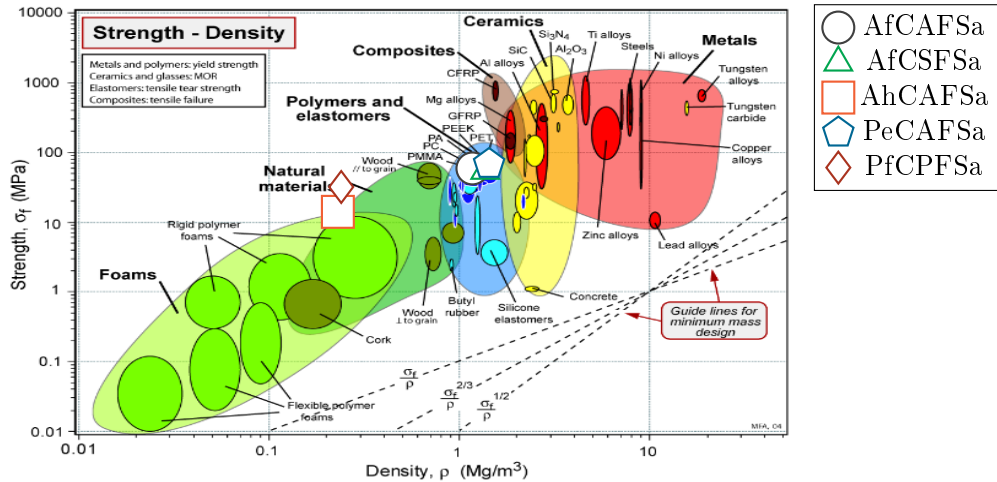


FIGURE 1.7: *Material selection chart, by strength  $\sigma_{eq}$  and density  $\rho_{eq}$ , derived and mapped by Ashby [2] for the sandwich materials.*

When applying the yielding criterion as failure stress the following observations are applicable from Figure 1.7 and Table 1.7: for the same thickness, the equivalent stress ( $\sigma_{eq}$ ) is much higher in the conventional solid with respect to the sandwich materials. When looking at the specific strength efficiency factor which is independent of the thickness of the material, the obtained

TABLE 1.7: *Optimal equivalent bending stress, expressed in [kN/m<sup>2</sup>], and specific efficiency, expressed in [kN<sup>1/2</sup>m<sup>2</sup>/kg], of the chosen sandwich materials and conventional solid materials.  $\rho$  = density,  $\sigma$  = bending stress*

	<b>ASo</b>	<b>SSo</b>	<b>AfCAFSa</b>	<b>AfCSFSa</b>	<b>AhCAFSa</b>	<b>PeCAFSa</b>	<b>PfCAFSa</b>
$\sigma_{eq}$	120.00	235.00	64.15	59.35	15.18	74.45	34.64
$\sigma_{eq}^{1/2}/\rho_{eq,\sigma}$	0.0040	0.0020	0.0065	0.0053	0.0160	0.0057	0.0238

strength per equivalent density is the highest for the **PfCPFSa** material, followed by **AhCAFSa** material.

### 3.2.4 Economic profile

To incorporate the cost aspect in the comparison, the total cost (and material cost) efficiency performance factors are calculated for both the bending stiffness and the bending strength. Three different elements are considered (Equation (1.6)): the material cost  $C_{mat}$  per weight; the production cost  $C_{prod}$  per weight and the operational costs  $C_{oper}$  per weight, expressed in the net present value (NPV), over the life cycle of the material.

$$C_{tot} = C_{mat} + C_{prod} + C_{oper} \quad (1.6)$$

#### Material costs

Based on literature [5], offers and common practise, Table 1.8 summarises the current material costs of the chosen materials.

TABLE 1.8: *Material cost, expressed in [€/kg] for the chosen sandwich materials and conventional solid materials.*

	<b>ASo</b>	<b>SSo</b>	<b>AfCAFSa</b>	<b>AfCSFSa</b>	<b>AhCAFSa</b>	<b>PeCAFSa</b>	<b>PfCPFSa</b>
Material cost	3	1	14	7	15	15	15

#### Production costs

The production costs of the metal configurations are solely dependent on the costs of the welding process  $C_{weld}$  and of the painting process  $C_{paint}$  of the structure, both expressed in [€/kg]. Based on the production cost data of solid materials of DAMEN, the welding cost amounts to 0.97 [€/kg] and the painting cost to 0.24 [€/kg] leading to a production cost of 1.21 [€/kg]. For the production of the PfCPFSa the production cost is set equal to 15 [€/kg] based on financial data of DAMEN.

$$C_{prod} = C_{weld} + C_{paint} \quad (1.7)$$

#### Operational costs

The operational cost during the life time of a ship is characterised by two main components: (1) the fuel cost for exploiting and (2) the cost regarding maintenance and repair of the ship. It should be reminded that the operational cost is not an initial cost in contrast to the material and production cost. Since it is difficult to measure the maintenance cost, only the fuel cost during the full life time is considered. In order to get the net present value, the total fuel cost will be reduced by a discount factor  $\mu$  (Equation (1.8)) which is dependent on the chosen discount ratio  $\xi$  and the total time period  $\gamma$ . In this context, the discount ratio is set at 5 [%], the time period at 15 [yr] and the fuel price  $C_{fuel}$  at 5.44 [€/15yr/kg]. The calculation on which the constant fuel

price  $C_{fuel}$  is based, is given in Subsection 3.2, Supplement B. The operational cost expressed in the net present value equals 3.67 [€/kg].

$$C_{oper} = \mu C_{fuel} = \sum_{t=1}^{\gamma} \frac{1}{\gamma (1 + \xi)^t} C_{fuel} \quad (1.8)$$

In order to compare the total cost efficiency, the bending stiffness and strength are divided by the product of the total cost and the equivalent density. [61]

$$CE_{tot,E} = \frac{E_{eq}^{1/3}}{C_{tot}\rho_{eq,E}} \quad (1.9)$$

$$CE_{tot,\sigma} = \frac{\sigma_{eq}^{1/2}}{C_{tot}\rho_{eq,\sigma}} \quad (1.10)$$

TABLE 1.9: Total costs, expressed in [€/kg], optimal bending stiffness cost efficiency, expressed in  $[10^{-3} \cdot kN^{1/3} m^{7/3} / \text{€}]$  and optimal bending strength cost efficiency, expressed in  $[10^{-3} \cdot kN^{1/2} m^2 / \text{€}]$  of the chosen sandwich materials and conventional solid materials.  $\rho$  = density,  $E$  = Young's modulus,  $\sigma$  = bending stress

	ASo	SSo	AfCAFSa	AfCSFSa	AhCAFSa	PeCAFSa	PfCPFSa
$C_{tot}$	9.56	7.65	20.65	13.65	21.65	21.65	35.44
$CE_{tot,E}$	1.500	0.895	1.300	2.000	4.700	1.100	1.600
$CE_{tot,\sigma}$	0.412	0.255	0.313	0.389	0.741	0.262	0.671
$CE_{mat,E}$	5.000	7.600	2.000	3.900	6.800	1.500	3.700
$CE_{mat,\sigma}$	1.300	2.000	0.461	0.758	1.100	0.378	0.0016

In general, the cost of the conventional plate is lower with respect to sandwich materials. The relative difference is lower for the total cost comparing to the pure material cost, because the production and operation costs are set constant for each {metal face sheet} sandwich and metal solid material. **AhCAFSa** materials have the highest bending stiffness and bending strength cost efficiency, followed by the **AfCSFSa** and the **PfCPFSa** configuration.

### 3.2.5 Conclusion

To create an overview of the performances of each sandwich material, the relative value per characteristic of the different sandwich materials to the AfCSFSa material is plotted (Figure 1.8). To map the relative value for the sandwich material versus the conventional solid, the AfCSFSa, AfCAFSa and ASo material are plotted with respect to the SSo material (Figure 1.9).

The AhCAFSa material is most promising following the comparison of material properties of the sandwich materials with respect to bending with a yield failure. The shear aspect and other failure modes are not included in the comparison. The important characteristic of a sandwich material is a low density core and high dense and strong face sheets, and these characteristics are most present in the AhCAFSa material. At the current stage, the metal foam types are not able to compete with the honeycomb core concerning the mechanical properties.

In the comparison of the metal foam based sandwich materials with respect to the conventional solid materials, the mechanical properties of the AfCSFSa material are promising and could create opportunities in replacing the SSo material.

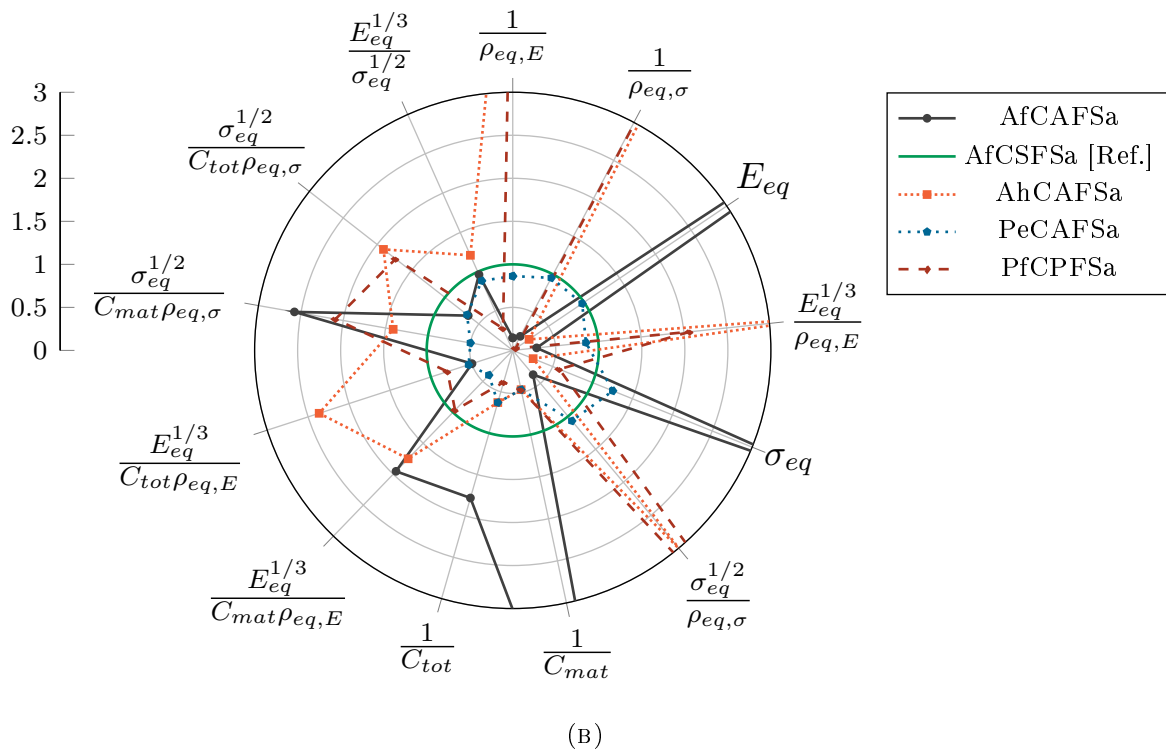
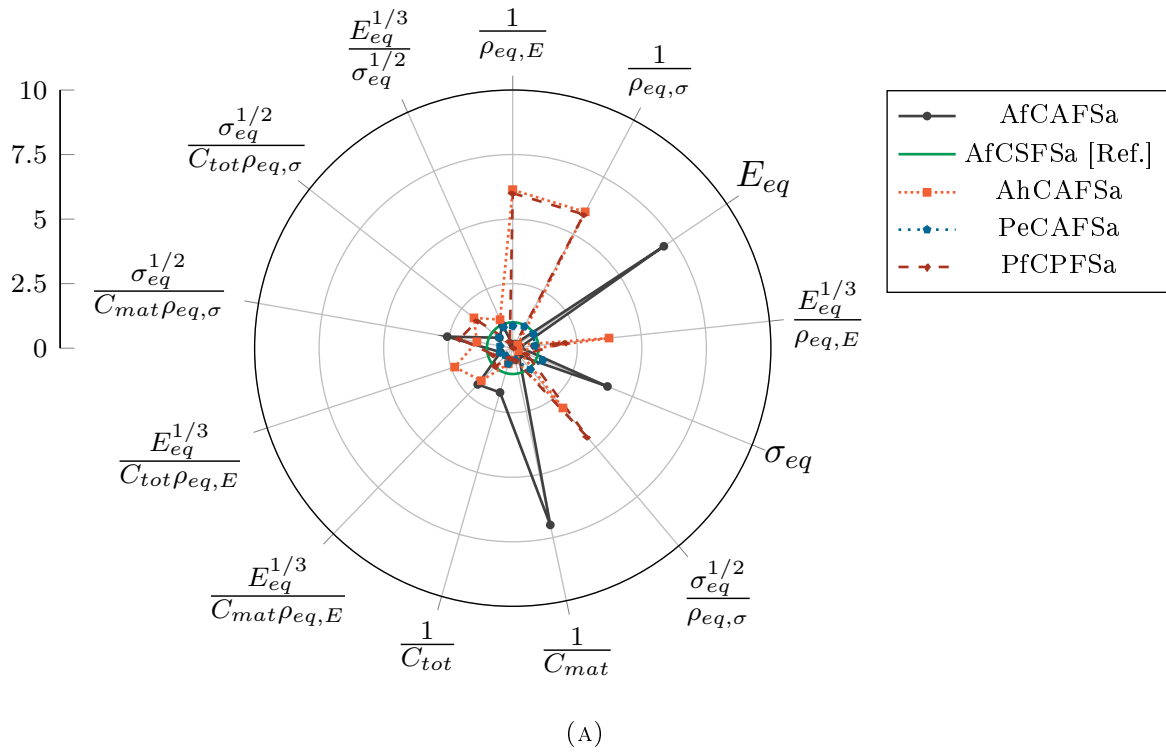


FIGURE 1.8: Relative performance plot of the chosen sandwich materials, with respect to the {aluminium foam core, steel face sheet} sandwich material (=unit circle), with regard to material properties following worse performance:  $< 1$ , better performance:  $> 1$ , equal performance:  $= 1$ . The numeral axis is given on the left on each figure. The legend for all plots is presented in subfigure (A). (A) overall plot, (B) detail plot.

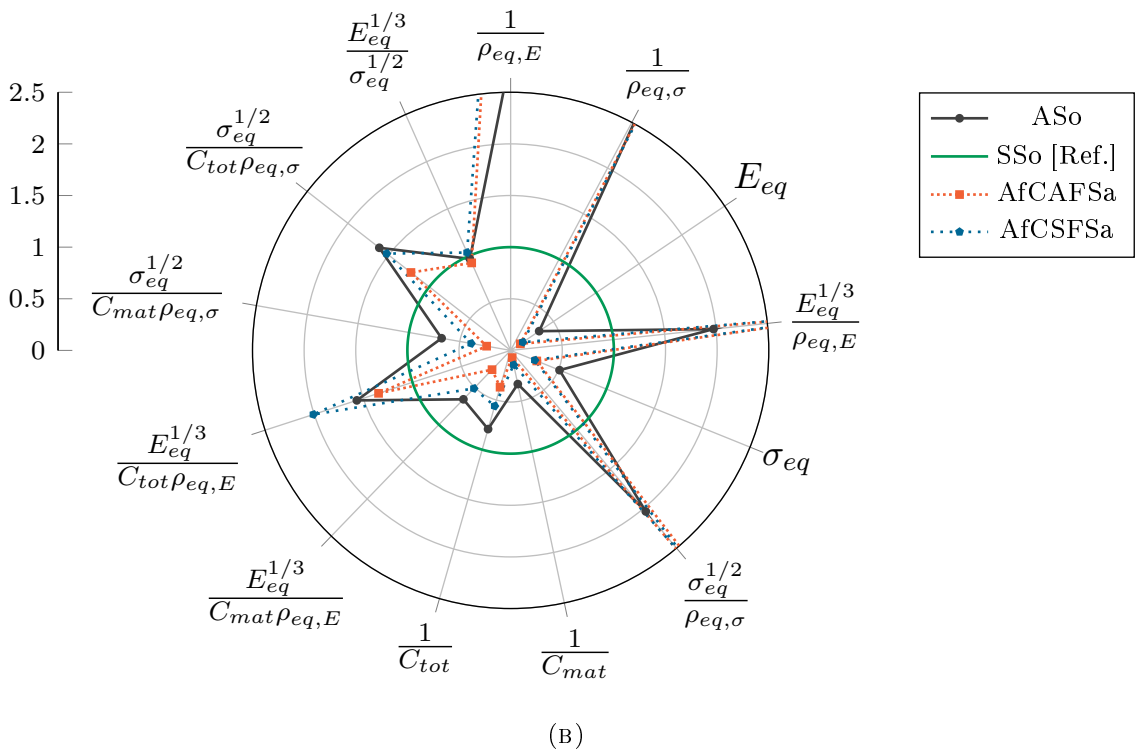
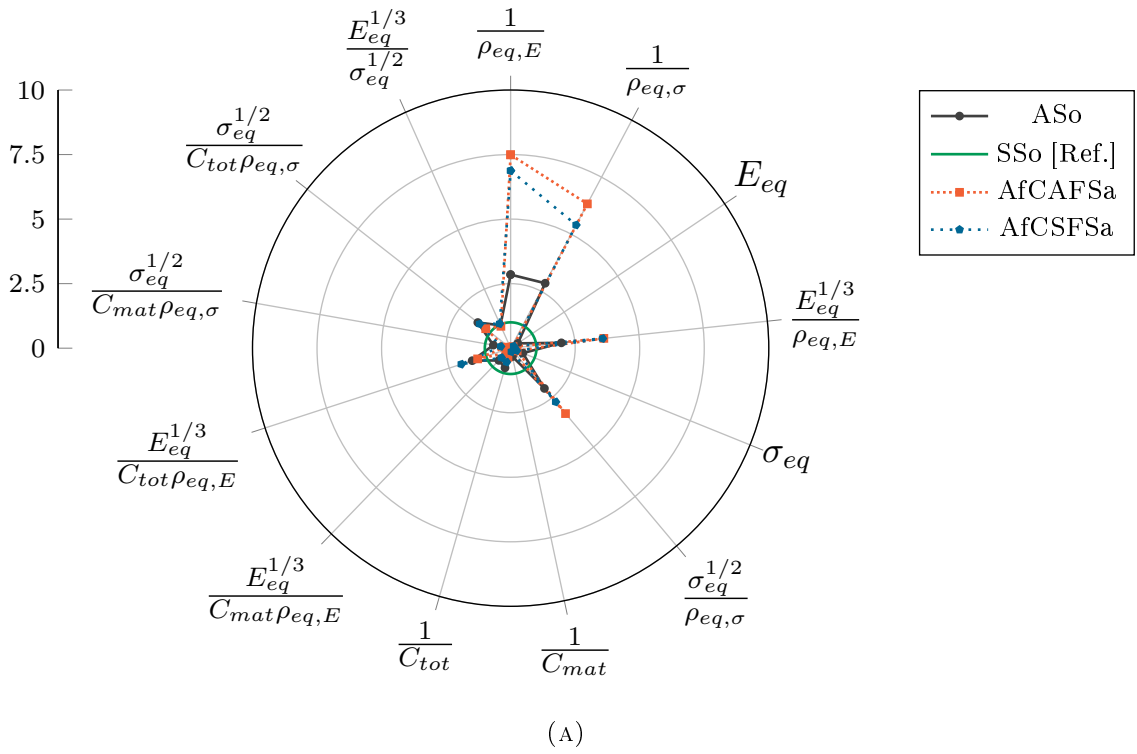


FIGURE 1.9: Relative performance plot of the {metal foam core, metal face sheet} sandwich materials and the aluminium solid material, with respect to the steel solid material (=unit circle), with regard to material properties following worse performance:  $< 1$ , better performance:  $> 1$ , equal performance:  $= 1$ . The numeral axis is given on the left on each figure. The legend for all plots is presented in subfigure (A). (A) overall plot, (B) detail plot.

### 3.3 Failure properties

In the comparison of the most likely failure modes, the following sandwich material and solid material context is assumed ( $\square$ ):

1. The same sandwich material configurations are used as in the calculations of the equivalent material properties.
2. All sandwich materials have the same face sheet thickness and core thickness.
3. Face sheets are considered to be thin/moderate: the core thickness approximates the total sandwich material thickness:  $t_c \approx h_{sm}$  and  $h_{sm}/t_f < 6.77$ .
4. The height of the solid is equal to twice the face sheet thickness of the sandwich material:  $h_p = 2t_f$ .

#### 3.3.1 Yielding

Two aspects play a role in the face sheet yielding failure mode: the membrane stress  $\sigma_m$  and the bending stress  $\sigma_b$ . The membrane stress, is uniform over the sectional area and results from an in-plane load  $F$  as load case, while the bending stress is linear distributed and caused by a bending moment  $M$ .

##### Membrane stress

The membrane stress  $\sigma_m$  is determined using Equation (1.11). In sandwich materials only the face sheets will carry the in-plane load  $F$ , while in the conventional solid material the full sectional area will contribute.

$$\sigma_m = \frac{F}{A} \longrightarrow \left\{ \begin{array}{l} \sigma_{m,sm} = \frac{F}{2t_f b} \\ \sigma_{m,p} = \frac{F}{h_p b} \end{array} \right\} \longrightarrow \text{ratio} = \frac{\sigma_{m,sm}}{\sigma_{m,p}} = \frac{2t_f}{h_p} \quad (1.11)$$

In the current context ( $\square$ ) of  $h_p = 2t_f$ , the in-plane stress for the sandwich material and the conventional solid material are equal, and thus there is no in-plane stress advantage for the sandwich material. A detailed explanation can be found in Section 5, Supplement A.

$$\sigma_{m,sm} = \sigma_{m,p} \quad (1.12)$$

##### Bending stress

The bending stress  $\sigma_b$  is calculated following Equation (1.13). Comparing the sandwich material with the solid material, the sectional modulus will increase for the sandwich material depending on the core thickness, leading to a lower bending stress.

$$\sigma_b = \frac{M}{Z} \longrightarrow \left\{ \begin{array}{l} \sigma_{b,sm} = \frac{M}{h_{sm} b t_f} \\ \sigma_{b,p} = \frac{6M}{b h_p^2} \end{array} \right\} \longrightarrow \text{ratio} = \frac{\sigma_{b,sm}}{\sigma_{b,p}} = \frac{1}{6} \frac{h_p^2}{h_{sm} t_f} = \frac{2}{3} \frac{t_f}{h_{sm}} \quad (1.13)$$

In the context ( $\square$ ) of thin/moderate face sheets, the bending stress of sandwich materials is 10 times reduced compared with the solid material. A detailed explanation can be found in Section 5, Supplement A.

$$\sigma_{b,sm} \approx \frac{1}{10} \sigma_{b,p} \quad (1.14)$$

When the stress is higher than the allowable face sheet stress  $\hat{\sigma}_{y,f}$ , the face sheets undergo face yielding. In the solid plate yielding failure occurs when the critical plate yielding stress  $\hat{\sigma}_{y,p}$  is

reached. Table 1.10 presents the critical yielding stress based on the material characteristics of Table 1.3. Since the solid material plate and the face sheets of the {metal face sheet} sandwich materials are all composed of aluminium or steel, no difference in allowable stress is present, except the {polymer face sheet} sandwich material has a higher critical yielding stress.

TABLE 1.10: *Allowable yielding stress, expressed in [MPa] for the chosen sandwich materials and conventional solid materials.*

	ASo	SSo	AfCAFSa	AfCSFSa	AhCAFSa	PeCAFSa	PfCPFSa
$\hat{\sigma}_{y,p}$	120	235					
$\hat{\sigma}_{y,f}$			120	235	120	120	250

### 3.3.2 Buckling

Euler buckling is present in both two types of the solid material and the four types of sandwich materials. Besides, sandwich materials have extra local buckling failure mode(s): face wrinkling and face dimpling.

#### Euler buckling

Euler buckling failure will occur when the stress  $\sigma_{gl}$ , present due to the global hull force  $F_{gl}$  is lower than the critical Euler buckling stress  $\hat{\sigma}_E$ . The global hull force stress  $\sigma_{gl}$  is dependent on the global moment present on the global structure. The effective area of the sectional area will incorporate the in-plane load. In the sandwich materials, only the face sheets will endure this in-plane force, while for the conventional solid material the overall thickness is effective. The critical Euler buckling stress  $\hat{\sigma}_E$  is determined using Equation (1.16) for the conventional solid plate. Since the flexural rigidity is implicitly taken into account, an adapted formula is required to calculate the critical Euler buckling stress for the sandwich material. Allen [1] has proposed the following formula. The derivation of the sandwich material formula can be found in Section 2, Supplement B.

$$\hat{\sigma}_E \geq \sigma_{gl} = \frac{F_{gl}}{A_{eff}} \rightarrow \left\{ \begin{array}{l} \hat{\sigma}_{E,sm} = \frac{\pi^2 E t_f h_{sm}^2}{2(1-\nu_f^2) b A_{eff}} K_1 \\ \hat{\sigma}_{E,p} = \frac{k\pi^2 E}{12(1-\nu^2)} \left(\frac{h_p}{b}\right)^2 \end{array} \right\} \rightarrow \text{ratio} = \frac{\hat{\sigma}_{E,sm}}{\hat{\sigma}_{E,p}} = \frac{3K_1 h_{sm}^2}{k h_p^2} \quad (1.15)$$

$$\hat{\sigma}_E = \frac{k\pi^2 E}{12(1-\nu^2)} \left(\frac{h_{eff}}{b}\right)^2 \geq \sigma_{gl} = \frac{F_{gl}}{A_{eff}} \quad (1.16)$$

In the chosen context ( $\square$ ), and assuming that the buckling coefficient is equal  $k = K_1$ , a higher critical Euler buckling stress is obtained for the sandwich material configuration.

$$\hat{\sigma}_{E,sm} \approx 3 \left(1 + \frac{t_c}{2t_f} + \frac{t_c^2}{4t_f^2}\right) \hat{\sigma}_{E,p} > \hat{\sigma}_{E,p} \quad (1.17)$$

#### Face wrinkling

The origin of wrinkling is an instability of the face sheets when the wavelength of the buckled form is of the same order as the thickness of the face sheets. The critical face wrinkling stress is

calculated using Equation (1.18) and is dependent on the Young's modulus of the face sheet  $E_f$  and the core  $E_c$  and the Poisson's ratio of the core  $\nu_c$ .

$$\hat{\sigma}_{wr,f} = C_w E_f^{\frac{1}{3}} E_c^{\frac{2}{3}} = 3 [12(3 - \nu_c)^2(1 + \nu_c)^2]^{-\frac{1}{3}} E_f^{\frac{1}{3}} E_c^{\frac{2}{3}} \quad (1.18)$$

For the four sandwich material types, the critical wrinkling stress  $\hat{\sigma}_{wr,f}$  is determined using the material characteristic given in Table 1.3. The Poisson's ratio is 0.3 for every sandwich material. Since the critical wrinkling stress values are lying far above the allowable face sheet yielding stress  $\hat{\sigma}_{y,f}$  values (Table 1.11), face wrinkling is likely to occur in the four chosen configurations of the sandwich materials.

TABLE 1.11: *Critical wrinkling stress, expressed in [MPa] for the chosen sandwich materials and conventional solid materials.*

	AfCAFSa	AfCSFSa	AhCAFSa	PeCAFSa	PfCPFSa
Critical wrinkling stress	1947	2808	4121	1930	368

### Face dimpling

The failure mode "face dimpling" only occurs with the {honeycomb core} sandwich materials. A large part of the face sheet is not supported and therefore local buckling of the face sheet occurs between the supports, called dimpling. Equation (1.19) describes the critical dimpling stress  $\hat{\sigma}_{dimp,f}$ , where  $s$  is the radius of the circle inscribed in the hexagonal cell. When the stress in the face sheets is higher than the critical dimpling stress  $\hat{\sigma}_{dimp,f}$ , face dimpling occurs.

$$\hat{\sigma}_{dimp,f} = \frac{2E_f}{1 - \nu^2} \left( \frac{t_f}{s} \right)^2 \quad (1.19)$$

### 3.3.3 Shear

Shear failure is present when the shear stress in the material exceeds the allowable shear yielding stress  $\hat{\tau}_y$ . Equation (1.20) gives the accompanying formulas for the general sandwich materials and the conventional solid material. A detailed explanation can be found in Section 5, Supplement A.

$$\tau = \frac{QS}{Ib} = \frac{Q}{Db} \sum \frac{SE}{b} \rightarrow \left\{ \begin{array}{l} \tau_{sm} = \frac{Q}{bh_{sm}} \\ \tau_p = \frac{Q \frac{bh_p^2}{8}}{\frac{bh_p^3}{12}b} = \frac{3Q}{2bh_p} \end{array} \right\} \rightarrow \text{ratio} = \frac{\tau_{sm}}{\tau_p} = \frac{2h_p}{3h_{sm}} = \frac{4t_f}{3h_{sm}} \quad (1.20)$$

For thin/moderate face sheets ( $\square$ ), the shear stress present in the sandwich material is 5 times lower compared to the solid material.

$$\tau_{sm} \approx \frac{1}{5} \tau_p \quad (1.21)$$

The allowable yielding shear stress  $\hat{\tau}_y$  for sandwich material is imposed by the core  $\hat{\tau}_{y,c}$  and is therefore different for each of the four sandwich types. For the solid material, no core is present and thus the allowable shear stress of the plate  $\hat{\tau}_{y,p}$  is applicable. Table 1.12 shows the value of the critical shear stress, calculated using the relation between the yielding stress and the shear stress:  $\tau = \sigma/\sqrt{3}$ .

TABLE 1.12: *Critical shear stress, expressed in [MPa], for the chosen sandwich materials and conventional solid materials.*

	<b>ASo</b>	<b>SSo</b>	<b>AfCAFSa</b>	<b>AfCSFSa</b>	<b>AhCAFSa</b>	<b>PeCAFSa</b>	<b>PfCPFSa</b>
Critical shear stress	69	136	6	6	6	9	2

Due to the geometry a reduction of factor 5 of the shear stress is present in sandwich material, but the critical shear stress is way lower than the conventional solid material. Therefore, shear failure is more likely to occur in sandwich materials.

### 3.3.4 Conclusion

Table 1.13 summarises the findings derived from the existing literature. No clear dominant advantage is present for one specific material type, so it depends on the load present which material would suit the best.

TABLE 1.13: *Qualitative comparison of the selected failure properties of the chosen sandwich materials relative to the conventional solid material, based on personal judgement. (-) property is worse, (- -) property is much worse, (=) property is equal, (+) property is better, (++) property is much better*

<b>Property</b>		<b>ASo</b>	<b>AfCAFSa</b>	<b>AhCAFSa</b>	<b>PfCAFSa</b>	<b>PfCPFSa</b>
Yielding (in-plane)	§3.3.1	1	=	=	=	+
Yielding (bending)	§3.3.1	1	+	+	+	++
Buckling (Euler)	§3.3.2	1	+	+	+	+
Buckling (Wrinkling)	§3.3.2	1	-	-	-	--
Buckling (Dimpling)	§3.3.2	1		-		
Shear	§3.3.3	1	-	-	-	-

## 3.4 Functional properties

### 3.4.1 Thermal and electric conductivity

Metals in general, bear the characteristic that the electrons inside their metal structure can move freely through the material, and transmit therefore both heat and electricity, or in other words metals have in general a high thermal conductivity. [32] A **AfCAFSa** core creates a large surface area density [3, 48], which in combination with the high thermal conductivity leads to a highly efficient and compact heat dissipation medium. The surface area density for a **AhCAFSa** core is larger, when comparing to a **AfCAFSa** core, leading to a faster heat dissipation. [48] In **PeCAFSa** and **PfCPFSa** materials, weak van der Waals bonds are present, resulting in a weak coupling and disordered structure characteristics; so the thermal conductivity is low. [32] The **PfCPFSa** material itself cannot resist high temperatures, because the fibres will melt. [80] For the electric insulation in **PfCPFSa** materials, the type of fibres is normative; glass FRP are near-perfect insulators while carbon FRP are electrically conductive. [32, 80] Because there is no core present in the **ASo** material to dissipate the heat, an insulation advantage is absent.

### 3.4.2 Impact and vibrations

Sandwich materials in general have good energy absorbing capacities. [5, 24, 78, 81] Looking specific at a **AfCAFSa** materials, their damping capacity is 10 times the capacity of the solid configuration, due to the high natural flexural vibration frequencies. [3, 18, 76]

### 3.4.3 Corrosion

Hasan and Shaw [36] demonstrated that the corrosion resistance of a **AfCAFSa** core is better than a **AhCAFSa** core. Both samples show the same corroded structure but for the **AhCAFSa** the structure is assaulted earlier: the face sheets have lost weight and pitting was observed while the core increased in weight due to a build up of deposits on the surface (foam) and within the core (honeycomb). [6, 36] The polyurethane elastomer core of the **PeCAFSa** configuration, increases the corrosion protection. [45] In **PfCPFSa** materials corrosion is not present, which is a major advantage.

### 3.4.4 Conclusion

For the functional properties (Table 1.14) sandwich materials perform overall better than the ASo material. Comparing the four different sandwich materials, there is no clear favourite; the choice depends on the design/purpose of the structure.

TABLE 1.14: *Qualitative comparison of the functional properties of the four chosen sandwich materials relative to the conventional solid material, based on personal judgement. (-) property is worse, (- -) property is much worse, (=) property is equal, (+) property is better, (++) property is much better*

Property		ASo	AfCAFSa	AhCAFSa	PfCAFSa	PfCPFSa
Thermal	§3.4.1	1	+	++	=	=
Electric	§3.4.1	1	=	=	-	-
Impact	§3.4.2	1	++	++	++	++
Vibrations	§3.4.2	1	++	++	++	++
Corrosion	§3.4.3	1	++	+	+	++

## 3.5 Practical properties

### 3.5.1 Plate dimensions

Like **ASo** material configurations, **AfCAFSa** panels also could have every desired panel dimension. Based on interviews with producers of Havel Metal Foam [37], the current obstacle is to have a production facility that can deal with these large dimensions. The current maximum dimension is 3000 [mm] x 1500 [mm]. [5] The same maximum dimensions are founded for **AhCAFSa** sandwich panels. The thickness of the **AfCAFSa** panel ranges up to almost 100 [mm] (face sheets: 0.6-10 [mm]; core 8-80 [mm]). For the **AhCAFSa** sandwich material, the total thickness goes up to 150 [mm]. [14] The length of a **PeCAFSa** plate is up to 16000 [mm]. [69]. For **PfCPFSa** the limiting factor is the mould. At this moment, the mould can produce larger panels in comparison with the **AfCAFSa** materials.

### 3.5.2 Pricing

Sandwich materials are still very costly in comparison to the conventional solid plate. Hopefully, with some technological improvements and broader application, the cost may decrease over the years. Today, universities can buy the **AfCAFSa** materials for 30 [€/kg]. For large amounts

a price of 14 [€/kg] is more realistic. [5, 37, 50] A price of 15 [€/kg] is valid for **PfCPFSa**, **AhCAFSa** and **PeCAFSa** materials [14] but, PfCPFSa and AhCAFSa will turn out cheaper because their weight is lower for the same volume as mentioned before.

TABLE 1.15: *Material cost, expressed in [€/kg] for the chosen sandwich materials and conventional solid materials.*

	<b>ASo</b>	<b>AfCAFSa</b>	<b>AhCAFSa</b>	<b>PeCAFSa</b>	<b>PfCPFSa</b>
Material cost	3	14	15	15	15

### 3.5.3 Waste reduction and recycling

Currently, the issue of waste reduction, recycling and environmental impact is on every agenda. [46] Because **ASo**, **AfCAFSa** and **AhCAFSa** materials are made out of pure metal, the material is 100% and easily recyclable. [37] When non-recyclable bonding glues are used this reasoning is no longer valid. **PeCAFSa** materials with the elastomer core are also fully recyclable. [69] On the contrary, the recycling of **PfCPFSa** materials is challenging and not fully possible. Core recycling depends on the chosen type; for example, PVC is fully recyclable. [77] A promising technique might be microwave pyrolysis for the polymer face sheets. This relatively new technique heats the material in the absence of oxygen and will degrade the glass FRP face sheets into glass and oil. [46]

### 3.5.4 Conclusion

The ASo material has better practical properties with respect to the four sandwich materials. **AfCAFSa** materials score better on the recycling properties within the group of sandwich materials.

TABLE 1.16: *Qualitative comparison of the selected practical properties of the chosen sandwich materials relative to the conventional solid material, based on personal judgement. (-) property is worse, (- -) property is much worse, (=) property is equal, (+) property is better, (++) property is much better*

Property		<b>ASo</b>	<b>AfCAFSa</b>	<b>AhCAFSa</b>	<b>PfCAFSa</b>	<b>PfCPFSa</b>
Plate dimensions	§3.5.1	1	=	=	=	=
Pricing	§3.5.2	1	-	-/- -	-/- -	-/- -
Wast reduction / recycling	§3.5.3	1	=	=	-	- -

## 4 Discussion

A qualitative comparison was performed of the selected properties of four types of sandwich materials and included also the currently most used conventional solid material. An overview of the different subtypes is lacking in the existing literature. The comparative analysis of selected general, functional and sales/waste properties is based on existing literature. In the project the formulas for the selected mechanical and failure properties were adapted using mathematical remodelling. The main conclusion is that the sandwich materials have to be chosen along its best properties, no overall overall conclusion can be made.

Comparing the four sandwich material types the following findings can be concluded taken the selected characteristics into account:

1. The PeCAFSa material has the lowest performance.
2. The choice between the AfCAFSa, the AfCSFSa, the AhCAFSa and the PfCPFSa is not straightforward and depends on the load case present and the shipyard's practise.
3. As stated before, the general and practical properties of all sandwich materials are not yet developed enough to compete with the conventional solid material, but the mechanical, failure and functional properties are promising. Therefore, it is recommended to start a business case to explore the possible advantages of the sandwich materials and to see what advantages can be found at a higher structural level (Chapter 2).

As limitation of the present study, it should be considered when data are interpreted that the properties are only compared at material level, which does not represent the "real world". Since the sandwich material would replace a conventional solid material including secondary stiffeners, it is recommended to further explore the difference of the chosen sandwich material types with the conventional solid material on a higher structural level, starting with the stiffened panel to the global construction level.

In conclusion, the choice for sandwich materials is dependent on the specific application according to specific properties, different for each sandwich material subtype. The weight lowering capacity is currently set off by a higher manufacturing price. Hybrid structures might be promising.

# Chapter 2 | Structural and economical modelling of metal foam based sandwich materials at the stiffened panel level

## 1 Introduction

Sandwich materials are promising in mechanical, failure and functional properties: they are stiffer than a dense sheet of equal mass, they have better bending properties, they have good insulation features et cetera (Chapter 1). [6, 80]

To accomplish the demand of the customer to reduce the initial purchase cost and maintenance cost, production efficiency is the key concept [30]. Metal based sandwich materials can play a role in smart designing, not to mention that these materials show a potential to incorporate smart functionality. Smart designing, including smart functionality has as objective to simplify the structural design and subsequently be effective to reduce the overall weight of the vessel [42]. Therefore there are potential advantages to get in the production cost and the operational cost with respect to the current conventional solid material design.

According to Barjis [8], modelling and simulation are two complementary tools that ensure studying the impact and deliverables of new technologies in a controlled environment. These techniques are of major importance for a company to keep current and to be swift to changes in a world characterised by competition, increasing capabilities of new arising technologies and growing customer demands. When not adopting modelling and simulation, it may have severe consequences: building a system is very expensive, time consuming and risky for the organisation itself. Early mitigation of these risks is undoubtedly a prerequisite of success and survival.

The second chapter compares the current design with a new design implementing {aluminium foam core, steel face sheet} sandwich material, with regard to both structural and financial aspects, using an analytical model. The calculations are performed at the level of a stiffened panel. A ship of the DAMEN portfolio (Stan Pontoon 12032) is used as reference. The ultimate goal is to answer the question whether there is an economic advantage for DAMEN and clients in adopting this novel material.

## 2 Methodology

The applied model, programmed using `Matlab R2016a`, is a combination of an analytical structural optimisation model [63] and a cost calculation model [7].

For the analytical structural optimisation model, a stiffened panel forms the starting-point. The structural design will be divided into 3 to 4 levels depending on the configuration, starting from the lowest to the highest in hierarchy: plate level, plate-stiffener level, plate-girder level and panel level. The structural detailed attachment and welding knees are not included in the opti-

misation.

For the current model, three cost components are considered: material costs, production costs and operational costs. The material costs and the production costs can be seen as the overhead fixed costs, from the prospective of the shipyard and the operational costs are variable since they are present during the life time of the vessel. The material costs and the operational costs are a function of the weight of the vessel and the production costs are a function of the weld seam volume and the paint area. The weight, weld seam volume and paint area will differ in every configuration.

## 2.1 Description of the model: variables and constraints per level

The comparison study consists of two different models: the conventional solid material configuration, and the sandwich material configuration, since different formulas are applicable due to differences in structural design. The load cases and objective function are the same for both models, but the design variables and design constraints alter. Figure 2.1 visualises the design of the stiffened panels where the model is based on. The analysis of the conventional solid material is carried out at four different levels, namely at the plate level (pink), at the plate-stiffener level (blue), at the plate-girder level (yellow) and at the panel level (white). For the sandwich material design the plate-stiffener level can be removed, since the extra stiffness obtained by the stiffeners is replaced by the material itself due to the layered material structure. Note that the figures are only a schematic representation of the stiffened panel (not to scale).

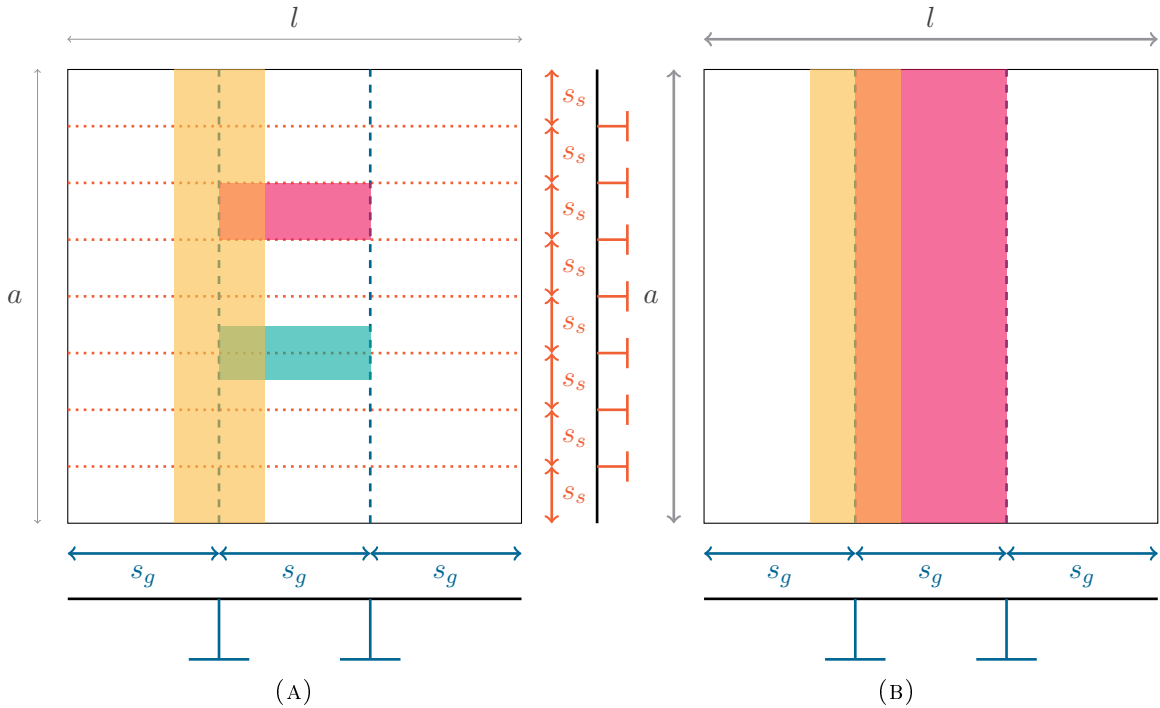


FIGURE 2.1: *Schematic visualisation of the stiffened panel with the indication of the separate levels for the conventional solid material configuration (A) and the sandwich material design (B).*

### 2.1.1 Load cases

The load cases that have been considered in the calculation are: (I) a bottom plate with local water pressure in combination with global sagging and hogging wave vertical bending moments and (II) a bottom plate with local water pressure only. Load case (I) is present in long ships (>40 [m]) operating in waves. These ships are subjected to still water pressure in combination

with global sagging and hogging wave vertical bending moment. Load case (II) is present in small ships ( $< 40$  [m]) that are mainly subjected to still water pressure. The global hull bending moment is still present in the latter, but this is not dominant for failure.

### 2.1.2 Objective function

Since the overall question in this chapter is linked to the economic advantage for DAMEN and her client in adopting this novel material, the total cost, expressed in the net present value (NPV), is set as the main objective function. This overall cost consists of the initial material cost, the initial production cost and the NPV of the operational cost of the stiffened panel configuration.

### 2.1.3 Design variables

The main design variables in the model are the scantlings of the stiffened panel that composes the ship structure, shown in Table 2.1 for both design configurations. For the conventional solid material the total plate thickness  $h_p$  will be varied, while for the sandwich material design only the core thickness  $t_c$  will alter. The required face sheet thickness  $t_f$  and the total plate thickness  $h_{sm}$  are automatically determined based on the design constraints.

TABLE 2.1: *Design variables for conventional solid material configuration and sandwich material configuration.*

Conventional solid	Sandwich material
Plate thickness $h_p$	Core thickness $t_c$
Number of girders $q$	
Girder web height $h_{w,g}$	

### 2.1.4 Design constraints

The design constraints of the current model can be subdivided into technological and structural design constraints. The first one incorporates the upper and lower bound of the design variables and the second type of design constraint guarantees welding quality, avoids failure due to yielding, buckling and limits deflections, stresses and the natural frequency. All design constraints are based on classification societies, structural theory books and DAMEN shipyard's best practice and standards. No extra safety factors are taken into account in the derived formulas.

The minimum and maximum values of the design variables can be entered in the constructed model to meet the desires of the company as *technological design constraints* of the model. Section 2.2 will discuss the values used in the model on which the results are based using the reference ship Stan Pontoon (SPo) 12032.

The *structural design constraints* that form the basis for the model are described below. Per level, first the conventional design will be discussed and thereafter the changes of the stiffened panel including a sandwich material baseplate.

#### Plate Level

In Figure 2.2 the plate is schematically visualised for the conventional solid material configuration and the sandwich material design. Table 2.2 gives an overview of the structural design constraints, applicable for the plate-level of both configurations and implemented in the model. Further explanation and derivations can be found in Subsection 1.1 and Subsection 2.1, Supplement B.

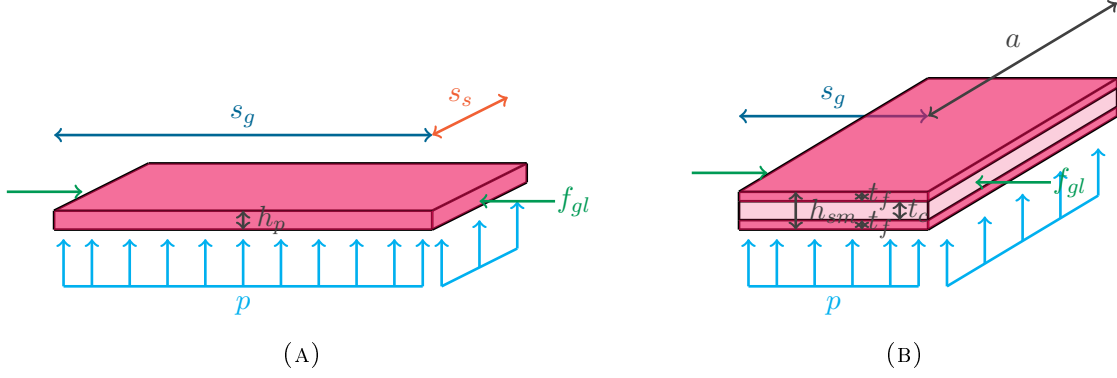


FIGURE 2.2: Schematic semi-3-dimensional visualisation of the plate level for the conventional solid material configuration (A) and the sandwich material design (B).

TABLE 2.2: Structural design constraints for conventional solid configuration and sandwich material configuration on plate level.

	Conventional solid material	Sandwich material
(a)	$\hat{\sigma}_{y,p} \geq \sqrt{\sigma_b^2 + \sigma_m^2} - \sigma_b \sigma_m$ $\sigma_b = \frac{\beta_1 p y^2}{h_p^2}$ $\sigma_m = \frac{M_{gl}}{D(m+1)(n+1)h_p s_s}$	$\hat{\sigma}_{y,f} \geq \sigma_b + \sigma_m$ $\sigma_b = \frac{\beta_1 p y^2}{6t_f h_{sm}}$ $\sigma_m = \frac{M_{gl}}{D(m+1)2t_f a}$
(b)	$f_{gl} \leq \frac{\pi^2 k E s_s h_p}{12(1-\nu_p^2)} \left(\frac{h_p}{s_s}\right)^2$	$f_{gl} \leq \frac{\pi^2 E t_f h_{sm}^2}{2(1-\nu_f^2)a} \frac{\left(\frac{a}{s_g} + \frac{s_g}{a}\right)^2}{1 + \left[\frac{\pi^2 E t_f h_{sm}}{2(1-\nu_f^2)G_c a} \left(\frac{a^2}{s_g^2} + 1\right)\right]}$
(c)	$\hat{\tau}_{y,p} \geq \frac{3Q}{2s_g h_p}$ $Q = \frac{p s_s s_g}{2}$	$\hat{\tau}_{y,c} \geq \frac{Q}{E I_{sm}} \left[ E_f t_f \frac{h_{sm}-t_f}{2} + E_c \left(\frac{t_c}{2}\right)^2 \right]$ $\hat{\tau}_{y,f} \geq \frac{Q}{E I_{sm}} \left[ E_f t_f \frac{h_{sm}-t_f}{2} \right]$ $E I_{sm} = \frac{E_c s_g t_c^3}{12} + \frac{E_f s_g t_f^3}{6} + \frac{E_f s_g t_f \left(\frac{h_{sm}-t_f}{2}\right)^2}{2}$ $Q = \frac{p a s_g}{2}$
(d)	na (not applicable)	$\sigma_f \leq C_w E_f^{\frac{1}{3}} E_c^{\frac{2}{3}}$ $C_w = 3 \left[ 12(3 - \nu_c)^2 (1 + \nu_c)^2 \right]^{-\frac{1}{3}}$

(a) Plate yielding

To examine plate yielding, both bending stress and membrane stress must be taken into account. Since both stresses have a different orientation for the design of the conventional solid material, the Von Mises principle must be applied. For the sandwich material, the stresses do not have a different orientation, so a single summation can be used. As long as the plate stress  $\sigma_p$  (conventional design) or the face sheet stress  $\sigma_f$  (sandwich material design) is lower than respectively the allowable plate yielding stress  $\hat{\sigma}_{y,p}$  and allowable the face sheet yielding stress  $\hat{\sigma}_{y,f}$ , plate yielding will not occur.

To determine the bending stress  $\sigma_b$ , the plate bending formula of Young and Budynas [79] is used, applying a uniform load over the entire plate and assuming clamped boundary conditions. Since this formula is applicable to conventional solid plates, a derivation for sandwich materials is done, which can be found in Subsection 2.1.1, Supplement B, leading to the formula shown in

Table 2.2. The membrane stress  $\sigma_m$  is in both configurations determined using the global hull bending moment  $M_{gl}$ .

(b) Euler plate buckling

The elastic plate buckling stress  $\hat{\sigma}_E$  will give a minimum required effective plate thickness to prevent Euler plate buckling. As long as global load  $f_{gl}$ , present in the structure, is lower than the calculated Euler buckling load  $f_E$ , derived from the elastic plate buckling stress with simply supported boundary conditions, overall buckling is not present. [55, Chapter 3: Section 6,9] [55, Chapter 5]

(c) Plate shear

To include the plate shear criterion, the maximum shear stress  $\tau_p$  that is present in the material is determined. As long as the plate shear stress  $\tau_p$  does not exceed the allowable plate yielding shear strength  $\hat{\tau}_{y,p}$ , shear failure is not occur for the conventional solid material. The effect of transverse shear in conventional plates must only be incorporated for thick plates. In thin plates, shear deformation is of less importance: the shear part is only a fraction of the bending part. Since the sandwich material is composed of different layers (thicker plate), the maximum shear stress must be calculated for both core and face sheet. The modification of the required formulas is given in Section 2.1.4, Supplement B.

According to Crupi et al. [18], Zu et al. [81] and Petras [59], the core absorbs the most significant part of the shear load for sandwich materials with thin face sheets with respect to the core thickness, because the maximum shear force is located at the neutral axis. In this case, only the core area is taken into account to incorporate the load. However, since no limitation is implemented to meet the requirement of having thin face sheets, this assumption will not be used in the model, and also the contribution of the face sheets will be taken into account. As long as the core shear stress  $\tau_c$  and face sheet shear stress  $\tau_f$  are lower than respectively the allowable core yielding shear strength  $\hat{\tau}_{y,c}$  and allowable face sheet yielding shear strength  $\hat{\tau}_{y,f}$ , core and face sheet shear will not be present.

(d) Face sheet wrinkling

The critical face sheet wrinkling instability stress  $\hat{\sigma}_{wr,f}$  is determined by Allen [1]. The buckling coefficient  $C_w$  depends on the Poisson's ratio of the core  $\nu_c$ . As long as the occurring stress in the face sheet  $\sigma_f$  is lower than the allowable wrinkling stress  $\hat{\sigma}_{wr,f}$ , no face sheet wrinkling will be present.

Plate-stiffener level

The stiffener level is removed from the sandwich material design. Therefore only the conventional solid configuration will have implemented plate-stiffener level criteria (Table 2.3). The strip is graphically displayed in Figure 2.3, including an effective width  $s_{s,eff}$ , related to the stiffener spacing  $s_s$  and the length of the stiffener ( $s_g$ ). The detailed description can be found in Subsection 1.2, Supplement B.

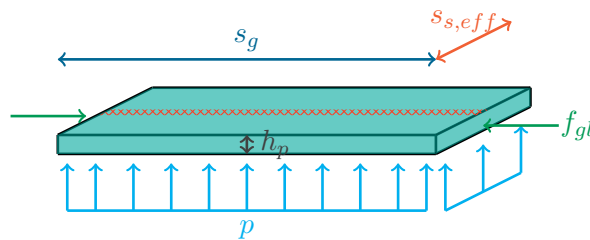


FIGURE 2.3: Schematic semi-3-dimensional visualisation of the plate-stiffener level for the conventional solid material configuration. The hatched area reflects the location of the stiffener.

TABLE 2.3: *Structural design constraints for conventional solid configuration and sandwich material configuration on plate-stiffener level.*

	Conventional solid material	Sandwich material
(a)	$\hat{\sigma}_{y,s} \geq \sigma_b + \sigma_m$ $\sigma_b = \frac{ps_g^2 s_{s,eff} e_{outer,s}}{12I_s}$ $\sigma_m = \frac{M_{gl}}{D(m+1)(n+1)(h_p s_{eff,s} + A_s)}$	na
(b)	$\sigma_s \leq \frac{\pi^2 EI_s}{\left(\frac{s_g}{2}\right)^2 (s_{s,eff} h_p + A_{HP})}$	na
(c)	$\frac{l}{800} \geq \frac{ps_{s,eff} l^4}{384}$	na
(d)	$h_{w,s} \geq \frac{Q\sqrt{3}}{2t_{w,s}\hat{\sigma}_{y,s}}$ $Q = ps_g s_s$	na

(a) Plate-stiffener yielding

For the plate-stiffener stress, both bending stress and membrane stress must be taken into account. Because both stresses have the same direction, summation is applicable. As long as the plate-stiffener stress  $\sigma_s$  is lower than the allowable stiffener yielding stress  $\hat{\sigma}_{y,s}$ , plate-stiffener yielding is not present.

To calculate the bending stress  $\sigma_b$ , the Euler beam bending formula with clamped boundary conditions is used. [79] The formula to calculate the membrane stress  $\sigma_m$  is identical to the one used at plate level, but the area of the plate-stiffener combination differs from the area of the plate at plate level.

(b) Euler plate-stiffener buckling

The Euler plate-stiffener buckling stress must be determined following Paik and Thayamballi [55, Chapter 2: Section 8] assuming simply supported boundary conditions, to check whether the plate-stiffener dimensions are sufficient to ensure that the stress does not exceed the Euler buckling value.

(c) Plate-stiffener deflection

Lloyd's Register [47] limits the plate-stiffener deflection to be not larger than the length of the stiffener divided by 800:  $\hat{\delta}_s = \frac{l}{800}$ . To calculate the deflection of the plate-stiffener combination, the Euler beam formula with clamped boundaries is used. [79]

(d) Shear force

The stiffener web (boundary) should carry the shear force that is transferred to girder. To avoid shear failure, a minimum stiffener web height  $h_{w,s}$  is set, following Paik and Thayamballi [55, Chapter 2: Section 6] to ensure that the occurring shear stress is not higher than the allowable yielding stiffener shear stress  $\hat{\tau}_{y,s}$ .

Plate-girder level

At plate-girder level, the required plate-girder dimensions are determined using a plate with an effective width  $s_{g,eff}$  depending on the girder spacing  $s_g$  and the length of the girder  $a$  [54]. The girder web height is the design variable, so the thickness of the girder is set to an initial value. When a larger girder web height is required than the technical design constraint of the web height ( $h_{w,g,max}$ ) and than is allowed to prevent failure, the girder web thickness will be adapted to satisfy the criteria. In Figure 2.4 the strip is schematically visualised for both configurations. An

overview of the criteria used is given by Table 2.4. The full derivation can be found in Subsection 1.3 and Subsection 2.2, Supplement B.

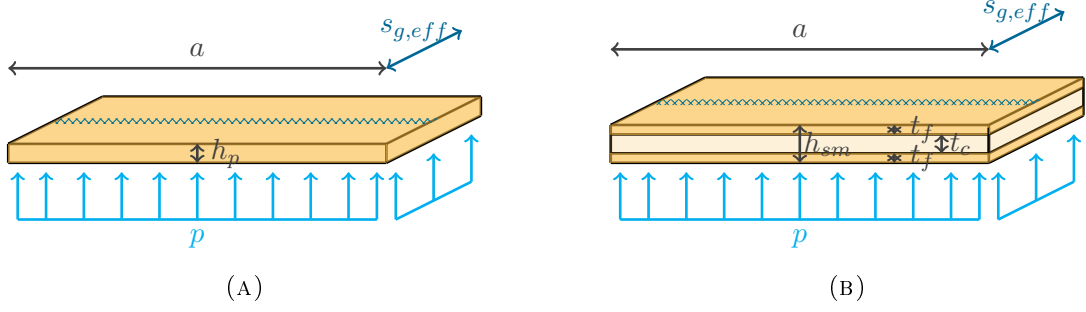


FIGURE 2.4: Schematic semi-3-dimensional visualisation of the plate-girder level for the conventional solid material configuration (A) and the sandwich material design (B). The hatched area reflects the location of the girder.

TABLE 2.4: Structural design constraints for conventional solid configuration and sandwich material configuration on plate-girder level.

	Conventional solid material	Sandwich material
(a)	$\hat{\sigma}_{y,g} \leq \sigma_b = \frac{pa^2 s_{g,eff}}{12(9.5a_{eff}^2 s_g D \cdot 10^{-3})}$	
(b)	$9.5a_{eff}^2 s_g D \cdot 10^{-3} \leq \frac{I_g}{e_{outer,g}}$	
(c)	$\frac{a}{1000} \geq \frac{ps_{g,eff} a^4}{384}$	
(d)	$t_{w,g} \geq \frac{h_{w,g}}{69} \sqrt{\frac{\hat{\sigma}_{y,g}}{235}}$	
(e)	$h_{w,g} \geq \frac{Q\sqrt{3}}{2t_{w,g}\hat{\sigma}_{y,g}}$ $Q = ps_g a$	

(a) Plate-girder yielding

To determine the plate-girder stress only the bending stress must be taken into account since orientation of the strip is perpendicular to the global bending induced force. To calculate the bending stress  $\sigma_b$ , the beam bending formula with clamped boundaries is applicable. For the section modulus  $Z$ , the required girder section modulus as stated by Lloyd's Register [47] is used.

(b) Required girder web height

To determine the minimal required girder web height  $h_{w,g}$ , the required section modulus  $\hat{Z}_g$  as stated by Lloyd's Register [47] and the section modulus based on the geometry of the girder are set equal to each other.

(c) Plate-girder deflection

Lloyd's Register [47] limits also the plate-girder deflection:  $\hat{\delta}_g = \frac{a}{1000}$ , where  $a$  equals the length of the girder. To ensure that the deflection, calculated following the Euler beam formula [79], assuming clamped boundary conditions, is below the critical one, the minimum girder web height  $h_{w,g}$  is set.

(d) Girder shear buckling

The girder web needs a corresponding girder web area, following the ENV 1993-1-1 1992 [29] to ensure the absence of girder shear buckling. A transversal girder is modelled without intermediate transverse stiffeners over the full height of the girder, yielding the formula given in Table 2.4. [55, Chapter 7: Section 2] Since the minimum web height is calculated to satisfy the required section modulus, the critical deflection and the shear force, the thickness will be adapted to avoid shear buckling of the girder.

(e) Shear force

The girder web (boundary) should carry the shear force that will be transferred to the side of the ship, while having a developed girder shear stress below the allowable girder yielding shear stress  $\hat{\tau}_{y,g}$ . [55, Chapter 2: Section 6] When a larger girder web height is required than the technical design constraint of the web height ( $h_{w,g,max}$ ) and than is allowed to prevent girder shear buckling, the girder web thickness will be adapted to satisfy the shear force criterion.

Panel level

At last, the full integrated stiffened panel must be taken into account. Because stiffeners and girders have an influence on the final natural frequency  $f$  of the panel, the effect at the full stiffened panel should be calculated.

TABLE 2.5: *Structural design constraints for conventional solid configuration and sandwich material configuration on panel level.*

	<b>Conventional solid</b>	<b>Sandwich material</b>
(a)	$f = \frac{1}{2\pi\sqrt{\rho h_{eq}}} \left[ D_x \left( \frac{C_A}{t} \right)^4 + 2H \left( \frac{C_C}{a^2 l^2} \right) + D_y \left( \frac{C_B}{a} \right)^4 \right]^{\frac{1}{2}}$ $C_A = 4.73$ $C_B = 4.73$ $C_C = 151.3$	
	$D_x = \frac{Eh_p^3}{12(1-\nu_p^2)} + \frac{Eh_p e_x^2}{(1-\nu^2)} + \frac{EI_s}{s_s}$ $D_y = \frac{Eh_p^3}{12(1-\nu_p^2)} + \frac{Eh_p e_y^2}{(1-\nu_p^2)} + \frac{EI_g}{s_g}$ $H = \frac{Eh_p^3}{12(1-\nu_p^2)} + \frac{G}{6} \left( \frac{h_{i,s} t_{i,s}^3}{s_s} + \frac{h_{i,g} t_{i,g}^3}{s_g} \right)$ $h_{eq} = h_p + \frac{nA_s}{s_s} + \frac{q(A_{w,g} + A_{f,g})}{s_g}$	$D_x = \frac{E(2t_f)^3}{12(1-\nu_f^2)}$ $D_y = \frac{E(2t_f)^3}{12(1-\nu_f^2)} + \frac{E(2t_f)e_y^2}{(1-\nu_f^2)} + \frac{EI_g}{s_g}$ $H = \frac{E(2t_f)^3}{12(1-\nu_f^2)} + \frac{G}{6} \left( \frac{h_{i,g} t_{i,g}^3}{s_g} \right)$ $h_{eq} = h_{sm} + \frac{q(A_{w,g} + A_{f,g})}{s_g}$

(a) Natural frequency

To avoid interference with the excitation frequencies of the equipment on board of the vessel, there is a desired range of the natural frequency of the stiffened panel itself. According to Schaefer [65] the main formula for the dry natural frequency  $f$  is derived. Based on hierarchy, it must be assumed that the boundaries of the stiffened panel, namely the bulkheads, remain stiff, and therefore should be considered as clamped. The full derivation of the natural frequency for a stiffened panel can be found in Subsection 1.4, Supplement B.

The natural frequency is not implemented as a fixed design criterion in the model because the desired frequency range will differ per ship type and small design modifications can be made to stay in the desired natural frequency range.

## 2.2 Required parameter information to run the model

### 2.2.1 Structural modelling

In Table 2.8 an overview is given of the input parameters required to run the model, including the values used in the version of the model on which the results are based using the SPo12032 as reference ship, chosen from the DAMEN portfolio (Figure 2.5). These parameters could be adapted if desired. Below, some parameters are explained in more detail.



FIGURE 2.5: *Stan Pontoon 12032 “Tobias” by DAMEN Shipyards Group [19].*

#### Lower limit natural frequency

Based on DAMEN Shipyard’s best practice, the natural frequency of the stiffened panel must lie above 20 [Hz] to avoid interference with the exciting frequency of components present in the vessel. Since a barge vessel is chosen as reference case (SPo12032), the 20 [Hz] lower limit is less relevant since no equipment is present on the ship.

#### Global hull bending moment

Following the rules of Lloyd’s Register (July 2018) [47], the hull bending strength is characterised by the wave bending moment  $M_w$  and the still water bending moment  $M_s$ . To maintain a fair comparison,  $M_w$  and  $M_s$  are set equal to those derived from the specifications of the SPo12032, for both the hogging and sagging condition. The global hull bending moment  $M_{gl}$  is the summation of both moments (Table 2.6).

TABLE 2.6: *Global hull bending moment, including both components: wave bending moment and still water bending moment.*

		Hogging	Sagging	
Wave bending moment	$M_w$	615220	633804	[kNm]
Still water bending moment	$M_s$	582809	583790	[kNm]
Global hull bending moment	$M_{gl}$	1198029	1217594	[kNm]

#### Stiffener properties

Since the stiffener level is not incorporated in the sandwich material configuration, the stiffener

properties are set as fixed for the conventional solid configuration. Since the SPo12032 is used as starting-point, 10 stiffeners are used in the longitudinal direction per stiffened panel and a Holland profile (HP200x9) is applicable.

### Girder properties

The girder properties are chosen to meet realistic values in combination with the design of the SPo12032. The girder amount range is set at no girders to 6 girders to have a realistic girder spacing and aspect ratio of the plate. The minimal girder web height for the conventional solid design has a value of 200 [mm] to avoid that the girder web height would be lower than the stiffener web height, and therefore switch from structural level. Furthermore, it is assumed that the girder flange area is half the girder web area: girder flange thickness  $t_{f,g}$  = girder web height  $h_{w,g}$  divided by two, girder flange height  $h_{f,g}$  = girder web thickness  $t_{w,g}$ .

### Plate/Face sheet thickness

To incorporate the technical feasibility to have a successful weld using arc welding, the minimal plate thickness  $h_{p,min}$  and the minimal face sheet thickness  $t_{f,min}$  are set at 5 [mm].

### 2.2.2 Economical modelling

The net present value (NPV) of the total cost  $C_{\text{€},tot}$ , expressed in [€], is the summation of the three components (Equation (2.1)): the material costs  $C_{\text{€},mat}$ , the production costs  $C_{\text{€},prod}$  and the operational cost  $C_{\text{€},oper}$ , expressed in the net present value.

$$C_{\text{€},tot} = C_{\text{€},mat} + C_{\text{€},prod} + C_{\text{€},oper} \quad (2.1)$$

Considering the costs, the needed input parameters to run the model are given below in Table 2.7, including the chosen values for the current version.

TABLE 2.7: *Input for the cost calculation implemented in the actual version of the model.*

Material cost characteristics	Conventional solid price	$C_{mat,p}$	1	[€/kg]
	Sandwich material price	$C_{mat,sm}$	7	[€/kg]
Production cost characteristics	Welding price	$C_{weld}$	1195273	[€/m <sup>3</sup> ]
	Painting price	$C_{paint}$	23	[€/m <sup>2</sup> ]
Operational cost characteristics	Fuel price	$C_{fuel}$	5.44	[€/15yr/kg]
	Lifetime	$\gamma$	15	[yr]
	Discount ratio	$\xi$	5	[%]
	Discount factor	$\mu$	0.69	[-]

### Material costs

The material cost  $C_{\text{€},mat}$ , expressed in [€], is determined based on the specific material price in Euro per kilograms, obtained from Havel Metal Foam [37] and the total weight of the stiffened panel configuration  $W_{tot}$  (Equation (2.2)).

$$C_{\text{€},mat} = C_{mat}W_{tot} \quad (2.2)$$

### Production costs

The production cost  $C_{\text{€},prod}$ , expressed in [€], is made dependent of the weld seam volume  $V_{weld}$  and the paint area  $A_{paint}$ , following Equation (2.3). The detailed derivation of the constant values of the specific welding price  $C_{weld}$  and the specific painting price  $C_{paint}$  and the calculation of

the weld seam volume  $V_{weld}$  and the paint area  $A_{paint}$  can be found in Section 3.1, Supplement B. The two values are calculated based on given financial data from DAMEN corresponding the Crane Brage 6324. The welding knees and small structural detail attachment are not included in the calculation.

$$C_{\epsilon,prod} = C_{weld}V_{weld} + C_{paint}A_{paint} \quad (2.3)$$

#### Operational costs

The operational cost during the life time of a ship is characterised by two main components: on the one hand the fuel cost for exploiting and on the other hand the cost regarding maintenance and repair of the ship. Since the maintenance cost is difficult to measure, only the fuel cost will be considered as operational cost  $C_{\epsilon,oper}$ . The latter, expressed in [€], is calculated using the specific fuel price  $C_{fuel}$  in [€/γ/kg] for the chosen life time  $\gamma$  of the vessel and the total weight of the stiffened panel configuration  $W_{tot}$  (Equation (2.4)).

$$C_{\epsilon,oper} = C_{oper}W_{tot} \quad (2.4)$$

Since the operational costs are not an initial cost comparing to the material and production cost, the fuel price will be multiplied with a discount factor  $\mu$  to get the net present value (Equation (2.5)). The discount factor is dependent on the chosen discount ratio  $\xi$  and the time period  $\gamma$  over which the costs will be spread. The calculation on which the constant fuel price  $C_{fuel}$  is based, is given in Subsection 3.2, Supplement B. The value is calculated based on given financial data from DAMEN corresponding the Stan Patrol 5009.

$$C_{oper} = \mu C_{fuel} \quad (2.5)$$

where,

$$\mu = \sum_{t=1}^{\gamma} \frac{1}{\gamma(1+\xi)^t}$$

TABLE 2.8: *Input for the geometry optimisation implemented in the actual version of the model.*

General characteristics	Length moulded ship	$L$	120	[m]
	Beam moulded ship	$B$	32.2	[m]
	Depth ship	$D$	8.1	[m]
	Amount of longitudinal bulkheads	$m$	5	[-]
	Amount of transversal bulkheads	$u$	10	[-]
	Density seawater	$\rho_w$	1025	[kg/m <sup>3</sup> ]
	Acceleration of gravity	$g$	9.81	[m/s <sup>2</sup> ]
	Lower limit natural frequency	$f_{min}$	20	[Hz]
Stiffener properties	Web height	$h_{w,s}$	200	[mm]
	Web thickness	$t_{w,s}$	9	[mm]
	Section modulus	$Z_{HP}$	77700	[mm <sup>3</sup> ]
	Area	$A_{HP}$	2366	[mm <sup>2</sup> ]
	Moment of inertia	$I_{HP}$	9420000	[mm <sup>4</sup> ]
	Circumference area	$Al_{HP}$	457	[m <sup>2</sup> /m]
	Amount of longitudinal stiffeners	$n$	10	[-]
	Girder properties	Initial web thickness	$t_{w,g}$	14
Lower limit girder amount		$q_{min}$	0	[-]
Upper limit girder amount		$q_{max}$	6	[-]
Lower limit girder web height		$h_{w,g,min}$	200	[mm]
Upper limit girder web height		$h_{w,g,max}$	1000	[mm]
Load properties	Loading factor	$\phi$	1	[mm]
	Global hogging bending moment	$M_{gl,hog}$	1198029	[kNm]
	Global sagging bending moment	$M_{gl,sag}$	1217594	[kNm]
	Water pressure	$p$	0.1	[MPa]
Conventional solid properties	Density	$\rho_p$	7850	[kg/m <sup>3</sup> ]
	Young's Modulus	$E_p$	210000	[MPa]
	Yield stress	$\hat{\sigma}_{y,p}$	235	[MPa]
	Poisson's ratio	$\nu_p$	0.3	[-]
	Lower limit plate thickness	$h_{p,min}$	5	[mm]
	Upper limit plate thickness	$h_{p,max}$	120	[mm]
Face sheet properties	Density	$\rho_f$	7850	[kg/m <sup>3</sup> ]
	Young's Modulus	$E_f$	210000	[MPa]
	Yield stress	$\hat{\sigma}_{y,f}$	235	[MPa]
	Poisson's ratio	$\nu_f$	0.3	[-]
	Lower limit face sheet thickness	$t_{f,min}$	5	[mm]
Core properties	Density	$\rho_c$	800	[kg/m <sup>3</sup> ]
	Young's Modulus	$E_c$	760	[MPa]
	Yield stress	$\hat{\sigma}_{c,y}$	10	[MPa]
	Poisson's ratio	$\nu_c$	0.3	[-]
	Lower limit core thickness	$t_{c,min}$	10	[mm]
	Upper limit core thickness	$t_{c,max}$	150	[mm]

### 3 Results

#### 3.1 Structural modelling

Per number of girders (0-6), the model searches for the minimal weight configuration that satisfies all the design constraints included, while altering the design variables for the two load cases per number of girders: plate thickness, core thickness, girder web height. This means that per data point given in the results, a different geometry is likely. With respect to the sandwich material, the minimal weight configuration are also given according to the a constant core thickness (50 [mm], 75 [mm], 100 [mm]).

##### 3.1.1 Load case (I): still water pressure in combination with global sagging and hogging wave vertical bending moments

For the **conventional solid material** configuration, the minimum required plate thickness  $h_p$  at plate level is 19 [mm], independent of the number of girders. The reason why a larger plate thickness is required to meet all the requirements for the case of zero or two girders, is that the stiffener scantlings are not sufficient in combination with a 19 [mm] thick base plate. Therefore, the required plate thickness is adapted (Table 2.9). The latter explains the steep curve for zero to one girder and the flattening out from two girders. For the girder web height a combination of the design criteria is limiting, in particular the required section modulus by Lloyd's Register [47], the girder-plate deflection by Lloyd's Register [47], shear force by Okumoto et al. [54] girder shear buckling by Okumoto et al. [54] and the technological design constraints (upper and lower limit) of the girder web height.

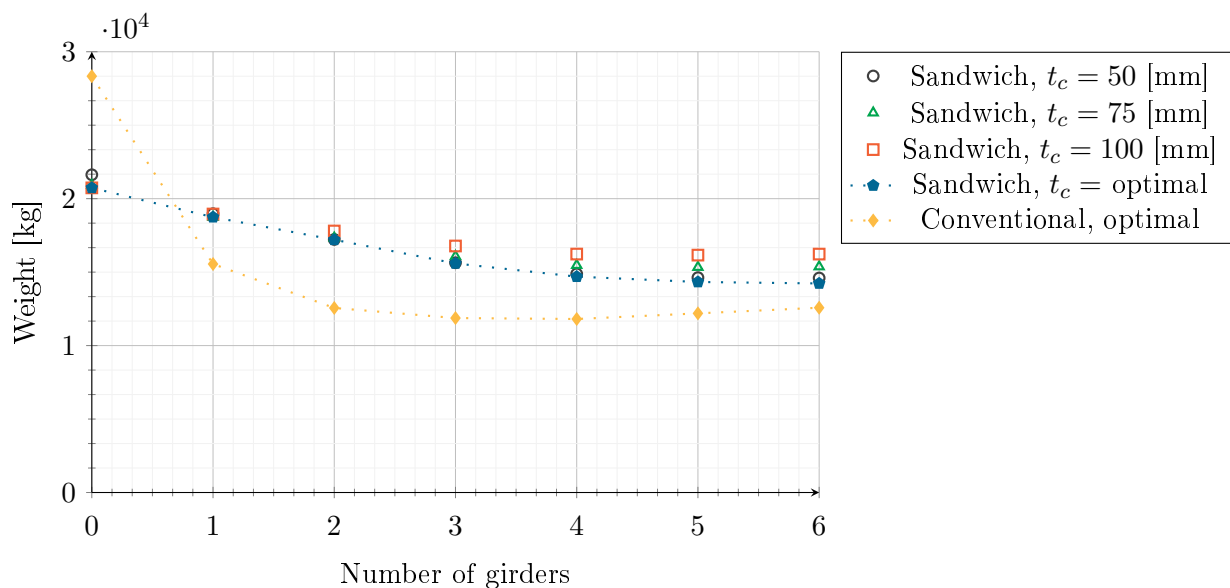


FIGURE 2.6: Load case (I): Total weight of the stiffened panel in function of amount of girders for the conventional solid design and the sandwich material configuration. Per point the minimum weight is plotted.

In case of the **sandwich material** design, a minimum face sheet thickness is required to endure the global sagging and hogging wave vertical bending moments as seen in Table 2.9. Table 2.9 also shows the accompanying girder web height and thickness to obtain the lowest weight of the stiffened panel, following the same design criteria as mentioned for the conventional solid material configuration. The failure criterion core shear is decisive for the minimum required core thickness  $t_{c,min}$ . Since the minimum required face sheet thickness is large, the face sheet will have a large contribution, resulting in a small minimum required core thickness. It is visible

TABLE 2.9: Load case (I): Values of the parameters of the optimal configurations, as shown in Figure 2.6. *So* = conventional solid material configuration, *Sa* = sandwich material configuration

			Number of girders							
			0	1	2	3	4	5	6	
<b>So</b>	Plate thickness	$h_p$	58	29	22	20	19	19	19	[mm]
	Girder web height	$h_{w,g}$	/	700	514	430	434	434	434	[mm]
	Girder web thickness	$t_{w,g}$	/	15	14	14	14	14	14	[mm]
<b>Sa</b>	Face sheet thickness	$t_f$	18	16	15	14	13	12	11	[mm]
	Core thickness	$t_c$	99	73	57	40	34	35	35	[mm]
		$t_{c,min}$	20	26	29	32	34	35	35	[mm]
	Girder web height	$h_{w,g}$	/	700	514	385	387	391	394	[mm]
	Girder web thickness	$t_{w,g}$	/	15	14	14	14	14	14	[mm]

that the minimal core thickness does not give per se the minimal weight configuration. Since a decreasing face sheet thickness is applicable and the core thickness and the girders cross sectional area does not change much over the range of girders, a slightly decreasing curve of the lines is expected. According to the influence of the core thickness on the results, the scatter between the data points of  $t_c = [50 - 100]$  increases with the number of girders.

When comparing the minimal weight configuration of the conventional solid material (girders = 3) to the minimal weight design of the sandwich material (girders = 6), the conventional solid configuration still has a lower weight.

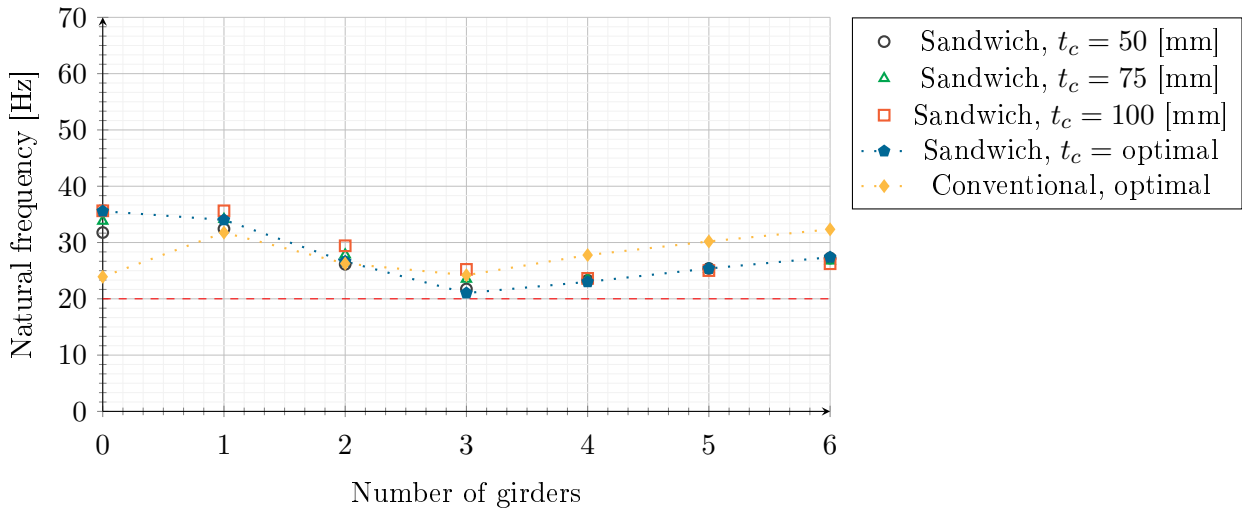


FIGURE 2.7: Load case (I): Natural frequency (dry) of the total stiffened panel. Dashed line represents the requirement of 20 Hz.

To avoid interference with the natural frequencies of the other equipment on board of the vessel, there is a desired range of the natural frequency of the stiffened panel itself. DAMEN shipyard demands that the natural frequency must be larger than 20 [Hz], determined by the two major elements: flexural rigidity and mass.

The natural frequency for the sandwich material design is lower than those of the conventional solid material (Figure 2.7). This can be clarified by the lower required web girder height for sandwich materials. The large drop in natural frequency between one and three girders for the conventional solid material and the sandwich material is caused by the fact that a lower web girder height is acceptable to satisfy the design criteria. This results in a lower flexural rigidity.

### 3.1.2 Load case (II): still water pressure only

In the circumstances of only still water pressure, the plate thickness  $h_p$  of the **conventional solid material** configuration is dominated by the plate yielding criterion at plate-level, leading to a minimal plate thickness of 8 [mm]. Similar as load case (I) the stiffener scantlings are not sufficient for zero to one girders: the plate thickness has to be increased to satisfy the structural design constraints. (Table 2.10). A step declining curve that evolves to flattening out is present, which is similar as load case (I). Since the total structure has to endure less load, the overall weight is lower in load case (II), with respect to load case (I).

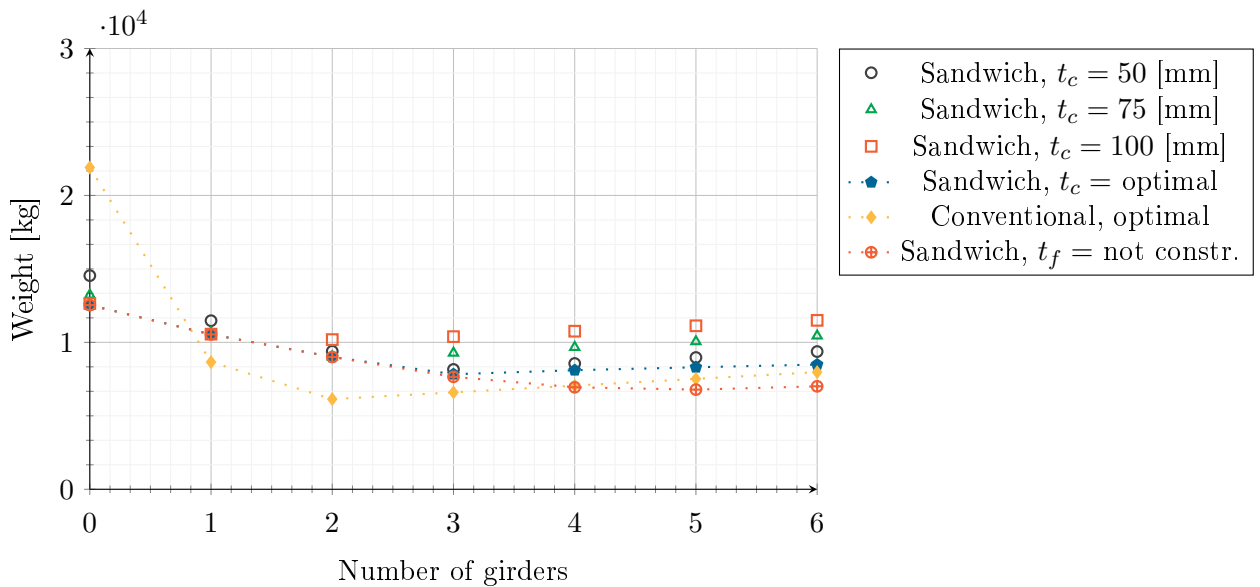


FIGURE 2.8: Load case (II): Total weight, expressed in kilograms, of the stiffened panel in function of amount of girders for the conventional solid design and the sandwich material configuration. Per point the minimum weight is plotted.

For the **sandwich material** the face sheet thickness  $t_f$  is no longer dominated by the global load, resulting in a smaller thickness (Table 2.10). However, it is dominated by the design constraint to guarantee welding ( $t_f \geq 5$  [mm]). Since the required face sheet thickness has decreased, the required core thickness should be larger to avoid core shear failure; a minimum core thickness around 40 [mm] is required, with respect to the minimal core thickness of 30 [mm] for load case (I).

The welding design constraint implies that the minimal effective plate thickness  $2t_f$  equals 10 [mm]. Comparing to the minimal plate thickness of the conventional plate (8 [mm]), the face sheets itself have a larger weight, and the core weight has still to be added for the total sandwich thickness.

Since the minimal weight of the conventional solid material configuration (girders = 2) is lower than the minimal weight sandwich material design (girders = 3), the extra weight due to the stiffeners and larger girder scantlings of the conventional design will not cancel out the larger weight of the sandwich material itself.

TABLE 2.10: *Load case (II): Values of the parameters of the optimal configurations shown in Figure 2.8. So = conventional solid material configuration, Sa = sandwich material configuration*

			Number of girders							
			0	1	2	3	4	5	6	
<b>So</b>	Plate thickness	$h_p$	44	14	10	6	6	6	6	[mm]
	Girder web height	$h_{w,g}$	/	700	700	519	519	519	519	[mm]
	Girder web thickness	$t_{w,g}$	/	15	14	14	14	14	14	[mm]
<b>Sa</b>	Face sheet thickness	$t_f$	8	6	5	5	5	5	5	[mm]
		$t_{f,nc}$	8	6	5	4	3	2	2	[mm]
	Core thickness	$t_c$	119	93	74	42	48	48	48	[mm]
		$t_{c,min}$	30	36	39	42	42	42	42	[mm]
	Girder web height	$h_{w,g}$	/	700	514	464	356	330	310	[mm]
	Girder web thickness	$t_{w,g}$	/	15	14	14	14	14	14	[mm]

When the welding criterion is not present, it is visible that an equal weight configuration is obtained for both configurations (girders = 2, girders = 5). The optimal face sheet thickness when no welding constraint is present  $t_{f,nc}$  is also given in Table 2.10.

Similar to load case (I), the sandwich material design has a lower natural frequency than the conventional solid material configuration in load case (II). This can be explained due to the lower required web girder height for sandwich materials. Comparing the natural frequency of one to four girders, there is a significant drop caused by a lower web girder height being acceptable to satisfy the design criteria (see Table 2.10).

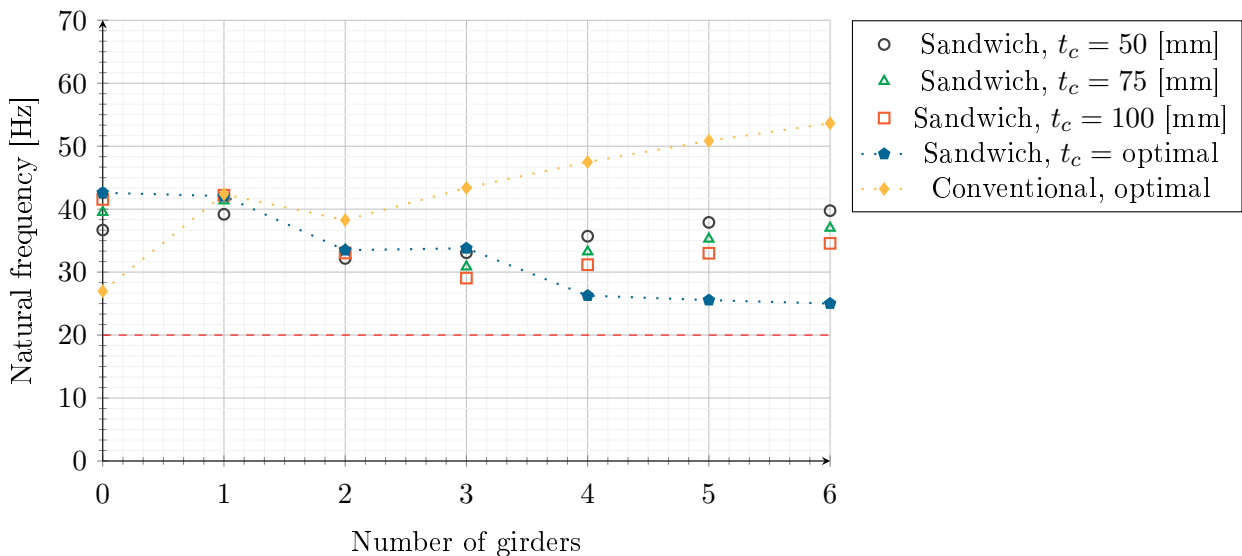


FIGURE 2.9: *Load case (II): Natural frequency (dry) of the total stiffened panel. Dashed line represents the present requirement of 20 Hz.*

### 3.1.3 Validation

Comparing the original design of the drawing of the SPo12032 and the conventional solid material optimised geometry using Table 2.11, two small differences are visible after the structural optimisation: (1) A lower amount of girders is seen as optimal. Together with a slight decrease in the girder volume each, this will lead to a lower total girder volume for the total stiffened panel. (2) A small increase in plate thickness is required. In the model, the plate thickness is defined at the plate level, by plate-yielding and plate buckling in load case (I). In the estimation of the membrane force that has to be incorporated, the vertical bulkheads are not included. This could clarify the small increase in plate thickness. Despite these small differences, the total weight lies in the same range as the original SPo12032, so the model reproduces the conventional solid design realistic. To make the validation conversion between the conventional solid material and the sandwich material model, small hand-calculations have been performed to check the derived and adapted formulas for the sandwich material design, yielding the same relations. Furthermore, the same reasoning behind the make-up of the model is valid. As such, the two models are correct implemented and therefore representative for the optimisation and design of a stiffened panel.

TABLE 2.11: *Validation structural optimisation model outcome for both configurations with the original SPo12032 drawing, for the two load cases.*

Load case	Parameter		Solid material		Sandwich material	
			Original	Optimum	Optimum	
(I)	Weight	$W_{tot}$	11.91	11.87	14.23	[ton]
	Plate thickness	$h_p, h_{sm}$	17	20	57	[mm]
	Face sheet thickness	$t_f$			11	[mm]
	Core thickness	$t_c$			35	[mm]
	Girder amount	$q$	4	3	6	[-]
	Girder spacing	$s_g$	2182	2727	1558	[mm]
	Girder web height	$h_{w,g}$	600	430	394	[mm]
	Girder web thickness	$t_{w,g}$	14	14	14	[mm]
	Girder flange height	$h_{f,g}$	250	215	197	[mm]
	Girder flange thickness	$t_{f,g}$	17	14	14	[mm]
Natural frequency	$f$		24	27	[Hz]	
(II)	Weight	$W_{tot}$	11.91	6.14	7.83	[ton]
	Plate thickness	$h_p, h_{sm}$	17	8	52	[mm]
	Face sheet thickness	$t_f$			5	[mm]
	Core thickness	$t_c$			42	[mm]
	Girder amount	$q$	4	2	3	[-]
	Girder spacing	$s_g$	2182	3636	2727	[mm]
	Girder web height	$h_{w,g}$	600	519	464	[mm]
	Girder web thickness	$t_{w,g}$	14	14	14	[mm]
	Girder flange height	$h_{f,g}$	250	260	232	[mm]
	Girder flange thickness	$t_{f,g}$	17	14	14	[mm]
Natural frequency	$f$		38	33	[Hz]	

### 3.2 Economical modelling

The results of the three different components of the total costs for the two different load cases are given by Table 2.12 and Table 2.13, expressed in values. Figure 2.10, Figure 2.11, Figure 2.12 and Figure 2.13 give a visual relation between the optimal configurations of the conventional solid material and the sandwich material design, including the welding design constraint.

#### 3.2.1 Load case (I): still water pressure in combination with global sagging and hogging wave vertical bending moments

The material price of an {aluminium foam core, steel face sheet} sandwich material is approximately seven times higher than the conventional steel price as seen in the **material costs** of the total stiffened panel (Figure 2.10a). The cost is not much affected by the number of girders.

With respect to the **production costs**, it is visible in Figure 2.10b that by implementing the sandwich material as baseplate the cost could be reduced by factor two. The production costs increase linear with the number of girders. From the subdivision of the production costs in the weld and paint contribution, one can conclude that the painting costs are grosso modo constant, while the welding costs do increase linear. The latter can be explained since the required welds do increase with a constant value per extra girder.

For the **operational costs** expressed the net present value (Figure 2.10c), the same graph is visible as the total weight graph, only the values alter since the weight is multiplied with the constant fuel price, which is identical for the sandwich material and the conventional solid material.

When combining the components, the **total costs**, expressed in net present value arise. From Figure 2.10d one can derive that for the first load case no cost advantage is present for the sandwich material with respect to the conventional solid material. The higher material costs cannot be offset by the advantage of lower production costs.

TABLE 2.12: *Load case (I): Values of the three components of the total costs for both the conventional solid (So) material and the sandwich (Sa) material design accompanying the optimal configuration as shown in Figure 2.6.*

			Number of girders							
			0	1	2	3	4	5	6	
<b>So</b>	Material cost	$C_{\text{€},mat}$	28	16	13	12	12	12	13	[k€]
	Production cost	$C_{\text{€},prod}$	10	12	13	15	16	18	19	[k€]
	Operational cost	$C_{\text{€},oper}$	107	59	47	45	44	46	47	[k€]
	Total cost	$C_{\text{€},tot}$	145	86	73	71	72	76	79	[k€]
<b>Sa</b>	Material cost	$C_{\text{€},mat}$	145	131	120	109	103	100	100	[k€]
	Production cost	$C_{\text{€},prod}$	3	5	6	7	8	9	9	[k€]
	Operational cost	$C_{\text{€},oper}$	78	71	65	59	55	54	54	[k€]
	Total cost	$C_{\text{€},tot}$	226	206	191	17	166	163	162	[k€]

Figure 2.11c illustrates the contribution of the three components of the total costs, expressed in [k€], for the **conventional solid design**. Figure 2.11e defines the share of the cost component, expressed in percentages. It is visible that the material costs and the production costs have an equal contribution, starting from two girders. In the region from zero to one girder, less production costs are required, in particular welding costs, since a lower amount of girders is present. The production costs belonging to the stiffeners are a constant value since the amount of stiffeners is fixed. The region for zero to one girder could require a different stiffener scantling,

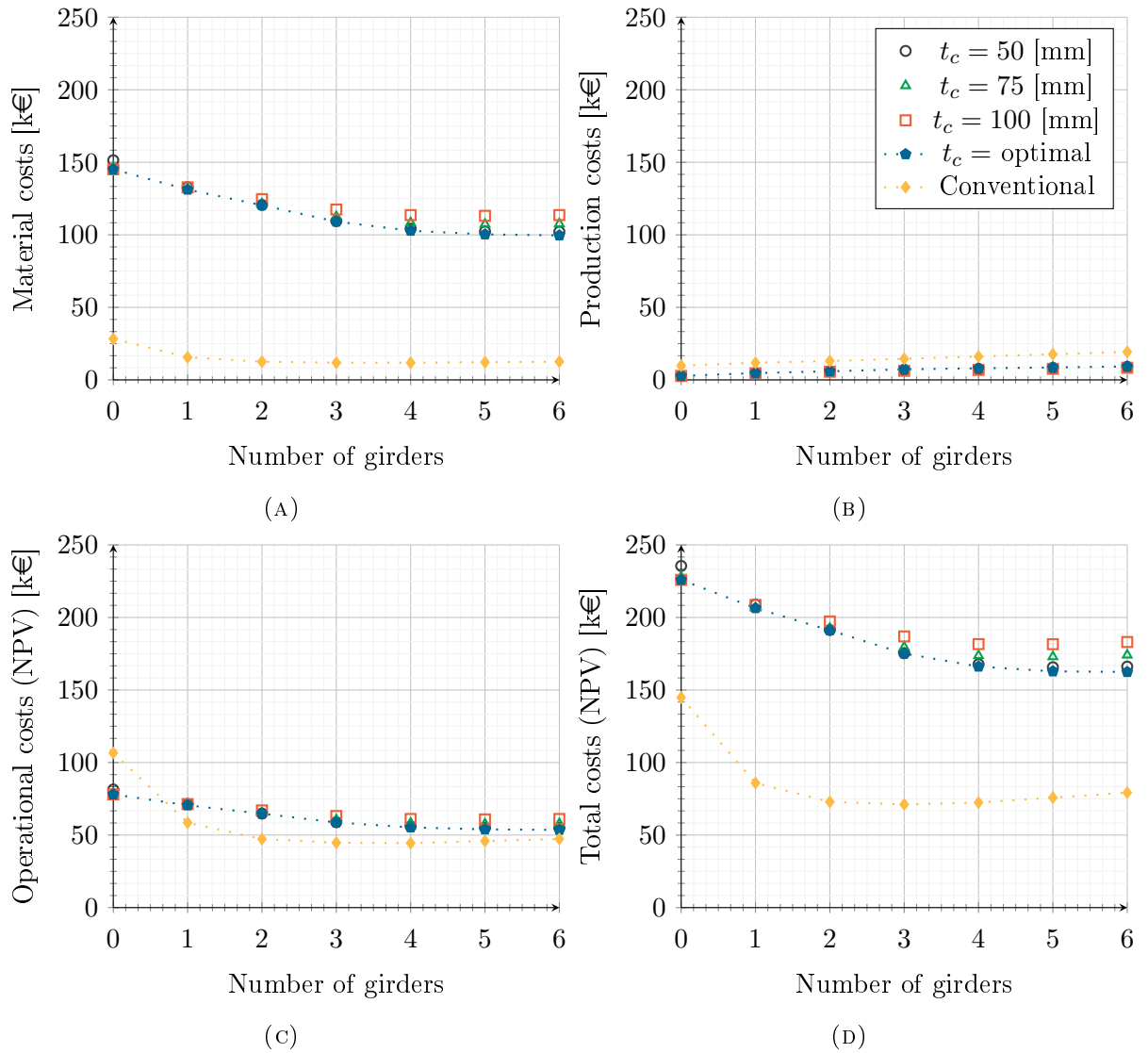


FIGURE 2.10: Load case (I): Calculation of the net present value (NPV) of the total costs (D), expressed in [k€], effect of material costs (A), production costs (B) and the operational costs (NPV) (C). The legend of the 4 graphs is depicted in Figure 2.10b. Per point the optimal design is plotted, of which the values of the design variables are given in Table 2.9.

which will affect the relation of the production costs and material costs. The operational costs do have the dominant contribution to the total costs (60%).

For the **sandwich material configuration**, the three components, expressed in [k€], are shown in Figure 2.11d, while the proportion, expressed in percentages, is given by Figure 2.11f. The relation between the material cost and the production cost differs tremendously with respect to the conventional solid design: the production costs are lower, while the material costs are becoming the dominant factor in the total costs (60%). Based on the percentages, the operational costs do have a lower share, but looking at the costs expressed in [k€], the operational costs are higher for the sandwich material configuration. The latter can be explained since the total weight of the stiffened panel is higher.

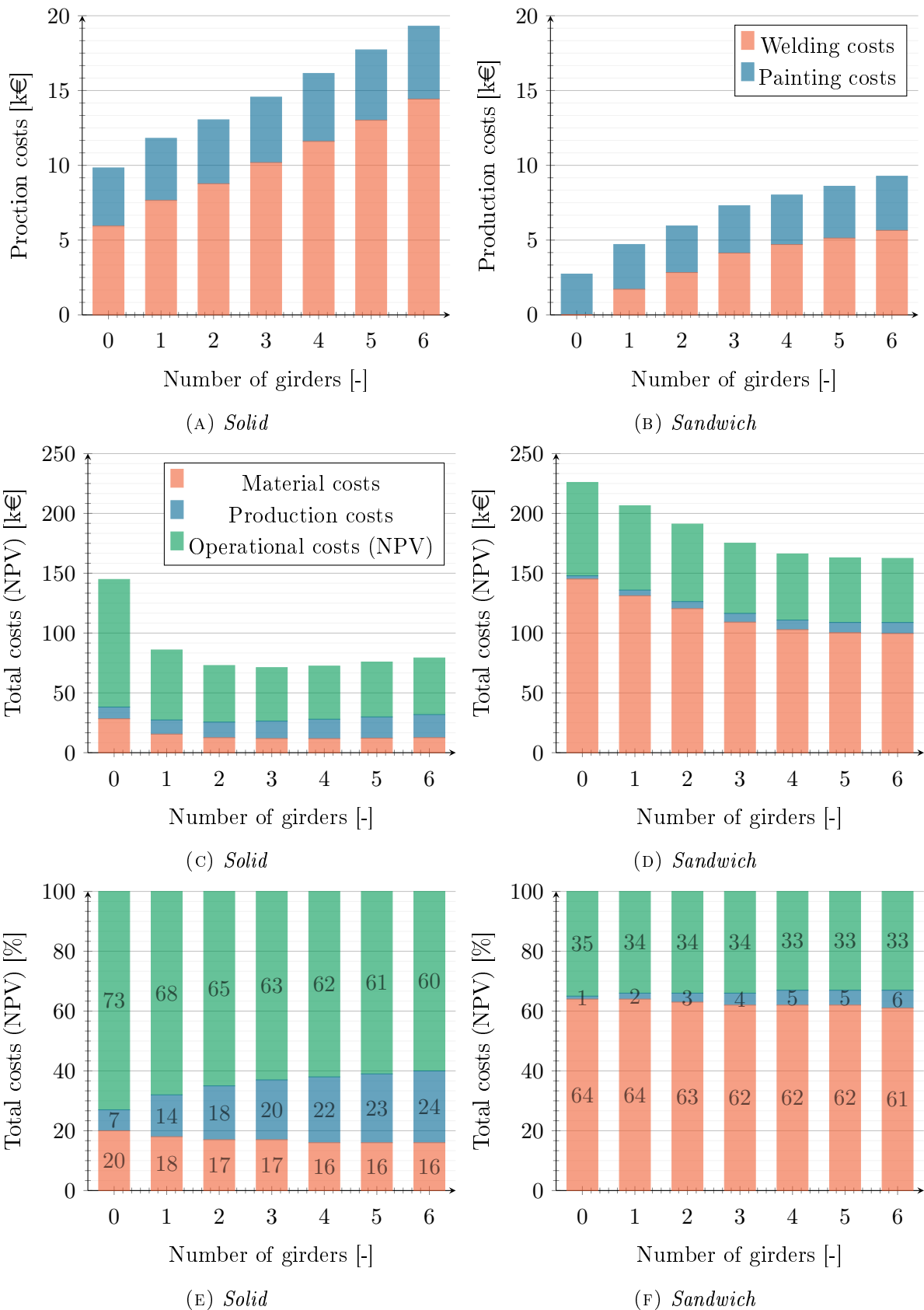


FIGURE 2.11: Load case (I): The distribution of production costs for the conventional solid material configuration (A) and the sandwich material design (B): effect of welding and painting cost part. Distribution of costs (NPV) for the conventional solid material configuration (C) and the sandwich material design (D) and in relative values for the conventional solid material configuration (E) and the sandwich material design (F) for the optimal configurations.

### 3.2.2 Load case (II): still water pressure only

The difference in **material cost** [k€] seems to be smaller than for load case (I), although the ratio of the pure material price [k€/kg] of seven is still present. Since the total weight of the sandwich material is higher with respect to the conventional design, the ratio factor is even increased to roughly nine. When the welding criterion is not present, the total weight of both configurations was equal to load case (I), so the same relation would be present.

The relation between the **production costs** of load case (II) and load case (I) is not different: by implementing the sandwich material as baseplate the cost could be reduced by factor 2. However, the conventional design curve is more horizontal compared to load case (I), implying that the production costs do not alter upon increasing girder amount. The changes in weld seam length and the paint area will cancel each other out over the range of girders (see Figure 2.13a). The increasing line for the sandwich material is more flat, comparing to load case (I), due to the lower welding costs. The weld seam volume formulation will clarify this fact: the required fillet radius is dependent on the smallest thickness between the plate and the girder web height. The presence of a smaller required face sheet thickness in load case (I) results in a lower required fillet radius, yielding a lower weld seam volume and finally lower welding costs.

Since the **operational costs** are calculated using a constant factor times the total weight of the stiffened panel, the same relation between the materials is obtained as presence in the total weight graph (Figure 2.8).

As shown in Figure 2.12d the reduction in the production costs are not able to withdraw the initial higher sandwich material cost. No advantage is present with respect to the **total costs** for sandwich materials comparing to the conventional solid design.

TABLE 2.13: *Load case (II): Values of the three components of the total costs for both the conventional solid (So) material and the sandwich (Sa) material design accompanying the optimal configuration as shown in Figure 2.8.*

			Number of girders							
			0	1	2	3	4	5	6	
<b>So</b>	Material cost	$C_{\epsilon,mat}$	22	9	6	7	7	8	8	[k€]
	Production cost	$C_{\epsilon,prod}$	10	12	10	11	11	12	13	[k€]
	Operational cost	$C_{\epsilon,oper}$	82	33	23	25	27	28	30	[k€]
	Total cost	$C_{\epsilon,tot}$	114	53	39	42	45	47	50	[k€]
<b>Sa</b>	Material cost	$C_{\epsilon,mat}$	87	74	63	54	57	58	59	[k€]
	Production cost	$C_{\epsilon,prod}$	3	3	3	4	4	4	5	[k€]
	Operational cost	$C_{\epsilon,oper}$	47	40	34	29	31	31	32	[k€]
	Total cost	$C_{\epsilon,tot}$	138	117	100	88	91	94	96	[k€]

The contribution of the three components of the total costs, expressed in [k€], for the conventional design and the sandwich material design are given by Figure 2.13c and Figure 2.13d. Comparing to load case (I) the same distribution is present. Figure 2.13e and Figure 2.13f present the relative results, which do not differ likewise with respect to load case (I). The same explanation is valid.

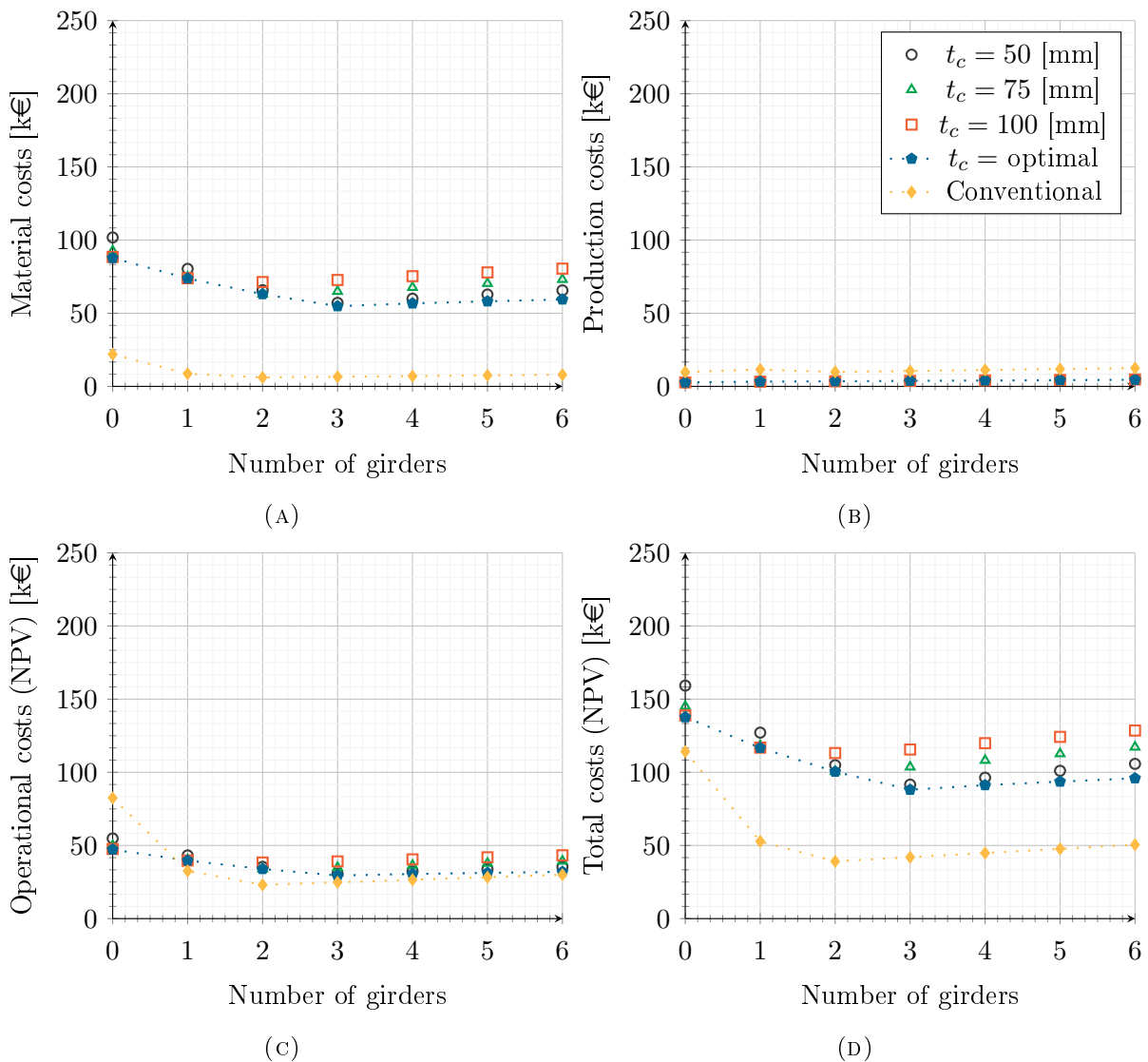


FIGURE 2.12: Load case (II): Calculation of the net present value (NPV) of the total costs (D), expressed in [k€], effect of material costs (A), production costs (B) and the operational costs (NPV) (C). The legend of the 4 graphs is depicted in Figure 2.10b. Per point the optimal design is plotted, of which the values of the design variables are given in Table 2.10.

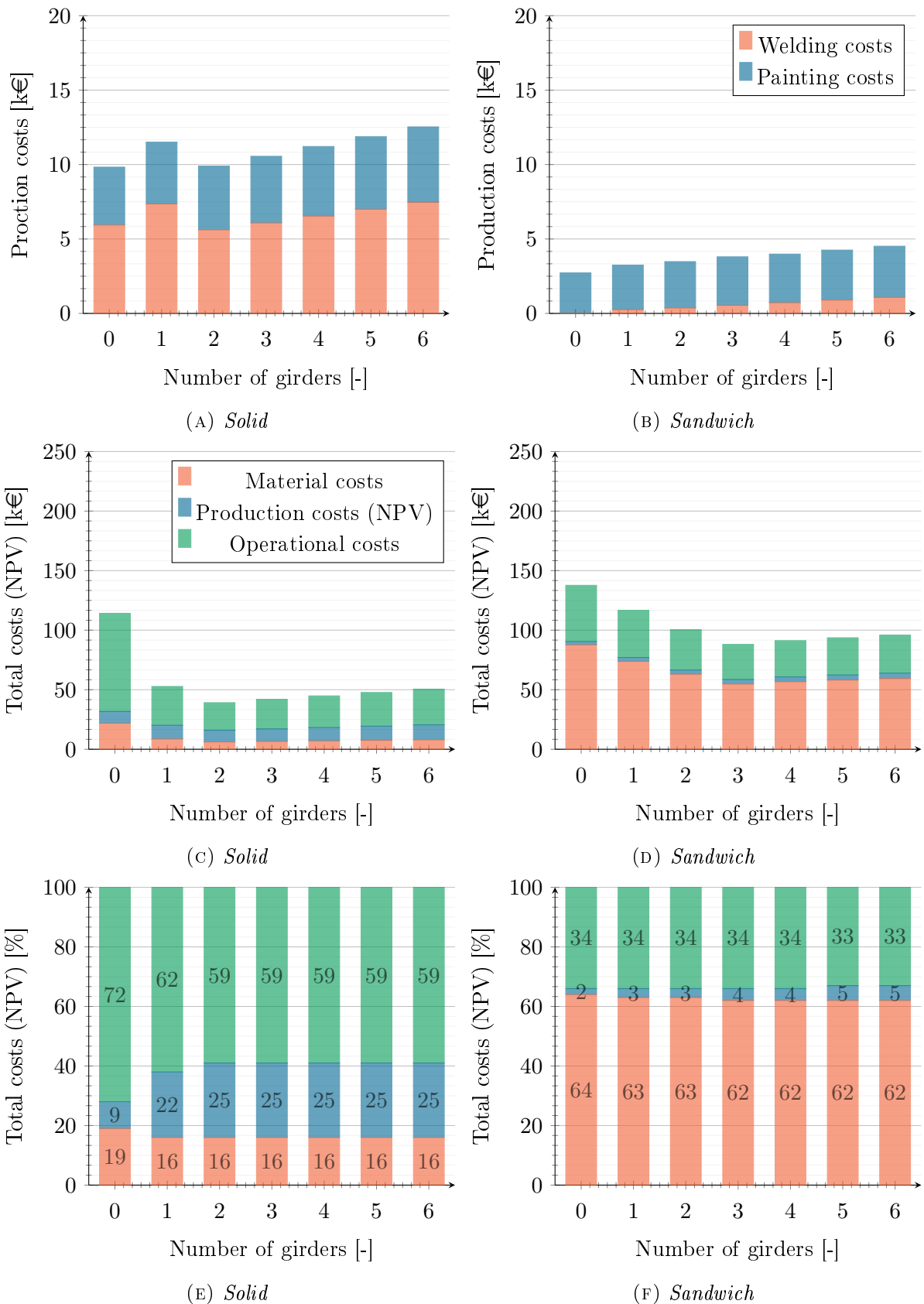


FIGURE 2.13: Load case (II): The distribution of production costs for the conventional solid material configuration (A) and the sandwich material design (B): effect of welding and painting cost part. Distribution of costs (NPV) for the conventional solid material configuration (C) and the sandwich material design (D) and in relative values for the conventional solid material configuration (E) and the sandwich material design (F) for the optimal configurations.

## 4 Discussion

The main findings of this study comparing the conventional steel plate and the {aluminium foam core, steel face sheet} sandwich material at the stiffened panel are firstly the confirmation of the higher initial material cost of the {aluminium foam core, steel face sheet} sandwich material; secondly, the 50% reduction in production cost for the sandwich material; and finally, the necessity of a larger number of girders for the minimal weight design of the sandwich material.

One of the elements responsible for the higher material cost is the absence of weight reduction. In load case (I), the in-plane force dominated the required face sheet thickness. Since only the steel face sheets carry the force ( $A_{eff} = 2t_f$ ), the face sheet thickness should be at least half the plate thickness of the conventional steel solid plate. As such, there will never be a major weight reduction. In load case (II) there was also no weight reduction realised by the sandwich material; the weight of the two face sheets with the thickness to allow arc welding was higher than the weight of the conventional steel solid plate, despite the fact that the thickness of the steel plate was modelled to be higher than the thickness required for the welding.

The material cost and the operational cost relate to the total weight. Since there is no weight decrease in both load cases, no cost benefit is obtained. Any cost benefit should be derived from a reduction in production costs, the only factor a shipyard can modify. There was a 50% reduction of the production costs thanks to the more simple stiffened panel when using the sandwich material. Unfortunately, this reduction was not sufficient to counter at least the higher material cost. Therefore, the only possible way is a probably unrealistic drop of the material price to 0.5 [€/kg], indicating a decrease of 95%.

The material could still be promising in configurations where multiple functional aspects are required and are seen as more important than a decrease in total weight and initial costs. The {aluminium foam core, steel face sheet} sandwich material could be incorporated in naval vessels when one needs a high resistance to impacts and blasting, and when one wants to conserve the limited internal space. Their application could result in a reduction of production costs in ships in which a high thermal and acoustical insulation is required. The duration and the cost of the class inspections will be lower due to the lower number of welds.

Two model techniques were brought together in the study: an analytical structural optimisation model and a cost calculation model. Rigo and Caprace [63] applied this technique to successfully diminish the GHG emissions by ship scantling optimisation, i.e. decreasing steel weight and keeping the production cost at an acceptable level. Our study suggests that this combined modelling technique should be common practise in structural optimisation business cases in shipbuilding. Furthermore, our model is not limited to the {aluminium foam core, steel face sheet} sandwich material, but is applicable for all different types of sandwich materials. Only in case special failure modes have to be introduced, small adaptations should be made in our model.

Some limitations of the present study should be considered when data are interpreted. At first, the operational costs are approximated by the fuel costs only, no maintenance cost is included since the latter is difficult to measure. This might be a missed benefit for the sandwich material design, since the maintenance costs could be lower due to lesser need for repairs, resulting from the lower number of welds. [6, 37]. Moreover, in the obtained results an abrupt transition in the value of a parameter could be present, with respect to a changing number of girders. This can be explained that depending on the configuration another design constraint is decisive. The choice of the design constraint cannot always be influenced, depending on the type of design constraint, but in the `CriteriaSM.m` and `CriteriaOR.m` files of the model the required criteria can be checked or adapted if desired so that the specific criterion is active or not. Thirdly, since

the stiffeners are removed in the sandwich material design, and the mechanical added value in implementing the {aluminium foam core, steel face sheet} sandwich materials in the stiffened panel was the base, the stiffener scantlings in the conventional solid material model are taken identically to the validation design (SPo12032) and are not optimised. The latter has as result that the conventional solid plate will be in some occasions too heavy. When the fixed stiffener dimensions are insufficient, the plate thickness will be adapted. Increasing the amount of stiffeners and/or the stiffener scantlings will be more effective to add stiffness to the construction, instead of increasing the plate thickness, as such a more heavy structure is obtained. For a higher number of girders, the stiffener scantlings could be larger than required, which will also increase the weight. However, the weight of the optimal configuration of the conventional solid design with respect to the validation case was equal, so the influence is eventual rather low. At last, the business case is focussed on the DAMEN portfolio and their demands and requirements. Also, the financial data and operational data known of the company are implemented in the case study. The obtained results will give an idea of the application possibilities of sandwich materials in general, but depending on the ship types, the production cost, and operational costs, the outcome of the business case may be different.

In conclusion, if implemented as stiffened panel, the {aluminium foam core, steel face sheet} sandwich material is not yet a potential alternative with respect to the conventional solid steel design. Besides the higher total costs concerning the construction, the model does even not have taken in consideration the required investments in new machines, educated personnel, and the organisation of the shipyard required to deal with the implementation of this new material.



# Chapter 3 | Metallographic and fatigue analysis of corner adstir fillet stationary shoulder friction stir welded double sided T-joints

## 1 Introduction

Friction stir welding (FSW) is a welding technique that has been developed by The Welding Institute (TWI) in the 1990s [73]. The principle is to create a weld by mixing materials, softened by heat which is induced by friction, followed by natural cooling. [17, 52] A machine-driven tool pushes its rotary tip at the starting point of the joint line of the two pieces visualised by Figure 3.1. The pin, rotating and advancing at pre-set speeds, produces heat by friction that softens the materials without melting them, and mixes the materials together along the weld path. An extra shoulder prevents that the softened materials can escape. [16] The weld includes two different zones: the advancing side (AS) and the retreating side (RS) of the weld. The advancing side is known as the zone where the travelling speed and rotational speed have the same direction, while the retreating side is characterised as the zone where both speeds have a different direction. [62]

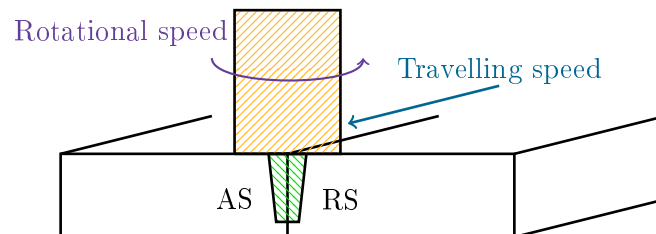


FIGURE 3.1: Schematic visualisation of the conventional friction stir welding tool and main process variables. pin (green hatched), shoulder (yellow hatched)

Beside the fact that FSW is a process with a good energy-efficiency, environment friendly and characterised by reduced labour process time, its main advantage is the reduced peak temperature compared with arc welding process. The lower temperature results in reduced residual stresses, with a smaller affected zone of the parent material. Lower residual stresses lead to a higher fatigue strength, joint strength and ductility, and lower corrosion susceptibility and longitudinal and transverse distortion. [16, 72] The residual stress is mainly influenced by the travelling and the rotational speeds (Figure 3.1) [74]. The affected zone, as shown in Figure 3.2a, consists of three different structures: the heat affected zone (HaZ) and the thermomechanically affected zone (TMaZ) which can be further divided into a unrecrystallised part and recrystallised part (nugget). The HaZ consists of materials adequately heated in order to change its properties but without plastic deformation. These changes encompass alterations in the strength, corrosion sensitivity and toughness. The TMaZ comprises all the plastic deformation. [16] When com-

paring to the affected zone caused by arc welding (Figure 3.2b), a higher crystallisation grade is visible, implying a larger degradation of the parent material. [72]

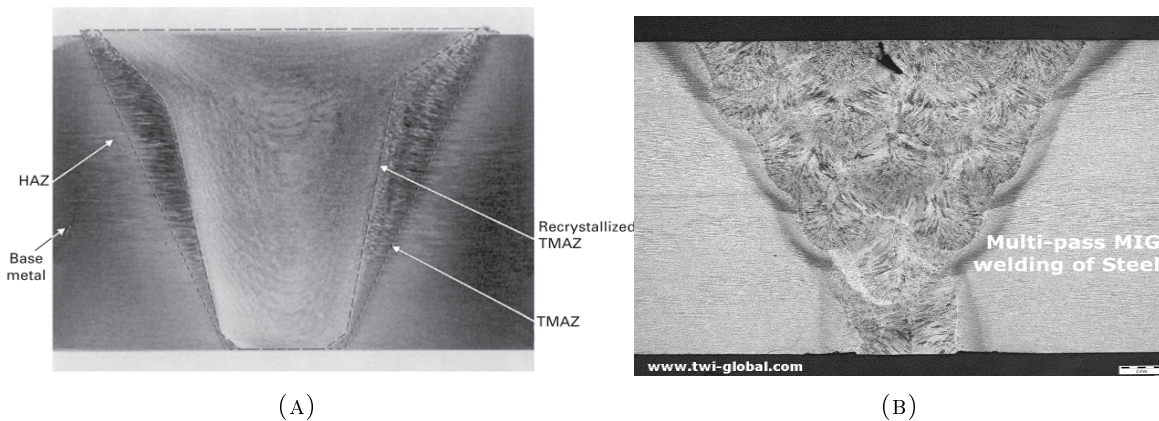


FIGURE 3.2: *Transverse section of a friction stir welded welded (A) and a conventional arc welded (B) butt-joint. [16, 72]*

Today, the largest application of the conventional FSW is the welding of butt-joints. The added value of FSW for butt-joints has been largely studied. Costa et al. [17] compared the fatigue of a butt-joint welded by FSW compared to that welded by conventional welding techniques; FSW increased the life time of the structure significantly. The role of the welding speed and the surface finishing treatment have been investigated by respectively Ericsson and Sandström [26] and Pedemonte et al. [58]. The life time of the FSW butt-joint was not influenced by the welding speed, but was enhanced by the surface finishing treatment.

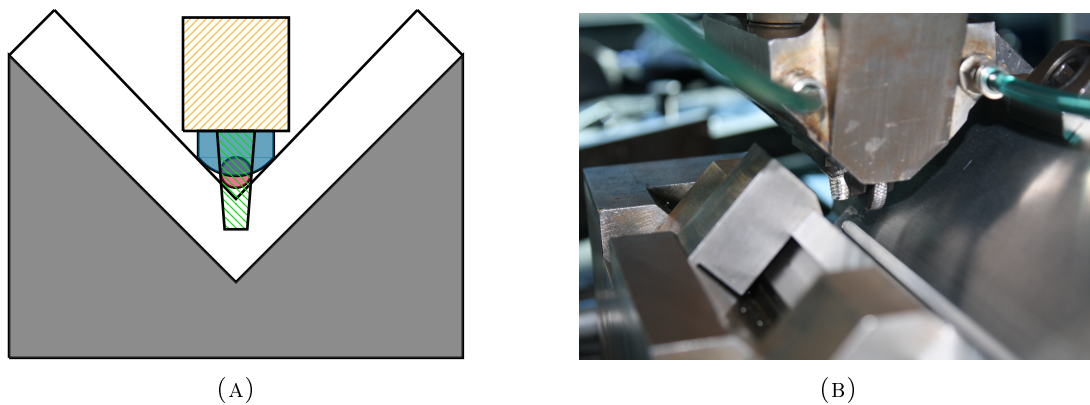


FIGURE 3.3: *Schematic (A) and real set-up (B) of the corner adstir fillet stationary shoulder friction stir welding. pin (green hatched), filler wire (red), augmented thin plate (blue), shoulder (yellow hatched+green hatched+blue) and the block to clamp construction detail (gray). [72]*

The conventional FSW technique, used for butt-joints, is not applicable on corner welds of a double sided (DS) T-joint structure. For that purpose, TWI has developed several adaptations, such as corner stationary shoulder FSW, corner fillet stationary shoulder FSW and corner adstir fillet stationary shoulder FSW. In the first technique, the position of the shoulder is fixed (*stationary shoulder*), but a sharp corner of  $90^\circ$  remains after the FSW process between the bottom and the cross plate. The second technique the shoulder is augmented with a small, thin plate at the back to obtain the desired rounding of the internal corner in the end (*fillet*), yielding a lower notch factor. In the third technique a filler wire is added into the corner weld additionally to the shaped shoulder during the process to provide extra material to fill up the corner (*adstir*) and to

have a more smooth corner transition (Figure 3.3). [49, 72] In contrast to the FSW butt-joint, FSW DS T-joints have not been researched extensively.

In this chapter, the metallography and the fatigue life time of DS T-joint welded by corner adstir fillet stationary shoulder FSW are analysed and the results are compared to the conventional arc welding technique data found in literature.

## 2 Methodology

### 2.1 Material and welding details

A material widely used in shipbuilding, 5083-H111 aluminium alloy, is used for the experiments. The material is known for the exceptional performance in extreme environments, since it is highly resistant to both seawater and industrial chemical environments. [71]

A bottom plate (400 [mm] x 100 [mm] x 10 [mm]) and a cross plate (400 [mm] x 75 [mm] x 10 [mm]), made of 5083-H111 aluminium alloy, were welded perpendicular using corner adstir fillet stationary shoulder FSW, using a 5183 aluminium alloy filler wire at the TWI Technology Centre (Figure 3.4).

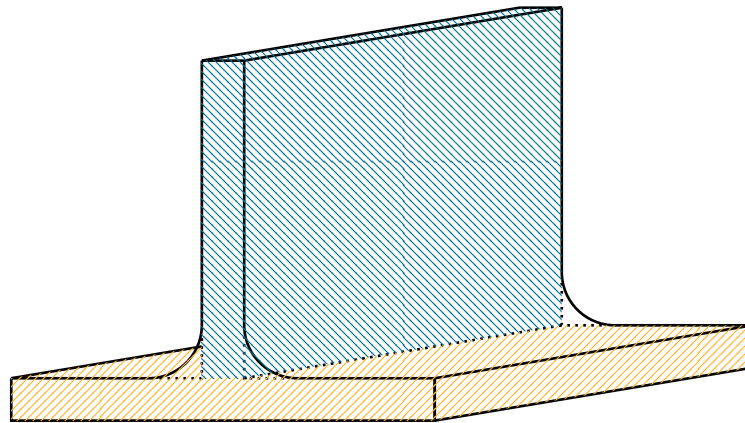


FIGURE 3.4: Schematic visualisation of the specimen: bottom plate (yellow hatched) welded perpendicular to cross plate (blue hatched).

The measured chemical composition of the parent material of the specimens and the filler wire are given in Table 3.1, with respect to the standard values. The mechanical properties of the aluminium alloy used, are presented in Table 3.2.

The following set-up of the FSW was used: a travelling speed of 180 [mm/min], a rotational speed of 1500 [rpm] and an applied force of 30 [kN]. The tool data is confidential with TWI.

Three weld specimens (I,II,III) were generated. Each specimen has two welds, one at each side of the DS T-joint, performed separately in time and in opposite direction. The weld is fully penetrated; this means that the welds from both sides of the DS T-joint are internally fused.

### 2.2 Metallographic details

#### 2.2.1 Preparation of the specimens

The beginning and ending of the weld pieces were cut off over a length of 60 [mm] each, since they are not representative for the current scope of the research. For the macrostructural photography and hardness test specimen, a strip with a width of 10 [mm] is cut off from each of the three weld pieces (I,II,III) (Figure 3.5, Table 3.3). In weld piece I, the strip is cut off from the middle, while for weld piece II and III the strip is cut off at one of the sides. Next, the test specimens are cold embedded using the Clarocit mixture, created by taking 2 units of Clarocit

TABLE 3.1: Chemical composition of 5083-H111 aluminium alloy and 5183 aluminium alloy filler wire (wt%) [72].

		Si	Fe	Cu	Mn	Mg	Cr	Ni	Zn	Ti	
<b>5083</b>	Measured	0.21	0.30	0.033	0.70	4.63	0.084	0.0057	0.12	0.014	Other
	Standard	≤0.40	≤0.40	≤0.10	0.40- 1.00	4.00- 4.90	0.05- 0.25	/	≤0.25	≤0.15	Other
<b>5183</b>	Standard	0.40	/	0.10	0.50- 1.00	4.30- 5.20	0.05- 0.25	/	0.25	/	Other

TABLE 3.2: Mechanical properties of 5083-H111 aluminium alloy and 5183 aluminium alloy filler wire (wt%) of tensile test, where  $R_m$  is the tensile strength,  $R_{p0.2}$  is the proof stress,  $A$  is the elongation,  $H$  is the hardness value; HB = Brinell, HV = Vickers. [31, 72]

		$R_m$ [MPa]	$R_{p0.2}$ [MPa]	$A$ [%]	$H$
<b>5083</b>	Measured	309	174	21	
	Standard	≥ 275	≥ 125	≥ 17	75HB
<b>5183</b>	Standard	285	140		77HV

Powder and 1 unit of Clarocit Liquid. A mould with diameter of 55 [mm] is used. To continue with the metallographic preparation of the specimens, three steps are done: grinding, polishing and etching. The grinding of the specimens is exerted using six different grain sizes: 80#, 180#, 320#, 800#, 1200# and 2000#. For the polishing, two different steps are performed: (1) MD-Mol surface with 3 [ $\mu\text{m}$ ] suspension and (2) MD-Nap surface with 1 [ $\mu\text{m}$ ] suspension, based on Struers [71]. Keller's etchant (190 ml  $\text{H}_2\text{O}$ , 5 ml  $\text{HNO}_3$ , 3 ml  $\text{HCl}$ , 2 ml  $\text{HF}$ ) is used to etch the specimens (90 sec) [4, 25, 34, 43, 53]. The chosen polishing and etching preparations are sufficient to analyse the macroscopic structure and for the hardness measurements.

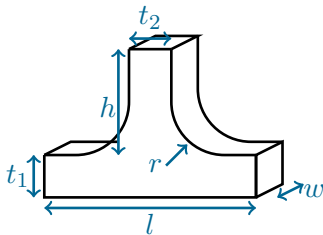


FIGURE 3.5: Schematic visualisation of the specimen for the metallographic tests.

TABLE 3.3: Parameter values

Length	$l$	45	[mm]
Width	$w$	10	[mm]
Thickness bottom plate	$t_1$	10	[mm]
Thickness cross plate	$t_2$	10	[mm]
Height cross plate	$h$	20	[mm]
Fillet radius	$r$	5	[mm]

### 2.2.2 Macrostructural analysis

To characterise the macrostructure, the specimen is investigated using the Olympus SZX9 microscope, in combination with a magnification factor of x3.15. When the required focus was obtained, the colour intensity has been chosen per specimen to make the weld contours as clear as possible.

### 2.2.3 Hardness measurements

The hardness tests were done using a Vickers hardness (HV) tester; a load of 500 gf (HV 0.5) using the DuraScan 70 model of Struers was applied. Per test location, a diamond indenter was pressed into the surface of the tested object with a specific load  $L$ . The Vickers hardness number is hereafter calculated by measuring the size of the impression left by the indenter, in combination with the indenter load  $L$  [kgf] (Equation (3.1)). The actual surface area of the impression  $A_c$  is based on the mean diagonal length  $d$  [mm], i.e.  $d = \sqrt{d_1^2 + d_2^2}$ . [11, 70]

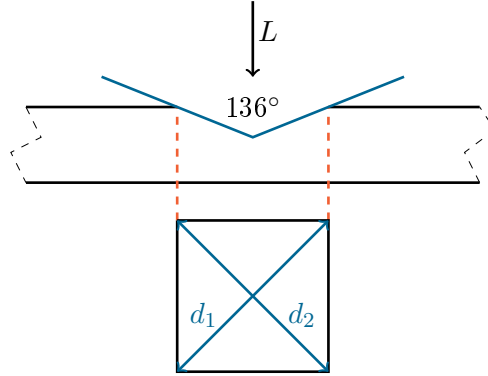


FIGURE 3.6: *Vickers Hardness test set-up.* [70]

$$\text{HV} = \frac{L}{A_c} = \frac{2L}{d^2} \sin \frac{136^\circ}{2} \quad (3.1)$$

Weld specimen II was used to carry out the hardness measurements. The locations of the HV measurements are shown by Figure 3.7, in successive positions with 0.4 [mm] of distance. Two different test geometries were executed: (1) four straight lines running over the base plate of the specimen, and (2) three lines running around each corner of the DS T-joint, resulting in six testing lines.

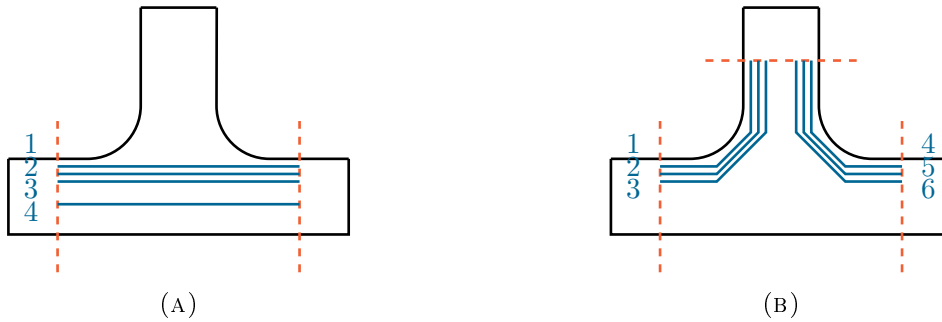


FIGURE 3.7: *Schematic visualisation of the position of the hardness measurements of the DS T-joint specimen for test geometry 1 (A) and test geometry 2 (B). The numbers correspond to the hardness line numbers, which will be used in the hardness results to specify the location.*

In test geometry 1 (Figure 3.7a), three lines were drawn starting at 1 [mm] from the top, in successive positions with 1 [mm] of distance and one at 4 [mm] from the bottom of the specimens baseplate, all lines starting and ending at 5 [mm] from the sides. The first three lines run through the parent material and the welded material, while the fourth line lies entirely in the parent material.

In test geometry 2 (Figure 3.7b), six lines, also at 1 [mm] distance from each other were analysed, starting at 7 [mm] from the top and 5 [mm] from the sides. All lines run through the parent material and the weld material in the middle of the measurement length.

When the indents of test geometry 2 are situated within the boundary ( $+d$  [mm]) of test geometry 1 (Figure 3.8a), the results of test geometry 1 will be used to avoid an erratic result. For the horizontal values of test geometry 2 (Figure 3.8b), the results of test geometry 1 will be used due to a 100% overlap.

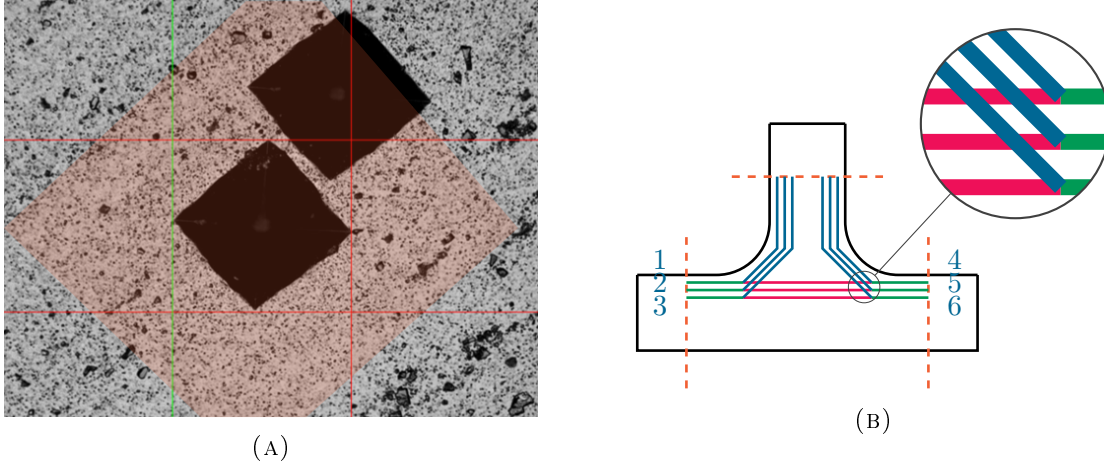


FIGURE 3.8: (A) Visualisation of critical indent boundary ( $+d$  [mm]), and (B) schematic visualisation of test geometry 2 (blue), test geometry 1 (pink), horizontal overlapping zones (green) and possible critical indent boundary locations.

## 2.3 Fatigue details

### 2.3.1 Preparation of the specimens

Every remaining part of the three weld pieces (270 [mm]) is cut into six equal pieces having a width of 45 [mm] (Table 3.4). The edges were milled with a radius of 2 [mm] to rule out crack initiation at the edges. In addition, if an irregularity was felt by hand in the transition zone of the weld towards the PM, a moderate finishing treatment was performed by using a hand file, until the irregularity was no longer felt.

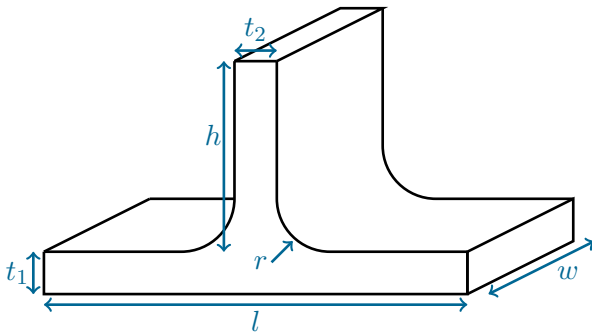


FIGURE 3.9: Schematic visualisation of the specimen for the fatigue test.

TABLE 3.4: Parameter values

Length	$l$	100	[mm]
Width	$w$	45	[mm]
Thickness bottom plate	$t_1$	10	[mm]
Thickness cross plate	$t_2$	10	[mm]
Height cross plate	$h$	45	[mm]
Fillet radius	$r$	5	[mm]

### 2.3.2 Test machine specification

Since the weld pieces are not perfectly flat after the weld process, a tensile test set-up cannot be used. In case of an axial load, there will be no pure membrane stress, but a bending moment will be present. Therefore, a bending moment test set-up must be chosen.

The available test machine has only a 3-point bending set-up; however a 4-point bending is desired. In a 3-point bending set-up, the maximal bending moment is present in the middle of the specimen. It is hard to apply the load exactly in the middle of the specimen, and the

maximum bending moment is shifted horizontally. In a 4-point bending set-up (Figure 3.10), an equal maximum bending moment is present between the two upper rollers.

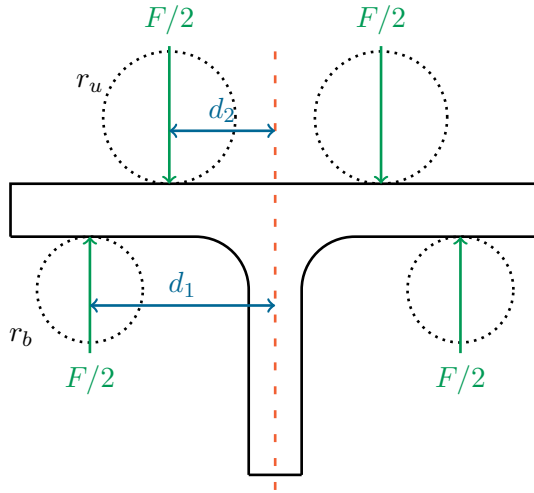


TABLE 3.5: *Parameter values*

Lever	$d_1$	35	[mm]
	$d_2$	20	[mm]
Radius upper roller	$r_u$	12.5	[mm]
Radius bottom roller	$r_b$	10	[mm]

FIGURE 3.10: *Schematic visualisation of the 4-point bending test set-up of the DS T-joint specimen.*

To convert the available 3-point bending into a 4-point bending one, an extra block must be created in order to divide the central force equal over the two upper rollers of the 4-point bending set-up. At the corners of the central roller notch and the two upper roller notches, a hole with a radius of 1 [mm] is added to avoid crack initiation. The notch dimensions are chosen so that the roller is clamped sideways, to ensure that the force is distributed equally. The modification block is made of high strength steel S690. The dimensions were derived from analytical stress calculations and a finite element model (FEM) calculation (see Section 1, Supplement C), avoiding failure of the block at the force range required for the fatigue tests. A schematic visualisation of the required test block is given in Figure 3.11, including the accompanying parameter values in Table 3.6. The final test machine is shown in Figure 3.12.

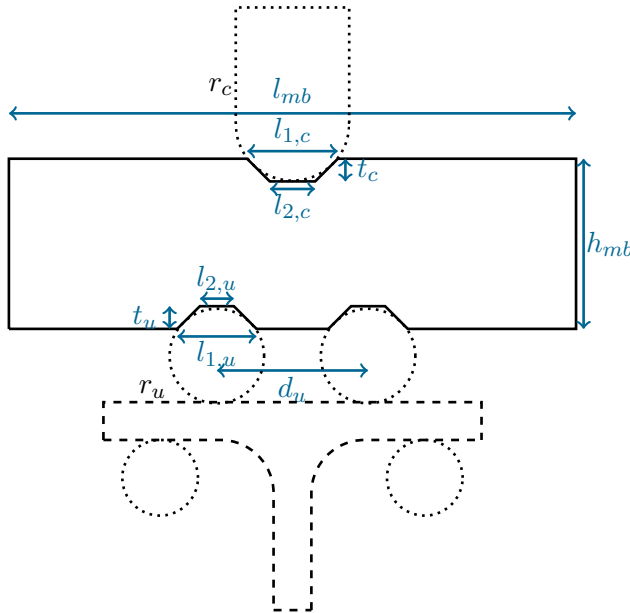


TABLE 3.6: *Parameter values*

Length	$l_{mb}$	150	[mm]
Height	$h_{mb}$	45	[mm]
Central roller notch	$l_{1,c}$	24	[mm]
	$l_{2,c}$	12	[mm]
	$t_c$	6	[mm]
Upper roller notch	$l_{1,u}$	12	[mm]
	$l_{2,u}$	9	[mm]
	$t_u$	6	[mm]
	$d_u$	40	[mm]
Radius central roller	$r_c$	15	[mm]
Radius upper roller	$r_u$	12.5	[mm]

FIGURE 3.11: *Schematic visualisation of the modification block to convert the 3-point bending test set-up to a 4-point bending set-up.*

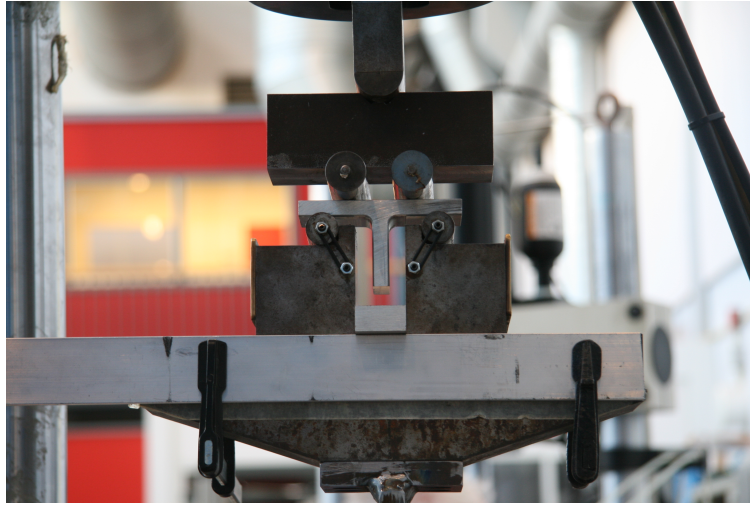


FIGURE 3.12: *Real test machine set-up, including modification block and test specimen.*

### 2.3.3 Estimate of required force

The force range in the fatigue analysis was estimated at different life cycles  $N$  ( $10^4$ ,  $10^5$ ,  $10^6$ ,  $10^7$ ), using three different methods.

1. Based on existent fatigue data results of a FSW butt-joint with respect to the conventional arc welded butt joint [17], a factor was calculated to up-scale the SN-curve for FSW DS T-joint. This factor was applied on the FATigue class design curve of an arc welded DS T-joint to estimate the life cycle fatigue curve (SN-curve) for the corner adstir fillet stationary shoulder FSW detail, and the accompanying stress range and thus the required applied force range in the test machine.
2. FEM was used to calculate the stress concentration factor (SCF) applicable on the DS T-joint structural detail. The SN-curve of the parent material was down-scaled to give an estimate of the location of the SN-curve for the corner adstir fillet stationary shoulder FSW DS T-joint.
3. Both Sidhom et al. [67] ( $r_l = 0.1$ ) and de Jesus et al. [22] ( $r_l = 0$ ) did a fatigue life time analysis on DS T-joints by comparable joining techniques. Sidhom et al. applied shot peening, which is an enhancement of the arc weld to obtain surface hardening and Jesus et al. applied the butt-joint welding technique on the underside of the DS T-joint and obtained the fillet radius by pressing material downwards into a prepared mould. A force estimation based on the fatigue data of these two techniques was made.

Figure 3.13 and Table 3.7 summarise the outcome applicable on a load ratio  $r_l$  of 0.1. The calculations of all strategies can be found in Section 2, Supplement C. The load ratio  $r_l$  reflects the ratio between the minimum and the maximum stress. The choice for the load ratio of 0.1 is to create a fluctuating stress with a constant amplitude loading that is consistently in tension.

Failure data of the FSW butt-joint indicate that the butt-joint will fail in the parent material [72]. Since the obtained weld material structure is not the weakest link, the downscaling of the SN-curve of the parent material will give a worse fatigue life time estimate that it is in reality. Since the values of the method 1 are lying in the same range as method 2, a preference is given to the force estimation offered by method 3.

Table 3.8 presents the final chosen stress ranges, expressed in a workable format, for the levels of  $10^4$ ,  $10^5$ ,  $10^6$  and  $10^7$  life cycles and the accompanying amount of specimens that will be tested.

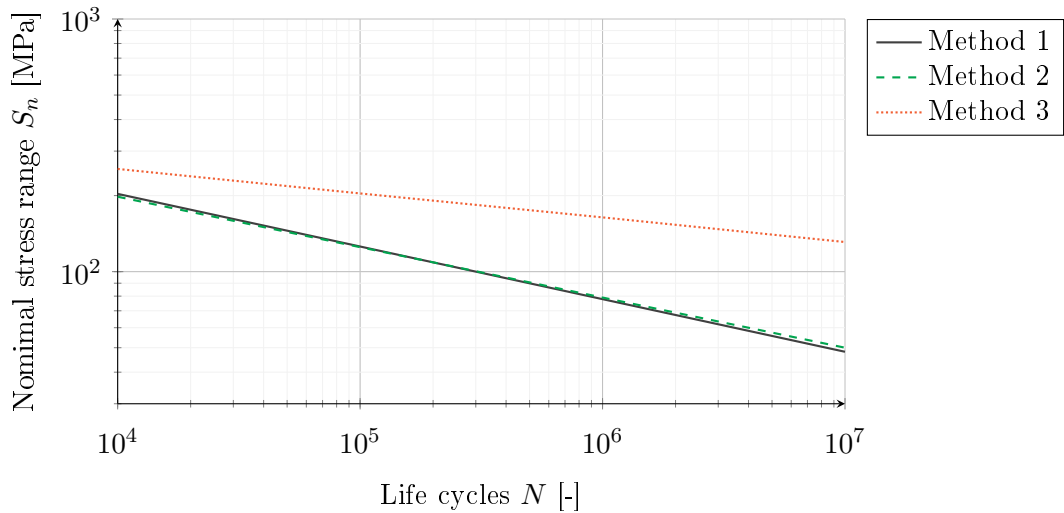


FIGURE 3.13:  $SN$ -curve for the three methods with reliability of 50%, a standard deviation  $\sigma$  of 0.3 and a load ratio  $r_l$  of 0.1.

TABLE 3.7: Overview of the required minimum and maximum force for the three methods based on the  $SN$ -curve with a reliability of 50%, a standard deviation  $\sigma$  of 0.3 and a load ratio  $r_l$  of 0.1. The stress range  $S$  is expressed in [MPa], and the forces  $F_{min}$  and  $F_{max}$  in [N].

Life cycles $N$	Method 1			Method 2			Method 3		
	$S$	$F_{min}$	$F_{max}$	$S$	$F_{min}$	$F_{max}$	$S$	$F_{min}$	$F_{max}$
$10^4$	203	2257	22575	198	2200	22000	255	2833	28333
$10^5$	126	1397	13973	125	1389	13889	204	2267	22667
$10^6$	78	865	8649	79	878	8778	164	1822	18222
$10^7$	48	535	5353	50	556	5556	131	1456	14556

$10^7$  life cycles should be included because marine structures are designed for very long life times at low stress levels. [23] If the specimen could endure a loading longer than  $1.3 \cdot 10^7$  cycles, than no failure is said to be present, i.e. a run-out. The run-out specimens will be re-used to obtain extra data points at higher stress range levels. The required minimal and maximal force exerted by the test machine are calculated on the basis of the geometry of the test set-up.

#### 2.3.4 $SN$ -curve

Fatigue resistance is described using the  $SN$ -curve, which displays the relation between the stress range  $S$  (alternating stress) and the number of cycles to failure  $N$ , both on logarithmic scales. To correlate the data between the applied stress range  $S$  and the fatigue life  $N$ , both a continuous single slope and a continuous dual slope approach are adopted.

The maximum likelihood approach is applied as regression analysis to estimate the model parameters, since this method is able to incorporate both the failure data and the run-outs [23]. The log-likelihood function is given by Equation (3.2), where  $f$  represents the probability density function (PDF) and  $F$  is the corresponding distribution function (CDF). Both the log-Normal distribution and the Weibull distribution are implemented to search for the best fit, i.e. largest value of  $\max_{\theta}\{\mathcal{L}\}$ . The full derivation is described in Section 4, Supplement C, including the

TABLE 3.8: Overview of the final chosen value based on the SN-curve with a reliability of 50%, a standard deviation  $\sigma$  of 0.3 and a load ratio  $r_l$  of 0.1. The stress range  $S$  is expressed in [MPa], and the forces  $F_{min}$  and  $F_{max}$  in [N].

Life cycles $N$	$S$	$F_{min}$	$F_{max}$	# specimens
$10^4$	220	244	2444	1
$10^5$	200	222	2222	3
	180	200	2000	2
$10^6$	160	177	1777	3
	140	155	1555	4
$10^7$	130	144	1444	1
	120	133	1333	1
	110	122	1222	1
	100	111	1111	1

formulations for the PDF and CDF following Pascual and Meeker [57] for both the log-Normal and the Weibull distribution for the two applied concepts.

$$\mathcal{L}(\boldsymbol{\theta}; N|S) = \sum_{j=1}^n \delta_j \{f(N_j|S_j; \boldsymbol{\theta}) + (1 - \delta_j)\{1 - F(N_j|S_j; \boldsymbol{\theta})\}\} \quad (3.2)$$

#### Continuous single slope concept

Following the continuous single slope concept, the SN-curve differs for the low cycle fatigue (LCF) range, the medium cycle fatigue (MCF) range and the high cycle fatigue (HCF) range. This approach is valid to compare the test results with the design curves stated by the International Institute of Welding (IIW) for the specific range. A design curve is established using a FAT class number, linked to the parent material or a structural detail. The FAT class number corresponds with the nominal stress range  $S_n$  at 2 million ( $2 \cdot 10^6$ ) cycles. Furthermore, the design curve covers 97.7% of the data; in other words only 2.3% of the data is expected to fall below the established curve, i.e. much earlier failure. A confidence level  $c_l$  is not explicitly taken into account.

The FAT class that corresponds with an arc welded aluminium DS T-joint structural detail is FAT28, with a SN-curve slope of  $m = 3$  in the MCF range, following the design curves by the IIW recommendations [40]. Since the Basquin-type of relation is assumed between the stress range and the number of life cycles (Equation (3.3)), the corresponding  $\log C$  value can be calculated:  $\log_{10} C = 10.6$ . For the aluminium material AA5000 (parent material), a FAT class of 71 is proposed by the IIW recommendations in combination with a slope of  $m = 5$  in the MCF range. Following the Basquin-type of relation,  $\log_{10} C = 15.6$  results.

$$\log N = \log C - m \log S \quad (3.3)$$

To make the design slopes of the IIW more concrete, arc welded test data for a comparable DS T-joint ( $r_l = 0.1$ ,  $t_1 = 10$  [mm],  $t_2 = 10$  [mm]) and parent material test data for 5083-H111 ( $r_l = 0.1$ ), both by Sidhom et al. [67], are added to the comparison.

#### Continuous dual slope concept

To correlate the MCF and HCF range at the same time, the continuous dual slope concept, i.e. random fatigue limit model, is applied. It is known that a random fatigue limit model only performs well if the number of data points in the HCF range is rather high. [23, 57] If so, a

strong curvature is present with an asymptotic behaviour towards a fatigue limit, which will be used to describe the distribution more precisely. The fatigue limit indicates the stress level where below no failure is present, in other words an infinite number of cycles can be sustained. The infinite life time stated by the fatigue limit theory can be questioned, since it is based on the HCF data and one is not able to test the specimens endless. Nevertheless, according to Pascual and Meeker [57], the random fatigue limit model is still very useful in the estimation of the fatigue resistance curvature and the non-constant variability. The relation present is given by Equation (3.4).  $S_f$  represents the fatigue limit and is considered as a stochastic variable  $(\mu_{S_f}, \sigma_{S_f})$ , of which the variables are estimated using the maximum likelihood regression analysis. A confidence level  $c_l$  is not explicitly taken into account. [23, 57]

$$\log N = \log C - m \log (S - S_f) \quad (3.4)$$

### 2.3.5 Fatigue data per stress range level

To evaluate the degree of dispersion and skewness per stress level, two different distributions are used: the log-Normal and the Weibull distribution. Because of the small amount of data points per level, the standard deviation  $\sigma$  should be modified ( $\sigma_{corr}$ ), and its value will be larger. The modification of the log-Normal distribution regards the number of test results  $n$  and the nDof:  $k = 1 | \theta = \{\mu, \sigma\}$  [23].

$$\sigma_{corr} = \begin{cases} \sigma \sqrt{\frac{n}{n-k}} & \text{log-Normal} \\ \sigma \frac{6}{\sqrt{\pi}} & \text{Weibull} \end{cases} \quad (3.5)$$

## 3 Results

### 3.1 Metallographic analysis

#### 3.1.1 Macrostructure

Upon inspection of the weld (specimen II), the welds from both sides are fused together, obtaining a fully penetrated weld and imperfections are absent in the weld. There is a transition between the stirred metal and the parent metal. On the advancing side, a more distinct boundary is seen due to the fact that the rotating tool is pulling metal from the parent material. The boundary is less clear on the retreating side, since the tool pushes the softer metal against the parent material. The used etchant does not reveal clearly the three different structures of the affected zone, though the light boundary between the parent material and the weld (TMaZ), can be seen as the HaZ. The similar macroscopical structure was present in specimen I and III [data not shown].

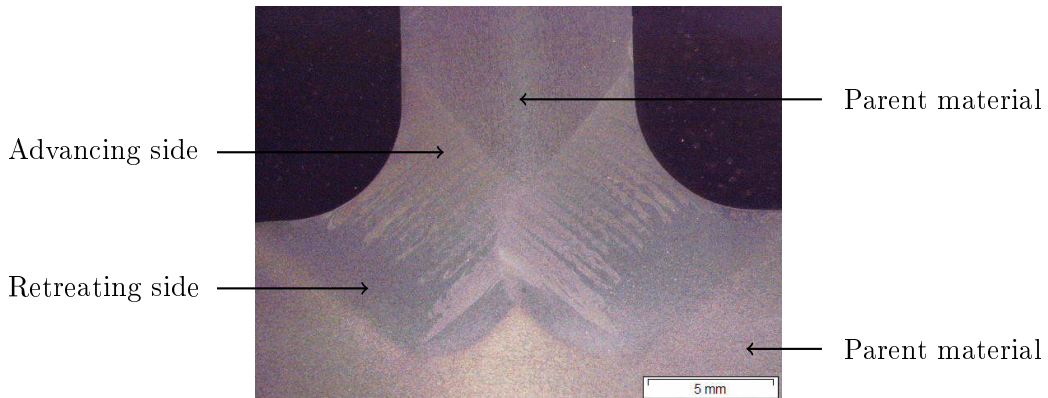


FIGURE 3.14: Macroscopic metallography  $\times 3.15$  for specimen II.

### 3.1.2 Hardness

The hardness measurements of test geometry 1 (Figure 3.15) identify three Vickers hardness (HV) zones, corresponding with the macroscopic metallography: parent material (white), advancing side of the weld (red) and retreating side of the weld (blue). The width of the weld zone differs according to the testing lines: the lower the lines, the smaller the weld zone, and vice versa.

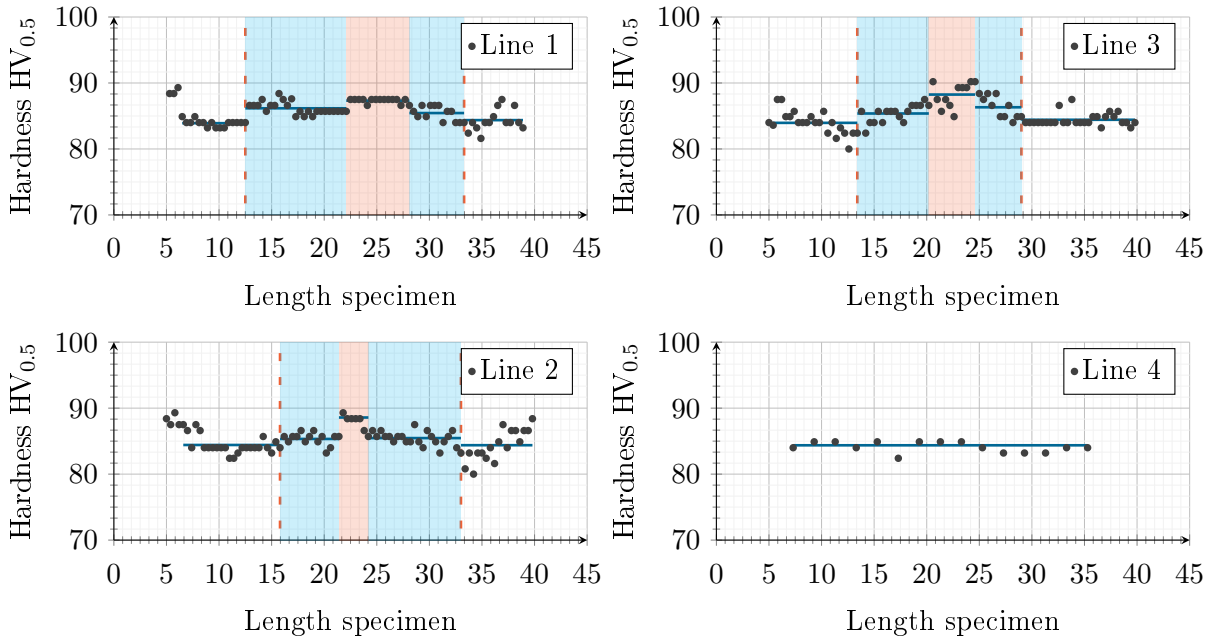


FIGURE 3.15: *Hardness measurements adopting test geometry 1 (Figure 3.7a), for specimen II, including the variance with respect to the piecewise constant function plotted in blue.*

With the indenter load  $L$  of 0.5 [kgf], a mean diagonal length  $d$  of 0.106 [mm] was found for the parent material, leading to the hardness value of 84HV<sub>0.5</sub>, using Equation (3.1). For the weld zone, the hardness of advancing side equalled 88HV<sub>0.5</sub> and the retreating side 86HV<sub>0.5</sub>, given a mean diagonal length  $d$  of 102 [ $\mu$ m] and 104 [ $\mu$ m] respectively. So, a small increase in hardness of 5% in the weld zone itself was present in comparison with that of the parent material. In addition, there was no difference in HV<sub>0.5</sub> value comparing the weld of the two sides.

In test geometry 2, identical hardness results are found as in test geometry 1, in both welds of the DS T-joint (Figure 3.16). Also here are the results of the “left” weld (line 1, 2 and 3) in compliance with those of the “right” weld (line 4, 5 and 6).

## 3.2 Fatigue analysis

### 3.2.1 Fatigue data

The constant loading experiments resulted in fatigue test results in the MCF and HCF range (Figure 3.17). Five run-outs were re-used to obtain fatigue data at a higher stress range level. Two locations of failure were identified: as expected at the corner with a finite notch stress radius ( $\rho = 5$  [mm]) (Figure 3.18c), and, not anticipated, at the external lining of the thin plate at the back of the FSW shoulder, i.e. the undercut, located at 11 [mm] from the side of the cross plate, with a notch stress radius going to zero ( $\rho \rightarrow 0$  [mm]) (Figure 3.18d).

The failure location at the corner is in accordance with the expected critical stress location of the DS T-joint, calculated according to FEM. A detailed description of the 2D FEM calculation can be found in Section 2, Supplement C.

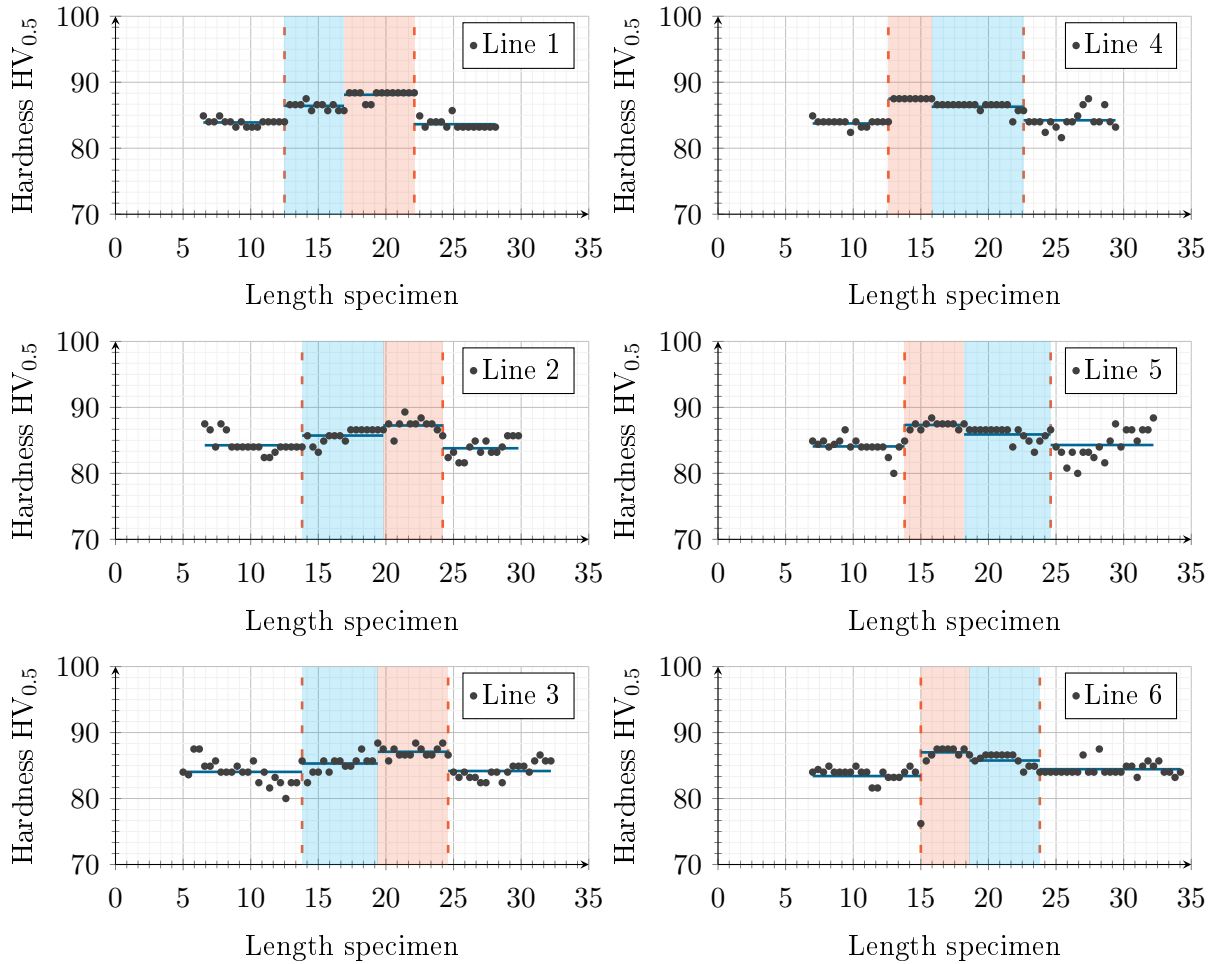


FIGURE 3.16: *Hardness measurements adopting test geometry 2 (Figure 3.7b), for specimen II, including the variance with respect to the piecewise constant function plotted in blue.*

TABLE 3.9: *Overview of the failure data per stress level, subdivided into failure at the corner, failure at the undercut and theoretically no failure (run-out). The stress range  $S$  is expressed in [MPa].*

	$S$								
	220	200	180	160	140	130	120	110	100
Failure in radius	3	3	3	2	2	0	0	0	0
Failure at undercut	1	0	0	1	1	0	0	0	0
Run-out	0	0	0	1	1	1	1	1	1

Due to presence of an undercut failure, it was necessary to adapt the initial 2D FEM to interpret the unexpected failure location (Section 5, Supplement C). Concretely, if an undercut is incorporated in FEM, the undercut becomes already the failure location when the undercut is only 0.1 [mm] thick; a higher stress concentration is present at the undercut compared to the radius, due to the sharp geometry transition. As such, the undercut should be taken into account as a different failure type in the calculation of failure resistance.

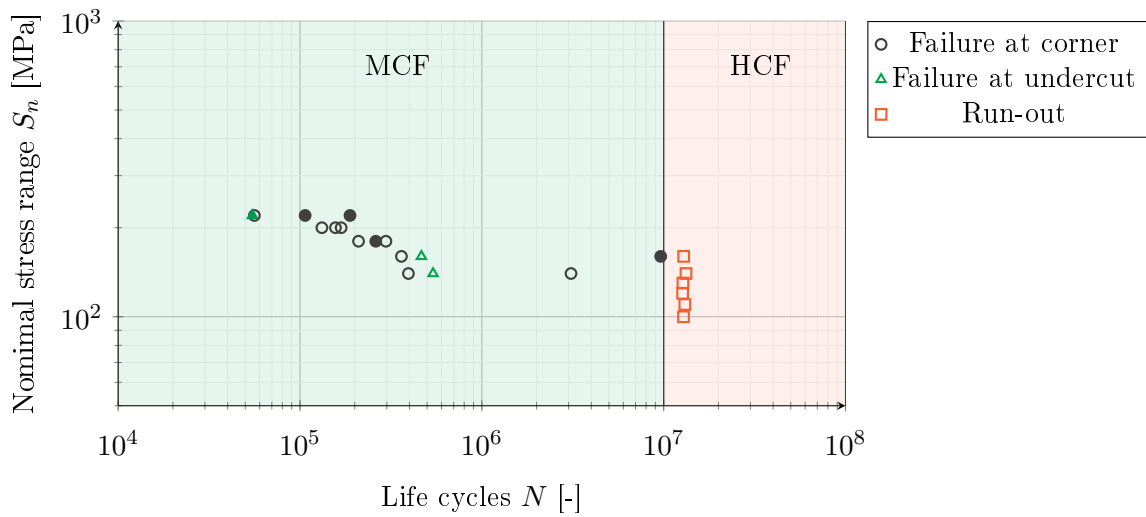


FIGURE 3.17: Fatigue data of corner adstir fillet stationary shoulder FSW, including the MCF range (green) and the HCF range (red). The solid data points indicate the re-used run-outs.

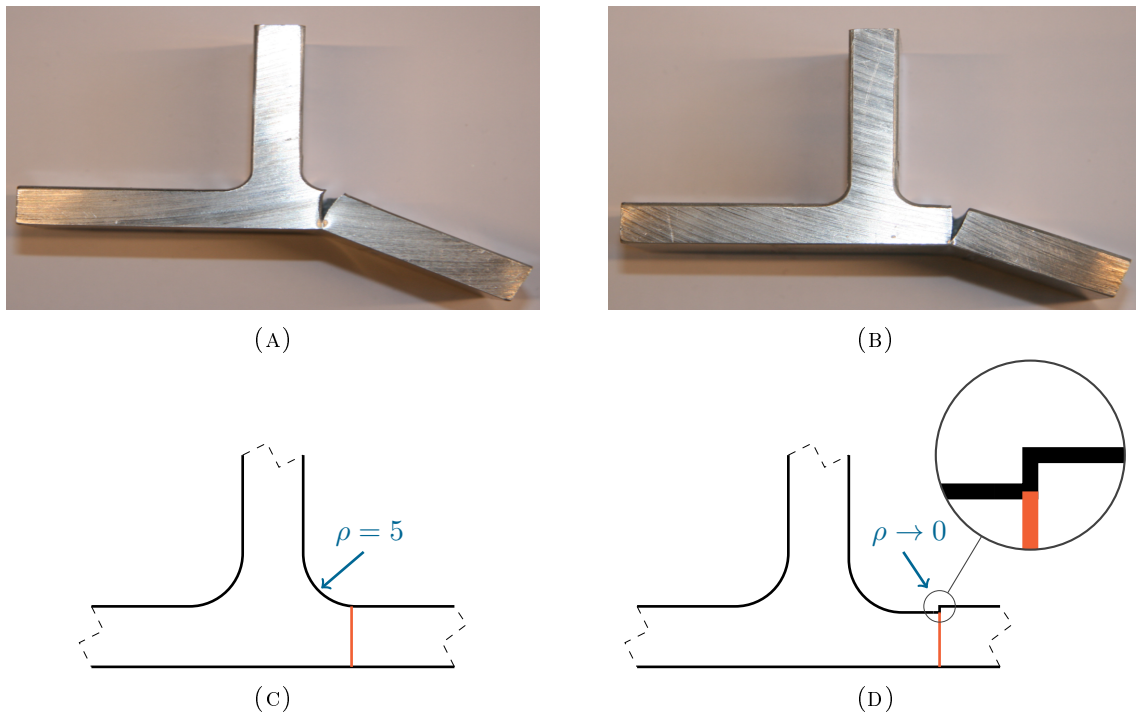


FIGURE 3.18: Real and schematic visualisation of the failure types. (A) and (C) failure at the corner, (B) and (D) failure at the undercut.

### 3.2.2 SN-curve

#### Continuous single slope concept

##### (a) Nominal stress concept

According to the nominal stress concept the data points related to the failure at the corner and failure at the undercut will be treated in a different way. A SN-curve of the MCF range is established using the available MCF range data  $[10^4-10^7]$ .

Comparing the values of the model parameters  $\theta = \{\log C, \mu, \sigma\}$  of the SN curves of the log-Normal and the Weibull distribution, a larger  $\max_{\theta}\{\mathcal{L}\}$  is found for the log-Normal distribution.

As such, the log-Normal distribution was used to establish the SN-curve.

TABLE 3.10: *Maximum Likelihood Estimates (MLEs) for the log-Normal and Weibull distributions including the value of the log-likelihood function, for the failure data at the corner, continuous single slope, following the nominal stress concept.*

Distribution	$\log_{10} C$	$m$	$\log_{10} \sigma$	$\max_{\theta} \{\mathcal{L}\}$
log-Normal	19.89	6.37	0.40	-17.2702
Weibull	26.49	9.18	0.46	-19.9968

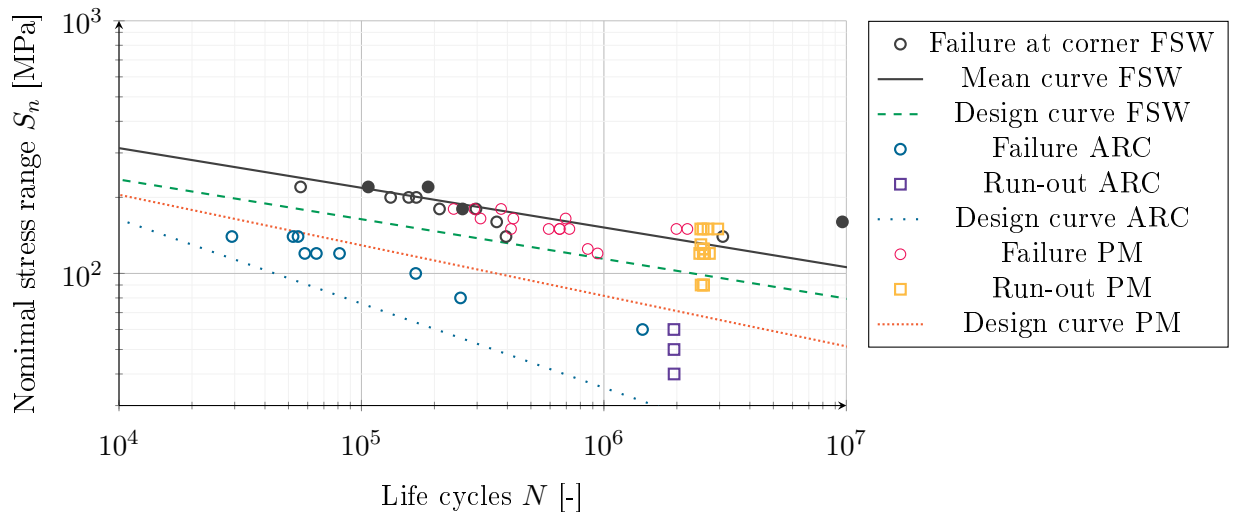


FIGURE 3.19: *Fatigue data of corner adstir fillet stationary shoulder FSW, including the established mean curve and design curve for the MCF range, compared with arc welded data of a comparable DS T-joint by Sidhom et al. [67], the design curve of the arc welded DS T-joint for the MCF range, parent material data for 5083-H111 by Sidhom et al. [67] and the design curve of the parent material (PM) for the MCF range. The solid data points indicate the re-used run-outs.*

The corner adstir fillet stationary shoulder FSW welds have a higher fatigue resistance compared to the arc welded data: a higher FAT class can be used in case of FSW DS T-joint (Figure 3.19). In particular the FAT class can be increased up to FAT103, with an accompanying slope of  $m = 6.4$ . This might be possible due to the fact that there is no substantial decrease in hardness in the FSW weld material [20]. Compared with the design curve of the AA5000 aluminium alloy proposed by the IIW recommendations, the parent material 5083-H111 stirred with the filler material 5183 results in a higher fatigue resistance: the design curve for the FSW DS T-joints is lying above the design curve of the parent material. With respect to the data points by Sidhom et al. [67] of the pure 5083-H111 aluminium alloy, an equal fatigue resistance is present in the MCF range comparing the FSW weld material and the actual parent material.

(b) Effective notch stress concept

Since the failure data did not only consist of failures at the corner, but also of failures at the undercut, and both failure locations correspond to a different failure type, the effective notch stress theory was applied to combine the test data of both failure types.

The main difference in the two failure locations is the value of the notch radius  $\rho$ . The notch

radius in case of failure at the corner is finite ( $\rho = 5$  [mm]), but for the undercut a sharp corner arises, reducing the notch radius to zero ( $\rho \rightarrow 0$  [mm]). So, since the notch radius becomes zero, the notch peak stress  $\sigma_{max}$  will reach infinity.

Since the notch peak stress goes to infinity, an averaged stress  $\sigma_{av}$  is assumed as effective notch stress. The value of  $\sigma_{av}$  is obtained by taking the average of the notch stress distribution over a micro-structural length  $\rho^*$  (Equation (3.6)). For the undercut failure, the formulation of a weld toe notch stress  $\sigma_n$  distribution of den Besten [23] is chosen as guidance (see Section 5, Supplement C) and the V-shaped notch concept as presented by den Besten [23] was adapted to an angle of  $90^\circ$  to satisfy the undercut geometry, i.e. the angle  $\alpha$  will become  $135^\circ$ .

$$S_e = \frac{1}{\rho^*} \int_0^{\rho^*} \sigma_n(r) dr = \frac{1}{\rho^*} \int_0^{\frac{\rho^*}{t_1}} t_1 \sigma_n \left( \frac{r}{t_1} \right) d \frac{r}{t_1} \quad (3.6)$$

In case of failure at the corner, the peak stress at the failure spot might be whether or not fully effective. [23]

In case the radius is fully effective, the effective notch stress equals the notch peak stress  $\sigma_{peak}$  and is calculated by multiplying the nominal stress with the obtained stress concentration factor from the FEM calculation ( $K_t = 1.36$ , see Section 2, Supplement C) (Equation (3.7)).

$$S_e = K_t S_n \quad (3.7)$$

When the radius is not fully effective, an artificially enlargement of the notch radius is present for this failure type  $\rho_f = \rho + s\rho^*$ , and the notch toe stress distribution for  $\rho > 0$  of den Besten [23] is valid (see Section 5, Supplement C). The V-shaped notch concept as presented by den Besten [23] is again adapted to an angle of  $90^\circ$  to satisfy the radius geometry present, i.e. the angle  $\alpha$  will become  $135^\circ$ .

To obtain the value for the most likely micro-structural length  $\rho^*$ , the maximum likelihood regression analyses is proposed based on the obtained data results. When all data points of the failure at the corner as well as failure in the undercut are taken into account, expressed in the effective notch stress, it is found that the log-Normal distribution again describes the distribution more precisely. The influence of the effectiveness of the radius of the corner of the DS T-joint is linked to the value of  $\rho^*$  and  $\log C$ , and thus to the vertical shift of the curve; no other values are changed (Table 3.11).

TABLE 3.11: *Maximum Likelihood Estimates (MLEs) for the log-Normal distribution including the value of the log-likelihood function, for the failure data at the corner and at the undercut, continuous single slope, following the effective notch stress concept.*

	Distribution	$\log_{10} C$	$m$	$\log_{10} \sigma$	$\rho^*$	$\max_{\theta} \{\mathcal{L}\}$
Fully effective	log-Normal	20.12	6.11	0.36	0.12	-19.7814
Not fully effective	log-Normal	19.74	6.11	0.36	0.29	-19.7814

Based on the current data sets, it is impossible to state which approach is most valid. Extra datasets need to be added to reflect the height of the curve (Figure 3.20). However, in order to fulfil a conservative design approach, the radius should be seen as not fully effective, since this leads to the lowest curve, and one will be on the safe side of the calculation.

#### *Hypothesis for obtained $\rho^*$ values*

When the radius of the DS T-joint is assumed to be fully effective, the maximum stress value is

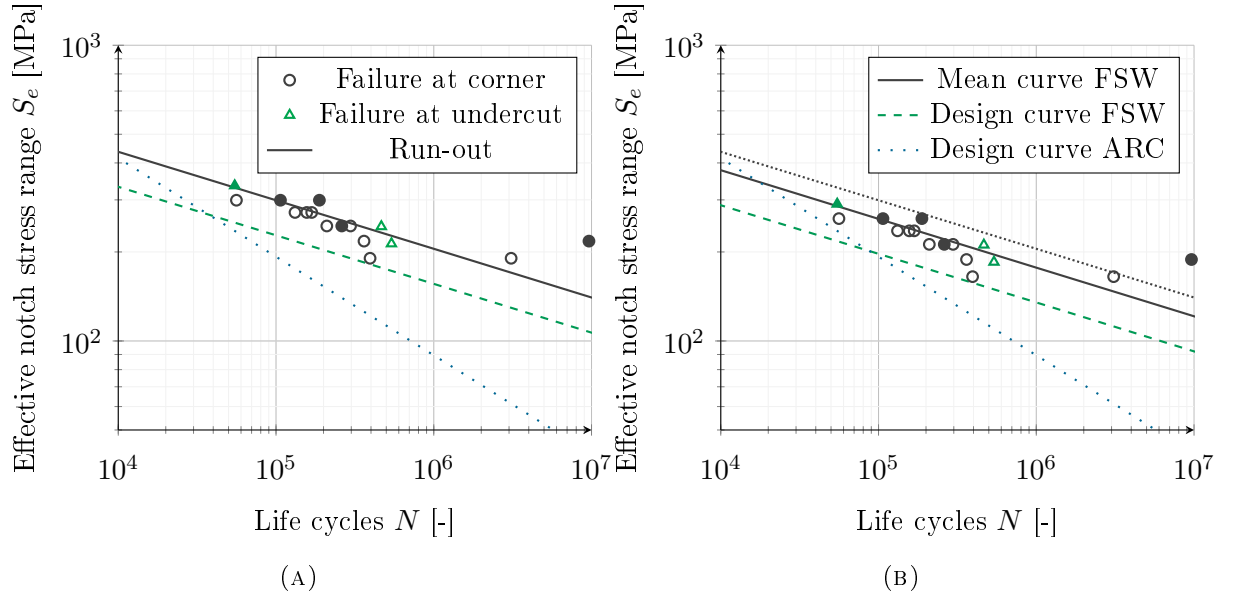


FIGURE 3.20: Fatigue data of corner adstir fillet stationary shoulder FSW, continuous single slope, following effective notch stress concept. (A) fully effective radius, (B) not fully effective radius. The gray densely dotted line in (B) represents the mean SN-curve FSW of (A). The solid data points indicate the re-used run-outs.

used to calculate the effective notch stress component, i.e.  $S_e = K_t S_n$ . According to the failure at the corner of the nominal stress range  $S_n$ , the curve will shift upwards by a factor 1.36, i.e. the value of the SCF applicable, when being displayed as the effective notch stress range  $S_e$ . Since the notch radius at the undercut goes to zero, the notch peak stress will go to infinity and the averaged stress  $\sigma_{av}$  might be assumed as effective notch stress,  $S_e = \sigma_{av}$ . The value of  $\sigma_{av}$  is obtained by taking the average of the notch stress distribution over a micro-structural length  $\rho^*$ . As the value of  $\rho^*$  increases, the value of the average stress decreases, according with the curve of the notch stress distribution, and the lesser the impact of the infinite notch peak stress. As a result of the fatigue resistance analysis, the micro-structural length  $\rho^*$  is most likely to equal 0.12 [mm], a rather small value for aluminium alloys based on literature [23, 66]. The main assumption in the concept of the effective notch stress is that the failure points of the radius and the undercut are considered as only one failure point, provided that their failure points are close together, by including more detailed geometry information. In the case when the radius is assumed to be fully effective, the value of  $\rho^*$  will only affect the height of the data points upon failure at the undercut. The small value of  $\rho^*$  can be explained since a high value of  $\sigma_{av}$  is required to shift the data points upwards, when failure at the undercut is present, to obtain that the data sets are lying close to each other. As such, the influence of the infinite notch peak stress  $\sigma_{peak}$  is larger (zone 1).

If the radius is not fully effective, two averaged values of the maximum stress are calculated, one for each failure type (corner and undercut). The value of  $\rho^*$  influences, therefore, the height of the two data point sets. To obtain the highest correlation when combining both data sets, both values of  $\sigma_{av}$  should lie in the same range. It is therefore required that the value of  $\rho^*$  should be much larger compared to the value of a fully effective radius. This is present with the currently obtained value for  $\rho^*$  of 0.29 [mm], a more likely value for aluminium alloys based on literature [23, 66]. This enlargement could be explained by the fact that the notch peak stress (zone 1), is going to infinity for the undercut notch stress distribution and when  $\rho^*$  increases, the influence of the notch stress gradient (zone 2) increases. As such, a lower  $\sigma_{av}$  can be obtained. Since the notch peak stress for the undercut notch stress distribution is still higher than the radius notch

stress distribution, the data points of the undercut failure will eventually shift more upwards.

### Continuous dual slope concept

Given the large amount of HCF range data, there were sufficient HCF range data points to apply the continuous dual slope concept.

#### (a) Nominal stress concept

Analysing the failure data at the corner, the MLEs of the model parameters  $\theta = \{\log C, \mu, \sigma, \mu_{S_f}, \sigma_{S_f}\}$  for the log-Normal distribution showed a small value for the standard deviation indicating a reliable fatigue resistance prediction.

TABLE 3.12: *Maximum Likelihood Estimates (MLEs) for the log-Normal distribution including the value of the log-likelihood function, continuous dual slope, following the nominal stress concept.*

Distribution	$\log_{10} C$	$m$	$\log_{10} \sigma$	$\mu_{S_f}$	$\log_{10} \sigma_{S_f}$	$\max_{\theta} \{\mathcal{L}\}$
log-Normal	16.66	1.17	0.12	142	0.045	-15.9467

Comparing the single slope and dual slopes (Figure 3.21), both SN-curves were quite similar in the range  $S = [180 - 200]$ , reflecting the MCF range. As such, the set-up of both distributions is correct. Furthermore, a fatigue limit for FSW data is clearly visible at  $S_f = 142$  [MPa]. In accordance with the random fatigue limit model, no failure is expected as long as the stress level stays below  $S = 142$  [MPa] and the life time reaches infinity. Based on the fatigue data of a comparable arc welded DS T-joint by Sidhom et al. [67], a fatigue limit of  $S_f = 48$  [MPa] is found. This demonstrates that the fatigue limit is almost three times higher when applying FSW.

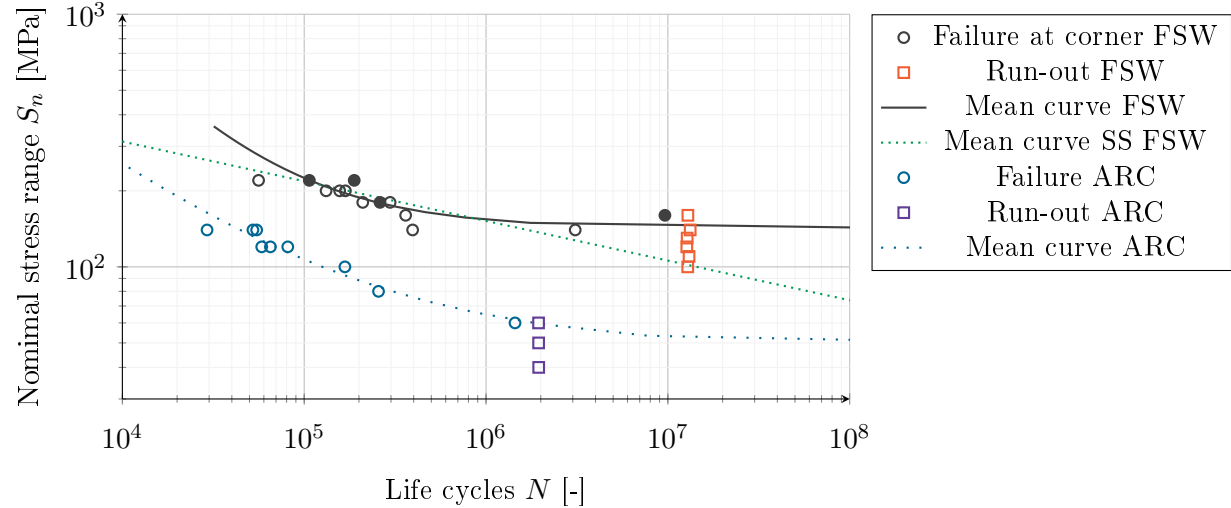


FIGURE 3.21: *Fatigue data of corner adstir fillet stationary shoulder FSW, following nominal stress concept. Comparison of dual and single slope concept, and arc welded data of comparable DS T-joint by Sidhom et al. [67]. The solid data points indicate the re-used run-outs.*

#### (b) Effective notch stress concept

To apply the random fatigue limit model to the combined test data, the micro-structural length  $\rho^*$  is derived based on the MLE approach, but implemented manually. Based on the largest value

of the maximum likelihood function  $\max_{\theta}\{\mathcal{L}\}$ , the most likely  $\rho^*$  is chosen.

TABLE 3.13: *Manually performed maximum likelihood estimate by searching for largest log-likelihood function, for the failure data at the corner and at the undercut (with run-outs included), continuous single slope, following the notch effective stress concept.*

Fully effective		Not fully effective	
$\rho^*$	$\max_{\theta}\{\mathcal{L}\}$	$\rho^*$	$\max_{\theta}\{\mathcal{L}\}$
0.26	-23.4835	0.11	-23.4943
0.264	-23.4826	0.116	-23.4828
0.266	-23.4825	<b>0.117</b>	<b>-23.4825</b>
<b>0.267</b>	<b>-23.4825</b>	0.118	-23.4826
0.268	-23.4825	0.12	-23.4842
0.269	-23.4826	0.13	-23.5151
0.27	-23.4828	0.14	-23.5786

The MLEs of the model parameters  $\theta = \{\log C, \mu, \sigma, \mu_{S_f}, \sigma_{S_f}\}$  (Table 3.14) show that the influence of the effectiveness of the radius of the corner is only linked to the vertical shift of the SN-curve; different values are obtained for  $\rho^*$ ,  $\log C$  and the fatigue limit  $\mu_{S_f}$ . When the radius is assumed to be fully effective, the fatigue limit is located at  $S_f = 188$  [MPa], while the fatigue limit lies at  $S_f = 163$  [MPa] when the radius is not fully effective. Following the conservative design approach, the lowest curve will be applied (Figure 3.22), but it is recommended to use the SN-curve height that bears the best approximation to reality.

TABLE 3.14: *Maximum Likelihood Estimates (MLEs) for the log-Normal distribution including the value of the log-likelihood function, continuous dual slope, following the effective notch stress concept.*

	Distribution	$\log_{10} C$	$m$	$\log_{10} \sigma$	$\mu_{S_f}$	$\log_{10} \sigma_{S_f}$	$\max_{\theta}\{\mathcal{L}\}$
Fully effective	log-Normal	18.73	1.54	0.10	188	0.058	-23.4825
Not fully effective	log-Normal	18.52	1.54	0.10	163	0.058	-23.4825

### 3.2.3 Fatigue data per stress range level

Based on the maximum likelihood function  $\max_{\theta}\{\mathcal{L}\}$  (Table 3.15), the log-Normal distribution characterises the data points to the best extent at the stress levels:  $S = 140$ ,  $S = 160$  and  $S = 220$  [MPa], while the Weibull distribution more accurately describes the data points at the stress levels  $S = 180$  and  $S = 200$  [MPa]. However, the log-Normal and Weibull distributions look quite similar graphically in Figure 3.23.

Comparing the degree of dispersion and skewness per stress level (Figure 3.23), the dispersion is the lowest in the range of  $S = [180 - 200]$  [MPa]. The latter is indicated by the lower value of the standard deviation  $\sigma$ . From  $S = [160 - 140]$  [MPa] and at  $S = 220$  [MPa] flattening out is observed. For the  $S = [160 - 140]$  [MPa] this can be explained by reaching the lower horizontal asymptote of the SN-curve, i.e. the fatigue limit. In the stress level at 220 [MPa], the higher horizontal asymptote is located at the ultimate strength  $\hat{\sigma}_u$ . [66]

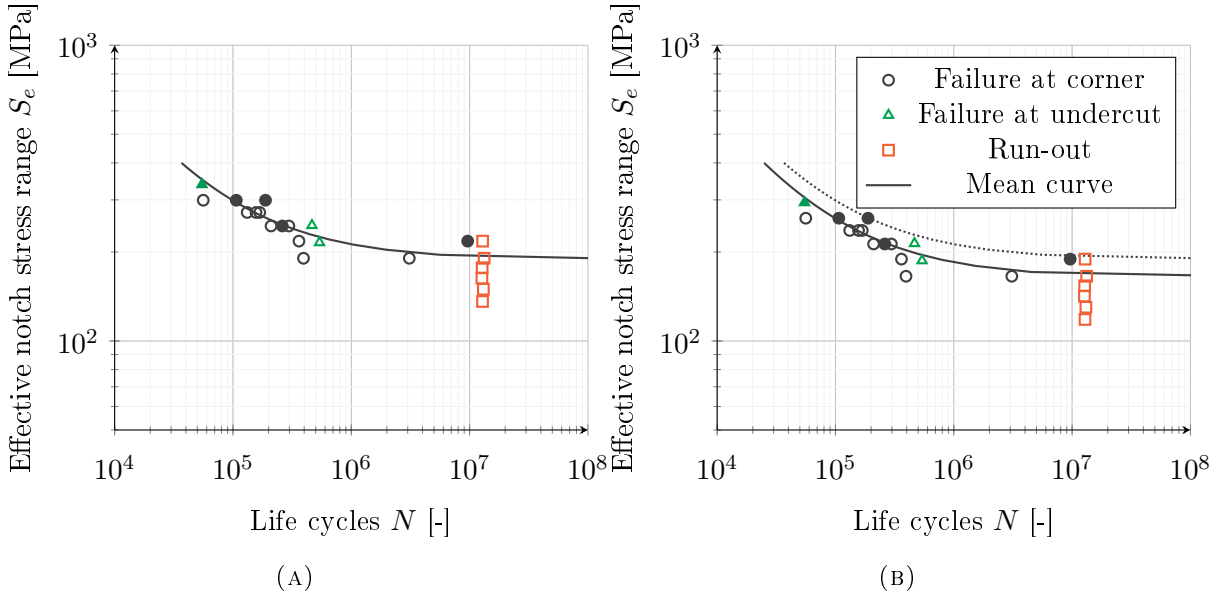


FIGURE 3.22: *Fatigue data of corner adstir fillet stationary shoulder FSW, continuous dual slope, following effective notch stress concept. (A) fully effective radius, (B) not fully effective radius. The gray densely dotted line in (B) represents the mean SN-curve FSW of (A). The solid data points indicate the re-used run-outs.*

TABLE 3.15: *Maximum likelihood estimates (MLEs) for the log-Normal and Weibull distributions at equal stress level including the value of the log-likelihood function.*

Level	Distribution	$\mu$	$\log_{10} \sigma$	$\max_{\theta} \{\mathcal{L}\}$	
$S = 220$	Log-Normal	1.0471	$10^5$	0.26	-2.1459
	Weibull	1.0471	$10^5$	0.24	-2.1582
$S = 200$	Log-Normal	1.5136	$10^5$	0.05	2.5807
	Weibull	1.5136	$10^5$	0.04	2.7998
$S = 180$	Log-Normal	2.5119	$10^5$	0.08	1.5766
	Weibull	2.5119	$10^5$	0.06	1.6968
$S = 160$	Log-Normal	5.8884	$10^6$	1.18	-5.2634
	Weibull	4.8978	$10^6$	0.90	-5.2955
$S = 140$	Log-Normal	3.8019	$10^6$	1.08	-5.1943
	Weibull	3.1623	$10^6$	0.99	-5.4744

### 3.2.4 Fracture surface analysis

A different fracture surface is visible for the two failure types. Figure 3.24a and Figure 3.24b show the fractography of two test specimens which are fractured respectively at the corner and at the undercut at the stress range of 220 [MPa]. Three different fracture zones can be noticed for the corner failure: (1) a smooth surface, (2) a slightly grainy surface and (3) a rough grainy surface, while only zone 2 and zone 3 can be distinguished for the undercut. In zone  $\{1+2\}$  the evolution of the crack is dominant and appears flat, while zone 3 is characterised by fast fracture, explaining the brittle structure [41].

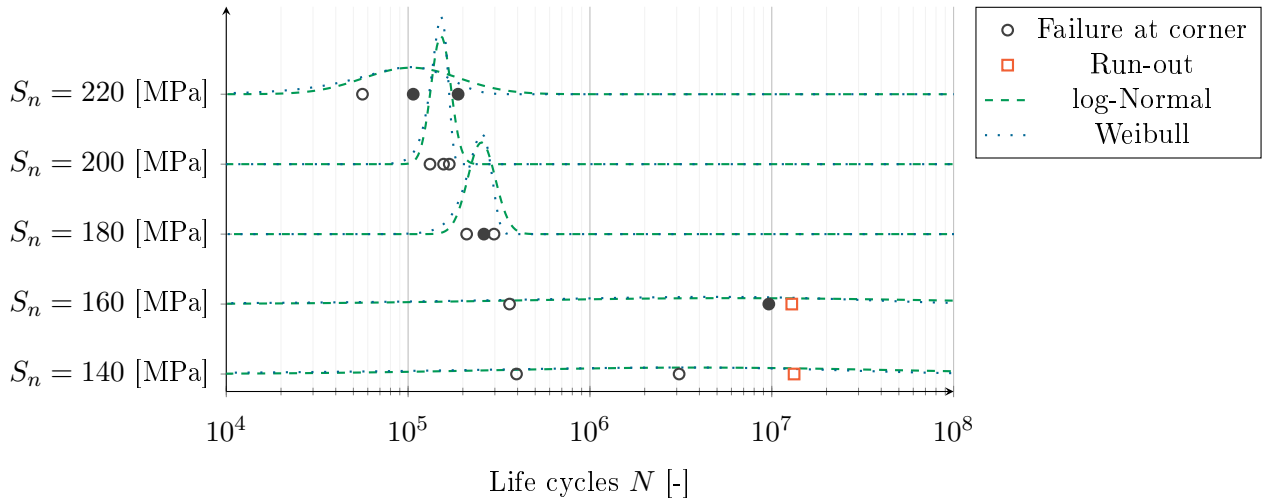


FIGURE 3.23: *log-Normal and Weibull distribution at the different stress levels, following nominal stress concept. The solid data points indicate the re-used run-outs.*

Given the same stress level and number of life cycles, this indicates that the failure location and its material composition is the only relevant variable. When the specimen has failed at the corner, the crack is located at the end of the weld zone, while for the failure at the undercut, the crack is located in the parent material (see Figure 3.14 and Figure 3.18). As such, zone 1 will be in relation with the weld zone material, and the more smooth fracture surface could be explained since grain refinement is present in the weld zone: the zone is plastically deformed due to the FSW shoulder pressure [41]. In the majority of the specimens, zone {1+2} is characterised by a moon-shape, mainly symmetrical over the width of the specimen. So the crack has initiated in the middle of the specimens, as intended in the fatigue test specimens (see Section 2.3). When a less clear moon-shape is present, crack initiation started simultaneously at different locations over the width of the test specimen. [9]

In situations with a higher stress level and a shorter life time (LCF) zone {1+2} is smaller, indicating a shorter crack initiation phase, meaning that the specimen has endured plasticity and the crack growth phase is dominant. On the contrary, in situations with a lower stress level and a longer life time (HCF) zone {1+2} is larger, indicating a longer crack initiation phase, meaning that the specimen has not endured plasticity. [23] This change in fracture surface is visible in case of failure at the corner as well as at the undercut. (Figure 3.24d)

## 4 Discussion

The main findings of this study on FSW of DS T-joints are firstly the 5% increase in hardness at the advancing side of the FSW weld compared to the parent material, an excellent reproducibility of the FSW technique and, the feasibility to use a higher FAT class, up to FAT103 with a slope value of  $m = 6.4$ . Secondly, an extra failure type at the undercut (if present) should be taken into account, next to the expected failure at the corner and the continuous dual slope approach leads to the best fitted curve across all obtained data points.

The 5% hardness increase is due to the grain refinement present in the stir zone of the weld: for a decreasing grain size, the hardness increases. [41] According to de Jesus et al. [20], the hardness value in arc welded structures decreases with approximately 15% with respect to the parent material for similar DS T-joints structural details.

Comparing the obtained hardness results for the corner adstir fillet stationary shoulder FSW to other FSW hardness data results in literature, the same relation is visible: a small increase is ob-



FIGURE 3.24: *Fracture surfaces of test specimen. (A) failure at corner,  $S = 220$  [MPa], (B) failure at undercut,  $S = 220$  [MPa], (C) failure at corner,  $S = 140$  [MPa], and (D) failure at undercut,  $S = 140$  [MPa].*

tained in the weld zone, but the variation with respect to the parent material is seen in literature as not significant, as well as the differences observed between the advancing and retreating sides, so at least an equal hardness is present in the weld as the parent material. [22, 21, 20, 44, 68, 75] Following the alloy 5083-H111 details based on literature, the Brinell hardness value, HB, equals 75HB, leading to a Vickers hardness value of 80HV using conversion tables stated by DIN 50150. The obtained results are lying in the same range. The small difference can be explained since 5083-H111 is a soft material. As such, the values obtained for the micro hardness measurements differ for the chosen indent load  $L$  and cannot be compared one-on-one. [15, 60]

There was a good reproducibility of the FSW technique, always with a fully penetrated weld and without any imperfections. This is important because in another FSW technique for DS T-joints of de Jesus et al. [22], they mention that a physical material separation (gap) was often visible in the test specimens, due to insufficient pressure to cause the bonding of the material.

The data of the fatigue experiment show an increase in fatigue resistance: the design curve FAT103, combined with a slope of  $m = 6.4$ , is possible in case of FSW DS T-joints. This implies that the corner adstir fillet stationary shoulder FSW welds will have a higher failure resistance compared to the arc welded data [67]. Compared with the fatigue resistance data of the parent material 5083-H111 by Sidhom et al. [67], an equal fatigue resistance is present; by stirring the parent material 5083-H111 with the filler material 5183, the weld is no longer the weakest link of the structural detail.

Compared to the fatigue data obtained in the comparable joining techniques of de Jesus et al. [22] (butt-joint FSW technique applied on the bottom of the DS T-joint) and Sidhom et al. [67] (shot-peening after-treatment), the data of the current fatigue experiments ( $r_l = 0.1$ ) lie in the same range as the data of de Jesus et al. [22] ( $r_l = 0$ ) and an increased fatigue resistance is present with respect to the data of Sidhom et al. [67]. The literature data of de Jesus et al. [22] were used to estimate the stress range level in combination with the fatigue life time, so a good force estimation was performed. Since a different load ratio is present for the own fatigue experiments with respect to the test results of de Jesus et al. [22], an effective nominal stress should be calculated to compare both results more accurate. This would imply that when the data results of de Jesus et al. [22] are converted to a load ratio of  $r_l = 0.1$ , the data points would shift downwards. As such, a slightly better fatigue resistance is obtained for the current applied FSW technique with respect to both Sidhom et al. [67] and de Jesus et al. [22].

Since the fatigue resistance is linked to the hardness of the material [20], a suggestion is to inverse the rotational direction in the FSW process, since the hardness is slightly increased at the advancing side compared with the retreating side of the weld. As such, the advancing side is located at the crack sensitive location, yielding an expected further increase in fatigue resistance. This expectation should be investigated.

The occurrence of two different failure types was not expected. In case of the presence of an undercut, created by the FSW, the undercut might interfere with the expected failure resistance. The undercut might be caused by several mechanisms. First, due to a poor set-up the force used to make the weld was too high and the tool has been plunged too deep into the material. E.g. if the heat sink of the supporting fixture is not consistent along the full length of the weld, heat propagation from the weld zone might be poor, leaving a small region to remain slightly hotter and softer than other parts, and the tool will sink in further at that point. Secondly, in case the parent materials have not a uniform thickness, the tool might undercut as the tool forces its way through this thickness variation. Finally, the weld might not be filled completely in case of insufficient filler wire.

Now, the applicable type of friction stir welds are made using pre-programmed parameters, e.g. rotation rate, travelling speed and force. The current sensing systems are not responsive enough to detect small, localised, changes in the weld conditions and to provide adequate feedback to correct for these in real time.

Based on FEM calculations, an undercut of even 0.1 [mm] (1% of the thickness of the bottom plate) will shift the failure location from the corner towards the undercut. The depth of the undercut should be explored in a specific research, offering more specific details about the influence of the undercut in the expected failure resistance and eventually to declare a weld unfit for use. The application of a suitable surface finish treatment to banish the influence of the undercut, as a possible solution, should be investigated.

The continuous dual slope concept with its extra fitting parameter ( $S_f$ ) more accurately describes the fatigue resistance of the DS T-joint. So, a preference is given for the dual slope model but a prerequisite is that sufficient data in the HCF range have been generated.

Some limitations of the present study should be considered. At first, the hardness measurements were only performed on one specimen; as internal check, also specimen I and III should have been measured. Since every weld specimen consists of two different FSW welds (left and right), made separately in time, the experiments demonstrate a similar weld hardness at the two sides of a welded DS T-joint. Secondly, during the experiments, it was not registered in which corner of the DS T-joint (left or right) the failure occurred. As such, no information is obtained about the influence of the order of welding. Thirdly, when the event of an undercut had been known on beforehand the undercut depth could be measured properly in order to validate the FEM calculation results and to analyse its impact more precisely when failure was present at the undercut and/or at the radius. Lastly, the most likely value of the micro-structural length  $\rho^*$  was calculated manually for its use in the continuous dual slope model, following the likelihood approach. This assumption is in line with the current literature; however it is better to generate it automatically upon the implementation of the regression analysis in the model.

In conclusion, the corner adstir fillet stationary shoulder FSW is favourable to the current existing arc welding technique concerning both the hardness and the fatigue resistance of the weld material. Since the properties of the weld material correspond very well to the parent material, the weld cannot be seen any more as the weakest link of the structural detail. The second failure type at the undercut needs further research, even as it might not impact the overall expected failure resistance in our data.



# Closing comments

Today, the four chosen sandwich materials are not developed enough to compete with the conventional solid materials on a large scale. Manufacturing facilities are lacking to up-scale the dimensions, joining possibilities in structural details have not been studied thoroughly and the initial material costs remain too high.

Reflecting on the qualitative comparison of sandwich materials at the material level, none of the four chosen sandwich materials [{metal foam core, metal face sheet}, {metal honeycomb core, metal face sheet}, {polymer elastomer core, metal face sheet} and {polymer foam core, polymer face sheet}] can be elected as most favourable material, since the advantages are non uniform throughout the selected properties. The failure resistance and some specific advantageous mechanical properties might be promising in hybrid constructions. Some added values of the metal foam metal sandwich material derives attention: first, its manufacturing is less complex; second, its corrosion resistance is higher compared with the other metal sandwich materials. On the contrary, the mechanical properties, such as the specific bending stiffness/strength efficiency are cumbersome, due to a higher weight, given the fact that the core material of the metal foam metal sandwich material has a higher density.

The structural and economical modelling of the {aluminium foam core, steel face sheet} sandwich material at the stiffened panel level illustrates that the sandwich material cannot compete to the conventional solid material even when it introduces a more simple construction (without stiffeners).

Since the core material of the sandwich material does not participate in the transmission of the global hull bending moment, its effective plate thickness matches that of the conventional solid material. As such, no weight reduction was found in the applied structural optimisation model. The advantage of the core material lies in the capacity to endure a larger local bending moment, generated by the local water pressure. Also in this load case no weight advantage was achieved. If no weight decrease can be realised, no reduction of the total costs is likely to occur. In a conventional solid material design, the production costs contribute for 50% of the initial costs. When the {aluminium foam core, steel face sheet} sandwich material is used in the simplified structure, the production costs are reduced by a factor 2, but this drop is not large enough to outweigh its higher material price. Not considered in the final calculation are the required investments in new machines, the education of the personnel, and the re-organisation of the shipyard required to deal with the implementation of this new material.

In order to explain the rather contrasting results of the {aluminium foam core, steel face sheet} sandwich materials at the material level and at the stiffened panel level, it should be noted that the sandwich material is a replacement of a plate with stiffeners. This consideration was disregarded in the analysis at the material level.

In order to recalculate the mechanical performance capacity of the sandwich material, one should look at the weight percentage of the sandwich material and the conventional steel plate at the stiffened panel level. The weight of the sandwich material plate is 85%, with 15% of the girders and that of the conventional steel plate is 60% with a contribution of 25% for the stiffeners

and a similar contribution of 15% of the girders. Translating these percentages towards the material level, a correction factor could be introduced: 1.42, expressing the relative weight ratio (85%/60%). The values of the sandwich material should be divided by the factor 1.42. The current optimal bending strength cost efficiency is 0.389 versus 0.255 [ $10^{-3} \cdot \text{kN}^{1/2}\text{m}^2/\text{€}$ ] for respectively the sandwich material and the conventional steel solid. When the ratio of 1.42 is taken into account, the optimal bending strength cost efficiency will reduce until 0.274 [ $10^{-3} \cdot \text{kN}^{1/2}\text{m}^2/\text{€}$ ]. This means that the sandwich material does not outperform the conventional solid. So, there is no clear added value. Alternatively, without a correction factor, the mechanical performance capacity at the material level should have been at least 50% or higher to have a potential weight advantage in comparison with the conventional steel plate, derived from our calculations at the stiffened panel level.

With regard to Allen [1], the optimal bending strength ratio of the thickness of the face sheet over the total {aluminium foam core, steel face sheet} sandwich material thickness was calculated as 1/25 (originally 4/100). This ratio could not be confirmed on the stiffened panel level. This is not so surprising since in the derivation of Allen [1] only the face sheet and the core contributed to the weight, while in our construction, the ratio is determined by an extra parameter, the girder.

In summary, the comparison at the material level is hampered by the structural difference of the sandwich material, overestimating its benefits. Therefore, it is too soon to implement sandwich materials as the primary material in the current ship portfolio, in addition to the higher material cost.

When the focus is not on a decrease in total weight and initial costs, but more on multi-functional aspects, the {aluminium foam core, steel face sheet} sandwich material could still be promising in a hybrid setting. Although the practical issues have not yet been studied properly, its use in naval vessels when one needs a high resistance to impacts and blasting, and when one wants to conserve the limited internal space. [37]

Our studies using conventional solid materials concentrated on the introduction of a specific type of friction stir welding (FSW) to assemble a double sided (DS) T-joint, instead of the current arc welding. The basic principle of FSW is to create of a weld by mixing the materials, which are softened by friction heat, followed by natural cooling.

The corner adstir fillet stationary shoulder FSW adds a filler wire to the welding process. The advantage of the filler wire is that extra material is added, as such, the corner of the DS T-joint can be shaped with the desired radius.

The DS T-joint using this welding technique is fully penetrated from both sides, with excellent reproducibility at both sides of the T-joint. The fatigue resistance of the corner adstir fillet stationary shoulder FSW is at least equivalent to that of the parent material 5083-H111. The fatigue limit of the FSW is almost three times higher as compared with arc welding. With regard to the mathematical description of the fatigue life time, preference should be given to the continuous dual slope analysis, since it incorporates all failure data and run-out data simultaneously; the prerequisite is that a sufficient amount of HCF data have been generated.

Compared with the parent material, we found consistently a 5% higher hardness at the FSW, thanks to an excellent grain refinement while in case of arc welding a 15% reduction in hardness at the weld is reported in the literature.

A noteworthy finding is the occasional occurrence of a second type of failure, besides the expected primary failure at the corner. This second failure occurs at the so called undercut, located at the external lining of the thin plate at the back of the FSW shoulder. Based upon our results, the impact of the undercut failure might not influence the expected failure resistance. However, the undercut failure occurred in a very limited case and the undercut failure was detected a

posteriori, so that the relevant information was not collected in detail. So, the influence of the undercut should be analysed more exploratory, with particular attention to the depth of the undercut, and to solutions to eliminate the undercut by using a suitable surface finishing treatment.

This master thesis research is a preparatory analysis for a larger project concentrating on the simultaneous use of {metal foam core, metal face sheet} sandwich materials and FSW. So, additional research will also look at different travelling and rotational speeds (low, standard and high), rotational direction and at different welding compositions (variations filler wires) and different material compositions (6082-T6, sandwich materials).

In conclusion, the outcome of the analyses of novel materials and techniques in shipbuilding is relevant for a current practice, and fits into the need for constantly looking for improvements in shipbuilding to optimise several aspects of the production process, economic issues and the life cycle of a ship. Based upon our analysis, there is not yet place for a widespread use of {aluminium foam core, steel face sheet} sandwich materials, but there is an added value for the corner adstir fillet stationary shoulder FSW.



# Supplement A |

## 1 Introduction to sandwich materials

The basic structure of a sandwich material consists of a low density core  $t_c$  flanked by equal face sheets  $t_f$ , as illustrated in Figure A.5. The overall height of the sandwich material is  $h_{sm}$ , the distance between the centre-lines of the opposite face sheets is  $d_{sm}$  and the width is  $b$ .

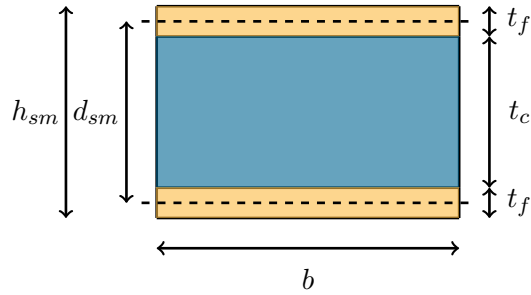


FIGURE A.1: Schematic visualisation of the sandwich material consisting of two face sheets of equal thickness  $t_f$  (yellow), separated by a core  $t_c$  (blue).

Allen [1] has proposed a classification of the thickness of a face sheet into thin, moderate and thick face sheets, based upon the ratio of the distance between the centre-lines of the opposite face sheet  $d_{sm}$  divided by one face sheet thickness  $t_f$ . In the sequel, it is more wanted to have the three categories expressed upon the overall height  $h_{sm}$  and the core thickness  $t_c$ . For the transformation to the overall height the expression  $d_{sm} = h_{sm} - t_f$  is used, while for the transformation to the core thickness  $d_{sm} = t_c + t_f$  is valid. The obtained ratios are given in Table A.1 with respect to the original ratios of Allen [1, Chapter 10].

TABLE A.1: Categorisation of the three face sheet types: thin, moderate and thick based upon three different thickness dimensions: the distance between the centre-lines of the opposite face sheet  $d_{sm}$  based on Allen [1], and two transformations, one to the overall height  $h_{sm}$  and one to the core thickness  $t_c$ .

	Transformation to overall height	Allen [1]	Transformation to core thickness
Thin face sheets	$\frac{h_{sm}}{t_f} > 101$	$\frac{d_{sm}}{t_f} > 100$	$\frac{t_c}{t_f} > 99$
Moderate face sheets	$101 > \frac{h_{sm}}{t_f} > 6.77$	$100 < \frac{d_{sm}}{t_f} > 5.77$	$99 < \frac{t_c}{t_f} > 4.77$
Thick face sheets	$6.77 > \frac{h_{sm}}{t_f}$	$5.77 < \frac{d_{sm}}{t_f}$	$4.77 < \frac{t_c}{t_f}$

To make the ratios more sensible, Figure A.2 graphically illustrates the three face sheet categories with respect to the core thickness.

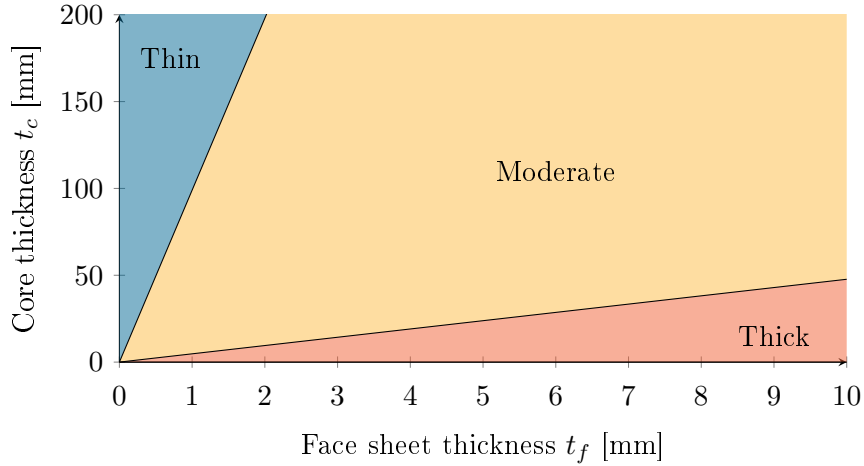


FIGURE A.2: Schematic visualisation of the three face sheet categories based upon the ratio of the core thickness  $t_c$  divided by one face sheet thickness  $t_f$  (Table A.1).

## 2 Material properties of sandwich materials

The material properties according to Allen [1] at material level are given and reviewed. In this context, the sandwich material is described as follows ( $\diamond$ ):

1. With respect to Table A.1, thin/moderate face sheets are considered, resulting that the core thickness approximates the total sandwich material thickness:  $t_c \approx h_{sm}$ .
2. The face sheet thickness is assumed to be symmetrical, because it is proven by Carlsson and Kardomateas [12] that in this configuration the highest flexural stiffness is obtained:  $t_{f1} = t_{f2} = t_f$ .
3. A sandwich material beam is examined, yielding a Poisson's ratio  $\nu_c$  elimination. The latter must be included for plate analysis.

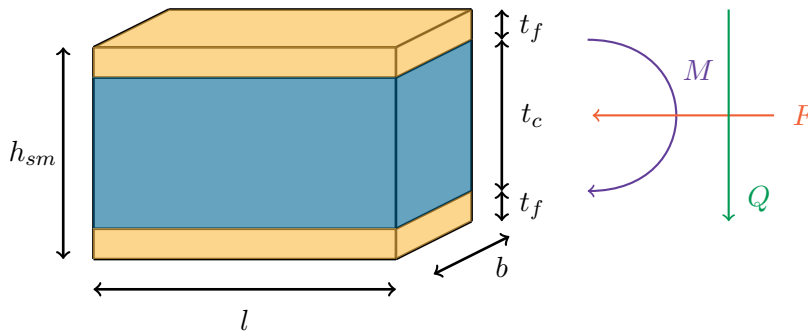


FIGURE A.3: Schematic visualisation of the sandwich material used to derive the material properties consisting of two face sheets of equal thickness  $t_f$  (yellow), separated by a core  $t_c$  (blue), including the three different load cases that are considered: in-plane ( $F$ ), bending ( $M$ ) and shear ( $Q$ ).

## 2.1 Stiffness

The stiffness of sandwich materials will be examined for its three different elements: the in-plane stiffness  $K$ , the flexural stiffness  $D$  and the shear stiffness  $AG$ .

### 2.1.1 In-plane stiffness

To study the in-plane stiffness  $K$ , in-plane tensile and compressive loads are applied. In a sandwich material, only the face sheets ( $2t_f$ ) will incorporate these loads while the contribution of the core is negligible. [76] Equation (A.1) represents the basis formula, simplified for the sandwich material beam following the assumed sandwich material context ( $\diamond$ ).

$$K_{sm} = \frac{2E_f t_f}{1 - \nu_f^2} \xrightarrow{\diamond} 2E_f t_f \quad (\text{A.1})$$

### 2.1.2 Flexural stiffness

Calculating the flexural stiffness  $D$ , both the core and the face sheets are incorporated. The general formula is presented in Equation (A.2), including the simplification ( $\diamond$ ).

$$D_{sm} = \frac{EI_{eq,sm}}{1 - \nu_f^2} \xrightarrow{\diamond} EI_{eq,sm} = E_c \frac{b(t_c)^3}{12} + 2E_f \left[ \frac{b(t_f)^3}{12} + bt_f \left( \frac{h_{sm}}{2} \right)^2 \right] \quad (\text{A.2})$$

In the formula of the flexural rigidity  $EI_{eq}$  of the sandwich material two terms are negligible. First, the contribution of the bending stiffness of the core {term 1} can be neglected, because its magnitude is small due to the low elasticity modulus of the core  $E_c$ . Second, the term  $t_f^3$  {term 2} is only significant in case of thick face sheets. The term is omitted because of the use of a sandwich material with thin/moderate face sheets. [12] In order to check if the chosen sandwich material meets these conditions, Equation (A.3) must be satisfied: [1, Chapter 10]

$$\begin{aligned} \frac{E_f t_f}{E_c h_c} \left( \frac{d_{sm}}{t_c} \right)^2 > 16.7 & \quad \longrightarrow \quad \text{neglect term 1 : } E_c \frac{b(2t_c)^3}{12} \\ \frac{d_{sm}}{t_f} > 5.77 & \quad \longrightarrow \quad \text{neglect term 2 : } 2E_f \left[ \frac{b(t_f)^3}{12} \right] \end{aligned} \quad (\text{A.3})$$

After neglecting the two terms from Equation (A.3), Equation (A.4) is obtained for the chosen sandwich material context ( $\diamond$ ).

$$EI_{eq,sm} = E_f \frac{bt_f h_{sm}^2}{2} \xrightarrow{\diamond} E_f \frac{bt_f t_c^2}{2} \quad (\text{A.4})$$

### 2.1.3 Shear stiffness

Equation (A.5) is used to determine the shear stiffness  $AG$  of a sandwich material. [1, Chapter 10]

$$AG_{sm} = \frac{Gbh_{sm}^2}{t_c} \xrightarrow{\diamond} bh_{sm}G_c \quad (\text{A.5})$$

## 2.2 Stress

To analyse the stress  $\sigma$ , three load cases are looked at: an in-plane load  $F$  following a membrane stress  $\sigma_m$ , a bending moment  $M$  following a bending stress  $\sigma_b$  and a shear force  $Q$  following a shear stress  $\tau$ .

### 2.2.1 Membrane stress

The basic equation is modified for sandwich materials (Equation (A.6)). Only the face sheets ( $2t_f$ ) will incorporate the in-plane load. [1, Chapter 2][76]

$$\sigma_m = \frac{F}{A} = \frac{F}{2t_f b} \quad (\text{A.6})$$

### 2.2.2 Bending stress

The bending stress for a sandwich material is described by Equation (A.7) by adapting the basic equation for sandwich materials. The simplified formulation of the moment of inertia for sandwich materials was used (Equation (A.4)).

$$\sigma_b = \frac{M}{Z} = \frac{M e_{outer,sm}}{I_{sm}} = \frac{M \frac{h_{sm}}{2}}{\frac{t_f b h_{sm}^2}{2}} = \frac{M}{t_f b h_{sm}} \quad (\text{A.7})$$

### 2.2.3 Shear stress

The shear stress  $\tau$  of the sandwich material should take into account all the moduli of elasticity of the different layers of the cross-section. The parameter  $z$  is the level at which the shear stress is determined. [1, Chapter 2] According to Crupi et al. [18], Zu et al. [81] and Petras [59], the core of the sandwich material will mainly absorb the shear load since the maximum shear force is located at the neutral axis. So, only the core area is taken into account to incorporate the load, as defined by Equation (A.8).

$$\tau_{sm} = \frac{QS}{Ib} = \frac{Q}{D} \sum \left( \frac{SE}{b} \right) = \frac{Q}{EI_{sm}b} \left[ E_f b t_f \frac{h_{sm} - t_f}{2} + E_c \frac{b}{2} \left( \left( \frac{t_c}{2} \right)^2 - z^2 \right) \right] \quad (\text{A.8})$$

In the formula of the shear stress  $\tau_{sm}$  of the sandwich material, the contribution of the bending stiffness of the core can be neglected, because its magnitude is small due to the low elasticity modulus of the core  $E_c$ . The latter is applicable on the the second term of the first moment of inertia times the Young's Modulus.

$$E_f \gg E_c \quad \longrightarrow \quad \text{neglect term 2 : } E_c \frac{b}{2} \left( \frac{t_c^2}{2} - z^2 \right)$$

When omitting the second term and substituting the simplified flexural stiffness  $EI_{eq}$  (Equation (A.4)), a simplified formulation is obtained given below.

$$\tau_{sm} = \frac{Q}{bt_c} \quad (\text{A.9})$$

## 3 Equivalent material properties of sandwich materials

With an equivalent material property, a uniform material property is created for the sandwich material to equal the geometry of a conventional solid plate. For the derivation of the equivalent properties of sandwich materials, the thickness of the sandwich material  $h_{sm}$  is set equal to the thickness of the conventional plate  $h_p$  (Figure A.4). The created formulas for sandwich materials are based on the renewed concept of Pflug and Verpoest [61].

In this context, the sandwich material is described as follows ( $\otimes$ ).

1. The face sheet thickness is assumed to be symmetrical, because it is proven by Carlsson and Kardomateas [12] that in this configuration the highest flexural stiffness is obtained:  $t_{f1} = t_{f2} = t_f$ .

### 3.1 Density

In contrast to a conventional solid material, a sandwich material is composed of different layers, and each layers may have a different density. An equivalent density must be derived to have one uniform density of the material in which the contribution of every layer is incorporated in the

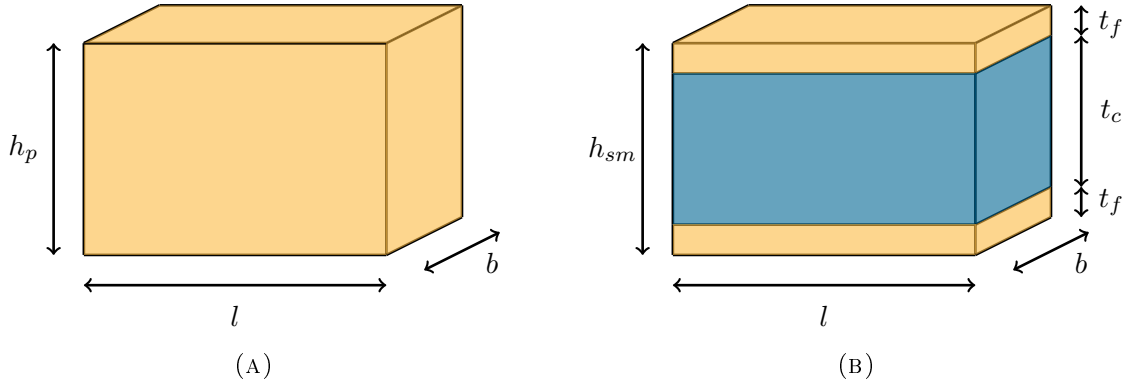


FIGURE A.4: *Basic concept of the equivalent material properties of the sandwich material (B), using the conventional solid material (A).*

correct weight. For the chosen sandwich material, the following derivation is valid. To derive a more compact equation formulation, the terms in the blue box are added.

$$\begin{aligned}
 \rho_{eq,sm} &= \frac{2t_f}{h_{sm}} \rho_f + \frac{t_c}{h_{sm}} \rho_c \\
 &= \frac{2t_f}{h_{sm}} \rho_f + \frac{h_{sm} - 2t_f}{h_{sm}} \rho_c \\
 &= \frac{2t_f}{h_{sm}} \rho_f + \left(1 - \frac{2t_f}{h_{sm}}\right) \rho_c \quad \boxed{+\rho_f - \rho_f} \\
 &= \rho_f - (\rho_f - \rho_c) \left(1 - \frac{2t_f}{h_{sm}}\right)
 \end{aligned} \tag{A.10}$$

### 3.2 Stiffness

The equivalent Young's Modulus  $E_{eq}$  for layered structures is derived by converting the geometry of a sandwich material to that of a conventional plate.

$$\begin{aligned}
 E_{eq,sm} &= \frac{EI_{eq,s}}{I_p} \\
 &= \frac{E_c \frac{b(h_{sm}-2t_f)^3}{12} + 2E_f \left( \frac{b(t_f)^3}{12} + bt_f \left( \frac{h_{sm}}{2} \right)^2 \right)}{\frac{bh_{sm}^3}{12}} \\
 &= bE_c \left( \frac{1-2t_f}{h_{sm}} \right)^3 + \frac{2E_f \left( \frac{b(t_f)^3}{12} + bt_f \left( \frac{h_{sm}}{2} \right)^2 \right) \boxed{+h_{sm}^3 - h_{sm}^3}}{\frac{bh_{sm}^3}{12}} \\
 &= E_f + (E_f - E_c) \left(1 - \frac{2t_f}{h_{sm}}\right)^3
 \end{aligned} \tag{A.11}$$

### 3.3 Stress

The equivalent bending stress  $\sigma_{b,eq}$  will give the stress that is present in the outer fibre  $e_{outer}$  with respect to the centre-line of a sandwich material converted to a conventional solid material geometry. For this, the ratio of the maximum stress formulation for a sandwich material and the conventional solid material is calculated.

The maximum bending stress in the outer fibre  $e_{outer}$  of a material is determined by Equation (A.12).

$$\sigma_{b,max} = \frac{M}{Z} = \frac{Me_{outer}}{I} \tag{A.12}$$

For the conventional solid is valid:

$$\left. \begin{aligned} I_p &= \frac{bh_p^3}{12} \\ e_{outer,p} &= \frac{h_p}{2} \end{aligned} \right\} \rightarrow Z_p = \frac{bh_p^2}{6}$$

For a sandwich material with two outer face sheets including one core is valid:

$$\left. \begin{aligned} I_{sm} &= 2\frac{b(t_f)^3}{12} + 2t_f b \left( \frac{h_{sm} - t_f}{2} \right)^2 \\ e_{outer,sm} &= \frac{h_{sm}}{2} \end{aligned} \right\} \rightarrow Z_{sm} = \frac{3h_{sm}^2 t_f - 6h_{sm} t_f^2 + 4t_f^3}{b3h_{sm}}$$

Substituting the section modulus  $Z$  in Equation (A.12) and set the thickness of the sandwich material equal to the conventional solid plate ( $h_{sm} = h_p$ ), the maximum bending stress follows for both the sandwich and the conventional solid material in Equation (A.13).

$$\left. \begin{aligned} \sigma_{b,sm} &= \frac{M3h_{sm}}{3h_{sm}^2 t_f - 6h_{sm} t_f^2 + 4t_f^3} \\ \sigma_{b,p} &= \frac{M6}{bh_{sm}^2} \end{aligned} \right\} \rightarrow \text{ratio} = \frac{\sigma_{b,p}}{\sigma_{b,sm}} = 6 \frac{t_f}{h_{sm}} \left[ 1 - 2 \frac{t_f}{h_{sm}} + \frac{4}{3} \left( \frac{t_f}{h_{sm}} \right)^2 \right] \quad (\text{A.13})$$

To obtain the equivalent stress formulation, the ratio from Equation (A.13) must be multiplied with the allowable yielding stress of the face sheet  $\hat{\sigma}_{y,f}$  leading to the equivalent stress (Equation (A.14)).

$$\sigma_{eq,sm} = \hat{\sigma}_{y,f} 6 \frac{t_f}{h_{sm}} \left[ 1 - 2 \frac{t_f}{h_{sm}} + \frac{4}{3} \left( \frac{t_f}{h_{sm}} \right)^2 \right] \quad (\text{A.14})$$

#### 4 Optimal ratio of core and face sheet thickness of sandwich materials

The fourth section will study the optimal core and face sheet thickness of the sandwich materials for the lowest weight at material level following Allen [1, Chapter 11] for three failure modes: bending stiffness, bending strength and face wrinkling. The following situation of the sandwich material ( $\square$ ) is considered to find the best ratio:

1. With respect to Table A.1, thin/moderate face sheets are considered, resulting that the core thickness approximates the total sandwich material thickness:  $t_c \approx h_{sm}$ .
2. The face sheet thickness is assumed to be symmetrical, because it is proven by Carlsson and Kardomateas [12] that in this configuration the highest flexural stiffness is obtained:  $t_{f1} = t_{f2} = t_f$ .
3. A sandwich material beam is examined with clamped boundary conditions.

##### 4.1 Calculation of the core thickness

Derived from the two stress equations, the required value of the core thickness will be taken into account in the final optimisation of the core and face sheet thickness according to the minimisation of the total weight of the sandwich material.

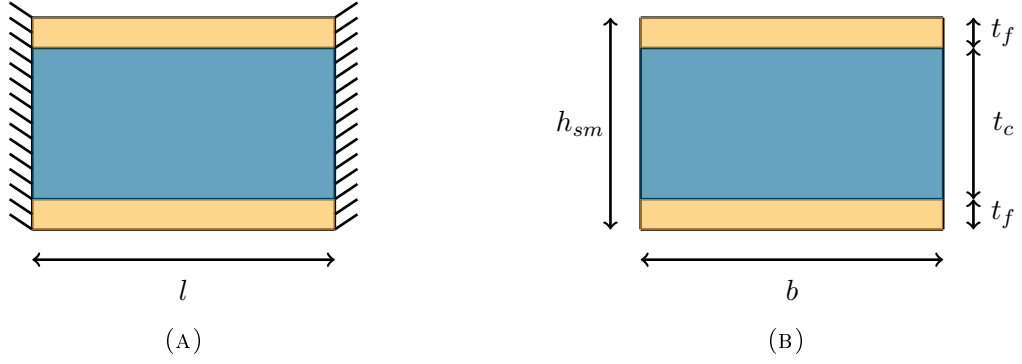


FIGURE A.5: *Basic concept for the derivation of the optimal core and face sheet thickness of a sandwich material. (A) represent the front view of the sandwich material of length  $l$  with the visualisation of the clamped boundaries, and (B) is the cross section with width  $b$ .*

#### 4.1.1 Bending stress

The minimum thickness of the core is derived from the stress equation because the bending stress may not be exceeded by the limiting yielding stress in the face sheet  $\hat{\sigma}_{y,f}$ . The bending stress equation (Equation (A.7)) will be rewritten, implementing the maximum moment  $M = \frac{pl^2b}{12}$  and the simplified section modulus  $Z_{sm} = t_f t_c b$ . The core thickness criterion is derived by implementing the tin/moderate face sheet assumption of the chosen sandwich material context ( $\square$ ) and is shown in Equation (A.15). [1, Chapter 11]:

$$\hat{t}_{c,1} \geq \frac{pl^2}{12t_f \hat{\sigma}_{y,f}} \quad (\text{A.15})$$

#### 4.1.2 Shear stress

Also the critical shear stress of the core  $\hat{\tau}_{y,c}$  may not be exceeded. The second core thickness criterion is derived by rewriting the shear stress formula of Equation (A.8) implementing the shear force of  $M = \frac{plb}{2}$  and the effective area of the face sheets  $A_{eff} = 2t_f b$ . [1, Chapter 11]

$$\hat{t}_{c,2} \geq \frac{pl}{2\hat{\tau}_{y,c}} \quad (\text{A.16})$$

## 4.2 Calculation of the face sheet thickness

Three different ratios of the weight of the core to the combined weight of the faces are set, based on the bending stiffness, the bending strength and face wrinkling. For each component the general formula for the weight per area [ $\text{kg}/\text{mm}^2$ ] is used (Equation (A.17)):

$$\frac{W_{sm}}{lb} = w_{sm} = t_c \rho_c + 2t_f \rho_f \quad (\text{A.17})$$

#### 4.2.1 Bending stiffness

The bending stiffness is defined by Equation (A.18), assuming thin face sheets. By re-writing the equation in terms of the face sheet thickness  $t_f$  and substituting the obtained formulation into the weight equation (Equation (A.17)), Equation (A.19) follows. When taking the derivative of the weight formula to the core thickness  $t_c$  and setting this derivative equal to zero, a formulation

for the core thickness follows as presented by Equation (A.20).

$$D_{sm} = \frac{E_f b t_f t_c^2}{2} \longrightarrow t_f = \frac{2D_{sm}}{E_f b t_c^2} \quad (\text{A.18})$$

$$w_{sm} = t_c \rho_c + \frac{4\rho_f D_{sm}}{E_f b t_c^2} \quad (\text{A.19})$$

$$\frac{dw_{sm}}{dt_c} = \rho_c - \frac{8\rho_f D_{sm}}{E_f b t_c^3} = 0 \longrightarrow t_c^3 = \frac{8\rho_f D_{sm}}{\rho_c b E_f} \quad (\text{A.20})$$

The core height formulation (Equation (A.20)) can be substituted in the ratio of the weight of the core to the combined weight of the faces in the [blue](#) box in Equation (A.21).

$$\text{ratio} = \frac{w_c}{w_f} = \frac{t_c \rho_c}{2t_f \rho_f} = \frac{t_c \rho_c}{\frac{4\rho_f D_{sm}}{E_f b t_c^2}} = \frac{t_c^3 \rho_c E_f b}{4\rho_f D_{sm}} = 2 \longrightarrow \frac{t_c}{t_f E} = \frac{4\rho_f}{\rho_c} \quad (\text{A.21})$$

Since in the formulas of the equivalent material properties a ratio is required based upon one face sheet thickness divided by the overall sandwich height, Equation (A.21) must be rewritten by substituting  $t_c = h_{sm} - 2t_f$  leading to Equation (A.22).

$$\frac{t_f}{h_{sm} E} = \frac{\rho_c}{4\rho_f + 2\rho_c} \quad (\text{A.22})$$

#### 4.2.2 Bending strength

According to the bending strength, the face thickness and core thickness must satisfy Equation (A.23).  $\hat{\sigma}_{y,f}$  is the allowable yield stress of the face sheets.

$$M = \hat{\sigma}_{y,f} t_f b t_c \longrightarrow t_f = \frac{M}{\hat{\sigma}_{y,f} b t_c} \quad (\text{A.23})$$

Eliminating of  $t_f$  from Equation (A.23) and substituting in the general weight formula leads to Equation (A.24). Thereafter, the derivative is taken with respect to  $t_c$ , which provides the optimal core height (Equation (A.25)).

$$w_{sm} = t_c \rho_c + \frac{2\rho_f M}{\hat{\sigma}_{y,f} b t_c} \quad (\text{A.24})$$

$$\frac{dw_{sm}}{dt_c} = \rho_c - \frac{2\rho_f M}{\hat{\sigma}_{y,f} b t_c^2} = 0 \longrightarrow t_c^2 = \frac{2\rho_f M}{\rho_c b \hat{\sigma}_{y,f}} \quad (\text{A.25})$$

When implementing the obtained formulation for the core height (Equation (A.25)) into the ratio of the core weight to the combined weight of the faces in the [blue](#) box, the following relation between the thickness of the core and the face sheets results (Equation (A.26)).

$$\text{ratio} = \frac{w_c}{w_f} = \frac{t_c \rho_c}{2t_f \rho_f} = \frac{t_c \rho_c}{\frac{2\rho_f M}{\hat{\sigma}_{y,f} b t_c}} = \frac{t_c^2 \rho_c \hat{\sigma}_{y,f} b}{2\rho_f M} = 1 \longrightarrow \frac{t_c}{t_f \sigma} = \frac{2\rho_f}{\rho_c} \quad (\text{A.26})$$

When rewriting Equation (A.26) by substituting  $t_c = h_{sm} - 2t_f$ , the ratio for the bending stress based upon one face sheet thickness divided by the overall sandwich height is described by Equation (A.27).

$$\frac{t_f}{h_{sm} \sigma} = \frac{\rho_c}{2\rho_f + 2\rho_c} \quad (\text{A.27})$$

### 4.2.3 Face wrinkling

When face wrinkling is expected to be the failing criterion, the limiting wrinkling stress  $\hat{\sigma}_{wr}$  is constant but proportional to  $t_f^2$ . When substituting the applicable allowable stress ( $\hat{\sigma}_{wr} = kt_f^2$ ) in the moment formula, Equation (A.28) follows.

$$M = \hat{\sigma} t_f b t_c = kt_f^3 b t_c \longrightarrow t_c = \frac{M}{kt_f^3 b} \quad (\text{A.28})$$

When rewriting the aforementioned formula in terms of the core thickness  $t_c$ , and minimising the weight with respect to  $t_f$ , the calculation yields the optimum face sheet thickness (Equation (A.30)):

$$w_{sm} = \frac{M}{kt_f^3 b} \rho_c + 2t_f \rho_f \quad (\text{A.29})$$

$$\frac{dw_{sm}}{dt_f} = -\frac{3\rho_c M}{kbt_f^4 b} + 2\rho_f = 0 \longrightarrow t_f^4 = \frac{3\rho_c M}{2\rho_f bk} \quad (\text{A.30})$$

Equation (A.31) results when substituting the formulation for the face sheet thickness (Equation (A.30)) into the ratio of the core weight to the combined weight of the faces in the blue box, with a further derivation of the optimal ratio of the thickness of the core and the face sheets:

$$\text{ratio} = \frac{w_c}{w_f} = \frac{t_c \rho_c}{2t_f \rho_f} = \frac{\frac{M\rho_c}{kt_f^3 b}}{2t_f \rho_f} = \frac{M\rho_c}{2k \boxed{t_f^4} b \rho_f} = \frac{1}{3} \longrightarrow \frac{t_c}{t_f \text{ wrink}} = \frac{2\rho_f}{3\rho_c} \quad (\text{A.31})$$

The ratio for the wrinkling failure based upon one face sheet thickness divided by the overall sandwich height (Equation (A.32)) is obtained by substituting  $t_c = h_{sm} - 2t_f$  in Equation (A.31).

$$\frac{t_f}{h_{sm \text{ wrink}}} = \frac{3\rho_c}{2\rho_f + 6\rho_c} \quad (\text{A.32})$$

## 4.3 Conclusion

In Figure A.6 the ratios for each component are plotted (Equation (A.21), Equation (A.26) and Equation (A.31)), with the following chosen densities for an aluminium core and faces:  $\rho_c = 700$  [kg/m<sup>3</sup>] and  $\rho_f = 2755$  [kg/m<sup>3</sup>]. The minimum required values of the core thickness of Equation (A.15) and Equation (A.16) are presented, based on the following values for an aluminium core and face sheets:  $l = 1000$  [mm],  $\hat{\sigma}_{y,c} = 10$  [MPa] and  $\hat{\sigma}_{y,f} = 120$  [MPa]. The three categories of the face sheet thickness are also included to check if the thin/moderate face sheet assumption is still valid.

Based on the expected failure mode, the optimal thickness of the core and the face sheets are derived from the intersection between the ratio-function and the highest function of the minimum core thickness. It goes without saying that the optimal relation differs with the length of the plate, the distributed load and the material features of the chosen core and face sheets. Some concluding thoughts:

1. When the water pressure increases, also the optimal ratio increases in core and face sheet thickness following the bending stress criterion. Looking at the shear stress criterion only a larger core thickness is required, since the relation constant over the face sheet thickness.
2. For the bending stiffness and bending strength ratio, the bending stress core criterion is decisive. In the optimal ratio according to face wrinkling, the core criterion of the shear stress is dominant.

3. The optimal ratio for the bending stiffness and bending stress lies in the area of thin/moderate face sheets, while the face wrinkling optimal ratio belongs to the thick face sheet category.
4. The bending stress criterion for the core thickness is derived using the thin/moderate face sheet assumption ( $\square$ ). This criterion is therefore not valid in the thick face sheet area. Since this criterion is only decisive in the optimal ratio of the bending stiffness and the bending strength, the choice for this assumption is still valid.

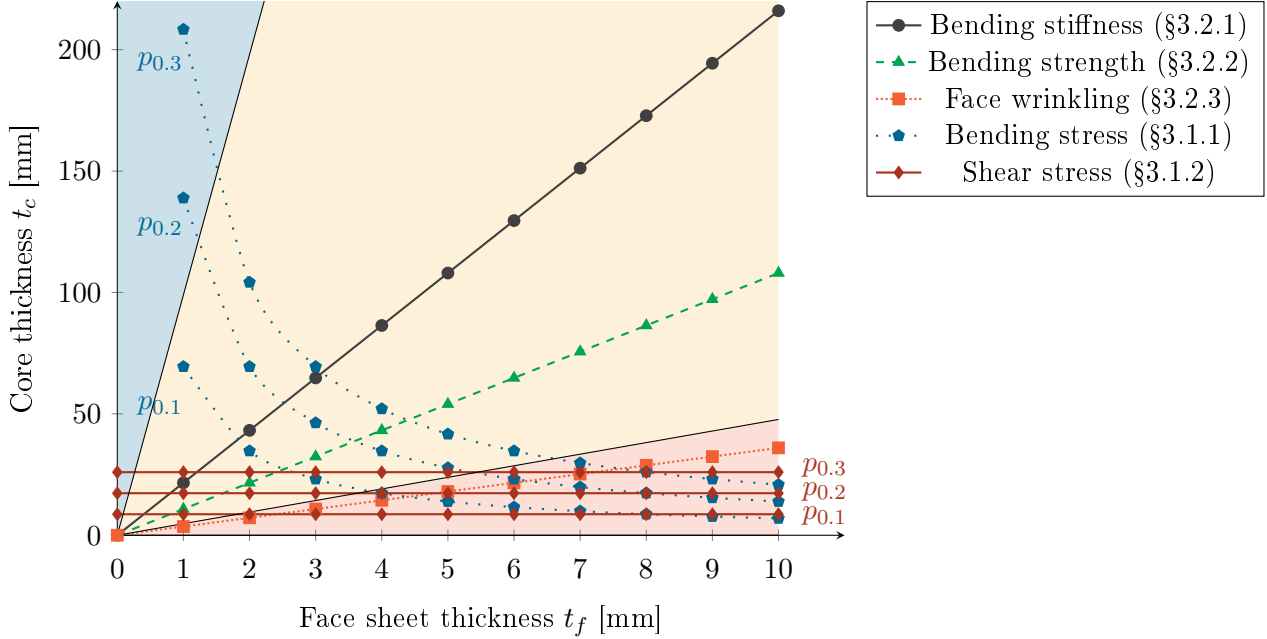


FIGURE A.6: Ratio between core thickness and face thickness for the three components: bending stiffness, bending strength and face wrinkling, at material level. The two core thickness criteria are calculated for a water pressure range of  $p = 0.1 - 0.3$  [MPa]. Other parameters used:  $l = 1000$  [mm],  $\rho_c = 700$  [kg/m<sup>3</sup>],  $\rho_f = 2755$  [kg/m<sup>3</sup>],  $\hat{\sigma}_{y,c} = 10$  [MPa] and  $\hat{\sigma}_{y,f} = 120$  [MPa]. The three face sheet thickness categories are included: thin (blue), moderate (yellow) and thick (red).

## 5 Comparison of material properties of sandwich materials to conventional solid materials

The technique to compare the material properties is based on Vinson [76]. For the comparison, half the thickness of the conventional solid plate is set equal to the face sheet thickness,  $h_p = 2t_f$ , as schematically visualised in Figure A.7. So, the effective area in the sandwich material and the conventional solid is equal. This geometry is chosen to express in which properties the advantages of sandwich materials lie with respect to the conventional solid material. In this context, the sandwich material is described as follows ( $\oplus$ ):

1. With respect to Table A.1, thin/moderate face sheets are considered, resulting that the core thickness approximates the total sandwich material thickness:  $t_c \approx h_{sm}$ .
2. The face sheet thickness is assumed to be symmetrical, because it is proven by Carlsson and Kardomateas [12] that in this configuration the highest flexural stiffness is obtained:  $t_{f1} = t_{f2} = t_f$ .

3. A sandwich material beam is examined, yielding a Poisson's ratio  $\nu_c$  elimination. The latter must be included for plate analysis.

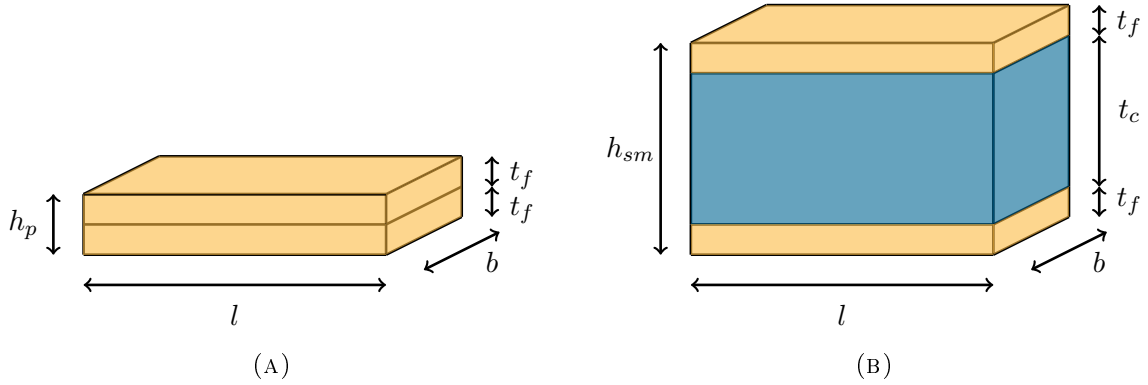


FIGURE A.7: Basic concept to compare the material properties of conventional solid material (A) and the sandwich material (B).

## 5.1 Weight

The weight  $W$  of the sandwich material will only differ from the conventional solid material with the same two face sheets, by the weight of the core (Equation (A.33)). The formula for the weight per area for both the sandwich and conventional solid material is given. [12, 61]

$$\left. \begin{aligned} \frac{W_{sm}}{lb} &= w_{sm} = h_{sm}\rho_{sm} = h_{sm} \left[ 2\frac{t_f}{h_{sm}}\rho_f + \frac{t_c}{h_{sm}}\rho_c \right] \\ \frac{W_p}{lb} &= w_p = h_p\rho_f \end{aligned} \right\} \rightarrow \text{ratio} = \frac{w_{sm}}{w_p} = 1 + \frac{t_c\rho_c}{2t_f\rho_f} \quad (\text{A.33})$$

Since in this context the sandwich material is described with a thin/moderate face sheet thickness ( $\oplus$ ), the ratio  $t_c/t_c = 4.77$  from Table A.1 can be used to make the ratio more sensible. For the density ratio,  $1/4$  is applicable for the aluminium configuration. The weight per area of a sandwich material will increase with  $3/5$  times the weight of the conventional solid. The weight addition is marked in blue.

$$w_{sm} \approx w_p + \boxed{\frac{3}{5}w_p} \quad (\text{A.34})$$

## 5.2 Stiffness

### 5.2.1 In-plane stiffness

For a sandwich material only the face sheets deal with the in-plane tensile and compressive loads. Equation (A.35) represents the accompanying ratio.

$$\left. \begin{aligned} K_{sm} &= 2E_f t_f \\ K_p &= E_f h_p \end{aligned} \right\} \rightarrow \text{ratio} = \frac{K_{sm}}{K_p} = \frac{2t_f}{h_p} \quad (\text{A.35})$$

In the chosen sandwich geometry,  $h_p = 2t_f$ , the in-plane stiffness for the sandwich material and the conventional solid material are equal. So, no in-plane stiffness advantage is present for the sandwich material.

$$K_{sm} = K_p \quad (\text{A.36})$$

### 5.2.2 Flexural stiffness

Both the flexural rigidity of the sandwich material and conventional solid material configurations are determined. Equation (A.37) shows their internal relation.

$$\left. \begin{aligned} EI_{eq,sm} &= \frac{E_f b t_f h_{sm}^2}{2} \\ EI_{eq,p} &= \frac{E_f b h_p^3}{12} \end{aligned} \right\} \longrightarrow \text{ratio} = \frac{EI_{eq,sm}}{EI_{eq,p}} = \frac{6 t_f h_{sm}^2}{h_p^3} = \frac{3}{4} \left( \frac{h_{sm}}{t_f} \right)^2 \quad (\text{A.37})$$

Assuming thin/moderate face sheets ( $\oplus$ ), the ratio  $h_{sm}/t_f = 6.77$  from Table A.1 is substituted resulting that the flexural rigidity of a sandwich material is 34 times increased with respect to the conventional solid material.

$$EI_{eq,sm} \approx 34 EI_{eq,p} \quad (\text{A.38})$$

### 5.2.3 Shear stiffness

The relation of the shear stiffness of the sandwich material and the conventional solid material is, as given by Equation (A.39) dependent on the relation of the shear modulus  $G$  of both materials.

$$\left. \begin{aligned} AG_{sm} &= b h_{sm} G_c \\ AG_p &= b h_p G_f \end{aligned} \right\} \longrightarrow \text{ratio} = \frac{AG_{sm}}{AG_p} = \frac{h_{sm} G_c}{h_p G_f} = \frac{h_{sm} G_c}{2 t_f G_f} \quad (\text{A.39})$$

Implementing the ratio  $h_{sm}/t_f = 6.77$  from Table A.1, the ratio  $G_c/G_f$  may not be smaller than  $2/7$  to obtain an increase in shear stiffness for the sandwich material is obtained. In the aluminium configuration, the Young's Modulus  $E$  ratio  $E_p/E_c$  is equal to 140. Since the Shear modulus and the Young's Modulus are linked via a constant relation  $G = 2E/(1 + \nu)$ , a ratio  $G_c/G_f$  of  $1/140$  is valid and thus smaller than  $2/7$ . So, no shear advantage is present in this configuration.

$$AG_{eq,sm} \approx \frac{7}{2} \frac{G_c}{G_f} AG_p \quad (\text{A.40})$$

## 5.3 Stress

### 5.3.1 In-plane stiffness

For a sandwich material only the face sheets can endure the in-plane tensile and compressive loads. Equation (A.41) represents the accompanying ratio.

$$\left. \begin{aligned} \sigma_{m,sm} &= \frac{F}{2 t_f b} \\ \sigma_{m,p} &= \frac{F}{h_p b} \end{aligned} \right\} \longrightarrow \text{ratio} = \frac{\sigma_{m,sm}}{\sigma_{m,p}} = \frac{2 t_f}{h_p} \quad (\text{A.41})$$

In the chosen sandwich geometry,  $h_p = 2 t_f$ , the in-plane stress for the sandwich material and the conventional solid material are equal, and thus no in-plane stress advantage is present for the sandwich material.

$$\sigma_{m,sm} = \sigma_{m,p} \quad (\text{A.42})$$

### 5.3.2 Bending stress

The bending stress equation for both the sandwich and the conventional solid material follows in Equation (A.43), including the mutual ratio.

$$\left. \begin{aligned} \sigma_{b,sm} &= \frac{M}{h_{sm} b t_f} \\ \sigma_{b,p} &= \frac{6M}{b h_p^2} \end{aligned} \right\} \longrightarrow \text{ratio} = \frac{\sigma_{b,sm}}{\sigma_{b,p}} = \frac{1}{6} \frac{h_p^2}{h_{sm} t_f} = \frac{2}{3} \frac{t_f}{h_{sm}} \quad (\text{A.43})$$

The bending stress is 10 times reduced with respect to the conventional solid, when assuming thin/moderate face sheets ( $\oplus$ ).

$$\sigma_{b,sm} \approx \frac{1}{10} \sigma_{b,p} \quad (\text{A.44})$$

### 5.3.3 Shear stress

When comparing the shear stress of the sandwich material and the conventional solid material applicable on the chosen sandwich material context ( $\oplus$ ), the ratio following Equation (C.4) is obtained.

$$\left. \begin{aligned} \tau_{sm} &= \frac{Q}{bh_{sm}} \\ \tau_p &= \frac{Q \frac{bh_p^2}{8}}{\frac{bh_p^3}{12} b} = \frac{3Q}{2bh_p} \end{aligned} \right\} \rightarrow \text{ratio} = \frac{\tau_{sm}}{\tau_p} = \frac{2h_p}{3h_{sm}} = \frac{4t_f}{3h_{sm}} \quad (\text{A.45})$$

For thin/moderate face sheets ( $\oplus$ ), the shear stress of the sandwich material could be 5 times reduced.

$$\tau_{sm} \approx \frac{1}{5} \tau_p \quad (\text{A.46})$$



# Supplement B |

## 1 Design constraints for conventional solid material

### 1.1 Plate level

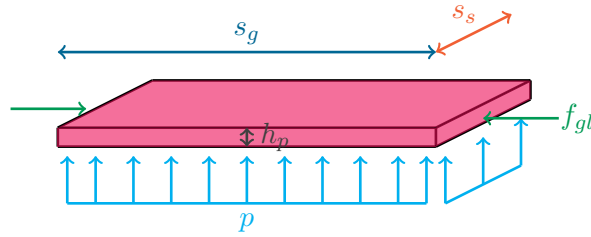


FIGURE B.1: *Schematic semi-3-dimensional visualisation of the plate level for the conventional solid material configuration.*

#### 1.1.1 Plate yielding

Plate yielding is present when the stress at the outer fibre reaches the in-plane strength (yield strength  $\hat{\sigma}_{y,p}$ ). To determine the yield stress in the plate  $\sigma_p$ , two kinds of stresses should be taken into account, depending on the load case present: bending stress  $\sigma_b$  and the membrane stress  $\sigma_m$ . Bending stress is present in the material as a result of a bending moment, while membrane stress originates from a normal force.

At plate level, both bending stress and membrane stress must be taken into account. Both stresses have a different orientation, the membrane stress has a longitudinal orientation and the bending stress a transversal orientation; single summation of both stresses cannot be applied. To determine the equivalent stress, the Von Mises principle is used, leading to Equation (B.1). As long as the plate stress  $\sigma_p$  is lower than the allowable plate yielding stress  $\hat{\sigma}_{y,p}$ , plate yielding will not be present.

$$\sigma_p = \sqrt{\sigma_b^2 + \sigma_m^2 - \sigma_b \sigma_m} \leq \hat{\sigma}_{y,p} \quad (\text{B.1})$$

where,

$$\begin{aligned} \sigma_b &= \frac{M}{Z} \\ \sigma_m &= \frac{F}{A} \end{aligned}$$

To determine the bending stress  $\sigma_b$ , the plate bending formulas of Young and Budynas [79] are used, applying a uniform loading over the entire plate in case of two different boundary conditions and locations. The formulas are presented by Equation (B.2), Equation (B.4) and Equation (B.3). In Table B.1 the specific values of the factors  $\beta$ ,  $\beta_1$  and  $\beta_2$  are given. Note that

$x$  represents the longer side of the plate, while  $y$  is the shorter side of the plate.

$$\sigma_b = \frac{\beta p y^2}{h_p^2} \quad \text{at center} \quad \text{simply supported} \quad (\text{B.2})$$

$$\sigma_b = \frac{\beta_1 p y^2}{h_p^2} \quad \text{at center of long edge} \quad \text{clamped} \quad (\text{B.3})$$

$$\sigma_b = -\frac{\beta_2 p y^2}{h_p^2} \quad \text{at center} \quad \text{clamped} \quad (\text{B.4})$$

where,

TABLE B.1:  $\beta$ ,  $\beta_1$  and  $\beta_2$  values, according to  $x/y$  relationship based on Young and Budynas [79].

$x/y$	1.0	1.2	1.4	1.6	1.8	2.0	3.0	$\infty$
$\beta$	0.2874	0.3762	0.4530	0.5172	0.5688	0.6102	0.7134	0.7500
$\beta_1$	0.3078	0.3834	0.4356	0.4680	0.4872	0.4974	0.5000	0.5000
$\beta_2$	0.1386	0.1794	0.2094	0.2286	0.2406	0.2472	0.2500	0.2500

The membrane stress  $\sigma_m$  is determined using Equation (B.5), by implementing the global bending moment  $M_{gl}$ , where  $m$  denotes the number of bulkheads in longitudinal direction and  $n$  denotes the number of stiffeners in longitudinal direction.

$$\sigma_m = \frac{F}{A} \quad (\text{B.5})$$

where,

$$F \longrightarrow f_{gl} = \frac{F_{gl}}{(m+1)(n+1)}$$

$$F_{gl} = \frac{M_{gl}}{D}$$

$$A \longrightarrow A_p = h_p s_s$$

### 1.1.2 Euler plate buckling

The elastic plate buckling stress of a solid plate  $\hat{\sigma}_E$  is calculated using Equation (B.6), where  $k$  is the buckling coefficient. In order to determine the minimum equivalent plate thickness required, the 'global hull force'-stress  $\sigma_{gl}$  is used to replace  $\hat{\sigma}_E$ . From this buckling stress the minimum required plate thickness  $h_p$  can be derived to prevent Euler plate buckling. As long as the plate stress  $\sigma_p$  is lower than the calculated critical Euler plate buckling stress, overall buckling will not be present. [55, Chapter 3: Section 6,9] [55, Chapter 5]

$$\sigma_{gl} \leq \hat{\sigma}_E = \frac{k\pi^2 E}{12(1-\nu^2)} \left( \frac{h_p}{s_s} \right)^2 \longrightarrow h_p = \left( \frac{f_{gl} 12(1-\nu^2) s_s}{\pi^2 k E} \right)^{\frac{1}{3}} \quad (\text{B.6})$$

$$\sigma_{gl} = \frac{f_{gl}}{s_s h_p}$$

### 1.1.3 Plate shear

The shear stress in a homogeneous material at a distance  $z$  from the neutral axis is defined by Equation (B.7). The maximum shear stress  $\tau_p$  is located at the neutral axis. As long as the plate shear stress  $\tau_p$  does not outreach the allowable plate yielding shear strength  $\hat{\tau}_{y,p}$ , shear failure is not present. In the classical analysis of the conventional solid material, the shear deformation is less important for long beams, the shear part is only a fraction of the bending part. For thin plates, the effect of transverse shear must not be included.

$$\tau_p = \frac{QS}{Ib} = \frac{3Q_p}{2bh_p} \leq \hat{\tau}_{y,p} \quad (\text{B.7})$$

where,

$$\begin{aligned} Q &\longrightarrow Q_p = \frac{ps_s s_g}{2} \\ S &\longrightarrow S_p = \frac{bh_p^2}{8} \\ I &\longrightarrow I_p = \frac{E_p b h_p^3}{12} \end{aligned}$$

## 1.2 Plate-stiffener level

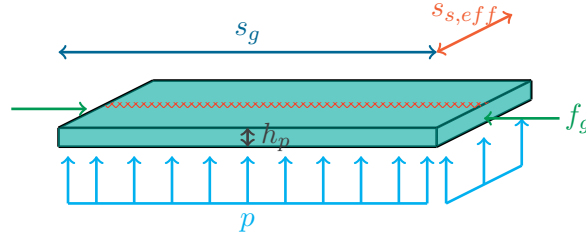


FIGURE B.2: *Schematic semi-3-dimensional visualisation of the plate-stiffener level for the conventional solid material configuration. The hatched area reflects the location of the stiffener.*

### 1.2.1 Effective stiffener spacing

For formulation of the effective width  $s_{s,eff}$  of the stiffener spacing several equations are studied and compared. The effective width must be taken into account due to the phenomenon *shear lag*, activated by lateral load or out-of-plane bending. The classical beam theory assumes a uniform stress distribution, while in reality a non-uniform stress distribution is present, as visualised in Figure B.3. [55, Chapter 2: Section 5]

This difference must be taken into account in equations where bending dominates: instead of the original stiffener spacing, the effective width of the stiffener spacing will be used, since only this part will contribute to the moment of inertia. Paik and Thayamballi [55] have already accomplished a full derivation of the exact solution with regard to the effective width. The final formula is given in Equation (B.8). There are also two approximations: Equation (B.9) and Equation (B.10) show the estimations of Paik and Thayamballi [55] and of Lloyds Register [47].

$$s_{s,eff} = \frac{4s_g \sinh\left(\frac{\pi s_g}{s_s}\right)}{\pi(1+\nu) \left[ (3-\nu) \sinh\left(\frac{2\pi s_g}{s_s}\right) - 2(1+\nu) \left(\frac{\pi s_g}{s_s}\right) \right]} \quad (\text{B.8})$$

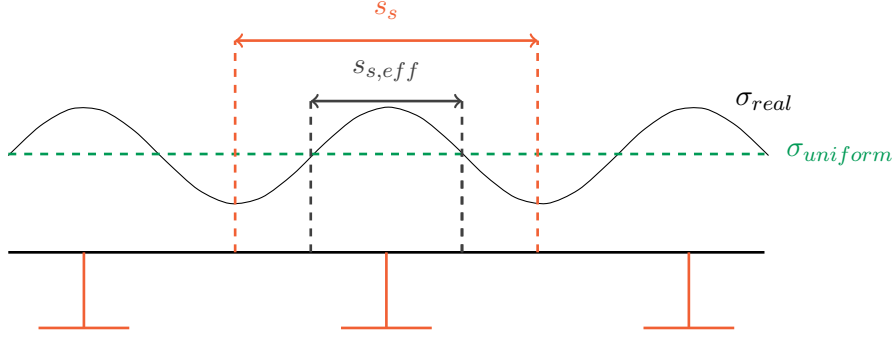


FIGURE B.3: Schematic presentation at the plate-stiffener level: stiffener spacing and effective width of the stiffener spacing, based on the shear lag effect.

Approximations:

$$s_{s,eff,PaikandThayamballi} [55] = \begin{cases} s_s & \text{for } \frac{s_s}{s_g} \leq 0.18 \\ 0.18s_g & \text{for } \frac{s_s}{s_g} > 0.18 \end{cases} \quad (\text{B.9})$$

$$s_{s,eff,Lloyd'sRegister} [47] = \min \left[ 0.3 \left( \frac{s_g}{s_s} \right)^{\frac{2}{3}} ; 1 \right] s_s \quad (\text{B.10})$$

All obtained relations are plotted aiming to find the best fitting curve in order to estimate the exact effective width. The exact solution leans one impropriety: the effective width  $s_{s,eff}$  can never be larger than the stiffener spacing  $s_s$  ( $>1$ ). Based on Figure B.4 the simplification of Paik and Thayamballi [55] is considered as the best fit.

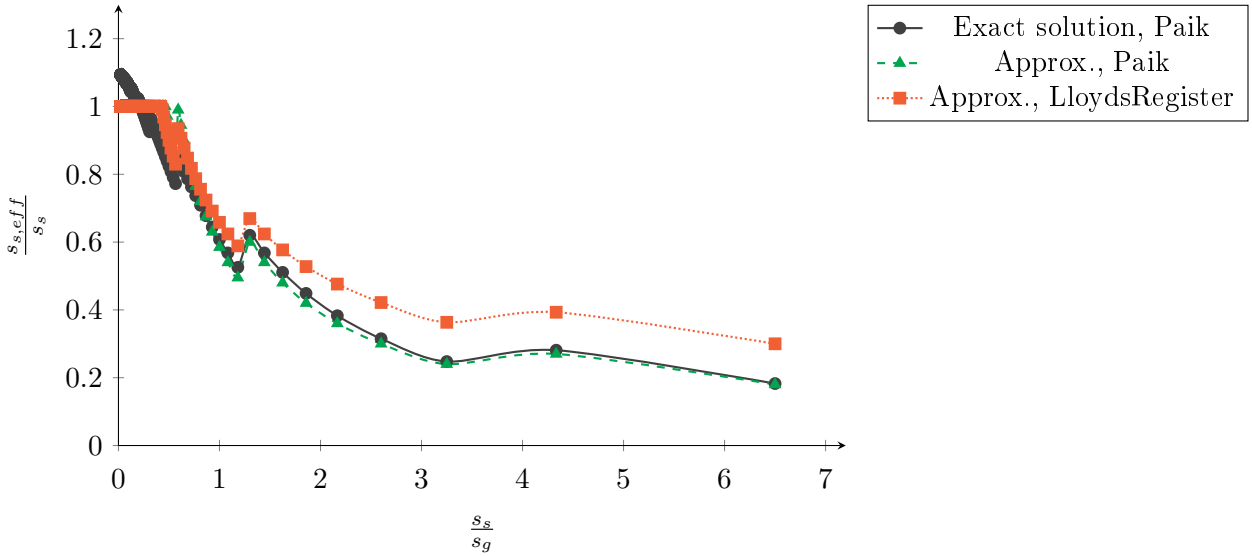


FIGURE B.4:  $\frac{s_s}{s_g}$  versus  $\frac{s_{s,eff}}{s_s}$ ; comparison of the exact solution given by Paik and Thayamballi [55] and the approximation formulas of Paik and Thayamballi [55] and Lloyd's Register [47].

### 1.2.2 Plate-stiffener yielding

At plate-stiffener level, both bending stress and membrane stress must be taken into account. Because both stresses have the same direction, summation is allowed (Equation (B.11)). As long

as the stiffener stress  $\sigma_s$  for the plate-stiffener combination is lower than the allowable stiffener yielding stress  $\hat{\sigma}_{y,s}$ , plate-stiffener yielding will not occur.

$$\sigma_s = \sigma_m + \sigma_b < \hat{\sigma}_{y,s} \quad (\text{B.11})$$

To calculate the bending stress  $\sigma_b$ , the beam bending formula for clamped boundaries can be used [79].

$$\sigma_b = \frac{M}{Z} \quad (\text{B.12})$$

where,

$$\begin{aligned} M &\longrightarrow M_s = \frac{ps_g^2 s_{s,eff}}{12} \\ Z &\longrightarrow Z_s = \frac{I_s}{e_{outer,s}} \\ I_s &= \sum_i [I_{m,i} + e_{diff,i}^2 A_i] \\ e_{outer,s} &= h_{HP} \end{aligned}$$

The formula to calculate the membrane stress  $\sigma_m$  equals the membrane stress equation of the plate-level (Equation (B.5)). The formula is identical, but the area of the plate-stiffener combination differs from the area of the plate at plate level.

$$A \longrightarrow A_s = s_{s,eff} h_p + A_{HP}$$

### 1.2.3 Euler plate-stiffener buckling

The Euler plate-stiffener buckling stress (Equation (B.13)) must be determined, following Paik and Thayamballi [55, Chapter 2: Section 8], in order to check whether the minimum plate thickness is sufficient. It should be verified whether the stress does not outreach the critical Euler buckling value.

$$\sigma_s \leq \hat{\sigma}_E = \frac{P_E}{A} = \frac{\pi^2 EI_s}{\left(\frac{s_g}{2}\right)^2 (s_{s,eff} h_p + A_s)} \quad (\text{B.13})$$

where,

$$P_E \longrightarrow P_{E,s} = \frac{\pi^2 EI_s}{\left(\frac{s_g}{2}\right)^2}$$

### 1.2.4 Plate-stiffener deflection

The classification society [47] limits the the maximum plate-stiffener deflection. The deflection for the stiffeners may not be larger than the length of the stiffener divided by 800:  $\hat{\delta}_s = \frac{l}{800}$ . To calculate the deflection of the plate-stiffener combination, the Euler beam formulas are used.

$$\begin{aligned} \delta_s &= \frac{5ps_{s,eff} l^4}{384} < \hat{\delta}_s = \frac{l}{800} && \text{simply supported} \\ \delta_s &= \frac{ps_{s,eff} l^4}{384} < \hat{\delta}_s = \frac{l}{800} && \text{clamped} \end{aligned}$$

### 1.2.5 Shear force

The stiffener web (boundary) should carry the shear force when it is transferred to the girder. Equation (B.14) is valid to calculate the shear force. [55, Chapter 2: Section 6] In order to avoid that shear stress will be higher than the yielding shear stress of the stiffener  $\hat{\tau}_{y,s}$ , the minimum stiffener web height  $h_{w,s}$  is calculated. The formulas for the shear stress  $\hat{\tau}_y$  and the shear force  $Q$  are entered in the final formula.

$$F_s = A_{w,s}\tau_y = h_{w,s}t_{w,s}\hat{\tau}_y \longrightarrow h_{w,s} = \frac{Q}{t_{w,s}\hat{\tau}_y} \quad (\text{B.14})$$

where,

$$Q \longrightarrow Q_s = \frac{ps_g s_s}{2}$$

$$\hat{\tau}_y \longrightarrow \hat{\tau}_{y,s} = \frac{\hat{\sigma}_{y,s}}{\sqrt{3}}$$

## 1.3 Plate-girder level

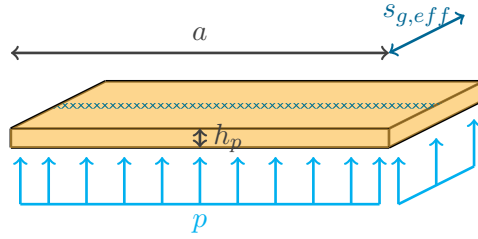


FIGURE B.5: Schematic semi-3-dimensional visualisation of the plate-girder level for the conventional solid material configuration. The hatched area reflects the location of the girder.

### 1.3.1 Effective girder spacing

Following the same approach for a plate-stiffener, the effective width  $s_{g,eff}$  of the girder spacing (Figure B.6) is examined: two approximations are studied and compared to the exact solution.

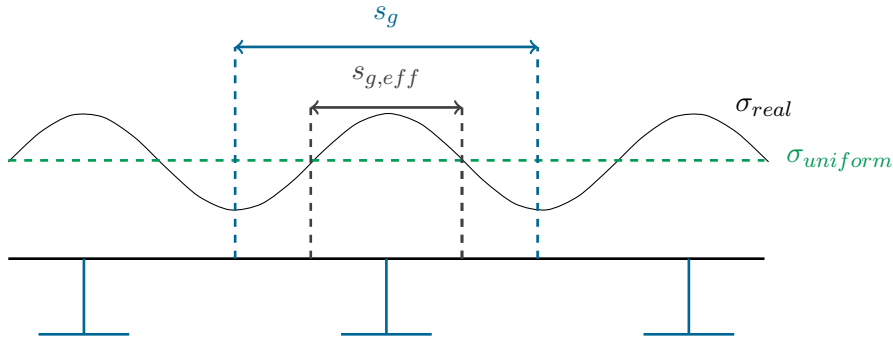


FIGURE B.6: Schematic presentation at the plate-girder level: girder spacing and effective width of the girder spacing, based on the shear lag effect.

The exact solution of Paik and Thayamballi [55] and the approximation of Paik and Thayamballi [55] and Lloyd's Register [47] are adapted for the effective girder spacing  $s_{g,eff}$ .

$$s_{g,eff} = \frac{4a \sinh\left(\frac{\pi a}{s_g}\right)}{\pi(1+\nu) \left[ (3-\nu) \sinh\left(\frac{2\pi a}{s_g}\right) - 2(1+\nu) \left(\frac{\pi a}{s_g}\right) \right]} \quad (\text{B.15})$$

Approximations:

$$s_{g,eff,PaikandThayamballi} [55] = \begin{cases} s_g & \text{for } \frac{s_g}{a} \leq 0.18 \\ 0.18a & \text{for } \frac{s_g}{a} > 0.18 \end{cases} \quad (\text{B.16})$$

$$s_{g,eff,Lloyd'sRegister} [47] = \min \left[ 0.3 \left( \frac{a}{s_g} \right)^{\frac{2}{3}} ; 1 \right] s_g \quad (\text{B.17})$$

In Figure B.7 all obtained results are plotted. It should be repeated that the exact solution has an incorrectness: the effective width  $s_{g,eff}$  can never be larger than the girder spacing  $s_g$ . From Figure B.7, it can be deduced that the simplification of Paik and Thayamballi [55] is the best fit to the exact solution.

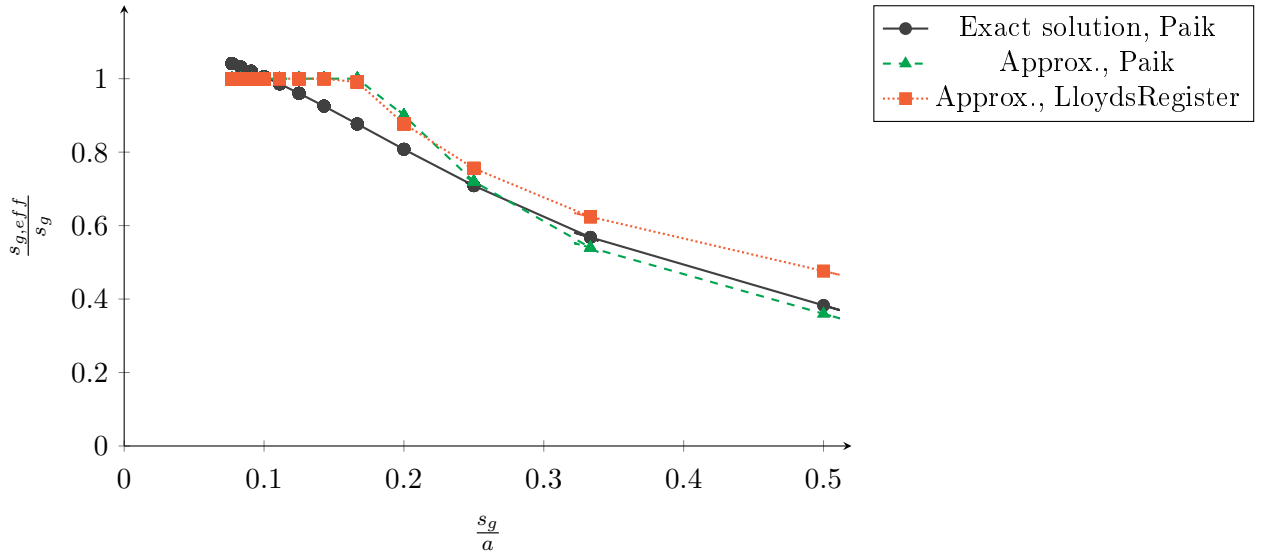


FIGURE B.7:  $\frac{s_g}{a}$  versus  $\frac{s_{g,eff}}{s_g}$ ; comparison of the exact solution given by Paik and Thayamballi [55] and the approximation formulas of Paik and Thayamballi [55] and Lloyd's Register [47].

### 1.3.2 Plate-girder yielding

At plate-girder level, only the bending stress must be taken into account, since orientation is perpendicular to the induced force by global bending. So no force originating from the global hull bending must be incorporated. Equation (B.11) is simplified. The beam bending formula for clamped boundaries can be used to calculate the bending stress  $\sigma_b$ . [79]. For the section modulus  $Z$ , the required girder section modulus as stated by [47] is used.

$$\sigma_g = \sigma_b = \frac{M}{Z} < \hat{\sigma}_{y,g} \quad (\text{B.18})$$

where,

$$\begin{aligned} M &\longrightarrow M_{gl} = \frac{pa^2 s_{g,eff}}{12} \\ Z &\longrightarrow \hat{Z}_g = 9.5a_{eff}^2 s_g D \cdot 10^{-3} \end{aligned}$$

### 1.3.3 Required section modulus

To determine the minimal required girder web height  $h_{w,g}$ , the required section modulus  $\hat{Z}_g$  as stated by Lloyd's Register [47] and the section modulus based on the geometry of the girder are set equal.

$$\hat{Z}_g = Z_g \quad (\text{B.19})$$

where,

$$\begin{aligned} Z_g &= \frac{I_g}{e_{outer,g}} \\ I_g &= \sum_i [I_{m,i} + e_{diff,i}^2 A_i] \\ A_{w,g} &= h_{w,g} t_{w,g} \\ A_{f,g} &= \frac{A_{w,g}}{2} \\ e_{outer,g} &= h_{w,g} \end{aligned}$$

### 1.3.4 Plate-girder deflection

To calculate the plate-girder deflection the same approach is used as the deflection at plate-stiffener level. Lloyd's Register [47] has a critical deflection for the girders:  $\hat{\delta}_g = \frac{a}{1000}$ . The deflection is also set as one of the criteria to calculate the minimum girder web height, one must ensure that the deflection is below the critical one.

$$\begin{aligned} \delta_g = \frac{5ps_{g,eff}l^4}{384} < \hat{\delta}_g = \frac{a}{1000} & \quad \text{simply supported} \\ \delta_g = \frac{ps_{g,eff}l^4}{384} < \hat{\delta}_g = \frac{a}{1000} & \quad \text{clamped} \end{aligned}$$

### 1.3.5 Girder shear buckling

The girder web has a corresponding girder web area, following the ENV 1993-1-1 1992 [29] to ensure the absence of shear buckling. Based on Paik and Thayamballi [55, Chapter 7: Section 2], Equation (B.20) is used because a transversal girder is modelled without intermediate transverse stiffeners over the full height of the girder. Since the minimum girder web height is calculated to satisfy the required section modulus, deflection and the shear force, the thickness is to be adapted to avoid shear buckling of the girder.

$$t_{w,g} \geq \frac{h_{w,g}}{69\epsilon} \quad (\text{B.20})$$

where,

$$\epsilon = \sqrt{\frac{235}{\hat{\sigma}_{y,g}}}$$

### 1.3.6 Shear force

The girder web (boundary) should carry the shear force that will be transferred to the sides of the ship. For this, Equation (B.21) is valid. [55, Chapter 2: Section 6] In order to check whether the developed shear stress will not be higher than the girder yielding shear stress  $\hat{\tau}_{y,g}$ , the minimum girder web height  $h_{w,g}$  is calculated, while implementing the formulas for the shear stress  $\hat{\tau}_y$  and the shear force  $Q$ . If the required girder web height  $h_{w,g}$  following the required section modulus

and the critical deflection is lower than the required girder web height  $h_{w,g}$  to carry the shear force, the required girder web height based on Equation (B.21) will be used, otherwise no change is present.

$$Q = A_{w,g}\hat{\tau}_y = h_{w,g}t_{w,g}\hat{\tau}_y \longrightarrow h_{w,g} = \frac{Q}{t_{w,g}\hat{\tau}_y} \quad (\text{B.21})$$

where,

$$\begin{aligned} Q &\longrightarrow Q_g = \frac{ps_g a}{2} \\ \hat{\tau}_y &\longrightarrow \hat{\tau}_{y,g} = \frac{\hat{\sigma}_{y,g}}{\sqrt{3}} \end{aligned}$$

## 1.4 Panel level

### 1.4.1 Natural frequency

To calculate the natural frequency (at first mode), the Rayleigh solving method has been proven to be a reliable solution. In this approximate energy method, the maximum kinetic energy of the plate [zero displacement] is set equal to the maximum potential energy of the plate [maximum displacement]. Because no energy is lost, damping of the system is also absent.

The method is based on the small deflection theory, which includes the following assumptions: elastic, homogeneous and isotropic material, small deflections, the middle of the plane of the plate does not stretch and the cross section is always perpendicular to the middle surface of the plate.

The stiffened panel will be further approximated using the orthotropic plate theory, which includes that the flexural rigidities differ in every principle direction of the plate. The major difference with an isotropic plate is the derivation of the flexural and torsional rigidities. According to Schaefer [65] the main formula for the dry circular frequency  $\omega$  is given by Equation (B.22). Based on hierarchy, it must be assumed that the boundaries of the stiffened panel, namely the bulkheads, remain stiff, and therefore must be considered clamped. To calculate the natural frequency, the circular frequency  $\omega$  must be divided by  $2\pi$ .

$$f = \frac{\omega}{2\pi} = \frac{1}{2\pi\sqrt{\rho h_{p,eq}}} \left[ D_x \left( \frac{C_A}{l} \right)^4 + 2H \left( \frac{C_C}{a^2 l^2} \right) + D_y \left( \frac{C_B}{a} \right)^4 \right]^{\frac{1}{2}} \quad (\text{B.22})$$

where,

$$\begin{aligned} C_A &= 4.73 && 4 \text{ edges are clamped} \\ C_B &= 4.73 && 4 \text{ edges are clamped} \\ C_C &= 151.3 && 4 \text{ edges are clamped} \\ D_x &= \frac{Eh_p^3}{12(1-\nu^2)} + \frac{Eh_p e_x^2}{(1-\nu^2)} + \frac{EI_s}{s_s} && \text{crossed stiffened} \\ D_y &= \frac{Eh_p^3}{12(1-\nu^2)} + \frac{Eh_p e_y^2}{(1-\nu^2)} + \frac{EI_g}{s_g} && \text{crossed stiffened} \\ H &= \frac{Eh_p^3}{12(1-\nu^2)} + \frac{G}{6} \left( \frac{h_{i,s} t_{i,s}^3}{s_s} + \frac{h_{i,g} t_{i,g}^3}{s_g} \right) && \text{crossed stiffened} \\ h_{p,eq} &= h_p + \frac{nA_{HP}}{s_s} + \frac{q(A_{w,g} + A_{f,g})}{s_g} && \text{crossed stiffened} \end{aligned}$$

The definition of  $e_x$  and  $I_s$  are given below for the stiffener based in Figure B.8. For  $e_y$  and  $I_g$  the same approach is valid but applied on the girder instead of the stiffener.

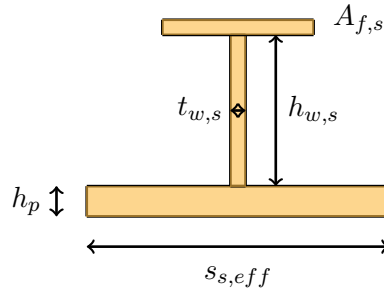


FIGURE B.8: *Plate-girder combination: base plate = conventional solid; stiffener = conventional solid*

$$I_s = \frac{t_{w,s} h_{w,s}^3}{12} + A_{w,s} \left( e_s - \frac{h_{w,s}}{2} \right)^2 + \frac{t_{f,s} h_{f,s}^3}{12} + A_{w,s} \left( h_{w,s} + \frac{h_{f,s}}{2} - e_s \right)^2$$

$$e_x = \frac{n A_s \left( e_x + \frac{h_p}{2} \right)}{a h_p + n A_s}$$

where,

$$A_s = A_{w,s} + A_{f,s}$$

$$e_s = \frac{\frac{t_{w,s} A_{w,s}}{2} + \left( \frac{h_{f,s}}{2} + h_{w,s} \right) A_{f,s}}{A_s}$$

## 2 Design constraints for sandwich material

### 2.1 Plate level

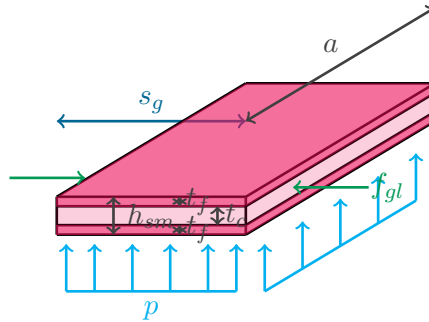


FIGURE B.9: *Schematic semi-3-dimensional visualisation of the plate level for the sandwich material design.*

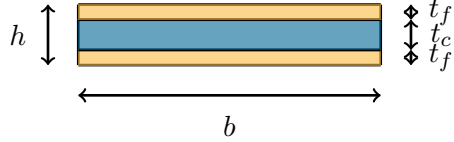
#### 2.1.1 Face sheet yielding

At plate level, both bending stress and membrane stress must be taken into account. Since both stresses have the same orientation, a summation of the stresses is applicable (Equation (B.11)).

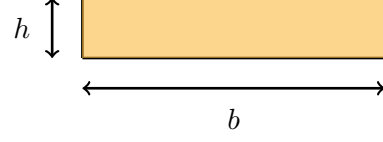
As long as the face sheet stress  $\sigma_f$  is lower than the allowable face sheet yielding stress  $\hat{\sigma}_{y,f}$ , face sheet yielding will not be present.

To calculate the bending stress  $\sigma_b$  the plate bending formulas of Young and Budynas [79] are used, for a uniform loading over the entire plate. Since these formulas are applicable on conventional solid plates, the adapted formulas for sandwich materials should be derived: three formulas for two different boundary conditions and locations. The specific values for the factor  $\beta$ ,  $\beta_1$  and  $\beta_2$  are given by Table B.1. The plate orientation is the same;  $x$  represents the longer side of the plate, while  $y$  is the shorter side of the plate.

----- BEGIN OF DERIVATION -----



(A) *Sandwich material*



(B) *Conventional solid material*

Following Young and Budynas [79], the maximum bending stress of a conventional solid material plate is determined using the following formulas, depending on the boundary conditions.

$$\begin{aligned} \sigma_b &= \frac{\beta p b^2}{h^2} = \frac{M}{Z} && \text{at center} && \text{simply supported} \\ \sigma_b &= \frac{\beta_1 p b^2}{h^2} = \frac{M}{Z} && \text{at center of long edge} && \text{clamped} \\ \sigma_b &= -\frac{\beta_2 p b^2}{h^2} = \frac{M}{Z} && \text{at center} && \text{clamped} \end{aligned}$$

The section modulus  $Z$  will vary for a conventional solid plate and a sandwich material plate. However, it is assumed that the moment  $M$ , exerted on the plate, will not change.

For a conventional solid material plate, the section modulus  $Z_p$  is as follows:

$$Z_p = \frac{b h^3}{12} \frac{2}{h} = \frac{b h^2}{6}$$

Substituting the formulation for the section modulus of the conventional solid plate  $Z_p$  into the aforementioned maximum bending stress equation, the formulation for the constant moment  $M$  is found.

$$\begin{aligned} M &= \sigma_b Z = \frac{\beta p b^2}{h^2} \frac{b h^2}{6} = \frac{\beta p b^3}{6} && \text{at center} && \text{simply supported} \\ M &= \sigma_b Z = \frac{\beta_1 p b^2}{h^2} \frac{b h^2}{6} = \frac{\beta_1 p b^3}{6} && \text{at center of long edge} && \text{clamped} \\ M &= \sigma_b Z = -\frac{\beta_2 p b^2}{h^2} \frac{b h^2}{6} = -\frac{\beta_2 p b^3}{6} && \text{at center} && \text{clamped} \end{aligned}$$

For a sandwich material plate, the section modulus  $Z_{sm}$  is as follows:

$$Z_{sm} = b t_f h$$

Substituting the formulation for the section modulus of the sandwich material plate  $Z_{sm}$  and the moment  $M$  formulation into the stress equations, the maximum bending stress in a sandwich material plate is obtained:

$$\begin{aligned}
\sigma_b &= \frac{\beta p b^3}{6 t_f h} = \frac{\beta p b^2}{6 t_f h_{sm}} && \text{at center} && \text{simply supported} \\
\sigma_b &= \frac{\beta_1 p b^3}{6 t_f h} = \frac{\beta_2 p b^2}{6 t_f h_{sm}} && \text{at center of long edge} && \text{clamped} \\
\sigma_b &= \frac{-\beta_2 p b^3}{6 t_f h} = -\frac{\beta_1 p b^2}{6 t_f h_{sm}} && \text{at center} && \text{clamped}
\end{aligned}$$

---

END OF DERIVATION

---

The membrane stress  $\sigma_m$  is determined following the same approach as for the conventional solid material plate, where  $m$  denotes the number of bulkheads in longitudinal direction.

$$\sigma_m = \frac{F}{A} = \frac{M_{gl}}{D(m+1)2t_f a}$$

where,

$$\begin{aligned}
F &\longrightarrow f_{gl} = \frac{F_{gl}}{(m+1)} \\
&F_{gl} = \frac{M_{gl}}{D} \\
A &\longrightarrow A_{sm} = 2t_f a
\end{aligned}$$

### 2.1.2 Euler plate buckling

The elastic plate buckling force  $\hat{f}_E$  of the sandwich material is calculated using Equation (B.23). From the buckling load the minimum required effective plate thickness ( $2t_f$ ) can be derived. As long as the face sheet plate stress  $\sigma_f$  is lower than the calculated critical Euler plate buckling stress, overall buckling is not present. [55, Chapter 3: Section 6,9] [55, Chapter 5]

$$f_{gl} \leq \hat{f}_E = \frac{\pi^2 E t_f h_{sm}^2}{2(1-\nu_f^2)a} K_1 \longrightarrow C_1 t_f^3 + C_2 t_f^2 + C_3 t_f + C_4 \quad (\text{B.23})$$

where,

$$\begin{aligned}
K_1 &= \frac{\left(\frac{a}{b} + \frac{b}{a}\right)^2}{1 + \psi \left(\frac{a^2}{b^2} + 1\right)} \\
\psi &= \frac{\pi^2 E t_f h_{sm}}{2(1-\nu_f^2) G a} \\
C_1 &= 4\pi^2 E \left(\frac{a}{b} + \frac{b}{a}\right)^2 \\
C_1 &= 4\pi^2 E t_c \left(\frac{a}{b} + \frac{b}{a}\right)^2 - \frac{2f_{gl}\pi^2 E}{G a} \left(\frac{a^2}{b^2} + 1\right) \\
C_1 &= \pi^2 E t_c^2 \left(\frac{a}{b} + \frac{b}{a}\right)^2 - \frac{f_{gl}\pi^2 E t_c}{G a} \left(\frac{a^2}{b^2} + 1\right) \\
C_1 &= -2(1-\nu_f^2) a f_{gl}
\end{aligned}$$

### 2.1.3 Face sheet wrinkling

The critical wrinkling instability stress is determined by Equation (B.24); the buckling coefficient  $C_w$  depends on the Poisson's ratio of the core  $\nu_c$ . [1, Chapter 8] As long as the stress is lower than the calculated critical wrinkling stress  $\hat{\sigma}_{wr,f}$ , face wrinkling will not be present.

$$\hat{\sigma}_{wr,f} = C_w E_f^{\frac{1}{3}} E_c^{\frac{2}{3}} \quad (\text{B.24})$$

where,

$$C_w = 3 [12(3 - \nu_c)^2(1 + \nu_c)^2]^{-\frac{1}{3}}$$

### 2.1.4 Plate shear

The formula for a homogeneous material (Equation (B.7)) must be modified to take the contribution of the Young's Moduli of the different layers into account, yielding Equation (B.25), to calculate the shear stress in a sandwich material. The maximum shear stress  $\tau_p$  is located at the neutral axis. As long as the core shear stress  $\tau_c$  and face sheet shear stress  $\tau_f$  are lower than the allowable core yielding shear strength  $\hat{\tau}_{y,c}$  and allowable core yielding shear strength  $\hat{\tau}_{y,f}$ , core and face sheet shear will not be present.

----- BEGIN OF DERIVATION -----

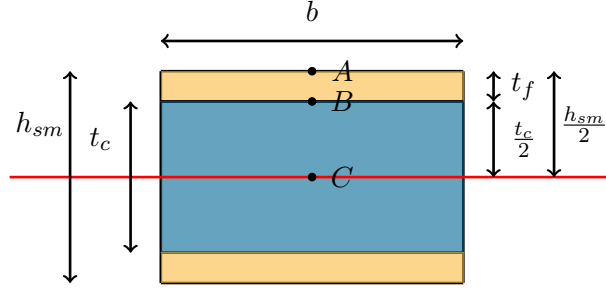


FIGURE B.11: Schematic visualisation for derivation of plate shear formula.

$$\tau_{sm} = \frac{Q}{EIb} \sum SE = \begin{cases} \tau_f = \frac{Q}{EI_{sm}b} SE_B \leq \hat{\tau}_{y,f} \\ \tau_c = \frac{Q}{EI_{sm}b} SE_C \leq \hat{\tau}_{y,c} \end{cases} \quad (\text{B.25})$$

where,

$$\begin{aligned} Q &\longrightarrow Q_{sm} = \frac{pasg}{2} \\ SE &\longrightarrow SE_A = 0 \\ &SE_B = E_f b t_f \left( \frac{h_{sm} - t_f}{2} \right) \\ &SE_C = E_f b t_f \left( \frac{h_{sm} - t_f}{2} \right) + E_c \frac{b}{2} \left( \frac{t_c}{2} \right)^2 \\ EI &\longrightarrow EI_{sm} = \frac{E_c b t_c^3}{12} + \frac{E_f b t_f^3}{6} + \frac{E_f b t_f \left( \frac{h_{sm} - t_f}{2} \right)^2}{2} \end{aligned}$$

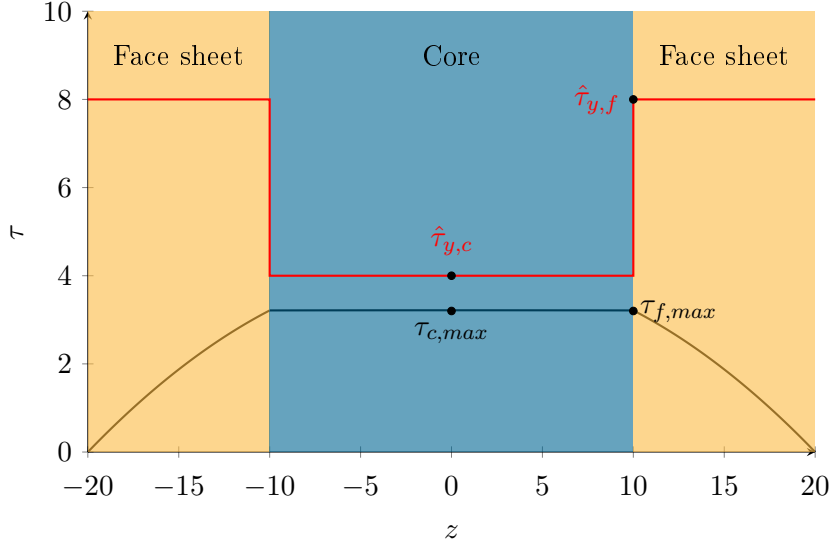


FIGURE B.12: Shear stress distribution for sandwich material according to Equation (B.26), for  $Q = 100$  [N],  $b = 1$  [mm],  $t_f = 20$  [mm],  $t_c = 20$  [mm],  $E_f = 210000$  [MPa] and  $E_c = 670$  [MPa], including the critical shear stress distribution. No shear failure:  $\tau_{c,max} \leq \hat{\tau}_{y,c}$  [core] and  $\tau_{f,max} \leq \hat{\tau}_{y,f}$  [face sheet]

To sketch the shear stress distribution in the sandwich material, the formulas for the change in range  $[\frac{t_c}{2}, \frac{h_{sm}}{2}]$  and  $[0, \frac{t_c}{2}]$  with respect to the neutral axis ( $z = 0$ ), need to be derived, using the general formula given by Equation (B.25), resulting in Equation (B.26), visualised in Figure B.12.

$$\tau_{sm} = \begin{cases} \tau_f = \frac{Q}{EI_{sm}b} \left[ E_f \frac{b}{2} \left( \left( \frac{h_{sm}}{2} \right)^2 - z^2 \right) \right] & \text{for } z = \left[ \frac{t_c}{2}, \frac{h_{sm}}{2} \right] \\ \tau_c = \frac{Q}{EI_{sm}b} \left[ E_f b t_f \frac{h_{sm} - t_f}{2} + E_c \frac{b}{2} \left( \left( \frac{t_c}{2} \right)^2 - z^2 \right) \right] & \text{for } z = \left[ 0, \frac{t_c}{2} \right] \end{cases} \quad (\text{B.26})$$

According to Crupi et al. [18], Zu et al. [81] and Petras [59], the core absorbs the most significant part of the shear load for sandwich materials with thin face sheets with respect to the core thickness, because the maximum shear force is located at the neutral axis. In this case, only the core area is taken into account to incorporate the load, as defined by Equation (B.27). However, since no limitation is implemented to meet the requirement of having thin face sheets, this assumption will not be used, and the contribution of the face sheets will be taken into account.

$$\tau_{sm} = \frac{Q}{EI_{sm}b} \left[ E_f b t_f \frac{h_{sm} - t_f}{2} + E_c \frac{b}{2} \left( \left( \frac{t_c}{2} \right)^2 - z^2 \right) \right] \rightarrow \frac{Q}{b t_c} \quad (\text{B.27})$$

In the formula of the shear stress  $\tau_{sm}$  of the sandwich material three terms are negligible. First, the contribution of the bending stiffness of the core can be neglected, because its magnitude is small due to the low elasticity modulus of the core  $E_c$ . The latter is applicable on the first term of the equivalent rigidity  $EI_{sm}$  and the second term of the first moment of inertia times the Young's Modulus. Second, the term  $t_f^3$  {term 3} of the equivalent rigidity is only significant in case of thick face sheets. The term is omitted because of the use of a sandwich material with thin/moderate face sheets. [12] [1, Chapter 10]

$$\begin{aligned}
E_f \gg E_c &\longrightarrow \text{neglect term1 : } \frac{E_c b t_c^3}{12} \\
&\longrightarrow \text{neglect term2 : } E_c \frac{b}{2} \left(\frac{t_c}{2}\right)^2 \\
\frac{h_{sm}}{t_f} > 5.77 &\longrightarrow \text{neglect term3 : } \frac{E_f b t_f \left(\frac{h_{sm}-t_f}{2}\right)^2}{2}
\end{aligned} \tag{B.28}$$

---

END OF DERIVATION

---

## 2.2 Plate-girder level

The plate-girder level of the sandwich material design is identical to that of the conventional solid material configuration (see Section 1.3).

## 2.3 Panel level

### 2.3.1 Natural frequency

The main formula for the natural frequency  $f$  as given in Section 1.4 for the conventional solid material is still applicable for the sandwich material design (Equation (B.29)), only the flexural rigidity and torsional terms  $D_x$ ,  $D_y$ ,  $H$  will differ. Below the formulation for the sandwich material design is given.

$$f = \frac{\omega}{2\pi} = \frac{1}{2\pi\sqrt{\rho h_{sm,eq}}} \left[ D_x \left(\frac{C_A}{l}\right)^4 + 2H \left(\frac{C_C}{a^2 l^2}\right) + D_y \left(\frac{C_B}{a}\right)^4 \right]^{\frac{1}{2}} \tag{B.29}$$

where,

$$\begin{aligned}
C_A &= 4.73 && 4 \text{ edges are clamped} \\
C_B &= 4.73 && 4 \text{ edges are clamped} \\
C_C &= 151.3 && 4 \text{ edges are clamped} \\
D_x &= \frac{E(2t_f)^3}{12(1-\nu^2)} && \text{uni-directional stiffened} \\
D_y &= \frac{E(2t_f)^3}{12(1-\nu^2)} + \frac{E(2t_f)e_y^2}{(1-\nu^2)} + \frac{EI_g}{s_g} && \text{uni-directional stiffened} \\
H &= \frac{E(2t_f)^3}{12(1-\nu^2)} + \frac{G}{6} \left(\frac{h_{i,g}t_{i,g}^3}{s_g}\right) && \text{uni-directional stiffened} \\
h_{sm,eq} &= h_{sm} + \frac{u(A_{w,g} + A_{f,g})}{s_g} && \text{uni-directional stiffened}
\end{aligned}$$

The parameters  $e_y$  and  $I_g$  are calculated following the same method as presented in Figure B.8 for the stiffener, but with a sandwich material as baseplate.

## 3 Input for cost calculation model

### 3.1 Production costs

The production process of a vessel is characterised by two main phases: the first phase consists of the welding of the hull components, in particular the hull plating and the hull stiffener components, and the second phase regards the paint cover of the construction to prevent corrosion.

Based on given financial data from DAMEN corresponding the Crane Barge 6324, the weld price and paint price per ton are given by Table B.2.

TABLE B.2: *Production cost data corresponding the Crane Barge 6324*

Weld price	$C_{weld}$	971	[€/ton]
Paint price	$C_{paint}$	241	[€/ton]

To obtain an objective comparison of the stiffened panel constructed with a sandwich material base plate with respect to a conventional solid material plate, the weld prices must be expressed in [€/V<sub>weld</sub>] and the painting price must be expressed in [€/A<sub>paint</sub>]. To create a single price value, the original configuration of the DAMEN SPo12032 will be used:

### Stan Pontoon (SPo) 12032

General characteristics stiffened panel

Bulkhead spacing transversal	$l$	10909	[mm]
Bulkhead spacing longitudinal	$a$	5367	[mm]
Stiffener spacing	$s_g$	488	[mm]
Stiffener amount	$n$	10	[mm]
Stiffener profile	–	HP200x9	[mm]
Girder spacing	$s_g$	2182	[mm]
Girder amount	$q$	4	[mm]
Girder profile	–	T-profile	[-]
Girder web height	$h_{w,g}$	600	[mm]
Girder web thickness	$t_{w,g}$	14	[mm]
Girder flange height	$h_{f,g}$	17	[mm]
Girder flange thickness	$t_{f,g}$	250	[mm]

#### 3.1.1 Weld seam volume

To calculate the weld seam volume  $V_{weld}$  of the total stiffened panel, first the required fillet weld size must be calculated. According to Blodgett [10], the required weld leg size can be determined using Equation (B.30). Three assumptions are applicable: (1) fillet weld on both sides of the plate, (2) fillet weld for the full length of the plate and (3) if the plates have a different thickness, the thinner plate thickness should be used.

$$t_{weld} = \frac{3}{4}h_{min} \longrightarrow A_{weld} = \frac{\left(\frac{3}{4}h_{min}\right)^2}{2} \quad (\text{B.30})$$

where,

$$h_{min} = \begin{cases} \min[h_p; t_{w,g}] & \text{for weld T-profile to base plate} \\ \min[t_{w,g}; t_{f,g}] & \text{for weld T-profile intern} \end{cases}$$

Thereafter, the weld seam volume for the total stiffened panel can be obtained using Equation (B.31). Since the stiffener profiles are Holland Profiles, only two welds need to be performed,

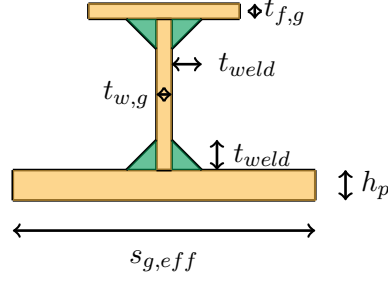


FIGURE B.13: Schematic representation of the fillet weld size  $t_{weld}$ .

while for the girder still 4 welds are required due to the T-shape of the profile. The plate itself does not need additional intermediate welding. For design of the stiffened conventional solid material panel using the SPo12032 data, a weld seam volume of  $0.0097 \text{ [m}^3\text{]}$  is obtained.

$$V_{weld} = 4qaA_{weld} + 2nlA_{weld} \quad (\text{B.31})$$

### 3.1.2 Paint area

To calculate the paint area  $A_{paint}$  of the total stiffened panel, Equation (B.32) is applicable, where  $Al_{HP}$  denotes the circumference of the Holland Profile. The plate needs a coating at both sides, and the stiffeners and girders need a coating for the full circumference. The design of the stiffened conventional solid material panel using the SPo12032 data has a paint area of  $1230.29 \text{ [m}^2\text{]}$ .

$$A_{paint} = 2al + nlAl_{HP} + qa(2h_{w,g} + 2h_{f,g} + t_{f,g}(1 - t_{w,g})) \quad (\text{B.32})$$

Since the prices are expressed in  $[\text{€}/\text{ton}]$ , also the weight of the original stiffened panel must be determined, according to Equation (B.33). The weight of  $11.91 \text{ [ton]}$  is obtained of the original design of the stiffened panel.

$$W = \rho_p [alh_p] + \rho_s [nlAl_{HP}] + \rho_g [qa(h_{w,g}t_{w,g} + h_{f,g}t_{f,g})] \quad (\text{B.33})$$

The final production cost data, expressed in  $[\text{€}/\text{mm}^3]$ , are calculated using the above mentioned formulas.

TABLE B.3: Production cost data corresponding the Crane Barge 6324.

Weld price	$C_{weld}$	$1.20 \cdot 10^{-3}$	$[\text{€}/\text{mm}^3]$
Paint price	$C_{paint}$	$2.33 \cdot 10^{-5}$	$[\text{€}/\text{mm}^2]$

## 3.2 Operational costs

The operational cost during the life time of a ship is characterised by two main components: on the one hand the fuel cost for exploiting and on the other hand the cost regarding maintenance and repair of the ship. Since the maintenance cost is difficult to measure, only the fuel costs will be considered. Based on given financial data from DAMEN, the average fuel consumption and the annually total operating hours are shown in Table B.2 applicable for the Stan Patrol 5009. To calculate the fuel consumption cost, the average fuel consumption is multiplied with the sum of operating hours per calendar year, and the current bunker price for diesel. The current bunker price in the Netherlands is set at  $0.42 \text{ [€}/\text{l}]$ . The operational life time of a vessel is approximately  $20 \text{ [yr]}$ , but to incorporate an early retirement, the service life is set at  $15 \text{ [yr]}$ . Therefore the

TABLE B.4: *Fuel cost data corresponding the Stan Patrol 5009*

Average fuel consumption	109	[l/hr]
Total operating hours	790	[hr/yr]

total fuel consumption cost is the sum of the annual fuel consumption costs for 15 [yr]. The total fuel consumption cost per kilogram is derived by dividing the total fuel consumption cost by the displacement of the Stan Pontoon 5009, which is set at 400 [ton].

TABLE B.5: *Fuel cost data corresponding the Stan Patrol 5009*

Total fuel consumption cost		36261.25	[€/15yr]
Total fuel consumption cost per kilogram	$C_{fuel}$	5.44	[€/15yr/kg]

# Supplement C |

## 1 Test machine specification

### 1.1 Analytical model

For the analytical calculation, two situations need to be considered: (1) The solid rollers will touch the bottom of the notch and (2) the solid rollers will not touch the bottom of the notch. Both force distribution will lead to a difference in the normal stress present in the mid section of the block.

#### 1.1.1 Situation 1: The solid rollers touch the bottom of the notch

To determine the maximum stress present in the mid section of the block, the maximum bending moment is determined using the force distribution (Equation (C.1)). The mid section of the modification block is characterised by the effective height, in particular the total height minus the height of the central roller notch and the upper roller notch.

$$\sigma_{max} = \frac{M_{max}}{Z} = \frac{M_{max}e_{outer}}{I} = \frac{3Fd_1}{wh_{eff}^2} = 23 \quad [\text{MPa}] \quad (\text{C.1})$$

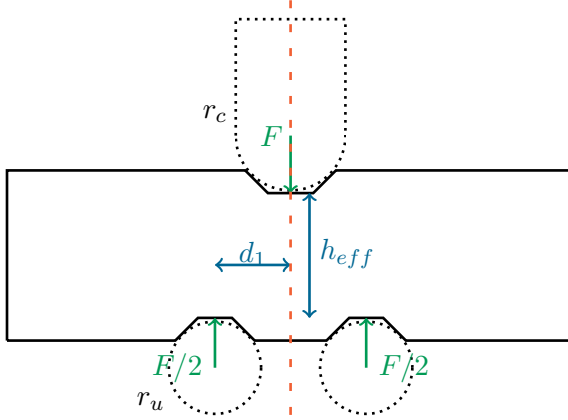


TABLE C.1: *Parameter values*

Force	$F$	25000	[N]
Lever	$d_1$	20	[mm]
Height	$h_{eff}$	33	[mm]
Width	$w$	60	[mm]
Radius central roller	$r_c$	15	[mm]
Radius upper roller	$r_u$	12.5	[mm]

FIGURE C.1: *Force distribution when the solid rollers touch the bottom of the notch.*

#### 1.1.2 Situation 2: The solid rollers do not touch the bottom of the notch

The main difference is that the effective height  $h_{eff}$  of the mid section of the modification block is increased, and the maximum moment  $M_{max}$  is reduced, since the lever is reduced with the distance  $d_3$ . This results in a lower maximum bending stress  $\sigma_{b,max}$  in the mid section (Equation (C.2)). Furthermore, a constant maximum bending moment is created between the two contact points of the central solid roller with the modification block.

$$\sigma_{b,max} = \frac{M_{max}}{Z} = \frac{M_{max}e_{outer}}{I} = \frac{3F \left( \frac{d_1+d_2}{2} - d_3 \right)}{wh_{eff}^2} = 8 \quad [\text{MPa}] \quad (\text{C.2})$$

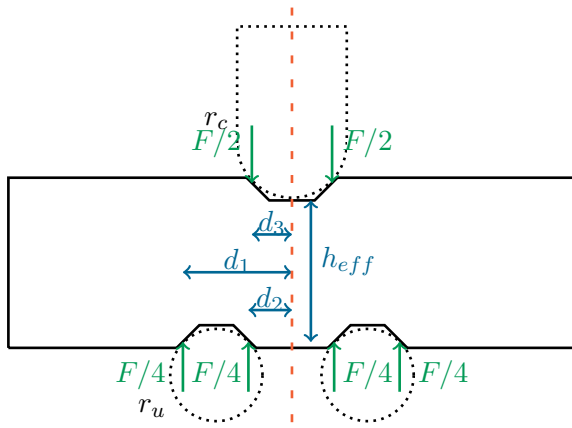


FIGURE C.2: Force distribution when the solid rollers not touch the bottom of the notch.

TABLE C.2: Parameter values

Force	$F$	25000	[N]
Lever	$d_1$	28.84	[mm]
	$d_2$	11.16	[mm]
	$d_3$	10.61	[mm]
Height	$h_{eff}$	37.43	[mm]
Width	$w$	60	[mm]
Radius central roller	$r_c$	15	[mm]
Radius upper roller	$r_u$	12.5	[mm]

## 1.2 Finite element model

A two dimensional (2D) FEM calculation is performed in *Ansys APDL 17.1* to check the stress distribution and the deformation of the modification block. Both the modification block and the central and upper rollers are modelled. Following the element description of *Ansys*, *PLANE42*-elements are used for the geometry of the block and the rollers. A non-linear calculation is conducted due to the use of contact elements, which are placed between the contact areas of the modification block and the rollers. For the contact area, *CONTA171*-elements are chosen, since this element is applicable to 2D structural and coupled-field contact analyses. These elements will be attached to the outer nodes of the solid rollers. Since pair-based contact is applicable, *TARGE169*-elements must be chosen to define the target area, in particular the notches of the modification block. The contact elements are characterised in the model in that way the contact area is bonded in all direction. For the target elements, no deformation and rotation restrictions are imposed. A point load is placed in the centroid of the center solid roller. The two upper rollers are constraint in both x- and y-direction. The central roller is only constrained in x-direction to allow a vertical displacement.

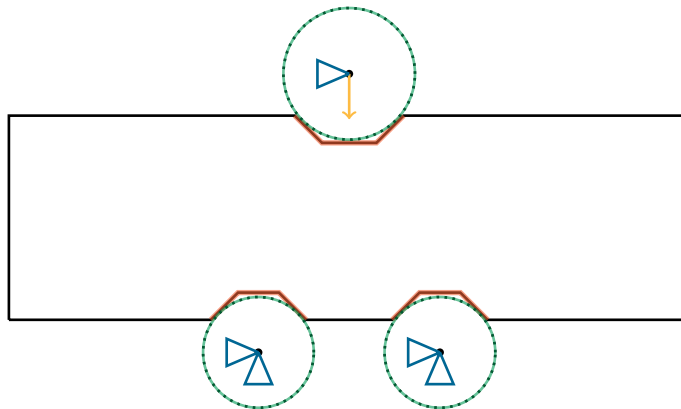


FIGURE C.3: Schematic visualisation of the contact area (green), the target area (red), the loading condition (yellow) and the boundary constraints (blue) of the modification block implemented in FEM.

Looking at the overall modification block, the critical spots are located at the contact points between the modification block and the solid rollers, as presented in Figure C.4a and Figure C.4b. It is visible that the rollers not touch the bottom of the notch. It is therefore expected that the stress in the mid section lies around the calculated stress in situation 2 of the analytical model.

Based on Figure C.4c, the stress range lies around the expected 8 [MPa].

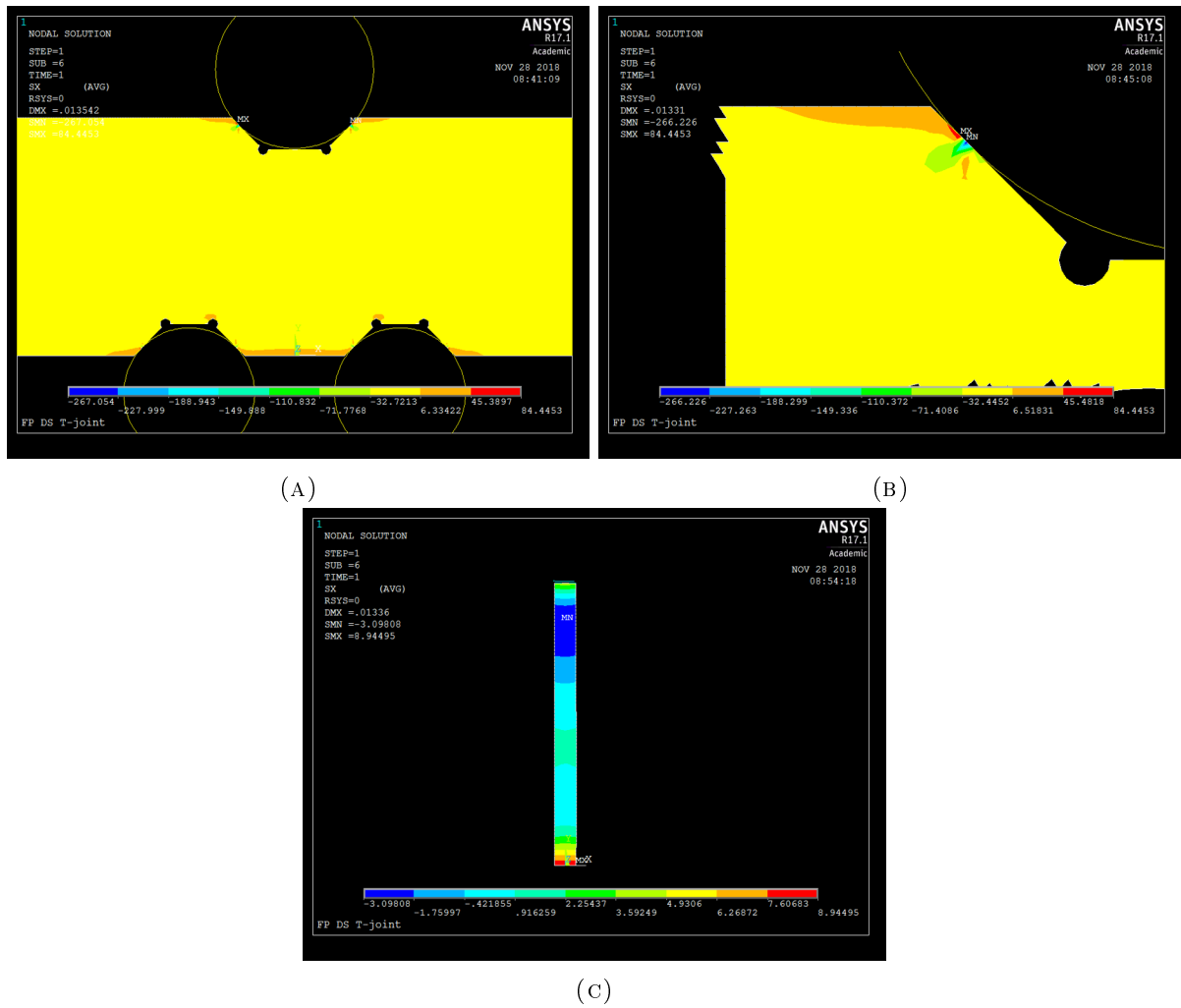


FIGURE C.4: Stress distribution calculated using FEM in the modification block. (A) overall view, (B) detail view and (C) strip of mid section of modification block. The inconsistencies at the edges of the detailed view (B) are due to the chosen element mesh, and element orientation.

## 2 Estimation of required force

To obtain fracture at a desired number of life cycles, a force range consisting of a minimum and maximum force value must be given to the test machine for causing a cyclic loading. These force values can be obtained following the SN-curve. For a chosen amount of life cycles, a given stress range  $S$  follows using the SN-relation (Equation (C.3)). The FAT Class curve from the recommendation of the IIW [40] which belongs to the right structural detail, can be used as given SN-curve. To determine the minimum and maximum stress, a chosen load ratio  $r_l$  is used. The load ratio  $r_l$  is the ratio between the minimum stress and the maximum stress and indicates if the load is in tension, compression or a combination of both. To obtain the forces that are required to give these minimum and maximum stress as result, the load set-up must be used for the conversion of the stress to the force that must be exerted by the test machine.

$$\log N = \log C - m \log S \quad (\text{C.3})$$

## 2.1 Method 1: Up-scaling the FAT Class curve of an arc welded DS T-joint

To estimate the actual required force, the fatigue data of Costa et al. [17] for a butt-joint made of the aluminium alloy 5083-H111 are used as starting-point. Costa et al. has compared the fatigue data of a FSW butt-joint to data of the conventional arc welding technique, of which the results are shown in Figure C.5.

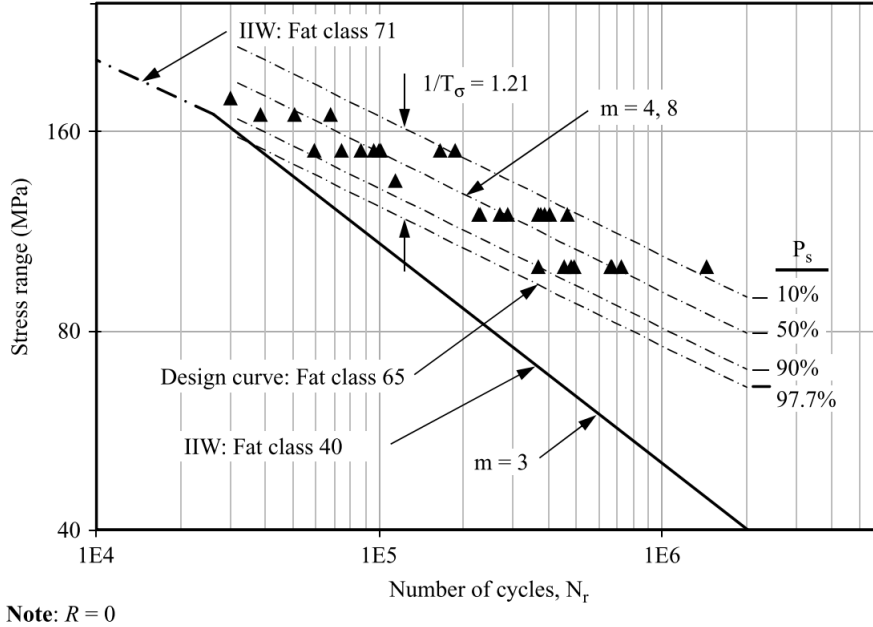


FIGURE C.5: Comparison by Costa et al. [17] for a butt-joint made of aluminium alloy, welded by friction stir welding and by the conventional arc welding technique.

As stated by the recommendations of the IIW [40], the parent material has a FAT class of 71, with the slope factor  $m = 5$ , while the butt-joint welded by the conventional arc welding technique follows FAT40 with the slope factor  $m = 3$ . FAT class curves are design curves and reflect a reliability of 97.7%. Following the fatigue results of a FSW butt-joint, the FAT class could be increased to FAT65 with the slope factor  $m = 4.8$ . As for the DS T-joint the same relation is expected between both welding techniques, the required force is calculated using the given ratio of the butt-joint following Costa et al. [17]. Thereafter, the FAT class and subsequently the required force range, linked to a DS arc-welded T-joint, will be multiplied by the obtained ratio for the estimation of the required force in case of a FSW DS T-joint.

For FAT class design curves is applicable that the value corresponds to the stress level at  $2 \cdot 10^6$  life cycles. Combining this fact with Equation (C.3), the constant value of  $\log C$  can be determined for both FAT40 and FAT65, resulting in 11.1 and 15.0 respectively. Using the value of  $\log C$  and the slope value  $m$ , the stress ranges  $S$  can be calculated. Costa et al. [17] used a tensile load test set-up, so to obtain the forces that are required to give these minimum and maximum stress as result, the stress value must be multiplied with the sectional area that goes into the grabber of the test machine. For Costa et al. [17] this area is equal to 60 [mm<sup>2</sup>].

Since the design curves reflect a reliability of 97.7% is it desired to calculate the force to create a mean curve with a 50% reliability, since it would be the curve representing the average location of the obtained data points (Equation (C.4)).  $\sigma_{cl}$  represents the standard deviation according to the confidence level and is set equal to a common value 0.3.  $p_s$  reflects the probability of survival required to shift the curve to the intended reliability,  $p_s = 50 - (97.7 - 50) = 2.3$ . Table C.3

follows.

$$\left. \begin{aligned} \log N &= \mu + \Phi(1 - p_s)\sigma_{cl} \\ \mu &= \log C - m \log S \end{aligned} \right\} \rightarrow \log S = \frac{\log N - \log C - \Phi(1 - p_s)\sigma_{cl}}{-m} \quad (\text{C.4})$$

TABLE C.3: Force calculation (50% reliability) for butt-joint specimen of the study of Costa et al. [17], leading to the ratio of the friction stir welding and arc welding,  $r_l = 0$

$N$	Arc welding					Friction stir welding					ratio
	$S_{97.7}$	$S_{50}$	$\Delta F_{50}$	$F_{50,min}$	$F_{50,max}$	$S_{97.7}$	$S_{50}$	$\Delta F_{50}$	$F_{50,min}$	$F_{50,max}$	
$10^4$	234	370	22221	0	22221	196	261	15673	0	15673	1.42
$10^5$	109	172	10314	0	10314	121	162	9701	0	9701	1.06
$10^6$	50	80	4787	0	4787	75	100	6005	0	6005	0.80
$10^7$	23	37	2222	0	2222	46	62	3717	0	3717	0.60

For the DS T-joint, FAT28 ( $m = 3$ ) is found to be the design curve for arc welding following the recommendations of the IIW [40]. Based on the found ratio to obtain the mean curve for the FSW version (Table C.3), an estimation of the force can be made that must be exerted in the test machine. Using Equation (C.3) a value for  $\log C = 10.6$  is obtained. For the estimated SN-curve for the FSW DS T-joint, the same slope value of Costa et al. [17] is used,  $m = 4.8$ . For the DS T-joint a four-point bending set-up will be used, therefore for the stress conversion to the required force Equation (C.5) must be maintained, using Figure C.6 and the parameter values as presented in Table C.4. Table C.5 shows the required stress and force range.

$$\sigma_b = \frac{M}{Z} = \frac{M e_{outer}}{I} = \frac{\frac{F}{2} (d_1 - d_2) \frac{t_1}{2}}{\frac{wt^3}{12}} \rightarrow \frac{F}{\sigma_b} = \frac{wt_1^2}{3(d_1 - d_2)} = 100 \quad (\text{C.5})$$

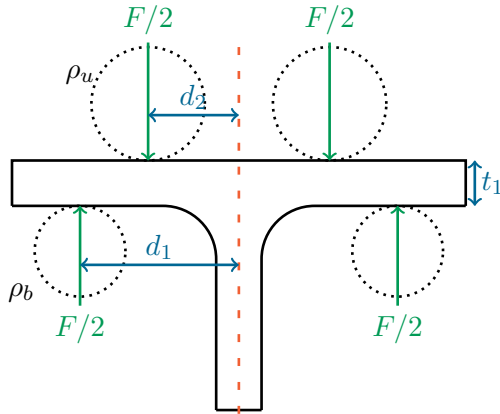


TABLE C.4: Parameter values

Lever	$d_1$	35	[mm]
	$d_2$	20	[mm]
Radius upper roller	$\rho_u$	12.5	[mm]
Radius bottom roller	$\rho_b$	10	[mm]
Width	$w$	45	[mm]
Thickness bottom plate	$t_1$	10	[mm]

FIGURE C.6: Schematic visualisation of the four-point bending test set-up.

## 2.2 Method 2: Down-scaling the FAT Class curve of the parent material.

As stated by the recommendations of the IIW [40], the AA5000 aluminium alloy has a FAT class of 71, with the slope factor  $m = 5$ . Using Equation (C.3)  $\log C$  has a value of 15.6. A two dimensional (2D) FEM calculation is performed using Ansys APDL 17.1 to obtain the stress concentration factor (SCF) in the DS T-joint.

TABLE C.5: *Estimated force calculation (50% reliability) for DS T-joint specimen, using the ratio derived for the butt-joint study of Costa et al. [17], comparing friction stir welding and arc welding,  $r_l = 0.1$*

N	Arc welding					Friction stir welding					ratio
	$S_{97.7}$	$S_{50}$	$\Delta F_{50}$	$F_{50,min}$	$F_{50,max}$	$S_{97.7}$	$S_{50}$	$\Delta F_{50}$	$F_{50,min}$	$F_{50,max}$	
$10^4$	164	259	25924	2880	28805	115	261	20317	2257	22575	1.42
$10^5$	76	120	12033	1337	13370	71	162	12576	1397	13973	1.06
$10^6$	35	56	5585	621	6206	44	78	7784	865	8649	0.80
$10^7$	16	26	2592	288	2880	27	48	4818	535	5353	0.60

Since the DS T-joint is symmetrical, modelling half a geometry with respect to the symmetrical axis is sufficient (one sides (OS) T-joint) presupposing the symmetrical axis is constraint in x-direction. Furthermore, the upper and lower roller are modelled. PLANE42-elements are used for the geometries of the OS T-joint and the rollers. A non-linear calculation is conducted due to the implementation of contact elements, which are placed between the contact areas of the OS T-joint and the rollers. For the contact area, CONTA171-elements are chosen, since this element is applicable to 2D structural and coupled-field contact analyses. These elements will be attached to the outer nodes of the solid rollers. Since pair-based contact is applicable, TARGET169-elements must be chosen to define the target area, in particular the flat part of the DS T-joint. The contact elements are characterised in the model in that way the contact area is bonded in all direction. For the target elements, no deformation and rotation restrictions are imposed. A point load is placed in the centroid of the upper solid roller. The two upper rollers are constraint in both x- and y-direction. The central roller is only constraint in x-direction to allow a vertical displacement. For the mesh an element size  $e_s$  of 0.15 is used to obtain mesh convergence.

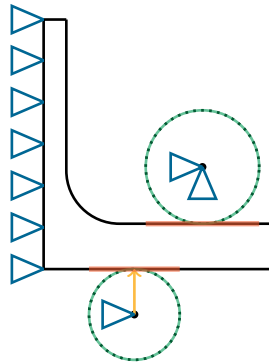


FIGURE C.7: *Schematic visualisation of the contact area (green), the target area (red), the loading condition (yellow) and the boundary conditions (blue) of the DS T-joint implemented in FEM.*

Looking at the overall DS T-joint block, the critical spot is located at the end of the fillet radius, as presented in Figure C.8a and Figure C.8b.

Implementing the obtained SCF ( $K_t = 1.36$ ) to down-scale the FAT Class curve of the parent material, FAT52 is created, leaving the slope factor unchanged ( $m = 5$ ). After applying the same method to shift the design curve with 97.7% reliability to the mean curve with 50% reliability, as explained in Section 2.1, Table C.6 follows.

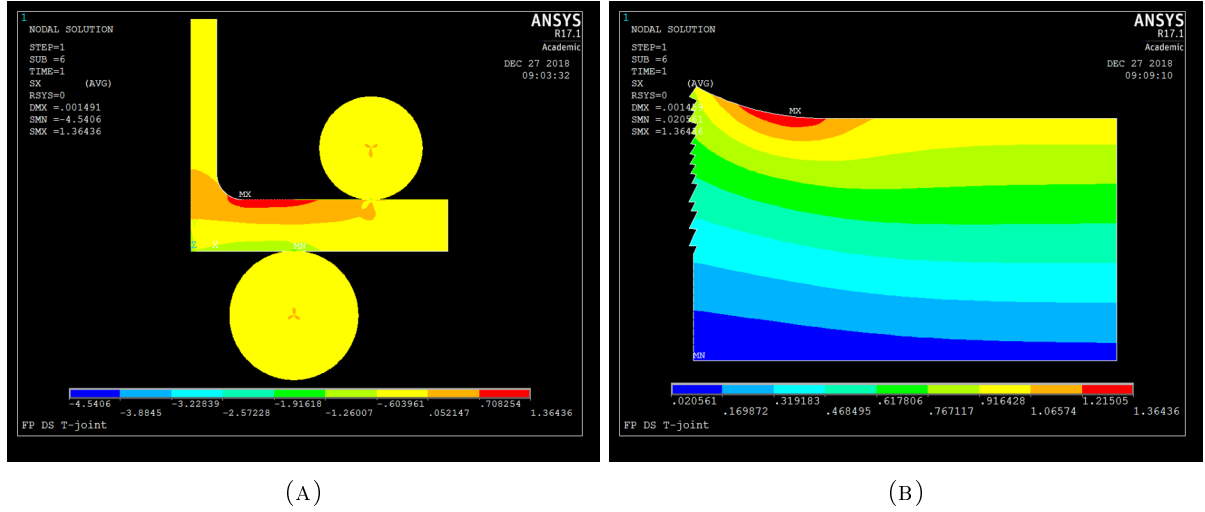


FIGURE C.8: *Stress distribution calculated using FEM in the DS T-joint. (A) overall view and (B) detail view. The inconsistencies at the edges of the detailed view (B) are due to the chosen element mesh, and element orientation.*

TABLE C.6: *Estimated force calculation (50% reliability) for DS T-joint specimen, using the SCF derived from the FEM, comparing FSW and arc welding,  $r_l = 0.1$ .*

$N$	Parent material					Friction stir welding				
	$S_{97.7}$	$S_{50}$	$\Delta F_{50}$	$F_{50,min}$	$F_{50,max}$	$S_{97.7}$	$S_{50}$	$\Delta F_{50}$	$F_{50,min}$	$F_{50,max}$
$10^4$	205	270	26989	2999	29988	151	198	19800	2200	22000
$10^5$	129	170	17029	1892	18921	95	125	12500	1389	13889
$10^6$	82	107	10745	1194	11938	60	79	7900	878	8778
$10^7$	51	68	6779	753	7533	38	50	5000	556	5556

### 2.3 Method 3: Existing fatigue data in literature.

Sidhom et al. [67] ( $r_l = 0.1$ ) and de Jesus et al. [22] ( $r_l = 0$ ) have performed a fatigue life time analysis on DS T-joints by comparable joining techniques. Sidhom et al. applied shot peening, which is an enhancement of the arc weld to obtain surface hardening. Jesus et al. applied the butt-joint welding technique on the underside of the DS T-joint and obtained the fillet radius by pressing material downwards in a prepared mould. Extra material is added at the bottom of the DS T-joint as a T-lab-joint or T-butt-joint (Figure C.9).

Figure C.10 shows the datasets for the three DS T-joint fatigue analyses, including with the accompanying mean SN-curve that will be used to calculate the corresponding stress range and the required minimum and maximum force for the load ratio  $r_l = 0.1$  (Table C.7).

## 3 Statistical analysis of fatigue data

Fatigue resistance is described using the SN-curve, which displays the relation between the stress range  $S$  (alternating stress) and the number of cycles to failure  $N$ , both on logarithmic scales. The relation can be established using the obtained fatigue test data.

The fatigue life is characterised by three different zones: low cycle fatigue (LCF), medium cycle fatigue (MCF) and high cycle fatigue (HCF) (Figure C.11). A high level stress range ( $S \rightarrow \hat{\sigma}_u$ ) is applicable for the LCF, resulting in a plastic/elasto-plastic region. The MCF is a predominantly



FIGURE C.9: Schematic view of DS T-lap-joint (A) and DS T-butt-joint (B) used as structural details in the fatigue analysis of de Jesus et al. [21]. The red lines represent the mould.

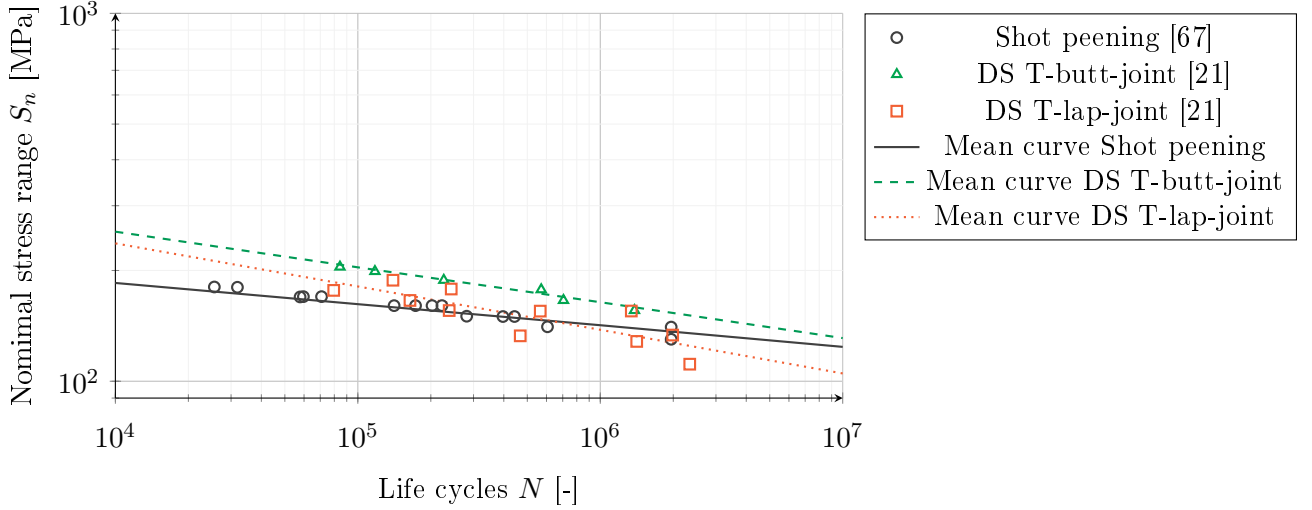


FIGURE C.10: Fatigue data of DS T-joint with comparable joining techniques ( $\circ$ ), including mean SN-curve. [21, 67]

elastic region, which endure medium stress level ranges ( $S \approx \hat{\sigma}_y$ ). The low stress level range indicates the HCF, and is present in a life time range starting at  $10^7$  cycles. In ferrous alloys and titanium alloys, the HCF region features a distinct limit, called the fatigue limit  $S_f$ . The fatigue limit indicates the stress level where below no failure seems to be present, in other words an infinite number of cycles can be sustained. Aluminium does not exhibit a distinct fatigue limit, but more a continuously decreasing SN-curve. A fatigue strength  $\hat{\sigma}_f$  for a given number of cycles must be specified (at  $10^8$  cycles). [23, 57]

#### 4 Log-likelihood principle

For the test results, a likelihood approach is adopted as regression analysis to estimate the model parameters which are captured in  $\theta$ , since this method is able to incorporate both the failure data and the run-outs. The likelihood function  $L$  is given by Equation (C.6) where  $f$  represents the probability density function (PDF) and  $F$  is the corresponding distribution function (CDF).

$$L(\theta; N|S) = \prod_{j=1}^n \{f(N_j|S_j; \theta)\}^{\delta_j} \{1 - F(N_j|S_j; \theta)\}^{1-\delta_j} \quad (\text{C.6})$$

TABLE C.7: *Estimated force calculation (50% reliability) for DS T-joint specimen, using existing fatigue data,  $r_l = 0.1$*

$N$	Shot peening [67]				FSW DS T-butt-joint [22]			
	$S_{50}$	$\Delta F_{50}$	$F_{50,min}$	$F_{50,max}$	$S_{50}$	$\Delta F_{50}$	$F_{50,min}$	$F_{50,max}$
$10^4$	185	18500	2056	20556	255	25500	2833	28333
$10^5$	162	16200	1800	18000	204	20400	2267	22667
$10^6$	142	14200	1578	15778	164	16400	1822	18222
$10^7$	124	12400	1378	13778	131	13100	1456	14556

$N$	FSW DS T-lap-joint [22]			
	$S_{50}$	$\Delta F_{50}$	$F_{50,min}$	$F_{50,max}$
$10^4$	237	23700	2633	26333
$10^5$	181	18100	2011	20111
$10^6$	138	13800	1533	15333
$10^7$	105	10500	1167	11667

where,

$$\begin{aligned} \delta_j = 1 & \quad \text{failure} \\ \delta_j = 0 & \quad \text{run-out} \end{aligned}$$

The log-likelihood function now simply is obtained by taking the the log of the likelihood function, which results in Equation (C.7).

$$\mathcal{L}(\boldsymbol{\theta}; N|S) = \log\{L(\boldsymbol{\theta}; N|S)\} \tag{C.7}$$

$$= \sum_{j=1}^n \mathcal{L}_j(\boldsymbol{\theta}; N_j|S_j) \tag{C.8}$$

$$= \sum_{j=1}^n \delta_j \{f(N_j|S_j; \boldsymbol{\theta}) + (1 - \delta_j)\{1 - F(N_j|S_j; \boldsymbol{\theta})\}\} \tag{C.9}$$

where,

$$\begin{aligned} \delta_j = 1 & \quad \text{failure} \\ \delta_j = 0 & \quad \text{run-out} \end{aligned}$$

Per chosen SN-curve formulation the PDF and CDF will differ. For the log-Normal distribution and the 2-parameter (scale, location) Weibull distribution with parameters  $\mu$  and  $\sigma$ , the following holds for the continuous single slope formulation, where erf denotes the Gauss error function:

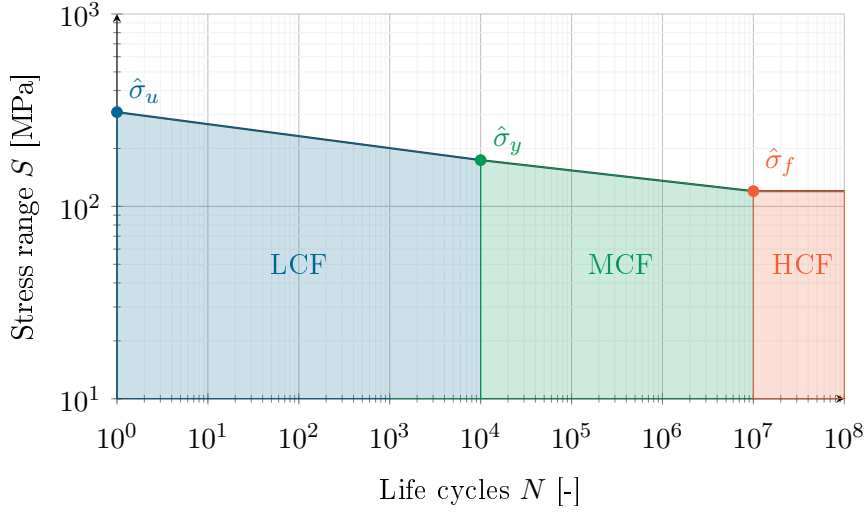


FIGURE C.11: Schematic visualisation of LCF, MCF and HCF region for the aluminium alloy 5083-H111 using Table 3.2.

$$\left. \begin{aligned} f &= \frac{1}{\sigma\sqrt{2\pi}} \exp\left[-\frac{(N-\mu)^2}{2\sigma^2}\right] \\ F &= \frac{1}{2} \left(1 + \operatorname{erf}\left[-\frac{N-\mu}{\sqrt{2}\sigma}\right]\right) \end{aligned} \right\} \text{log-Normal}$$

$$\left. \begin{aligned} f &= \frac{1}{\sigma} \exp\left[\frac{x-\mu}{\sigma} - \exp\left[-\frac{x-\mu}{\sigma}\right]\right] \\ F &= \exp\left[-\exp\left[-\frac{x-\mu}{\sigma}\right]\right] \end{aligned} \right\} \text{Weibull}$$

where,

$$\begin{aligned} \mu &= \log C - m \log(S) \\ \operatorname{erf}(x) &= \frac{1}{\sqrt{\pi}} \int_{-x}^x \exp[-t^2] dt \end{aligned}$$

For the continuous dual slope formulation, the PDF and CDF are chosen following Pascual and Meeker [57] for both the log-Normal and the Weibull distribution.  $S_f$  denotes the fatigue limit.

$$\left. \begin{aligned} f &= \frac{1}{2\pi\sigma\sigma_{S_f}} \exp\left[-\frac{(N-\mu)^2}{2\sigma^2}\right] \exp\left[-\frac{(S_f-\mu_{S_f})^2}{2\sigma_{S_f}^2}\right] \\ F &= \frac{1}{2\sqrt{2\pi}\sigma_{S_f}} \left(1 + \operatorname{erf}\left[-\frac{N-\mu}{\sqrt{2}\sigma}\right]\right) \exp\left[-\frac{(N-\mu_{S_f})^2}{2\sigma_{S_f}^2}\right] \end{aligned} \right\} \text{log-Normal}$$

$$\left. \begin{aligned} f &= \frac{1}{\sigma\sigma_{S_f}} \exp\left[\frac{N-\mu}{\sigma} - \exp\left[-\frac{N-\mu}{\sigma}\right]\right] \exp\left[\frac{S_f-\mu_{S_f}}{\sigma_{S_f}} - \exp\left[-\frac{S_f-\mu_{S_f}}{\sigma_{S_f}}\right]\right] \\ F &= \frac{1}{\sigma_{S_f}} \exp\left[-\exp\left[-\frac{N-\mu}{\sigma}\right]\right] \exp\left[\frac{S_f-\mu_{S_f}}{\sigma_{S_f}} - \exp\left[-\frac{S_f-\mu_{S_f}}{\sigma_{S_f}}\right]\right] \end{aligned} \right\} \text{Weibull}$$

where,

$$\mu = \log C - m \log (S - S_f)$$

$$\operatorname{erf}(x) = \frac{1}{\sqrt{\pi}} \int_{-x}^x \exp [-t^2] dt$$

## 5 Effective notch stress distribution

### 5.1 Weld toe notch stress distribution for notch radius $\rightarrow 0$

The stress distribution for the weld toe notch is given below, of which the full derivation of the required parameters  $\{\mu_s, \mu_a, \lambda_s, \lambda_a, \chi_s, \chi_a\}$  is expressed by den Besten [23]. The value of the weld load carrying stress coefficient has to be obtained in an implicit way.

$$\sigma_n \left( \frac{r}{t_1} \right) = \sigma_s \left[ \left( \frac{r}{t_1} \right)^{\lambda_s - 1} \mu_s \lambda_s (\lambda_s + 1) \{ \cos ((\lambda_s + 1)\beta) - \chi_s \cos ((\lambda_s - 1)\beta) \} + \left( \frac{r}{t_1} \right)^{\lambda_a - 1} \mu_a \lambda_a (\lambda_a + 1) \{ \sin ((\lambda_a + 1)\beta) - \chi_a \sin ((\lambda_a - 1)\beta) \} + C_{bw} \left( 2 \left( \frac{r}{t_1} \right) - 1 \right) - 2r_s \left( \frac{r}{t_1} \right) \right]$$

Since the value of  $C_{bw}$  cannot be calculated analytically, one is required to tune the  $C_{bw}$  value so that the analytical notch stress distribution and the stress distribution in the cross section of the FEM calculation match. The same 2D FEM calculation is performed as stated in Section 2.2, only with the addition of the undercut. The undercut is localised at 11 [mm] from the side of the cross plate. Looking at the overall DS T-joint block, the critical spot is located at the undercut, as presented in Figure C.12a and Figure C.12b.

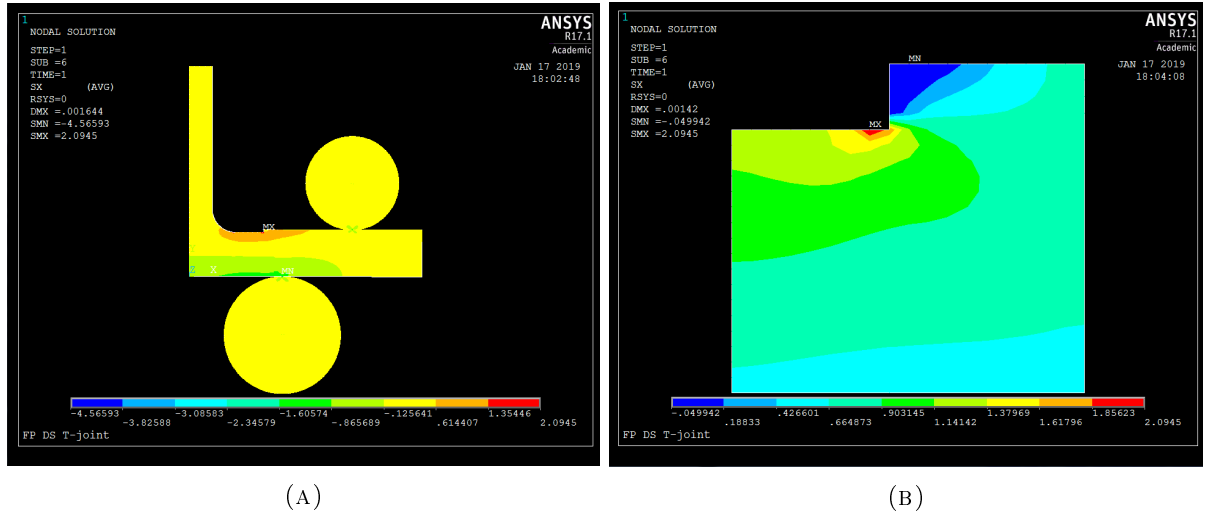


FIGURE C.12: Stress distribution calculated using FEM in the DS T-joint including an undercut of 0.5 [mm]. (A) overall view and (B) detail view.

Figure C.13 gives the structural field stress  $\sigma_f$ , the FEM calculation data and the analytical notch stress distribution  $\sigma_n$  including the tuned value of the  $C_{bw}$ , which equals 0.17, all expressed relatively to the structural stress  $\sigma_s$ .

Since a pure bending stress component follows from the applied load case in the 4-point bending, one may assume that the structural bending stress ratio  $r_s$  equals 1:  $\sigma_s = r_s \sigma_b = \sigma_b$ . For the structural field stress distribution  $\sigma_f$ , the linearised distribution is applied, characterised by Equation (C.10).

$$\sigma_f \left( \frac{r}{t_1} \right) = \sigma_s \left[ 1 - 2r_s \left( \frac{r}{t_1} \right) \right] \quad \forall \left\{ 0 \leq \left( \frac{r}{t_1} \right) \leq 1 \right\} \quad (\text{C.10})$$

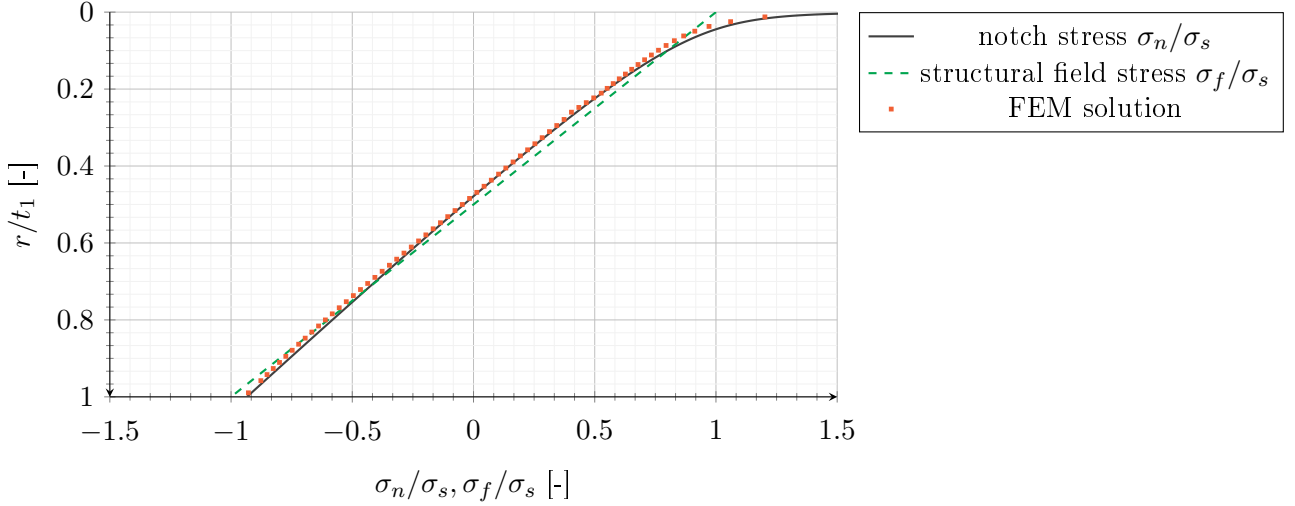


FIGURE C.13: Notch stress distribution of the DS  $t$ -joint, including an undercut of 0.5 [mm].

In Table C.8 the parameters to describe the notch stress distribution are presented. The obtained value of the  $C_{bw}$  should be in relation with the stress concentration factor, by  $K_t \approx 1 + C_{bw}$ . Applied on the stress distribution located at the undercut, one find:  $K_t \approx 1.77$ ,  $(1 + C_{bw}) \approx 1.19$ . The value of  $K_t$  is not really close to  $(1 + C_{bw})$ .

TABLE C.8: Calculated values in the analysis of the notch stress distribution of the DS  $T$ -joint, including an undercut.  $\alpha$  and  $\beta$  are expressed in [rad].

$\alpha$	$\beta$	$\mu_s$	$\mu_a$	$\lambda_s$	$\lambda_a$	$\chi_s$	$\chi_s$
2.3562	0.7854	0.0110	0.3814	0.5445	0.9085	-1.8414	4.5678

## 5.2 Weld toe notch stress distribution for notch radius $> 0$

When the fillet radius of the test specimen is assumed to be not fully effective, the weld toe notch stress distribution for a notch radius larger than zero is applicable. This formulation is given below following den Besten [23], who has derived the required parameters  $\{\mu_s, \mu_a, \lambda_s, \lambda_a, \chi_s, \chi_a, \zeta_s, \zeta_a, \omega_{s1}, \omega_{s2}, \omega_{a1}, \omega_{a2}\}$  to solve the equation. The value of the weld load carrying stress coefficient has to be obtained in an implicit way.

$$\begin{aligned}
\sigma_n \left( \frac{r}{t_1} \right) = \sigma_s \left[ \mu_s \left\{ \left( \frac{r''}{t_1} \right)^{\lambda_s - 1} \lambda_s (\lambda_s + 1) \{ \cos((\lambda_s + 1)\beta) - \right. \right. \\
\chi_s \cos((\lambda_s - 1)\beta) \} + \\
\left. \left( \frac{r''}{t_1} \right)^{\zeta_s - 1} \left( \frac{r_0}{t_1} \right)^{\lambda_s - \zeta_s} \lambda_s \frac{2\alpha}{4 \left( \frac{2\alpha}{\pi} - 1 \right)} \cdot \right. \\
\left. \{ \omega_{s1} \cos((\zeta_s + 1)\beta) + \right. \\
\left. \omega_{s2}(\zeta_s + 1) \cos((\zeta_s - 1)\beta) \} \right\} + \\
\mu_a \left\{ \left( \frac{r''}{t_1} \right)^{\lambda_a - 1} \lambda_a (\lambda_a + 1) \{ \sin((\lambda_a + 1)\beta) - \right. \\
\chi_a \sin((\lambda_a - 1)\beta) \} + \\
\left. \left( \frac{r''}{t_1} \right)^{\zeta_a - 1} \left( \frac{r_0}{t_1} \right)^{\lambda_a - \zeta_a} \lambda_a \frac{1}{4(\zeta_a - 1)} \cdot \right. \\
\left. \{ \omega_{a1} \sin((\zeta_a + 1)\beta) + \right. \\
\left. \omega_{a2}(\zeta_a + 1) \sin((\zeta_a - 1)\beta) \} \right\} + \\
C_{bw} \left( 2 \left( \frac{r}{t_1} \right) - 1 \right) - 2r_s \left( \frac{r}{t_1} \right) \Big]
\end{aligned}$$

Since the value of  $C_{bw}$  cannot be calculated analytically, one is required to tune the  $C_{bw}$  value so that the analytical notch stress distribution and the stress distribution in the cross section out of the FEM calculation match.

Figure C.14 gives the structural field stress  $\sigma_f$ , the FEM calculation data and the analytical notch stress distribution  $\sigma_n$  including the tuned value of the  $C_{bw}$ , which equals 0.39, all expressed relatively to the structural stress  $\sigma_s$ .

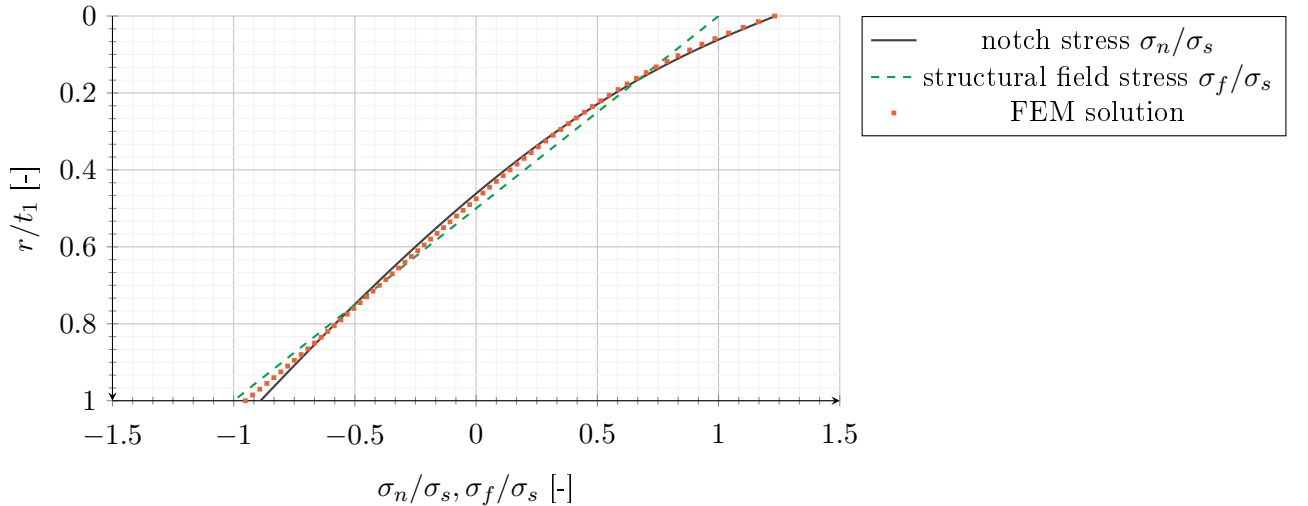


FIGURE C.14: *Notch stress distribution of the DS t-joint.*

In Table C.9 the parameters to describe the notch stress distribution are presented. Comparing the value of the stress concentration factor  $K_t$  with  $(1 + C_{bw})$ , one obtains:  $K_t \approx 1.36$ ,  $(1 + C_{bw}) \approx 1.39$ . Both figures correspond with each other, which tells that the prediction seems to be good.

TABLE C.9: *Calculated values in the analysis of the notch stress distribution of the DS T-joint.  $\alpha$  and  $\beta$  are expressed in [rad].*

$\alpha$	$\beta$	$\mu_s$	$\mu_a$	$\lambda_s$	$\lambda_a$	$\chi_s$	$\chi_a$
2.3562	0.7854	0.0110	0.3814	0.5445	0.9085	-1.8414	4.5678
$\zeta_s$	$\zeta_a$	$\omega_{s1}$	$\omega_{s2}$	$\omega_{a1}$	$\omega_{a2}$		
0.0879	0.9220	0.7782	-1.0958	0.7144	-1.7025		

# Bibliography

- [1] H. G. Allen. *Analysis and design of structural sandwich panels: the commonwealth and international library: structures and solid body mechanics division*. Elsevier, 2013.
- [2] M. F. Ashby. Materials Selection in Mechanical Design Third Edition. *Design*, page 624, 2005. doi: 10.1016/B978-1-85617-663-7.00001-1.
- [3] M. F. Ashby, A. G. Evans, N. A. Fleck, L. J. Gibson, J. W. Hutchinson, and H. N. G. Wadley. Metal Foams : A Design Guide Metal Foams : A Design Guide. *Library*, 54(Report Number CUED/C-MICROMECH/TR3):251, 2000. ISSN 00036900. doi: 10.1115/1.1421119.
- [4] S. Balos, D. L. Zlatanovic, P. Janjatovic, M. Dramicanin, D. Rajnovic, and L. Sidjanin. Wear Resistance Increase by Friction Stir Processing for Partial Magnesium Replacement in Aluminium Alloys. *IOP Conference Series: Materials Science and Engineering*, 329(1), 2018. ISSN 1757899X. doi: 10.1088/1757-899X/329/1/012017.
- [5] J. Banhart and H. W. Seeliger. Aluminium foam sandwich panels: Manufacture, metallurgy and applications, 2008. ISSN 14381656.
- [6] J. Banhart and H. W. Seeliger. Recent trends in aluminum foam sandwich technology. In *Advanced Engineering Materials*, volume 14, pages 1082–1087, 2012. doi: 10.1002/adem.201100333.
- [7] U. Bankhofer, V. Nissen, S. Straßburger, and D. Stelzer. A cost calculation model for determining the cost of business process modelling projects. 2013.
- [8] J. Barjis. Enterprise, Organization, Modeling, Simulation: Putting Pieces Together. In *Proceedings of EOMAS 2008*, 2008.
- [9] J. Belan, A. Vaško, L. Kuchariková, and E. Tillová. The fractography analysis of IN718 alloy after three-point flexure fatigue test. *MATEC Web of Conferences*, 157:1–8, 2018.
- [10] O. W. Blodgett. *Design of weldments*. James F. Lincoln Arc Welding Foundation, 1963.
- [11] E. Broitman. Indentation Hardness Measurements at Macro- , Micro- , and Nanoscale : A Critical Overview. 2017. doi: 10.1007/s11249-016-0805-5.
- [12] L. A. Carlsson and G. A. Kardomateas. Structural and failure mechanics of sandwich composites. *Solid Mechanics and its Applications*, 121:1–399, 2011. ISSN 09250042. doi: 10.1007/978-1-4020-3225-7\_1.
- [13] A. Carrado, O. Sokolova, G. Ziegmann, and H. Palkowski. Press Joining Rolling Process for Hybrid Systems. *Key Engineering Materials*, 425:271–281, 2010. ISSN 1662-9795. doi: 10.4028/www.scientific.net/KEM.425.271.
- [14] Celcomponents, 2018. URL <http://pdf.nauticexpo.com/pdf/cel-components-srl/alu-alu-fr/34324-88038.html>.

- [15] C. Chuenarrom, P. Benjakul, and P. Daosodsai. Effect of Indentation Load and Time on Knoop and Vickers Microhardness Tests for Enamel and Dentin. 12(4):473–476, 2009.
- [16] K. J. Colligan. *The friction stir welding process: An overview*. Woodhead Publishing Limited, 2009. ISBN 9781845694500. doi: 10.1533/9781845697716.1.15.
- [17] J. D. Costa, J. A. M. Ferreira, and L. P. Borrego. Influence of spectrum loading on fatigue resistance of AA6082 friction stir welds. *International Journal of Structural Integrity*, 2(2): 122–134, 2011. ISSN 1757-9864. doi: 10.1108/17579861111135888.
- [18] V. Crupi, G. Epasto, and E. Guglielmino. Comparison of aluminium sandwiches for lightweight ship structures: Honeycomb vs. foam. *Marine Structures*, 30:74–96, 2013. ISSN 09518339. doi: 10.1016/j.marstruc.2012.11.002.
- [19] DAMEN Shipyards Group, 2018. URL <https://www.damen.com/en>.
- [20] J. S. de Jesus, A. Loureiro, J. M. Costa, and J. M. Ferreira. Journal of Materials Processing Technology Effect of tool geometry on friction stir processing and fatigue strength of MIG T welds on Al alloys. 214:2450–2460, 2014.
- [21] J. S. de Jesus, M. Gruppelaar, J. M. Costa, A. Loureiro, and J. M. Ferreira. Effect of geometrical parameters on Friction Stir Welding of AA 5083-H111 T- ScienceDirect ScienceDirect ScienceDirect Effect of geometrical parameters on Friction Stir Welding of AA 5083-H111 T-joints modeling of a high pressure turbine blade of an airplane gas turbine engine. *Procedia Structural Integrity*, 1(July):242–248, 2016. ISSN 2452-3216. doi: 10.1016/j.prostr.2016.02.033.
- [22] J. S. de Jesus, J. M. Costa, A. Loureiro, and J. M. Ferreira. Assessment of friction stir welding aluminium T-joints. *Journal of Materials Processing Tech.*, 255(December 2017): 387–399, 2018. ISSN 0924-0136. doi: 10.1016/j.jmatprotec.2017.12.036.
- [23] J. H. den Besten. Fatigue resistance of welded joints in aluminium high-speed craft: a total stress concept, 2015.
- [24] R. Dou, S. Qiu, Y. Ju, and Y. Hu. Simulation of compression behavior and strain-rate effect for aluminum foam sandwich panels. *Computational Materials Science*, 112:205–209, 2016. ISSN 09270256. doi: 10.1016/j.commatsci.2015.10.032.
- [25] H. El-Fahar, H. Abd El-Hafez, M. Ahmed, E. Ahmed, and A. El-Nikhaily. Effect of tool geometry on microstructure and mechanical Properties of friction stir processed AA2024-T351 aluminium alloy. *Materials Today: Proceedings*, 5(1):2965–2979, 2018. ISSN 22147853. doi: 10.1016/j.matpr.2018.01.095.
- [26] M. Ericsson and R. Sandström. Influence of welding speed on the fatigue of friction stir welds, and comparison with MIG and TIG. *International Journal of Fatigue*, 25(12):1379–1387, 2003. ISSN 01421123. doi: 10.1016/S0142-1123(03)00059-8.
- [27] S. O. Erikstad. Modularisation in Shipbuilding and Innovation in Global Maritime Production – 2020. (May), 2015.
- [28] European Commision. Best Practice Guide for Sandwich Structures in Marine Applications. page 279, 2013.
- [29] European Committee for Standardization (CEN). Eurocode 3 : Design of Steel Structures; Part 1.1: General rules and rules for buildings —. Technical report, 1993.

- [30] D. J. Eyres and G. J. Bruce. *Ship construction: Seventh edition*. 2012. ISBN 9780080972398. doi: 10.1016/C2010-0-68324-6.
- [31] V. Gaur, M. Enoki, T. Okada, and S. Yomogida. Influence of Weld Parameters and Filler-Wire on Fatigue Behavior of MIG- Fatigue life and crack growth behavior of post welded Aluminum 5183 alloy. 2018. doi: 10.1007/978-3-319-70365-7.
- [32] L. J. Gibson and M.F Ashby. *Cellular Solids, structure and properties*. 1997. ISBN 0521499119. doi: 10.1557/mrs2003.79.
- [33] H. R. Greve. ‘Exploration and exploitation in product innovation’. *Industrial and Corporate Change*, 2007. ISSN 0960-6491. doi: 10.1093/icc/dtm013.
- [34] B. Gungor, E. Kaluc, E. Taban, and A. SIK ŞŞ. Mechanical and microstructural properties of robotic Cold Metal Transfer (CMT) welded 5083-H111 and 6082-T651 aluminum alloys. *Materials and Design*, 54:207–211, 2014. ISSN 18734197. doi: 10.1016/j.matdes.2013.08.018.
- [35] M. Harhash, O. Sokolova, A. Carrado, and H. Palkowski. Mechanical properties and forming behaviour of laminated steel / polymer sandwich systems with local inlays – Part 1. *Composite Structures*, 118:112–120, 2014. ISSN 0263-8223. doi: 10.1016/j.compstruct.2014.07.011.
- [36] S. T. Hasan and C. Shaw. A method of detecting corrosion damage in aluminium honeycomb and metallic aluminium foam sandwich panels. pages 1–7, 2006.
- [37] Havel Metal Foam, 2018. URL <http://en.havel-mf.com>.
- [38] S. Hellgren. The Bayesian Model for Cruise Shipbuilding: a Process for Production Efficiency and Organisation. *Doctoral Dissertation*, 2016.
- [39] P. Hess, S. Aksu, M. Vaz, G. Feng, L. Li, P. Jurisic, M. R. Andersen, P. Caridis, P. Boote, H. Murayama, N. Amila, N. Leira, M. Tammer, J. Blake, N. Chen, and A. Egorov. Committee V.7: Structural longevity. In M.L. Kaminski and P Rigo, editors, *Proceedings of the 20th International Ship and Offshore Structures Congress (ISSC 2018)*, volume II, 2018. ISBN 9781138028951. doi: 10.3233/978-1-61499-864-8-391.
- [40] A. Hobbacher. IIW document IIW-1823-07 Recommendations for fatigue design of welded joints and components. 2008.
- [41] W. Hussein and M. A. Al-shammari. Fatigue and Fracture Behaviours of FSW and FSP Joints of AA5083-H111 Aluminium Alloy Fatigue and Fracture Behaviours of FSW and FSP Joints of AA5083-H111 Aluminium Alloy Fatigue and Fracture Behaviours of FSW and FSP Joints of AA5083- H111 Aluminium Alloy. *International Conference on Materials Engineering and Science*, 2018. doi: 10.1088/1757-899X/454/1/012055.
- [42] L. Josefson, S. van Duin, B. de Carvalho Pinheiro, N. Yang, L. Yu, A. Zamarin, H. Remes, F. Roland, M. Gaiotti, N. Osawa, A. M. Horn, M. H. Kim, and B. Mishra. Committee V.3: Materials and fabrication technology. In Mirek Kaminski and P Rigo, editors, *Proceedings of the 20th International Ship and Offshore Structures Congress (ISSC 2018)*, volume II, pages 143–191, 2018. ISBN 9781614998648. doi: 10.3233/978-1-61499-864-8-143.
- [43] S. Kasman, F. Kahraman, A. Emiralioglu, and H. Kahraman. A Case Study for the Welding of Dissimilar EN AW 6082 and EN AW 5083 Aluminum Alloys by Friction Stir Welding. *Metals*, 7(1):6, 2016. ISSN 2075-4701. doi: 10.3390/met7010006.
- [44] D. Klob, L. Kosec, A. Pietras, and A. Smolej. Friction-stir welding of aluminium alloy 5083. (May), 2016.

- [45] P. Kujala and A. Klanac. Steel Sandwich Panels in Marine Applications (PDF Download Available). 56:305–314, 2005. ISSN 0007215X.
- [46] Life07 ENV/S/000904. Recycling of Waste Glass Fibre Reinforced Plastic With Microwave Pyrolysis. page 8, 2012.
- [47] Lloyd’s Register. Rules and Regulations for the Classification of Ships. *Notice No. 9*, (July): 28, 2014.
- [48] T. J. Lu. Heat transfer efficiency of metal honeycombs. *International Journal of Heat and Mass Transfer*, 42(11):2031–2040, 1998. ISSN 00179310. doi: 10.1016/S0017-9310(98)00306-8.
- [49] J. P. Martin, C. Stanhope, and S. Gascoyne. Novel Techniques for Corner Joints Using Friction Stir Welding. *TMS 2011 Annual Meeting & Exhibition*, pages 6–10, 2011.
- [50] Metalfoam, 2017. URL <http://metalfoam.de/metalfoam/>.
- [51] Migatronic, 2018. URL <https://www.migatronic.com/en/types-of-welding/mig-mag>.
- [52] R. S Mishra and M. W. Mahoney. Friction Stir Welding and Processing. *ASM International*, page 368, 2007. ISSN 1523-1747. doi: 10.1361/fswp2007p001.
- [53] K. Mutombo and M. Du. Corrosion Fatigue Behaviour of Aluminium 5083-H111 Welded Using Gas Metal Arc Welding Method. *Arc Welding*, 2011. ISSN 18684408. doi: 10.5772/25991.
- [54] Y. Okumoto, Y. Takeda, M. Mano, and T. Okada. *Design of ship hull structures: A practical guide for engineers*. 2009. ISBN 9783540884446. doi: 10.1007/978-3-540-88445-3.
- [55] J. K. Paik and A. K. Thayamballi. *Ultimate limit state design of steel-plated structures*. John Wiley & Sons, 2003.
- [56] H. Palkowski, O. Sokolova, and A. Carrado. Sandwich Materials. *Encyclopedia of Automotive Engineering*, page 17, 2014. doi: 10.1002/9781118354179.auto163.
- [57] F. G. Pascual and W. Q. Meeker. Estimating Fatigue Curves With the Random Fatigue-Limit Model. 1999.
- [58] M. Pedemonte, C. Gambaro, E. Lertora, and C. Mandolino. Fatigue assessment of AA 8090 friction stir butt welds after surface finishing treatment. *Aerospace Science and Technology*, 27(1):188–192, 2013. ISSN 12709638. doi: 10.1016/j.ast.2012.08.006.
- [59] A. Petras. Design of Sandwich Structures. *Proceedings of the Estonian Academy of Sciences*, pages 4–8, 1998.
- [60] J. Petrik, P. Palfy, V. Mikloš, and M. Horváth. The Influence of Operators and Applied Load on Micro-Hardness of the Standard Block. 11(9):183–196, 2014.
- [61] J. Pflug and I. Verpoest. Sandwich materials selection charts. *Journal of Sandwich Structures and Materials*, 8(5):407–421, 2006. ISSN 10996362. doi: 10.1177/1099636206065521.
- [62] A. Ravi Raja, M.Z. Khan Yusufzai, and M. Vashista. Characterization of Advancing and Retreating Weld of Friction Stir Welding of Aluminium. *International Conference on Advances in Material & Manufacturing*, 2016.
- [63] P. Rigo and J. D. Caprace. Optimization of ship structures. *Marine Technology and Engineering*, II, 2011.

- [64] F. Roland, L. Manzon, P. Kujala, M. Brede, and J. R. Weitzenbock. Advanced joining techniques in European shipbuilding. *Journal of Ship Production*, 2004. ISSN 87561417.
- [65] E. D. Schaefer. A Practical Guide for Determining the Vibration Characteristics of Plate Structures. 1979.
- [66] J. Schijve. *Fatigue of structures and materials*. Springer science & Business Media, second edition edition, 2009. ISBN 9781402068072.
- [67] N. Sidhom, A. Laamouri, R. Fathallah, C. Braham, and H. P. Lieurade. Fatigue strength improvement of 5083 H11 Al-alloy T-welded joints by shot peening : experimental characterization and predictive approach. 27:729–745, 2005. doi: 10.1016/j.ijfatigue.2005.02.001.
- [68] N. Sidhom, C. Braham, and H. P. Lieurade. Fatigue life evaluation of shop peened al-alloys 5083 H11 T-welded joints by experimental and numerical approaches. 51:50–57, 2007.
- [69] SPS, 2018. URL <http://www.ie-sps.com/about-sps>.
- [70] Streurs, 2018. URL <https://www.struers.com/en>.
- [71] Struers. Metallographic preparation of aluminium and aluminium alloys, 2018.
- [72] The Welding Institute. *Fundamentals of friction stir welding*. The Welding Institute, 3rd edition, 2016. ISBN 978-1-903761-11-3.
- [73] W. M. Thomas and E. D. Nicholas. Friction stir welding for the transportation industries. *Materials & Design*, 1997. ISSN 02613069. doi: 10.1016/S0261-3069(97)00062-9.
- [74] A. Toumpis, A. Galloway, S. Cater, and N. McPherson. Development of a process envelope for friction stir welding of DH36 steel - A step change. *Materials and Design*, 62:64–75, 2014. ISSN 18734197. doi: 10.1016/j.matdes.2014.04.066.
- [75] P. Vilaça, N. Pépe, and L. Quintino. Metallurgical and corrosion features of friction stir welding of AA5083-H111. pages 1–13, 2006.
- [76] J. R. Vinson. *The Behavior of Sandwich Structures of Isotropic and Composite Materials*. Number April. 1999. ISBN 1566766990. doi: 10.1016/S0029-8018(01)00013-0.
- [77] VinylPlus. PVC recycling technologies. 2013.
- [78] J. Wijker. *Spacecraft structures*. 2008. ISBN 9783540755524. doi: 10.1007/978-3-540-75553-1.
- [79] W. C. Young and R. G. Budynas. *Roarks’s Formulas for Stress and Strain*. 2002. ISBN 0-07-072542-X. doi: 10.1115/1.3423917.
- [80] D. Zenkert. *The handbook of sandwich construction*. Emas publishing, 1997.
- [81] G. Zu, B. Song, Z. Zhong, X. Li, Y. Mu, and G. Yao. Static three-point bending behavior of aluminum foam sandwich. *Journal of Alloys and Compounds*, 540:275–278, 2012. ISSN 09258388. doi: 10.1016/j.jallcom.2012.06.079.



“Er zijn veel vlinders die ontkennen ooit rups geweest te zijn.”

— Gerd De Ley

